Variations paléomagnétiques rapides au cours de l'Holocène : apport de nouveaux enregistrements sédimentaires marins du Groenland et lacustres varvés du Labrador dans la reconstitution de la dynamique du champ géomagnétique

Thèse présentée

dans le cadre du programme de doctorat en océanographie

en vue de l'obtention du grade de philosophiae doctor (Ph.D)

PAR

© JULIETTE GIRARD

Février 2026

Composition du jury :

André Rochon, président du jury, Université du Québec à Rimouski

Guillaume St-Onge, directeur de recherche, Université du Québec à Rimouski

Jean-Carlos Montero-Serrano, codirecteur de recherche, Université du Québec à Rimouski

Pierre Francus, codirecteur de recherche, Institut National de la Recherche Scientifique

Annick Chauvin, examinatrice externe, Université de Rennes

Dépôt initial le 12 septembre 2025 Dépôt final le 10 février 2026

REMERCIEMENTS

Je remercie Annick Chauvin et André Rochon d'avoir accepté de faire partie de mon jury, de relire ma thèse et d'évaluer mon travail.

Je remercie mon superviseur, Guillaume pour m'avoir permis de travailler sur ce projet. Merci Guillaume pour ta confiance, pour m'avoir laissé une grande liberté au cours de ce doctorat qui m'a permis de faire ce que je voulais, et pour ton optimisme qui m'a permis de toujours trouver du positif dans mes données. Merci pour les très nombreuses opportunités que tu m'as offertes, d'expériences diverses et de collaborations. Je remercie également mes co-superviseurs Jean-Carlos et Pierre, pour m'avoir permis, avec Guillaume, de faire plusieurs campagnes de terrain qui ont toutes été d'incroyables expériences.

J'ai eu la chance de travailler avec deux personnes sans qui ce doctorat n'aurait pas été la même expérience, France Lagroix et Brendan Reilly. France, merci d'avoir fait partie de mon comité de thèse, et de m'avoir accueillie dans ton labo. Merci pour ton aide, ta disponibilité et ta bienveillance depuis le début de ce doctorat, et jusqu'à aujourd'hui encore. *Brendan, thank you for welcoming me in your lab, for everything you've taught me. Thank you for your help and availability beyond our work together. Thank you for the many discussions we had, for which you were always available and happy to have. I have learned so much from you. Thank you, Beth and Alsea for making my time in Nyack so great.* Merci pour vos enseignements en paléomagnétisme environnemental, géomagnétisme, sédimentologie, j'ai eu la chance d'apprendre beaucoup de choses auprès de vous.

J'ai aussi eu la chance de travailler avec plein de personnes de qui j'ai beaucoup appris. *Marit-Solveig Seidenkrantz and Christof Pearce, thank you for providing the material for my second chapter and for the numerous discussions we had. Anne Jennings, thank you for trusting me to work with you and for sharing your knowledge of Baffin bay and Nares Strait* *with me. Thank you to the Sed Mag Seminar team. Joe, Rob, Lindsey, Deepa, Sami, Olga, Maggie, I learned a lot during our meetings and I hope we continue to male it work. I look forward to the next conference where I get to see you.*

Un immense merci à Ericka, Martine, Nancy, Brigitte, Katia, Marielle pour votre aide précieuse tout au long de mon séjour à l'ISMER. Merci Dominique pour ton aide pour les analyses de granulométrie au laboratoire.

Je tiens à remercier toutes les personnes qui ont participé à la campagne d'échantillonnage à Grand Lake, Bruno, Quentin, Marie-Eugénie, Arnaud et Milena. Merci à Dave Blake notre guide, sans qui ce terrain n'aurait pas été possible.

J'ai aussi eu la chance tout au long de mon doctorat de travailler avec mes amis. Quentin et Arthur, merci pour votre accueil à Rimouski, à l'ISMER et à la grotte, et de m'avoir appris les bases du paléomagnétisme. J'ai eu la chance de pouvoir vous poser toutes mes questions débiles, merci pour votre soutien précieux pendant toutes les étapes du doctorat. Merci Quentin pour ton aide précieuse pour toutes mes analyses de labo, pour avoir toi aussi subi mes nombreuses questions. Morgane, merci pour tes nombreux conseils et pour l'exemple de chercheuse que tu donnes. J'ai une pensée particulière pour les personnes avec qui j'ai commencé et terminé ce doctorat, Camille, Kelsey et Florian. On a partagé toutes les joies et les peines du doctorat, de l'exam doc, à la rédaction finale, en passant par le terrain. Merci pour votre présence et votre aide dans toutes ces étapes. Daniel, Alfred, Naomi, Daniel, Elodie et toustes les autres étudiant.es de la grotte, merci d'avoir apporté une ambiance de travail joyeuse. Merci Charlotte, Danie et Christian pour tous les bons moments à bord de l'Amundsen et pour ceux ensuite à Rimouski.

Un immense merci à Elizabeth Claveau et Marie-Claude Fournier pour votre soutien moral, chacune à votre manière au cours de cette dernière année.

En plus de celles et ceux déjà remerciés plus haut, merci à mes ami.es rimouskois.es d'avoir partagé avec moi ces quatre années et les aventures, les bières au baro, les petits sauts en Gaspésie, les festivals, les randos, les chalets, les sorties d'escalade et les parties de tarot et de pétanques qui les ont accompagnées. Alice, Delphine, Leïla, Valentin, Elodie, Guillaume, Candice, Baptiste, Camille, Sarah, Thomas, Jeanne, Julie, Nathan, Antho, Joelle, Tessie, Luca, Cath, Greg, cette expérience n'aurait pas été la même sans vous. Merci d'avoir partagé tous ces bons moments et merci pour votre présence dans les moins bons moments. Merci à ma coloc Léa, sans qui mon arrivée à Rimouski aurait été bien plus difficile.

Mes ami.es de l'autre côté de l'Atlantique, Zoé, Cécile, Lewis, Sofia, Marie, Laurie, Raph, Lorraine, Lucie, merci d'avoir toujours été à mes côtés dans les étapes qui m'ont menée ensuite à Rimouski. Merci Manon et Juliette, mes partenaires de tp, de terrain, de révisions à la bibliothèque, grâce à vous j'ai commencé la géologie et sans vous j'aurais probablement fait de la bio.

Enfin, merci à ma famille d'avoir été à mes côtés tout au long de mon expérience québécoise et pour toutes les précédentes, à mes parents de m'avoir soutenue dans tous mes projets et de m'avoir permis d'en arriver là, à mes grands-parents de suivre de loin mais avec attention, tout ce que je fais de l'autre côté de l'Atlantique, à Florence de toujours faire en sorte qu'on puisse passer du temps ensemble. Sido et Louise merci pour votre soutien, votre présence et tous les bons moments depuis toujours. Etienne, merci pour ton soutien ces quatre années, pour les nombreuses relectures, pratiques, merci de m'avoir soutenue dans les moments difficiles et d'avoir partagé les bons moments au Québec.

AVANT-PROPOS

Ce projet de doctorat en océanographie, réalisé à l'Institut des sciences de la mer (ISMER) de l'Université du Québec à Rimouski (UQAR) et intitulé *Variations paléomagnétiques rapides au cours de l'Holocène : apport de nouveaux enregistrements sédimentaires marins du nord du Groenland et lacustres varvés du Labrador dans la reconstitution de la dynamique du champ géomagnétique* a été réalisé sous la supervision du professeur Guillaume St-Onge (ISMER-UQAR) et sous la co-supervision des professeurs Jean-Carlos Montero-Serrano (ISMER-UQAR) et Pierre Francus (INRS-ETE). Ce projet a pour but de reconstituer les variations paléomagnétiques à partir d'enregistrements sédimentaires marins et lacustres du Groenland et du Labrador, dans le but de décrire les variations paléomagnétiques séculaires et d'essayer de comprendre leur origine et leur lien avec la dynamique globale du champ géomagnétique. Cette thèse de doctorat a été rendue possible grâce au soutien financier et matériel de nombreuses institutions, que je tiens à reconnaitre ici. Les quatre années de thèse ont été financées premièrement par la bourse d'excellence de l'ISMER et par le Programme de Bourse d'Excellence pour les Etudiants Etrangers (PBEEE) des Fonds de Recherche du Québec – Nature et Technologies (FRQNT) n°334533. Les frais d'analyses, de fonctionnement et de déplacements ont été assurés en grande partie par la chaire de géologie marine, les programmes de subventions à la découverte du Conseil de Recherches en Sciences Naturelles et en Génie du Canada (CRSNG) de Guillaume St-Onge, Jean-Carlos Montero-Serrano et Pierre Francus. La participation à des congrès et séjours de recherche a également été financée par le centre de recherche du GEOTOP et les fonds de recherche de Brendan Reilly. Une bourse de déplacement d'ECORD-IODP a permis la participation au *21st century drilling workshop*. La collecte des carottes sédimentaires étudiées dans cette thèse de doctorat a été possible grâce à ArcticNet, Amundsen Science, le *Danish Centre for Marine Research* et le programme de suppléments aux subventions à la découverte en recherche nordique du CRSNG.

RÉSUMÉ

Les changements spectaculaires récents du champ géomagnétique comme la diminution de l'intensité dipolaire et la migration du pôle nord magnétique, ont soulevé de nombreuses questions à propos de l'origine de ces variations rapides. Les carottes sédimentaires marines et lacustres constituent des enregistrements continus des variations de l'intensité et de la direction du champ géomagnétique. Les particules magnétiques les constituant s'orientent selon le champ géomagnétique et en conservent l'intensité au moment du dépôt.

L'objectif principal de cette thèse est de reconstituer les variations paléomagnétiques séculaires à différents endroits de l'Arctique et du milieu subarctique afin d'identifier de potentielles variations rapides, de comprendre leur origine et d'examiner leur lien avec les différentes caractéristiques du champ géomagnétique, telles que les lobes de flux géomagnétiques. Pour cela, nous utilisons des carottes sédimentaires marines du fjord Petermann, de la plateforme continentale nord-est du Groenland et de Young Sound (fjord au Groenland), et des carottes sédimentaires lacustres varvées de Grand Lake au Labrador. Ces enregistrements comblent le manque de données paléomagnétiques sédimentaires dans l'Arctique, dans le but de mieux comprendre la dynamique du champ à ces latitudes.

Dans le premier chapitre, nous avons ajouté la carotte AMD1902-10GC du fjord Petermann (Groenland) au *Petermann stack*. Cela a permis notamment de créer un stack de paléointensité relative pour cette région. Les forts taux de sédimentation et la minéralogie ferrimagnétique en font un enregistrement paléomagnétique robuste et fiable, dont les variations directionnelles sont cohérentes avec d'autres enregistrements de l'Arctique et de l'Atlantique Nord et dont les variations de paléointensité relative sont similaires aux modèles géomagnétiques. La trajectoire du pôle géomagnétique virtuel, reconstituée grâce aux données directionnelles, montre que la migration récente du pôle nord magnétique est cohérente avec les variations observées à l'échelle de l'Holocène. Ces résultats combinés, suggèrent que les variations temporelles et spatiales de l'intensité du champ géomagnétique, sont liées à la dynamique des lobes de flux géomagnétiques et ont une influence sur la trajectoire de migration du pôle géomagnétique virtuel.

Dans le deuxième chapitre, les analyses paléomagnétiques conduites sur trois carottes sédimentaires du plateau continental nord-est du Groenland et de Young Sound ont permis de reconstituer les variations paléomagnétiques directionnelles et de paléointensité relative. Bien qu'ils soient éloignés de seulement 1000 km du fjord Petermann, ces enregistrements montrent moins de similarités avec ceux du premier chapitre qu'avec les enregistrements du nord de l'Europe et de l'Atlantique Nord. La comparaison de l'enregistrement de paléointensité relative avec les modèles géomagnétiques et les taux de production des isotopes cosmogéniques met en évidence le caractère global des variations géomagnétiques de cette région. La trajectoire du pôle géomagnétique virtuel, reconstituée à partir des données directionnelles pour les derniers 8 ka, a été comparée à l'intensité du champ géomagnétique à la limite noyau-manteau sur le même intervalle de temps. Cette comparaison montre qu'en période de forte intensité, les lobes de flux géomagnétiques auraient un effet sur les migrations du pôle géomagnétique virtuel, soutenant les observations du premier chapitre.

Le troisième chapitre porte sur deux séquences sédimentaires prélevées à Grand Lake au Labrador, ayant permis de reconstituer les variations paléomagnétiques des derniers 2500 ans. Les variations paléomagnétiques séculaires présentent des similarités avec les enregistrements de l'est du Canada et du sud du Groenland, ainsi qu'avec les observations et mesures des variations récentes (400 ans). Ces enregistrements apportent une reconstitution des derniers 1000 ans, rarement enregistrés dans les carottes sédimentaires marines. L'étude des propriétés magnétiques des couches déposées rapidement de la séquence GL23-20 montre que l'amplitude de variation de l'inclinaison au sein des événements est reliée à l'épaisseur des couches et donc à l'intensité de l'événement et de la turbulence. De plus, les données paléomagnétiques concordent avec la littérature, au sujet des mécanismes à l'origine du dépôt de ces couches, notamment l'origine sismique probable d'une couche récente.

Cette thèse répond donc à la problématique générale et apporte une contribution significative à la compréhension de la dynamique du champ géomagnétique, notamment en soulignant un lien entre les variations d'intensité des lobes de flux géomagnétiques et la migration des pôles géomagnétiques virtuels. Ces observations soulèvent alors de nouvelles questions sur l'origine interne de ces variations. Par ailleurs, ces résultats montrent que les enregistrements des hautes latitudes suivent globalement les variations dipolaires globales à l'échelle de l'Holocène.

Mots clés : Holocène, Groenland, Labrador, carottes sédimentaires, varves, variations séculaires paléomagnétiques, paléointensité relative, isotopes cosmogéniques, pôles géomagnétiques virtuels, lobes de flux géomagnétiques

ABSTRACT

Recent spectacular changes in the geomagnetic field, such as the decrease in dipole intensity and the migration of the north magnetic pole, have raised many questions about the origin of these rapid variations. Marine and lacustrine sediment cores provide continuous records of variations in the intensity and direction of the geomagnetic field and allow to study its behavior in the past. The magnetic particles in the sediment align with the geomagnetic field and record its intensity at the time of deposition.

The main objective of this thesis is to reconstruct paleomagnetic secular variations at different locations in the Arctic and subarctic regions in order to identify potential rapid variations, understand their origin, and examine their relationship with different characteristics of the geomagnetic field, such as geomagnetic flux lobes. To this end, we used marine sediment cores from Petermann Fjord, the northeast Greenland continental shelf, and Young Sound, as well as varved lake sediment cores from Grand Lake in Labrador. These records fill the gap in sedimentary paleomagnetic data in the Arctic, in order to better understand the field dynamics at these latitudes.

In the first chapter, we added the AMD1902-10GC core from Petermann Fjord (Greenland) to the Petermann stack. It allowed us to create a relative paleointensity stack for this region. The high sediment accumulation rates and the ferrimagnetic carriers make it a robust and reliable paleomagnetic record. The directional variations are consistent with those of other records from the Arctic and North Atlantic, and the relative paleointensity variations are similar to geomagnetic models. The trajectory of the virtual geomagnetic pole, reconstructed from directional data, shows that the recent migration of the north magnetic pole is consistent with the variations observed over the Holocene. These combined results suggest that temporal and spatial variations in geomagnetic field intensity are linked to the dynamics of geomagnetic flux lobes and influence the migration of the virtual geomagnetic pole.

In the second chapter, paleomagnetic analyses conducted on three sediment cores from the northeast Greenland shelf and Young Sound enabled the reconstruction of paleomagnetic directional variations and relative paleointensity. Although only 1,000 km away from Petermann Fjord, these northeastern Greenland records show fewer similarities with those in the first chapter than with records from northern Europe and the North Atlantic. Comparison of the relative paleointensity record with geomagnetic models and cosmogenic isotope production rates highlights the global nature of geomagnetic variations in this region. The trajectory of the virtual geomagnetic pole, reconstructed from directional data for the last 8 ka, was compared to the intensity of the geomagnetic field at the core-mantle boundary over the same time interval. This comparison shows that during periods of high intensity, geomagnetic flux lobes would have an effect on the migration of the virtual geomagnetic pole, supporting the results from the first chapter.

The third chapter focuses on two sedimentary sequences collected at Grand Lake in Labrador, which enabled to reconstruct paleomagnetic variations over the last 2,500 years. The secular paleomagnetic variations show similarities with records from eastern Canada and southern Greenland, as well as with observations and measurements of recent variations (400 years). These records provide a reconstruction of the last 1,000 years, which is rarely recorded in marine sediment cores. The study of the magnetic properties of the rapidly deposited layers of the GL23-20 sequence shows that the amplitude of variation in inclination within events is related to the thickness of the layer and therefore to the intensity of the event and turbulence. Furthermore, the paleomagnetic data are consistent with the literature on the mechanisms responsible for the deposition of these layers, in particular the probable seismic origin of the most recent massive layer.

This thesis therefore addresses the main objective and constitutes a significant contribution to better understanding the dynamics of the geomagnetic field, in particular by highlighting a link between variations in the intensity of geomagnetic flux lobes and the migration of virtual geomagnetic poles. These observations raise new questions about the internal origin of these variations. Furthermore, these results show that high-latitude records generally follow global dipole variations over the Holocene.

Keywords: Holocene, Greenland, Labrador, sediment cores, varves, paleomagnetic secular variations, relative paleointensity, cosmogenic isotopes, virtual geomagnetic pole, geomagnetic flux lobes

TABLE DES MATIÈRES

REMERCIEMENTS vii

AVANT-PROPOS xi

RÉSUMÉ xiii

ABSTRACT xv

TABLE DES MATIÈRES xvii

LISTE DES TABLEAUX xxiii

LISTE DES FIGURES xxv

LISTE DES ABRÉVIATIONS, DES SIGLES ET DES ACRONYMES xxxvii

LISTE DES SYMBOLES xli

INTRODUCTION GÉNÉRALE 1

1. LE CHAMP MAGNETIQUE TERRESTRE : ORIGINE ET FONCTIONNEMENT 1
2. LE CHAMP GEOMAGNETIQUE AUX HAUTES LATITUDES DE L'HEMISPHERE NORD 5
3. VARIATIONS DU CHAMP GEOMAGNETIQUE 6
4. PALEOMAGNETISME SEDIMENTAIRE 9
5. L'ARCTIQUE 10
6. OBJECTIFS, QUESTIONS ET HYPOTHESES DE RECHERCHE 11
7. SITES D'ETUDES 14
    - 7.1 Fjord Petermann 16
    - 7.2 Plateau continental du nord-est du Groenland et Young Sound 21
    - 7.3 Grand Lake 24
8. METHODOLOGIE 29
    - 8.1 Échantillonnages des carottes sédimentaires 29

8.2 Mesures des propriétés physiques et chimiques continues 32
8.3 Mesures paléomagnétiques continues 34
8.4 Mesures de magnétisme environnemental 35
8.5 Granulométrie 38
8.6 Établissement du signal de paléointensité relative 39
8.7 Chronologies 40

9. ORGANISATION DE LA THESE 45

CHAPITRE 1 Variations séculaires paléomagnétiques à 81°N au nord du Groenland au cours des derniers 6000 ans 51

1.1 RESUME EN FRANÇAIS DU PREMIER ARTICLE 51

1.2 PALEOMAGNETIC SECULAR VARIATIONS IN NORTH GREENLAND AT 81°N OVER THE LAST 6,000 YEARS 53

1.2.1 Abstract 53
1.2.2 Plain Language Summary 53

1.3 INTRODUCTION 54

1.4 MATERIALS AND METHODS 56

1.4.1 Petermann Fjord Sediment cores 56
1.4.2 Physical properties: X-Ray Imaging and Multi-Sensor Core Logger Analysis 58
1.4.3 Grain size analysis 59
1.4.4 Continuous paleomagnetic measurements 59
1.4.5 Rock magnetic measurements 60
1.4.6 Chronology 61

1.5 RESULTS 63

1.5.1 Lithology 63
1.5.2 Continuous paleomagnetic measurements 64
1.5.3 Magnetic Assemblage 68
1.5.4 RPI determination 73
1.5.5 Paleomagnetic stack 74
1.5.6 Age model 78
1.5.7 PSV variations 79

1.6 DISCUSSION 84

1.6.1 Age model, magnetic lock-in depth and ΔR Variations 84
1.6.2 Paleointensity and paleomagnetic secular variations in the Arctic and the Northern North Atlantic 87

1.7 CONCLUSIONS 92

1.8 DATA AVAILABILITY STATEMENT 93

1.9 ACKNOWLEDGMENTS 93

1.10 REFERENCES 94

1.11 SUPPORTING INFORMATION (FIGURES AND TABLES) 106

CHAPITRE 2 Des enregistrements paléomagnétiques du nord est du Groenland suggèrent l'influence des lobes de flux géomagnétiques sur la migration du pôle géomagnetique virtuel au cours de l'holocène 113

2.1 RESUME EN FRANÇAIS DU DEUXIEME ARTICLE 113

2.2 NORTHEASTERN GREENLAND PALEOMAGNETIC RECORDS SUGGEST THE INFLUENCE OF GEOMAGNETIC FLUX LOBES ON THE VIRTUAL GEOMAGNETIC POLE MIGRATION DURING THE HOLOCENE 115

2.2.1 Abstract 115
2.2.2 Plain Language Summary 115

2.3 INTRODUCTION 116

2.4 MATERIAL AND METHODS 117

2.4.1 Northeast Greenland Shelf sediment cores and setting 117
2.4.2 Physical and geochemical properties: X-ray fluorescence and imaging 120
2.4.3 Grain size analysis 120
2.4.4 Continuous paleomagnetic analysis 121
2.4.5 Rock magnetic measurements 122
2.4.6 Chronology 123

2.5 RESULTS 125

2.5.1 Lithology 125
2.5.2 Continuous magnetic properties 127
2.5.3 Rock magnetic properties 128
2.5.4 Relative paleointensity determination 132
2.5.5 Paleomagnetic secular and relative paleointensity variations 135

2.6 DISCUSSION 138

2.6.1 PSV and RPI variations 138
2.6.2 Virtual Geomagnetic Poles path 144

2.7 CONCLUSIONS 150

2.8 ACKNOWLEDGMENTS 150

2.9 OPEN RESEARCH 151

2.10 REFERENCES 151

2.11 SUPPORTING INFORMATION (FIGURES AND TABLES) 160

CHAPITRE 3 Variations paléomagnétiques à haute résolution au cours des derniers 2500 ans enregistrées dans les sédiments varvés de Grand Lake, Labrador, Canada 181

3.1 RESUME EN FRANÇAIS DU TROISIEME CHAPITRE 181

3.2 HIGH-RESOLUTION PALEOMAGNETIC VARIATIONS FOR THE LAST 2,500 YEARS RECORDED IN VARVED SEDIMENTS FROM GRAND LAKE, LABRADOR, CANADA 183

3.2.1 Abstract 183

3.3 INTRODUCTION 184

3.4 SETTING 185

3.4.1 Deglaciation 186
3.4.2 Sedimentation 186

3.5 MATERIAL AND METHODS 187

3.5.1 Sediment cores 187
3.5.2 Physical and geochemical properties 190
3.5.3 Continuous paleomagnetic analysis 191
3.5.4 Rock magnetic measurements 192
3.5.5 Chronology 193

3.6 RESULTS 198

3.6.1 Downcore physical, geochemical and magnetic properties 198
3.6.2 Rock magnetic results 202
3.6.3 Continuous paleomagnetic results 207

3.7 DISCUSSION 212

3.7.1 Identification and impact of the rapidly deposited layers on the detrital remanent magnetization 212
3.7.2 Paleoenvironmental interpretations supported by paleomagnetic data 219

3.7.3 Paleomagnetic variations record over the last 3000 years......................221
3.7.4 Focus on the last 350 years (-45 to 305 cal years BP)...........................227

3.8 SUMMARY AND PERSPECTIVES...228

3.8.1 Acknowledgments..229

3.9 REFERENCES...230

3.10 SUPPORTING INFORMATION (FIGURES)..239

CONCLUSION GÉNÉRALE...244

RÉFÉRENCES BIBLIOGRAPHIQUES..256

LISTE DES TABLEAUX

Tableau 1.Tableau récapitulatif des carottes étudiées dans cette thèse. Les carottes pour lesquelles les enregistrements avaient déjà été établis dans de précédentes études ne sont pas indiquées dans ce tableau. 31

Table 2. Sediment cores used in this study. 57

Table 3. Radiocarbon results. The age in italics was not used for the age-depth model. Radiocarbon ages were calibrated using the Marine20 (Heaton et al., 2020) calibration curve with a ΔR = 430 ± 145 yrs in the R package ‘rbacon’ (Blaauw & Christen, 2011). 63

Table 4. Hysteresis and S-ratio measurements results (heated samples in grey). 69

Table 5. Factors of multiplication describing magnetic changes in hysteresis parameters after heating. 69

Table 6. Paleomagnetic tie points used to modify the depth of the radiocarbon ages and to calculate the magnetic age depth model. 86

Table 7. Calculation of the magnetic depth for the radiocarbon ages for the Petermann stack. The updated depths were used to construct the magnetic age model in the R package ‘rbacon’. 86

Table 8. Radiocarbon ages for core 213G. 124

Table 9. Characteristics of the sediment cores collected. 188

Table 10. Overview of the methods used for establishing the chronology of core GL17-13. 194

Tableau 11. Comparaison des enregistrements de RPI, de taux de production d'isotopes cosmogéniques et de moment dipolaire décrits par les modèles géomagnétiques à différents intervalles de temps des derniers 3 ka. 250

LISTE DES FIGURES

Figure 1. A. Vue schématique de l’intérieur de la Terre (Gubbins, 2008). Le champ géomagnétique terrestre provient du noyau externe. **B.** Schéma des particules et rayons solaires déviés par les lignes de champ de la magnétosphère (modifiée d'après Heaton et al., 2021). Le CMT s’apparente à un dipôle tel que schématisé sur la figure. 2

Figure 2. Le champ magnétique peut être défini par trois éléments en tout point de la surface terrestre. Le vecteur F est le vecteur magnétique total. La déclinaison (D) est l’angle entre le Nord géographique et le méridien magnétique (composante horizontale H du champ). L’inclinaison (I) est l’angle entre le méridien magnétique et le vecteur magnétique. (x) représente le nord orthogonal, (y) l’est et (z) la composante vers le bas. Modifiée d'après Thompson and Oldfield (1986). 3

Figure 3. Schéma de la convection dans le noyau terrestre externe et de sa résultante en surface. La circulation des fluides en colonnes est à l'origine des lobes de flux géomagnétiques, tandis que la circulation au sein du cylindre tangentiel résulte en de plus faibles intensités en surface. L’intensité en surface est indiquée par des courbes d’isointensité (nT). Modifié d’après Lawrence et al. (2009); Lund et al. (2016). 6

Figure 4. Schéma des processus lacustres et marins amenant à l’enregistrement de la rémanence dans les sédiments dans un milieu non-floculant **(a)** et dans un milieu floculant **(b)**. D’après Tauxe & Yamazaki (2015). 10

Figure 5. Carte des sites d'études abordés dans cette thèse. Le premier chapitre porte sur la carottes du fjord Petermann dans le détroit de Nares (mauve). Le deuxième chapitre porte sur les carottes de la marge Nord Est du Groenland (rouge). Le troisième chapitre porte sur les carottes prélevées à Grand Lake au Labrador (rose). 15

Figure 6. Carte géologique du détroit de Nares (**A**) et du fjord Petermann (**B**). Modifiée d’après Dawes et al. (2000). **C.** Carte bathymétrique du Fjord Petermann avec l’emplacement de la carotte AMD1902-10GC (étoile jaune) étudiée dans le premier chapitre. Les données bathymétriques proviennent de Jakobsson et al. (2018). 18

Figure 7. Schéma de la morphologie du fjord Petermann d'après Jennings et al. (2022).. 19

Figure 8. Variations de la langue de glace Petermann au cours des derniers 9000 ans. Modifiée d'après Reilly et al. (2019). L'ombrage indique les intervalles de temps de la déglaciation (gris), de l'absence de langue glaciaire stable et des conditions marines saisonnières ouvertes dans le fjord (rouge), du rétablissement de la langue glaciaire (bleu clair) et d'une langue glaciaire avec des étendues stables comme l'enregistrement historique 1876-2010 (bleu foncé). Les données d'insolation à 65°N indiquent la tendance à la diminution à long terme de l'insolation dans l'hémisphère Nord (Laskar et al., 2004). Les estimations de l'anomalie régionale de la température de l'air en surface (SAT) sont reconstituées à partir de la carotte de glace Agassiz par rapport au niveau pré-industriel de 1750 CE (Lecavalier et al., 2017). 20

Figure 9. Cartes de la zone d'étude du chapitre 2. **A.** Circulation océanique globale dans le nord de l'océan Atlantique Nord. Flèche rouge : courant chaud. Flèche bleue : courant froid. Flèche orange : courant intermédiaire. Les points jaunes indiquent la localisation des carottes étudiées dans ce chapitre. **B.** Plateforme continentale du nord est du Groenland. Les flèches indiquent les courants océaniques. AAW - Arctic Atlantic Water, EGC - Eastern Greenland Current, RAC - Return Atlantic Current. Les traits en pointillés indiquent les polynies. NØIB: Norske Øer Ice Barrier, SWP: Sirius Water Polynya. Le rectangle rouge indique l'emprise de la carte C. Les étoiles jaunes indiquent les carottes étudiées dans ce chapitre. **C.** Système de Young Sound-Tyrolerfjord. Les lignes rouges en pointillés indiquent les seuils internes et externes du fjord. ZR (Zackenberg River), LR (Louise River), TR (Tyroler River) et CB (Clay Bay) indiquent les affluents majeurs. Les étoiles jaunes indiquent les carottes étudiées dans ce chapitre. 24

Figure 10. **A.** Carte de la province de Grenville au Canada et de son extension jusque dans la région des Adirondacks aux États-Unis (carte du ministère des Ressources naturelles et des Forêts du Québec). **B.** Carte géologique du Labrador aux alentours de Grand Lake. Modifiée d'après Wardle et al. (1997). Les étoiles jaunes représentent la localisation des carottes...................... 25

Figure 11. Carte de l'étendue de la calotte de glace Laurentidienne (Laurentide Ice Sheet) à environ 8.45 ka et de la localisation de Grand Lake (étoile jaune). Les lignes rouges indiquent les positions des moraines associées au recul de LIS, notamment la moraine Sebaskachu au sud-est de Grand Lake. D'après Trottier et al. (2020).. 27

Figure 12. Photographie des varves des 20 premiers cm de la carotte de surface GL23-20-Up1. 28

Figure 13. Déploiement du carottier à gravité géant à bord du NGCC Amundsen dans le détroit de Nares lors du Leg 3 de l'expédition 2023. Photo de Daniel Amirault, Amundsen Science. 29

Figure 14. N/R Dana dans Young Sound lors de l'expédition NorthGreen2017. Photo de Claus Persson, Capitaine du Dana (DTU-AQUA). 30

Figure 15. Photos de la campagne d'échantillonnage à Grand Lake au Labrador. **A.** Plateforme de carottage sur le lac vue de l'extérieur. Les arbres servent de signalisation pour les personnes qui circulent sur le lac. **B.** Déploiement du carottier à percussion avec Bruno Cayouette, vue de l'intérieur de la tente (photo de Quentin Beauvais). 32

Figure 16. Photos du banc MSCL de GEOTEK à l'ISMER. **A.** Banc utilisé pour les carottes entières et ouvertes. **B.** Montage avec le pistolet XRF (1), le spectrophotomètre (2), la susceptibilité magnétique (3) et le système d'imagerie digitale (4) pour les mesures sur les demi-sections ouvertes. 33

Figure 17. A. U-channel sous-échantillonné dans une carotte de sédiments. **B.** Magnétomètre cryogénique 755SRM-1.65 de 2G Enterprises à l'ISMER. 35

Figure 18. Photo de l'intérieur de l'AGM à l'ISMER. Le sédiment est placé sur la sonde. 37

Figure 19. Montage pour les mesures de magnétisme environnemental sur le magnétomètre à échantillon vibrant (VSM) à l'IPGP. Une capsule (à gauche) est remplie de sédiment bien tassé (2-3 g), puis placée dans le VSM à droite, tenue grâce à une paille en plastique pour les mesures de boucles d'hystérésis, FORC, acquisition d'IRM, entre autres. 37

Figure 20. Acquisition de courbes de susceptibilité magnétique en fonction de la température avec un susceptibilimètre AGICO KLY-3 à l'IPGP. Le sédiment est pesé et déposé dans un tube (à gauche) qui est ensuite placé dans le susceptibilimètre (à droite) dans lequel il va être chauffé. 38

Figure 21. Granulomètre Malvern PANalytical Mastersizer 3000 de l'ISMER. 39

Figure 22. Parc instrumental des spectromètres de masse par accélération (AMS) au laboratoire Ion Beam Physics de l'ETH de Zürich. Photo ETH Zürich. 40

Figure 23. Schéma du cycle du ^{14}C représentant la production de ^{14}C cosmogénique dans l'atmosphère par les rayons cosmiques et la distribution du ^{14}C dans le cycle global du carbone. D'après Hughen (2007). 41

Figure 24. A. Schéma du cycle du ^{210}Pb dans l'environnement (Swarzenski, 2014). B-D. Analyses au GEOTOP à l'UQAM. B. Digestion par différents acides sur des plaques chauffantes. C. Disques à sécher. D. Compteur alpha. 43

Figure 25. Exemple d’identification et de comptage de varves avec le logiciel Pak Counter. Le profil µXRF de Sr et le profil de niveaux de gris sont superposés à l’image haute résolution de la carotte GL23-20-Up1 44

Figure 26. Figure en matériel supplémentaire de Nilsson et al., (2022), indiquant quels enregistrements sont pris en compte dans le modèle pfm9k.2. Les données archéomagnétiques des latitudes moyennes et basses sont nombreuses tandis que les données sédimentaires sont beaucoup plus rares, et que certaines régions ne sont quasiment pas représentées, dont l’Arctique. 45

Figure 27. **(a)** Location of study site in Nares Strait, with bathymetric data from the International Bathymetric Chart of the Arctic Ocean (IBCAO, Jakobsson et al., 2020). Blue arrows represent the cold polar waters becoming the Baffin Current, Purple arrows represent the West Greenland Current. **(b)** Location of the comparison records mentioned in this study. **(c)** Map of the study sites in Petermann Fjord. Multibeam bathymetry of the Petermann Fjord and Hall Basin were obtained from Jakobsson et al. (2018). Black dots = cores composing the outer fjord splice; yellow dots = cores composing the stack. 10GC was collected during AMD1902 expedition, 03PC/TC, 41GC, 04GC, 40TC during OD1507 (Reilly et al., 2019). Surface Polar Waters are represented by white arrows and subsurface Atlantic Waters are represented by red arrows. 57

Figure 28. **(a)** Downcore physical and magnetic properties in core AMD1902-10GC including: high-resolution core image (HRI), X-ray computed tomography (X-CT) scan image, Ti/Ca profile, magnetic susceptibility (kLF), a* red color indicator, relative abundance of the sand, silt and clay, ice rafted debris (IRD) counts based on XCT images (>2 mm clasts), grain size proxy D90 (um), kARM/kLF (magnetic grain size proxy), Median Destructive Field values (mT) of natural remanent magnetization (NRM), anhysteretic remanent magnetization (ARM) and isothermal remanent magnetization (IRM) (magnetic mineralogy indicator). **(b)** Downcore continuous paleomagnetic measurements of core AMD1902-10GC including demagnetization steps 0–100 mT, NRM (A/m), ARM (A/m), IRM 300 mT (A/m), saturation isothermal remanent magnetization (SIRM) 950 mT (A/m), characteristic remanent magnetization (ChRM) Inclination (°) and GAD value, ChRM relative Declination (°) and maximum angular deviation (MAD) values (°). 68

Figure 29. Rock magnetic analysis results. **(a)** Magnetic susceptibility heating and cooling thermomagnetic curves. **(b)** Hysteresis loops of samples before and after heating to 700°C. **(c)** Isothermal remanent magnetization (IRM) acquisition curves and IRM unmixing. **(d)** FORC diagrams. **(e)** Day & King plots.. 72

Figure 30. Determination of the 10GC relative paleointensity signal (20–60 mT). R: correlation coefficient for anhysteretic remanent magnetization (ARM) (red) and isothermal remanent magnetization (IRM) (green); profiles for slope method; profiles for ratio method. Determination coefficient r2 between the normalized signal and the normalizer for ARM (red) and IRM (green) for the whole core, core top (0–70 cm) and core bottom (71–265 cm)....74

Figure 31. **(a)** Conversion of 10GC (independent depth, cm) to the Correlated Equivalent Depth (CED, cm) using Ti/Ca X-ray fluorescence (XRF) ratio from the outer fjord splice (OFS; 03PC, 03TC, 41GC). **(b)** Comparison of Ti/Ca XRF ratio of the four cores composing the stack (04GC, 41GC, 04TC, 10GC) on CED. **(c)** Age model and accumulation rates for Petermann stack using ^{14}C dates from cores 41GC, 03UW (Reilly et al., 2019) and 10GC (this study), Marine 20 calibration curve and ΔR = 430 ± 145 years. Red = planktic foraminifera, blue = benthic foraminifera, purple = mixed benthic and planktic, black = uncalibrated dates, white = date not used in the age model....77

Figure 32. Petermann paleomagnetic secular variations stack: inclination, declination, relative paleointensity (RPI), angular difference (α95) and number of cores contributing to the stack (N)....78

Figure 33. Comparison of inclination (a) and declination (b) profiles from different paleorecords: pfm9k.2 geomagnetic model (Nilsson et al., 2022), JPC15 (Lund et al., 2016), Petermann stack (this study), 204casq (Caron et al., 2019), U1305 (Stoner et al., 2013), GREENICE stack (Stoner et al., 2007), North Karelian stack (Haltia-Hovi et al., 2010), MD99-2220 (St-Onge et al., 2003). Key features (1, 3.7, and 6 ka) mentioned in the text are underlined in the figure....82

Figure 34. Comparison of absolute and relative paleointensities profiles for different paleorecords: CALS10k.2 (Constable et al., 2016) and pfm9k.2 geomagnetic models (Nilsson et al., 2022), Petermann stack (this study), 204casq (Baffin Bay relative paleointensity (RPI) record, Caron et al., 2019), U1305 (North Atlantic RPI record, Stoner et al., 2013), GREENICE stack (Northern North Atlantic RPI record, Stoner et al., 2007), North Karelian stack (lacustrine RPI record from Finnish lakes, Haltia-Hovi et al., 2010), Virtual Axial Dipole Moment, Western Eurasia (absolute paleointensity from archeological artifacts and volcanic products; Genevey et al., 2008), Eastern Canadian stack (St-Lawrence RPI record, Barletta, Channell, & Rochon, 2010), Lake LeBoeuf (lacustrine RPI record from North America, King et al., 1983)....83

Figure 35. Construction of the magnetic age model for the Petermann stack. (a) Paleomagnetic tie points based on Petermann and GREENICE stack comparison. (b) Bayesian magnetic age-depth model for the Petermann stack. Yellow points = paleomagnetic tie points; red, blue, purple points = calibrated ^{14}C ages; red curve = magnetic age model; black curve radiocarbon age model; gray curve = ΔR variation. (c) GREENICE and Petermann Paleomagnetic Secular Variation stack comparisons based on the Bayesian magnetic age model. Gray shaded bars indicate inclination >85° where important declination changes should be interpreted carefully. 87

Figure 36. (**a**) Longitude variations of virtual geomagnetic poles based on the record's directional data. (**b**) Latitude variations of Virtual Geomagnetic Pole. Red = Petermann stack; purple = International Geomagnetic Reference Field; orange = ARCH3K.1; green = U1305. (**c**) Relative and absolute paleointensities curves in Petermann (red), Northern Atlantic (light green), over Europe (blue), and global dipole moment according to pfm9k.2 model (dark green, Nilsson et al., 2022) and CALS10k.2 model (gray, Constable et al., 2016). (**d**) Projection of VGP paths reconstructions based on Petermann stack directional data at time-intervals 0–2 ka; 2–4 ka; 4–6.3 ka overlaid on maps of radial field strength at Core Mantle Boundary from CALS10k.2 model respectively at 1.5, 2.7, 5 ka. The projections and maps were designed on ArcGIS. 91

Figure 37. (a) Map of the sampling sites and surface currents: AAW - Arctic Atlantic Water, EGC - Eastern Greenland Current, RAC - Return Atlantic Current. NØIB: Norske Øer Ice Barrier, SWP: Sirius Water Polynya. NT: Norske Trough; WT: Westwind Trough; YST: Young Sound Tyrolerfjord. Bathymetry data from General Bathymetric Chart of the Ocean, 2023 version (GEBCO Compilation Group, 2023). Map were made using ArcGIS and CorelDraw software. (b) General location of the study area and cores used in this study: Petermann Stack (Girard et al., 2024), Fennostack (Snowball et al., 2007), U1305 (Stoner et al., 2013), GREENICE15k (Reilly et al., 2023), North Karelian Stack (NKS; Haltia-Hovi et al., 2010), British master curve (BMC; Turner & Thompson, 1981). TC 70°N indicates the surface projection of the tangent cylinder. 120

Figure 38. **(a)** Physical and geochemical continuous properties of cores 039G, 073G, and 213G. From left to right: X-radiography, Ti/Ca, low-field magnetic susceptibility (k_{LF}), Zr/Rb, grain size (sand, silt, clay) composition (%), median grain size (µm), k_{ARM}/k_{LF}, MDF (mT). **(b)** Continuous magnetic properties of cores 039G, 073G and 213G. From left to right: NRM, ARM, IRM and SIRM intensities (A/m), inclination and GAD value (°), declination (°) and MAD values (°). Beige horizontal bars in (a) and (b) indicate sand layers. 127

Figure 39. Rock magnetic results. (**a**) Temperature-dependent magnetic susceptibility measurements; heating curves up to 700°C. (**b**). Cooling curves down to room temperature. (**c**) Hysteresis loops. (**d**) FORC diagrams. (**e**) IRM acquisition curves unmixing. (**f**) IRM acquisition curves. (**g**) King plot. For a, b, c, d, e, left to right: cores 039G, 073G and 213G. Dotted lines in panels a, b and c represent sand samples. 131

Figure 40. Core 213G age depth model. Horizontal beige bars represent the identified rapidly deposited layers (RDL). Left to right: grain size parameters median grain size (black) and D_{90} (grey) ; k_{ARM}/k_{LF}; Ca/Fe; Ti/Ca; Zr/Rb; Bayesian age-depth model. Grey curve = sediment accumulation rate (SAR, cm/kyr). Red curve = median modelled age. Dashed grey lines = min/max modelled ages. Yellow dots = ages obtained from shells. Blue dots = ages obtained from foraminifera. The age at 140.5 cm in RDL 2 is not used in the age-depth model. The Event Free Depth refers to the depth scale used to build the age-depth model, without the RDL, corresponding to an event-free stratigraphy (grey axis)...134

Figure 41. Inclination, declination and relative paleointensity (RPI) comparisons. CALS10k.2 geomagnetic field model projected to the location of core 073G. Data include cores 039G (green), 073G (blue), and 213G (red), along with reference records from the North Karelian Stack, FENNOSTACK, U1305, and GREENICE Stack. Absolute paleointensity data from western Eurasia (VADM) are also included, based on archeological artefacts and volcanic products (Genevey et al., 2008). Yellow stars represent the features indicated in Fig. 42. The declination change in CALS10k.2 record does not reflect a real change, only a scaling choice according to the declination averaging to 0° and covering a maximum variation range of 360°. 138

Figure 42. Comparison of inclination and declination records from core 073G (blue) and GREENICE15k (grey) record. Records are on their independent age models. The x-axis (age) is offset by 300 years to illustrate the match between the two records. Dashed red lines and yellow stars indicate similar features in both records on their independent age models. The features chosen are the tops of peaks and middle of troughs..141

Figure 43. Comparison of inclination (a) and declination (b) records for GREENICE15k (grey), the North Karelian Stack (brown), and core 073G (blue) for the last 5 kyr. Comparison of paleointensities and cosmogenic isotope production rates for the last 5 kyr: average Northern Hemisphere ^{10}Be production rate (green), average global ^{14}C production rate (orange) (Nilsson et al., 2024), core 073G RPI record (blue), VADM Western Eurasia (dark blue), and U1305 RPI record (grey). Core 073G is plotted on

its own independent chronology. Yellow stars indicate the same features as in Fig. 41 and 42. 143

Figure 44. VGP projections from the different records for 0-2 ka, 2-4 ka, 4-6 ka, 6-8 ka time intervals. 146

Figure 45. VGP positions reconstructed from core 073G at different time intervals: 0-2 ka (a, b), 2-4 ka (c), 4-6 ka (d, e, f), 6-8 ka (g), projected onto the radial field strength (intensity μT) at the core mantle boundary at 1.05 (a), 1.5 (b), 2.6 (c), 4.0 (d), 4.5 (e), 5.4 (f), and 6.6 (g) cal ka BP. The radial field strength is from the CALS10k.2 model (Constable et al., 2016). 149

Figure 46. Map of the study location. **A.** Location of Grand Lake in Labrador. Yellow star represents the location of the cores in Grand Lake. Black dots indicate location of comparison records. **B.** Map of Grand Lake and location of the cores collected in 2023 and 2017. **C.** Zoom on GL17-13 core location and bathymetry at the site. **D.** Zoom on GL23-20 core location and bathymetry at the site. The figure was made using ArcGIS and CorelDraw. The bathymetry data is from Trottier et al., (2020). 190

Figure 47. Age model for core GL17-13 . **A.** Age model from Lapointe et al. (2025) based on two individual lamination counts (A.G.P. and C.G.) from thin section using Image Analysis (IA) and from ^{137}Cs and AMS ^{14}C dating. Age-depth model was performed with the ClamR software version 2.2 (Blaauw 2010) using a linear interpolation for the site GL-13 with 95% confidence interval . **B.** Age model from this study, based on Lapointe et al. (2025) for the top 220 cm. The package 'bacon' in R studio was used to extrapolate the age model down to 333 cm, including an RDL (pale yellow bar). Because there are no more constraints at the base of the core, there is a large uncertainty towards the bottom of the core, that must be interpreted carefully. 195

Figure 48. Age-depth model for GL23-20. A. ^{210}Pb activity profile (black curve), ^{210}Pb excess (grey curve), ^{137}Cs (brown curve). The brown bar represents the surface mixed layer. Linear fit curves for the ^{210}Pb excess profiles are used to infer sediment accumulation rates. B. Age depth model from R Tofu calculations: median age (red curve), minimum and maximum ages (grey curves), RDL (grey bars). X axis indicates ages in cal yr BP and date in yr CE. 197

Figure 49. GL17-13 down core properties. High-resolution image, Pseudo S-ratio and S ratio, k_{ARM} (magnetic susceptibility of the ARM), MDF of the NRM, ARM and IRM, Ca/Fe from XRF analyses, Hcr/Hc and Mrs/Ms from hysteresis loop measurements. The thin yellow bar indicates the RDL. The zoom profiles on the right show Zr/Rb and Ca/Fe profiles for the RDL. 199

Figure 50. GL23-20 composite downcore properties. From left to right: magnetic susceptibility (k_{LF}), a*, L*, Pseudo S-ratio, S-ratio, k_{ARM}/k_{LF}, MDF (NRM, ARM and IRM), Ca/Fe and grain size data (D_{50} and D_{90}). Beige horizontal bars indicate RDL....201

Figure 51. Magnetic susceptibility variations curves depending on the temperature. Heating curves in red, cooling curves in blue....203

Figure 52. Rock magnetic results of core GL17-13 samples. **A**. IRM unmixed curves indicating the samples main coercivities. **B.** FORC diagram. **C.** Hysteresis loops**.**....203

Figure 53. Hysteresis loops for GL23-20 composite core. **A.** Hysteresis loops for samples at the top of the composite sequence (0-200 cm). **B.** Hysteresis loops for samples in the composite sequence (200-1800 cm) **C.** Hysteresis loops for samples at the base of the composite sequence (1900-2050 cm) **D.** Hysteresis loops for RDL samples....205

Figure 54. King plot (King et al., 1983). RDL samples are represented by blue dots, background sedimentation is represented by pink dots....206

Figure 55. Day plot (Day et al., 1977). Blue dots are samples from core GL17-13. Red dots are samples from GL23-20 core....206

Figure 56. Continuous paleomagnetic analyses for GL23-20 composite sequence. From left to right: NRM, ARM, IRM and SIRM intensity for the different demagnetization steps mentioned in the methods, inclination and GAD values, declination values, MAD values. Beige horizontal bars indicate RDL....207

Figure 57. Relative paleointensity determination. **A.** Slope NRM-ARM 20-60 mT . **B.** Slope NRM-IRM 20-60 mT. **C.** Ratio NRM/ARM 20-60 mT. **D.** Ratio NRM/IRM 20-60 mT. **E.** Correlation coefficient (R) for ARM (blue curve) and IRM (brown curve) for the slope method. **F.** ARM against IRM values, indicator of magnetic grain-size and concentration variations. **G.** ARM determination coefficient r^2 for the ratio method. H. IRM determination coefficient r^2 for the ratio method....208

Figure 58. Continuous paleomagnetic analyses for GL23-20 composite sequence. From left to right: NRM, ARM, IRM and SIRM intensity, inclination and GAD values, declination values, MAD values. Beige horizontal bars indicate RDL. Blue and green rectangles indicate the changes in sedimentary environment indicated in Kury et al., (2025)....210

Figure 59. Relative paleointensity determination for GL23-20 composite sequence. **A.** Slope NRM-ARM 20-60 mT. **B.** Slope NRM-IRM 20-60 mT. **C.** Ratio

NRM/ARM 20-60 mT. **D.** Ratio NRM/IRM 20-60 mT. **E.** Correlation coefficient (R) for ARM (green curve) and IRM (purple curve) for the slope method. **F.** ARM against IRM values, indicator of magnetic grain-size and concentration variations. **G.** ARM determination coefficient r^2 for the ratio method. **H.** IRM determination coefficient r^2 for the ratio method. 211

Figure 60. Physical, elemental and magnetic properties of RDL 16. 214

Figure 61. Physical, elemental and magnetic properties of RDL 33. 214

Figure 62. Physical, elemental and magnetic properties of RDL 37. 215

Figure 63. Physical, elemental and magnetic properties of RDL 49 and 50. 215

Figure 64. Physical, elemental and magnetic properties of RDL 56. 216

Figure 65. Physical, elemental and magnetic properties of RDL 57. 216

Figure 66. Physical, elemental and magnetic properties of RDL 58. 217

Figure 67. For all RDL, amplitude of inclination (**A**) and k_{LF} (**B**) changes as a function of RDL thickness. **C.** Amplitude of inclination changes for RDL>8cm thickness **D.** Amplitude of k_{LF} changes as a function of RDL thickness, excluding RDL 59 and 67, the two higher points in panel B. The blue line is the best fit logarithmic curve, dotted lines represent the confidence interval. Correlation coefficients and p-values are indicated on each graph. 218

Figure 69. Inclination (°) comparison over the last 2500 years (cal yr BP) between GL17-13 record, GL23-20 record, GREENICE15k record, MD99-2220 record from the St. Lawrence Estuary and the IGRF and GUFM1 models. All records and models are projected to Grand Lake location via their VGP paths. 222

Figure 70. Absolute and relative paleointensity comparison over the last 2,500 years (cal yr BP) between IGRF and GUFM1 models, CALS3k.4 model, Petermann stack, GL17-13 record, U1305 record, and MD99-2220 record from the St-Lawrence estuary. 224

Figure 71. Projections of the geomagnetic field intensity at the core mantle boundary and the Earth surface from CALS10k.2 geomagnetic model (Constable et al., 2016, supporting information) at different time: 2500 cal yr BP (**A**), 2100 cal yr BP (**B**), 2010 cal yr BP (**C**), 1010 cal yr BP (**D**), and 500 cal yr BP (**E**). **F** represents GL17-13 RPI curve. The different time of CALS10k.2 projections are indicated with letters in the panel. Yellow stars indicate the location of Grand Lake; orange dot indicate the location of Petermann

Fjord; grey dot indicate the location of MD99-2220; black dot indicate the location of U1305. 226

Figure 72. Intensity, declination and inclination comparisons between IGRF calculations and GUFM1 model (for Grand Lake location) and GL23-20 composite sequence (RPI calculated with the slope method). 228

Figure 73. Figure de synthèse. **A.** Taux de production moyennés des isotopes cosmogéniques ^{14}C (global) et ^{10}Be (hémisphère Nord). Les courbes plus foncées sont les courbes des tendances. **B.** Moments dipolaires globaux enregistrés par différents modèles géomagnétiques : CALS10k.2 (courbe noire) (Constable et al., 2016), pfm9k.2 (courbe grise) (Nilsson et al., 2022) et CALS3k.4 (courbe marron) (Korte and Constable, 2011). **C.** Petermann Fjord RPI stack (Girard et al., 2024). La partie claire de la courbe (0-700 ans) représente l'intervalle incertain décrit dans le chapitre 1. **D.** Enregistrement de paléointensité relative à Grand Lake (carotte GL17-13). L'encart agrandi contient les enregistrements de paléointensité relative établis à partir de la carotte GL17-13 (rouge), GL23-20 (vert) et l'intensité du champ (nT) (bleu) d'après les calculs d'IGRF et du modèle GUFM (Jackson et al., 2000) pour les derniers 400 ans. **E.** Enregistrement de paléointensité relative sur la marge Nord-Est du Groenland (carotte 073G). Les trois enregistrements de RPI ont chacun été normalisés à 1 afin de faciliter la comparaison. La flèche représente l'intervalle de temps où LIAA (Levantine Iron Age Anomaly) a été enregistré (Shaar et al., 2016, 2017). **F.** Projection de l'intensité globale du champ (moment dipolaire CALS10k.2 ; Constable et al., 2016) à 1.4 ka. **G.** Projection de l'intensité globale du champ (moment dipolaire CALS10k.2 ; Constable et al., 2016) à 2.6 ka. **H.** Projection de l'intensité globale du champ (moment dipolaire CALS10k.2 ; Constable et al., 2016) à 4.5 ka. Pour F, G, et H. Les étoiles représentent les sites d'études Grand Lake (rouge), Fjord de Petermann (orange) et la marge nord-est du Groenland (bleu). Les points représentent les reconstitutions du VGP à partir des enregistrements de Petermann (orange) et de 073G (bleu). Les cercles jaunes indiquent la position du cylindre tangentiel. La figure a été réalisée avec Grapher, CorelDraw et ArcGIS pour les cartes F, G, H, en utilisant un fond de carte provenant de la NOAA, Esri, USGS, contributeurs Open Street Map et de la communauté GIS. Les fichiers de traits de côte proviennent de GADM version 2.8 (*https://gadm.org*)......................................252

LISTE DES ABRÉVIATIONS, DES SIGLES ET DES ACRONYMES

AAS	Anomalie Atlantique Sud
AF	*Alternating field* – champ alternatif
AMS	*Accelerator mass spectrometer* – spectromètre de masse par accélération
ARM	*Anhysteretic remanent magnetization* – aimantation rémanente anhystérétique
BP	*Before Present* – âge avant 1950
Cal BP	*Calendar age Before Present* – âge calendaire avant 1950
CE	*Common Era* – Ere commune
ChRM	*Characteristic Remanent Magnetization* – aimantation rémanente caractéristique
CMT	Champ magnétique terrestre
CT	Cylindre tangentiel
DC	*Direct current* – courant continu
DRM	*Detrital remanent magnetization* – aimantation rémanente détritique
GAD	Geocentric axial dipole – dipole axial géocentrique
Hc	*Coercive force* – force de coercivité
Hcr	*Remanent coercive force* - coercivité rémanente

INRS-ETE	Institut National de la Recherche Scientifique – centre Eau Terre et Environnement
IPGP	Institut de Physique du Globe de Paris
IRD	*Ice-Rafted Debris* – débris transportés et déposés par la glace
IRM	*Isothermal Remanent Magnetization* – aimantation rémanente isotherme
ISMER	Institut des sciences de la mer
k_{LF}	Susceptibilité magnétique en champ faible
k_{ARM}	Susceptibilité magnétique de l'ARM
LDEO	*Lamont Doherty Earth Observatory*
LIAA	*Levantine Iron Age geomagnetic anomaly* – anomalie géomagnétique Levantine de l'âge de fer
LIS	*Laurentide Ice Sheet* – calotte glaciaire laurentidienne
MAD	*Maximum angular deviation* – déviation angulaire maximale
MD	*Multi domain* – domaine multiple
MDF	*Median destructive field* – champ de destruction médian
MICADAS	*MIni CArbon DAting System*
Mr	*Saturation remanence* – aimantation rémanente de saturation
Ms	*Saturation magnetization* – aimantation de saturation
MSCL	*Multi Sensor Core Logger*
NRM	*Natural Remanence Magnetisation* – aimantation rémanente naturelle

pDRM	*Post-depositional remanent magnetisation* – aimantation rémanente après dépôt
PNM	Pôle Nord Magnétique
PSM	Pôle Sud Magnétique
PSD	*Pseudo single domain* – pseudo simple domaine
PSV	*Paleomagnetic secular variations* – variations paléomagnétiques séculaires
SAR	*Sediment accumulation rate* – taux d'accumulation de sédiments
SD	*Single domain* – simple domaine
SIRM	*Saturation Isothermal Remanent Magnetization* – aimantation rémanente isotherme de saturation
RDL	*Rapidly Deposited Layer* – couche déposée rapidement
RPI	*Relative Paleointensity* – paléointensité relative
UQAM	Université du Québec à Montréal
UQAR	Université du Québec à Rimouski
VADM	*Virtual Axial Dipole Moment* – moment dipolaire axial virtuel
VGP	*Virtual Geomagnetic Pole* – Pôle Géomagnétique Virtuel
WMM	*World Magnetic Model* – modèle magnétique mondial

LISTE DES SYMBOLES

ΔR	Delta R – correction d'âge réservoir
^{10}Be	Béryllium 10
^{14}C	Carbone 14
^{210}Pb	Plomb 210
^{137}Cs	Césium 137

INTRODUCTION GÉNÉRALE

1. LE CHAMP MAGNETIQUE TERRESTRE : ORIGINE ET FONCTIONNEMENT

Les récentes observations du champ magnétique terrestre (CMT), via des mesures directes sur le terrain ou indirectes par des satellites, ont montré des variations spectaculaires depuis le début du XX^{e} siècle, telles que la migration du pôle Nord magnétique (PNM), la diminution de l'intensité de la composante dipolaire du champ magnétique (16 nT/an depuis le milieu du XIX^{e} siècle) et l'expansion d'une anomalie d'intensité négative située dans l'océan Atlantique Sud (ex. Gillet et al., 2013; Gubbins et al., 2006; Hulot et al., 2002). En effet, le PNM dont la trajectoire de migration se limitait à l'Arctique Canadien pour les 400 ans dernières années (Jackson et al., 2000), migre maintenant dans l'océan Arctique, vers la Sibérie. Sa vitesse de migration a fortement augmenté dans les années 1990 passant de plus ou moins 10 km/an à environ 55 km/an, avant de diminuer de nouveau à environ 35 km/an en 2015. L'accélération et la décélération rapides étaient toutes les deux sans précédent dans les données de la période historique (400 dernières années). D'après les calculs du Modèle Magnétique Mondial (*world magnetic model*, WMM), le PNM se situe à 85.762°N et 139.298°E en 2025 (National Centers for Environmental Information, 2023, 2022, 2021).

Le CMT trouve son origine par le mouvement de fluides dans le noyau terrestre externe (ex. Buffett, 2000; Bullard, 1949; Glatzmaiers & Roberts, 1995). Le noyau terrestre comprend une couche externe liquide et un noyau interne solide, composés majoritairement de fer et de nickel, et soumis à des gradients de température et de densité (Figure 1A). Ce serait ces gradients qui entraineraient une convection des fluides, générant une dynamo auto-alimentée, et créant ainsi le champ magnétique terrestre ou champ géomagnétique. Selon, les études les plus récentes, les traces les plus anciennes du champ magnétique terrestre remontent maintenant à quatre milliards d'années (Tarduno et al., 2020, 2010; Usui et al., 2009). Les lignes de champ composent la magnétosphère qui protège la Terre des rayons et particules cosmiques et solaires (Figure 1B).

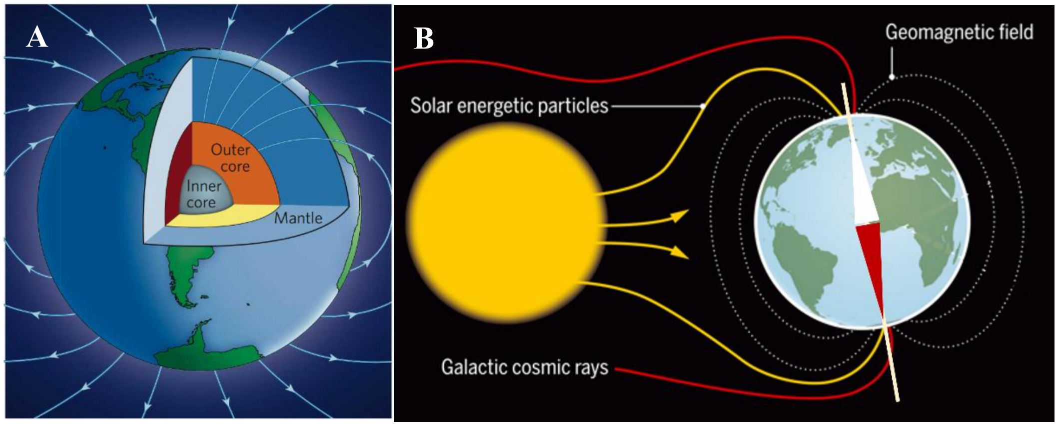

Figure 1. A. Vue schématique de l'intérieur de la Terre (Gubbins, 2008). Le champ géomagnétique terrestre provient du noyau externe. **B.** Schéma des particules et rayons solaires déviés par les lignes de champ de la magnétosphère (modifiée d'après Heaton et al., 2021). Le CMT s'apparente à un dipôle tel que schématisé sur la figure.

À la surface de la Terre, le CMT peut être décrit comme un vecteur à trois composantes : inclinaison, déclinaison et intensité (Thompson & Oldfield, 1986; Figure 2). L'inclinaison I est le pendage des lignes de champ dans le plan vertical par rapport à l'horizontale, soit +90° au PNM, -90° au pôle Sud magnétique (PSM) et 0° proche de l'équateur. La déclinaison est l'angle entre la composante horizontale du champ magnétique et le Nord géographique. L'intensité du champ est la norme du vecteur (Tauxe, 2010; Thompson and Oldfield, 1986).

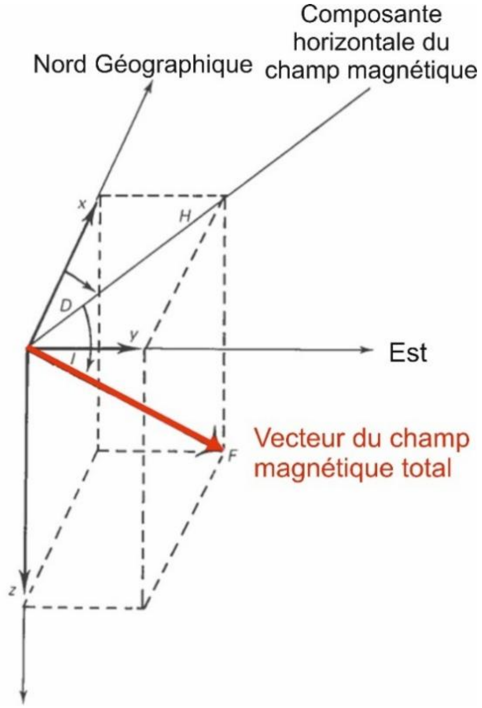

Figure 2. Le champ magnétique peut être défini par trois éléments en tout point de la surface terrestre. Le vecteur F est le vecteur magnétique total. La déclinaison (D) est l'angle entre le Nord géographique et le méridien magnétique (composante horizontale H du champ). L'inclinaison (I) est l'angle entre le méridien magnétique et le vecteur magnétique. (x) représente le nord orthogonal, (y) l'est et (z) la composante vers le bas. Modifiée d'après Thompson and Oldfield (1986).

Différents pôles permettent de décrire le champ géomagnétique (ex. Tauxe, 2010). Les **pôles géomagnétiques** sont les deux pôles de l'axe du meilleur dipôle décrivant le CMT, à la surface de la Terre. Ceux-ci peuvent servir d'approximation lorsque la composante non-dipolaire du champ est faible. Les **pôles magnétiques** (pôles Nord et Sud), sont situés là où les lignes de champ sont précisément verticales par rapport à la surface de la Terre (avec I = ± 90°). L'étude du comportement du CMT et donc du dipôle dans le passé, se base la plupart du temps sur des mesures ou des observations locales (e.g. Jackson et al., 2000), nécessitant d'imaginer le dipôle axial géocentrique (dipôle virtuel) duquel résulterait la direction observée (Tauxe, 2010). Le **Pôle Géomagnétique Virtuel (PGV)** est le pôle géomagnétique correspondant à ce dipôle virtuel.

Sur une période de temps suffisamment longue (>10 ka), la composante principale du CMT peut être assimilée à un dipôle, aligné avec l'axe de rotation de la Terre (dipôle axial géocentrique ; GAD ; Creer et al., 1954; Hospers, 1953; Merrill & McFadden, 2003). Bien que décrit à 90% comme un dipôle, le champ géomagnétique est tout de même plus complexe et compte également des structures non-dipolaires. Par exemple, l'Anomalie magnétique de l'Atlantique Sud (AAS) est une zone de très faible intensité dans l'océan Atlantique Sud et constitue actuellement la déviation la plus importante du champ dipolaire axial (ex. Campuzano et al., 2019; Hartmann & Pacca, 2009; Pavón-Carrasco & De Santis, 2016; Terra-Nova et al., 2017). L'origine des contributions dipolaire et non dipolaire du champ géomagnétiques sont différentes : le champ dipolaire axial est généré en profondeur dans le noyau externe tandis que le champ non dipolaire axial provient de mouvements complexes de fluides à la surface du noyau (ex. Constable, 1992; Hoffman, 1992; Hoffman & Singer, 2008; Singer et al., 2014). Aujourd'hui il est entendu que le champ géomagnétique s'apparente à un dipôle sur des échelles de temps d'au moins 10^{4-5} années, sans certitude pourtant de l'échelle minimale de ces variations dipolaires : les variations séculaires reflètent-elles les variations dipolaires globales ou reflètent-elles uniquement des variations régionales ?

Plusieurs études ont émis l'hypothèse de cyclicités des variations paléomagnétiques (Mackereth, 1971; Opdyke, 1972). Des études sédimentaires combinées à des observations directes ont permis de mettre en évidence une cyclicité millénaire dans les variations directionnelles au cours de l'Holocène (ex. Nilsson et al., 2011; St-Onge et al., 2003). Bien que ces variations directionnelles soient liées aux variations d'intensité du champ géomagnétique, en particulier des lobes de flux (Nilsson et al., 2011), les périodicités des variations d'intensité ont fait l'objet de moins d'études et les liens entre les variations séculaires à millénaires d'intensité et de direction du CMT sont encore peu documentés (Stoner et al., 1995; St-Onge et al., 2003). Nilsson et al. (2022) ont mis en évidence des asymétries du champ quasi-récurrentes (semblables à l'AAS) au cours des derniers 9 000 ans, avec des variations quasi-périodiques du moment dipolaire à l'échelle millénaire, en soulignant que les minima d’intensité du moment dipolaire ont tendance à coïncider avec de fortes anomalies du champ géomagnétique.

2. LE CHAMP GEOMAGNETIQUE AUX HAUTES LATITUDES DE L’HEMISPHERE NORD

Des modèles numériques basés sur des observations ont montré que malgré la composante dipolaire dominante, le champ géomagnétique est plus complexe. Que le champ géomagnétique ne soit pas un parfait dipôle géomagnétique centré serait dû en partie à la présence du noyau interne solide. En effet, le cylindre tangentiel (CT) est une zone de circulation de fluide dans le noyau externe, dans un cylindre tangent au noyau interne solide au niveau de l’équateur, parallèle à l’axe de rotation de la Terre (ex. Jackson et al., 2000; Lawrence et al., 2009; Olson & Aurnou, 1999). En dehors de ce CT, la convection des fluides se fait en colonne du fait des forces de Coriolis. Au sein du CT, du fait de la présence du noyau solide, la convection est moins organisée, les forces de Coriolis plus faibles, résultant en une intensité plus faible au niveau de la surface terrestre. On observe ainsi des différences d’intensité en surface, plus faible à l’intérieur du CT, plus forte à l’extérieur. On observe notamment des lobes de flux géomagnétiques, plus ou moins stationnaires, deux dans chaque hémisphère, à environ 20° des pôles géographiques (Bloxham et al., 1989; Bloxham and Jackson, 1992; Jackson et al., 2000; Tauxe, 2010). Dans l’hémisphère Nord ces zones se situent en Amérique du Nord et Sibérie, avec un potentiel troisième lobe au niveau de l’Europe. St-Onge & Stoner (2011) ont fait l’hypothèse que les variations dans le Haut-Arctique ont des caractéristiques uniques au sein de la projection en surface du CT, tandis que les variations enregistrées dans l’Arctique inférieur présenteraient plus de similarités avec les latitudes moyennes (Lund & Banerjee, 1985; St-Onge & Stoner, 2011; Verosub et al., 1986).

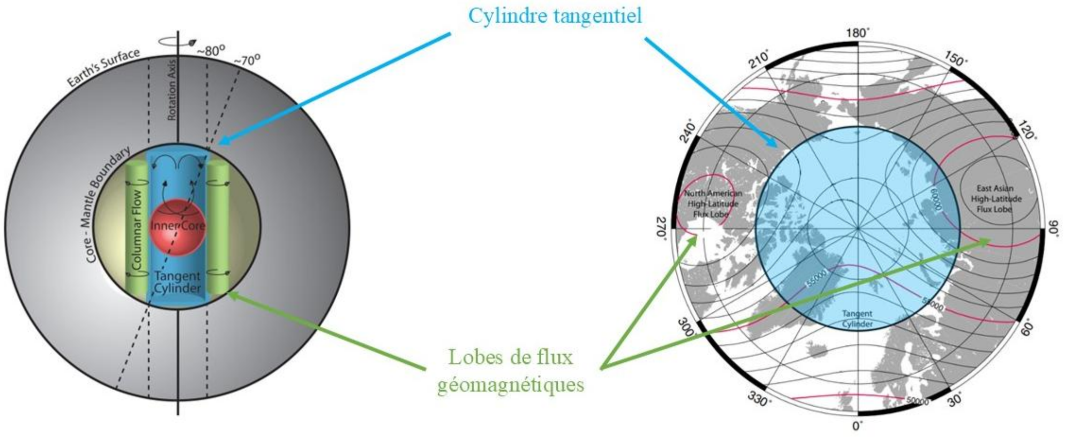

Figure 3. Schéma de la convection dans le noyau terrestre externe et de sa résultante en surface. La circulation des fluides en colonnes est à l'origine des lobes de flux géomagnétiques, tandis que la circulation au sein du cylindre tangentiel résulte en de plus faibles intensités en surface. L'intensité en surface est indiquée par des courbes d'isointensité (nT). Modifié d'après Lawrence et al. (2009); Lund et al. (2016).

3. VARIATIONS DU CHAMP GEOMAGNETIQUE

Le champ géomagnétique n'est pas stable au cours du temps et connaît des variations de différentes ampleurs et à différentes échelles de temps. Le CMT a notamment connu des périodes de polarités différentes (Brunhes, 1906; Lowrie and Fichtner, 1997; Ogg, 2020; Thompson and Oldfield, 1986). Les inversions délimitent des périodes de polarité constante appelées chrons, sub-chrons ou superchrons, dépendamment de leur durée (Opdyke and Channell, 1996). Ce sont des événements se produisant dans des intervalles temps relativement courts (quelques milliers à quelques dizaines de milliers d'années, Gubbins, 1999, 2008), associés à de faibles intensités géomagnétiques (diminution d'environ 10% ; Tauxe, 2010), définis par le déplacement des pôles géomagnétiques dans l'hémisphère opposé à celui dans lequel ils se trouvaient (Merrill and McFadden, 1994). L'inversion de Brunhes-Matuyama, il y a 780 000 ans, délimite l'actuel chron Brunhes (Brunhes, 1906). La polarité peut être normale (même que l'actuelle) ou inverse (opposée à l'actuelle) (Harland et al., 1983; Ogg, 2020). De nombreuses questions se posent toujours concernant les mécanismes à l'origine des inversions, et ce qui se produit pendant une inversion. De plus, la fréquence des inversions n'est pas constante (Gubbins et al., 2006), avec des périodes de polarité constante allant jusqu'à plusieurs dizaines de millions d'années comme le superchron du Crétacé (e.g. Helsley & Steiner, 1968; Larson & Pitman, 1972; Yoshimura, 2022). Les excursions sont définies comme des périodes relativement courtes de quelques milliers d'années, voire moins dans le cas de l'excursion de Laschamp (Bonhommet and Babkine, 1967; Channell and Vigliotti, 2019; Cooper et al., 2021), au cours desquelles, les PGV migrent à plus de 45°, avant de revenir à leur position initiale (Cande and Kent, 1992; Gubbins, 1999; Verosub and Banerjee, 1977). Elles sont habituellement nommées d'après l'endroit où elles sont observées pour la première fois. L'excursion la mieux documentée du chron Brunhes est l'excursion de Laschamp qui a eu lieu il y a 41 ka (Bonhommet and Babkine, 1967; Bonhommet and Zahringer, 1969; Laj and Channell, 2007; Velle et al., 2021). Les excursions et les inversions du champ géomagnétique représentent des marqueurs stratigraphiques très utilisés pour corréler des enregistrements à l'échelle globale : c'est le principe de la magnétostratigraphie, qui repose sur l'échelle de temps de polarité géomagnétique (Geomagnetic Polarity Time Scale, GPTS ; e.g. Laj & Channell, 2007; Ogg, 2020). À plus petite échelle, les variations paléomagnétiques séculaires (*paleomagnetic secular variations*, PSV) représentent les variations directionnelles et de magnitude du vecteur magnétique décrit plus haut et elles reflètent la dynamique de la convection dans le noyau externe. Ces variations peuvent être observées sur des échelles de temps annuelles, décennales, séculaires et millénaires. Elles peuvent également être utilisées dans l'établissement d'une chronologie à des échelles locale, régionale et même parfois globale (Barletta et al., 2010; Ólafsdóttir et al., 2019, 2013; Stoner et al., 2013; Stoner and St-Onge, 2007).

Les variations récentes du champ géomagnétique sont bien documentées grâce aux observations directes sur le terrain et via des satellites. Seulement, ces données récentes instrumentales ne couvrent que les 400 dernières années environ et on parle alors de données historiques. Les données historiques ont mis en évidence des changements récents du CMT tels que la diminution de l'intensité dipolaire du CMT depuis les premières mesures (Gauss, 1833; Gubbins, 2008), l'accélération de la vitesse de migration du PNM et le renforcement de l'AAS. Ces changements ont soulevé de nombreuses questions au sein de la communauté scientifique : quelle est l'origine de ces variations récentes ? Quel est le moteur de la migration du PNM ? Ces variations sont-elles les signes précurseurs d'un changement du CMT de plus grande amplitude telle qu'une inversion ? Observe-t-on des fluctuations rapides au cours de l'Holocène ? La direction de la migration du PNM est-elle liée aux fluctuations des lobes de flux ? À quelles échelles de temps (séculaires, millénaires) observe-t-on des variations dipolaires globales ?

Une autre manière indirecte d'étudier les variations du champ magnétique est d'étudier les isotopes cosmogéniques, créés par réactions de spallation entre les rayons cosmiques de haute énergie et certains atomes dans l'atmosphère, dont le taux de production est en lien avec les variations d'intensité du champ géomagnétique. Le ^{10}Be est issu de réactions entre les rayons cosmiques et les atomes d'oxygène et d'azote dans la stratosphère (65%) et la troposphère (35%) (Dunai and Lifton, 2014; Lal and Peters, 1967). Le ^{14}C provient de l'interaction entre les rayons cosmiques et les atomes d'azote (Lal and Peters, 1967). La magnétosphère protège la Terre des rayons et particules cosmiques en agissant comme une sorte de bouclier et les taux de production des isotopes cosmogéniques varient à l'inverse (de manière non linéaire), de l'intensité du champ géomagnétique (Elsasser et al., 1956; Kovaltsov et al., 2012; Masarik and Beer, 1999; Simon et al., 2016). Ces taux de production dépendent également d'autres paramètres tels que l'activité solaire, qui est liée au champ magnétique du Soleil. Il est parfois difficile de différencier les signaux du champ géomagnétique de l'activité solaire, mais de manière générale, on estime que les variations d'isotopes cosmogéniques sont modulées par l'activité solaire sur des échelles décennales à séculaires, et par le champ géomagnétique sur des échelles de temps millénaires (Snowball et Muscheler, 2007). Les variations des taux de production d'isotopes cosmogéniques peuvent être utilisées pour caractériser les variations de paléointensité relative par comparaison (ex. St-Onge et al., 2003).

Afin de reconstituer les variations du CMT au cours du temps, il est possible d'utiliser du matériel géologique et archéomagnétique qui enregistre les variations passées du champ et permettent de caractériser les variations du champ paléomagnétique des derniers milliards d'années. Les artefacts archéomagnétiques (poteries) et les laves volcaniques enregistrent l'intensité et les directions du champ lors de leur refroidissement. Ces matériaux enregistrent l'intensité absolue du champ, mais ne représentent que des enregistrements ponctuels du champ géomagnétique, en plus de présenter une distribution spatiale hétérogène, en étant rares dans de nombreuses régions comme l'Arctique. De plus, les archives archéomagnétiques ne constituent que des enregistrements très récents (dernières centaines à milliers d'années). Les sédiments marins et lacustres représentent un enregistrement continu du CMT et présentent une plus grande couverture spatiale, permettant d'étudier les variations paléomagnétiques tout autour du globe.

4. PALEOMAGNETISME SEDIMENTAIRE

Bien qu'offrant la possibilité d'étudier les variations continues du champ paléomagnétique, l'étude à partir des sédiments est complexe. L'hypothèse de base du paléomagnétisme sédimentaire est que l'aimantation portée par les sédiments détritiques (DRM) est une réponse linéaire directe du champ appliqué (e.g. Tauxe, 1993, 2006; Tauxe & Yamazaki, 2007). Les particules magnétiques sédimentaires enregistrent les propriétés du champ géomagnétiques au moment de leur dépôt, tant qu'elles sont libres de leur mouvement (Figure 4). Cependant l'aimantation enregistrée dépend également des propriétés du sédiment telles que la granulométrie, la minéralogie et la concentration des particules magnétiques (Amerigian, 1974; Chave et Denham, 1979; Guyodo et Channell, 2002; Kent, 1982).

En réalité, il est généralement établi que les sédiments acquièrent leur aimantation via le processus de l'aimantation rémanente après dépôt (*post-depositional remanent magnetization*, pDRM ; deMenocal et al., 1990; Irving & Major, 1964; Kent, 1973; Verosub, 1977). Les particules qui se déposent au fond de l'océan continuent de s'orienter selon le champ géomagnétique lors des processus de compaction et d'assèchement du sédiment. Il y a donc un décalage vertical en profondeur entre l'interface eau/sédiment où les sédiments se déposent, et la profondeur à laquelle les particules fixent l'aimantation rémanente, appelée

« profondeur de blocage ». La profondeur de blocage dépend des conditions environnementales de dépôt, notamment du taux d'accumulation des sédiments. Elle peut varier de 0 à quelques dizaines de centimètres, mais le processus et les détails de l'enregistrement de l'aimantation restent encore débattus (e.g. deMenocal et al., 1990; Guyodo & Channell, 2002; Liu et al., 2008; Suganuma et al., 2010, 2011; Tauxe, 2006; Tauxe & Yamazaki, 2007).

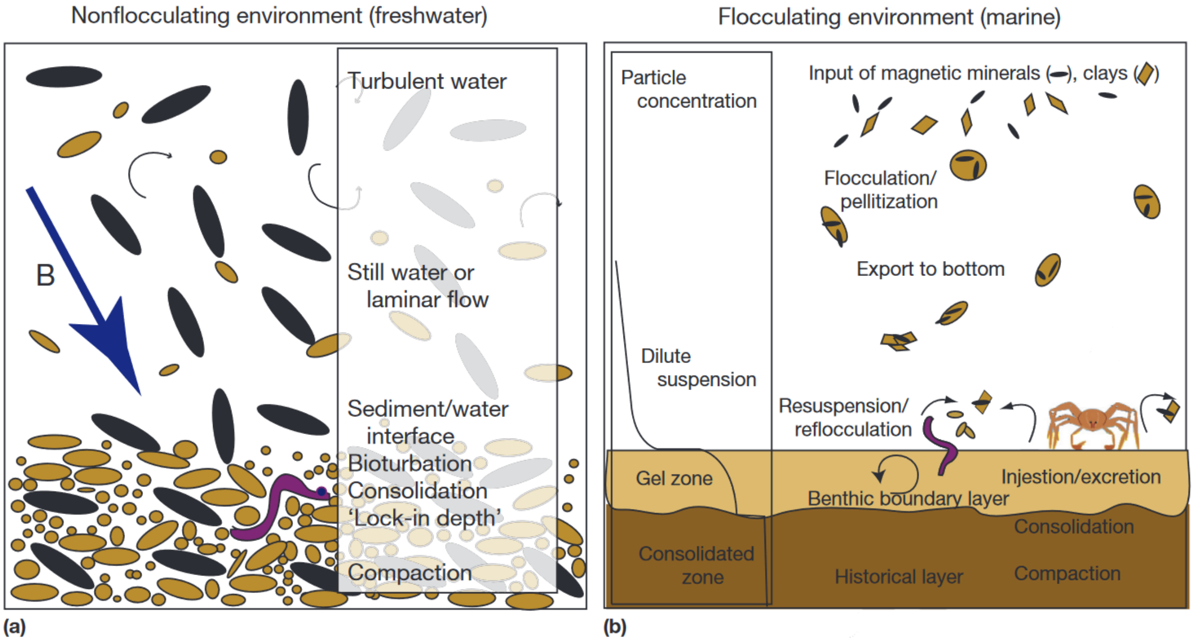

Figure 4. Schéma des processus lacustres et marins amenant à l'enregistrement de la rémanence dans les sédiments dans un milieu non-floculant **(a)** et dans un milieu floculant **(b)**. D'après Tauxe & Yamazaki (2015).

5. L'ARCTIQUE

L'Arctique est un endroit privilégié pour les études paléomagnétiques et géomagnétiques (St-Onge and Stoner, 2011), notamment pour étudier les variations du PNM et des lobes de flux géomagnétiques, qui sont des manières indirectes d'étudier les processus dans le noyaux externe ou à la limite avec le manteau terrestre. La projection en surface du CT est observée dans l'Arctique à environ 70°N (Lawrence et al., 2009). De plus, la proximité du PNM permet d'enregistrer des variations directionnelles (inclinaison, déclinaison) séculaires d'amplitudes plus importantes dans les séquences sédimentaires arctiques. Cependant, les études dans l'Arctique représentent un défi. C'est une zone difficile d'accès du fait de son éloignement et de la présence de glace de mer la majorité de l'année. Les enregistrements paléomagnétiques sédimentaires provenant de l'Arctique sont donc rares, et manquent quelques fois dans les modèles du champ géomagnétique, comme par exemple dans le modèle récent pfm9k.2 (Nilsson et al., 2022). De plus, l'établissement d'une chronologie reste complexe pour les sédiments en Arctique. Les sédiments holocènes sont de manière générale facilement datables au radiocarbone, mais le matériel carbonaté biogénique dans la région de l'Arctique est souvent rare à cause de la dissolution du $CaCO_3$, car la profondeur de compensation des carbonates est plus faible dans les eaux froides (Jutterström et Anderson, 2005) et la correction de l'âge réservoir pour le carbone est parfois difficile à établir (Hanslik et al., 2010; Heaton et al., 2023, 2020). Le paléomagnétisme devient alors un outil important de datation dans l'Arctique pour le Quaternaire supérieur (ex. Barletta et al., 2008, 2010; Lisé-Pronovost et al., 2009; Ólafsdóttir et al., 2013; Reilly et al., 2019; Stoner et al., 2013).

6. OBJECTIFS, QUESTIONS ET HYPOTHESES DE RECHERCHE

L'objectif principal de cette thèse de doctorat est d'étudier les variations paléomagnétiques séculaires à millénaires à différents endroits de l'Arctique et du milieu subarctique afin d'identifier des potentielles fluctuations rapides, de comprendre leur origine et d'examiner leur lien avec les différentes caractéristiques du champ géomagnétique, notamment les lobes de flux et le cylindre tangentiel. De plus, ces nouveaux enregistrements participeront à combler le manque d'enregistrements sédimentaires paléomagnétiques de haute à très haute latitude, dans le but de mieux comprendre le comportement du champ à ces latitudes.

Afin de répondre à cet objectif, trois sous-objectifs spécifiques ont été définis, chacun étant associé à un ou plusieurs chapitres de la thèse.

Reconstituer les variations du champ magnétique terrestre séculaires à millénaires à partir d'enregistrements holocènes de très haute latitude (>75°N)

➔ Chapitres 1 et 2

De nouveaux enregistrements paléomagnétiques aux très hautes latitudes (>75°N) seront établis afin de reconstituer les variations du champ géomagnétique (PSV), et en particulier la paléointensité relative (*relative paleointensity*, RPI) à ces latitudes. L'enregistrement du fjord Petermann (81°N) permettra d'étudier à la fois le lien entre les PSV et le CT, ainsi que l'influence du lobe de flux nord-américain. Les enregistrements du nord-est du Groenland établiront une connexion entre les enregistrements des hautes latitudes et celles de l'Atlantique Nord, mais aussi avec l'Europe, où de nombreux enregistrements holocènes existent déjà et où l'apparition d'un troisième lobe de flux est parfois observée. Si elles s'avèrent de bonne qualité, les données directionnelles (inclinaison et déclinaison) pourront être utilisées pour reconstituer les variations du pôle géomagnétique virtuel et les comparer aux variations globales de l'intensité du champ géomagnétique.

Reconstituer les fluctuations multi-décennales à séculaires du champ géomagnétique au cours de l'Holocène supérieur à partir des sédiments varvés de Grand Lake (Labrador)

➔ Chapitre 3

À partir des sédiments varvés de Grand Lake, nous espérons pouvoir étudier des enregistrements à très haute résolution (taux de sédimentation supérieur aux enregistrements marins, chronologie varvée annuelle). La méthode de carottage utilisée permettra d'échantillonner les sédiments de surface avec peu de déformation et d'obtenir un enregistrement des variations récentes (au moins les derniers 1000 ans). Cet enregistrement permettra alors de faire le lien entre les observations et la modélisation de la période instrumentale (les 400 dernières années) et les enregistrements holocènes qui sont nombreux, mais qui n'enregistrent que très rarement les variations du dernier millénaire.

Comparer les variations paléomagnétiques aux hautes et moyennes latitudes (Arctique, Atlantique Nord, Europe) afin de déterminer les similarités et différences spatiales des variations du champ magnétique terrestre, notamment en lien avec les lobes de flux géomagnétiques.

➔ Chapitres 1, 2 et 3

Dans chacun des chapitres, les nouveaux enregistrements établis seront comparés à d'autres enregistrements sédimentaires de PSV et de RPI de l'Arctique, de l'Atlantique Nord et de l'Europe ainsi qu'à des modèles géomagnétiques locaux et globaux et aux variations des taux de production des isotopes cosmogéniques ^{14}C et ^{10}Be, dans le but d'identifier des similarités ou différences qui pourraient être attribuées à des caractéristiques du CMT (lobes de flux, CT, variations d'intensité dipolaires ou non dipolaires…).

L'atteinte de ces trois objectifs spécifiques permettra d'aborder des questions liées aux fluctuations du champ magnétique dans l'Arctique, au rôle potentiel des lobes de flux et du cylindre tangentiel, aux échelles temporelles et spatiales de variation du champ géomagnétique, ainsi qu'au lien entre les variations géomagnétiques et le taux de production d'isotopes cosmogéniques :

- Au cours de l'Holocène, le champ magnétique terrestre varie-t-il uniformément aux hautes et très hautes latitudes ?

- La migration actuelle du PNM reflète-t-elle une réorganisation du CMT ? Des variations similaires à aujourd'hui se sont-elles déjà produites au cours de l'Holocène ?

- Les paramètres géomagnétiques (RPI, inclinaison, déclinaison) dans l'Arctique sont-ils similaires à ceux hors de l'Arctique, dans l'Atlantique Nord ou en Europe ?

- Les variations des lobes de flux géomagnétiques influencent-elles la migration des VGP ?

- À quelles échelles temporelles observe-t-on une migration des VGP (décennies, siècles, millénaires) ?

- Les changements rapides dans l'Arctique (ex. migration des VGP) coïncident-ils avec d'autres événements ailleurs ?

- Observe-t-on un lien entre les variations de paléointensité provenant des nouveaux enregistrements et les taux de production globaux et/ou dans l'hémisphère nord d'isotopes cosmogéniques ?

- Les incertitudes des modèles d'âge sont-elles liées à des variations de ΔR dans le temps ? Est-il possible de les déterminer ? Est-il possible de les distinguer des incertitudes liées au magnétisme sédimentaire (i.e. la profondeur de blocage) ?

7. SITES D'ETUDES

Afin de répondre aux questions et objectifs énoncés ci-dessus, des carottes sédimentaires ont été sélectionnées pour être étudiées, en fonction de leur localisation (Figure 5).

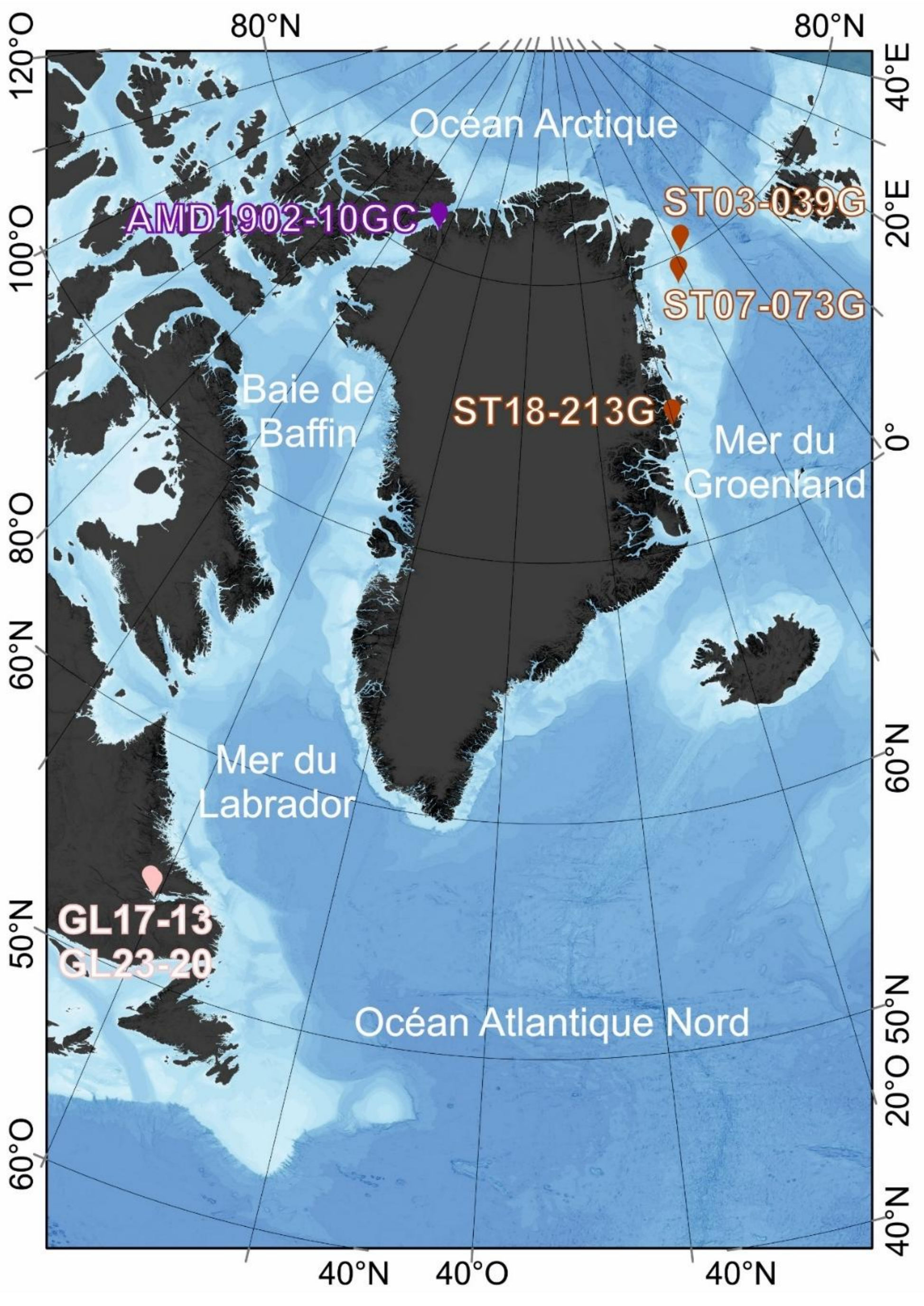

Figure 5. Carte des sites d'études abordés dans cette thèse. Le premier chapitre porte sur la carottes du fjord Petermann dans le détroit de Nares (mauve). Le deuxième chapitre porte sur les carottes de la marge Nord Est du Groenland (rouge). Le troisième chapitre porte sur les carottes prélevées à Grand Lake au Labrador (rose).

Les carottes sédimentaires marines des deux premiers chapitres, localisées à très hautes latitudes (75-81°N) permettront d'étudier les variations dans cette région de l'Arctique, notamment l'influence des lobes de flux géomagnétiques. Les sédiments du fjord Petermann, du fait de leur taux d'accumulation important, ont un grand potentiel pour les études paléomagnétiques, comme démontré par Reilly et al. (2019). Les carottes varvées de Grand Lake (Labrador, Canada) permettront d'obtenir des variations paléomagnétiques à très haute résolution (chronologie annuelle, résolution multi-décennale à séculaire), ainsi que les variations des derniers 1000 ans, afin de lier les observations récentes (derniers 400 ans) aux enregistrements holocènes. La répartition des carottes des trois chapitres permettra de caractériser l'étendue de l'influence du lobe de flux Nord-Américain.

7.1 Fjord Petermann

Le Fjord Petermann se situe au nord-ouest du Groenland, dans le détroit de Nares (Figure 6). Il mesure environ 90 km de long, 20 km de large et atteint une profondeur de 1 100 m. Le glacier Petermann draine environ 4% de la calotte glaciaire du Groenland (Rignot & Kanagaratnam, 2006) vers le Fjord, puis vers le détroit de Nares (Münchow et al., 2016). Il se prolonge par une langue de glace flottant au-dessus des eaux du Fjord, qui est la deuxième plus importante de tout l'hémisphère Nord. Le glacier a été relativement stable au cours de son histoire récente, excepté pour deux événements de vêlage majeurs survenus en 2010 et 2012, qui ont réduit presque de moitié la longueur de la langue de glace, passant de 81 à 48 km (Falkner et al., 2011; Johnson et al., 2011; Münchow et al., 2014; Nick et al., 2013), soit sa plus faible longueur depuis les premières mesures effectuées en 1876 (Nares, 1878).

Le Fjord se situe dans le bassin Franklien composé de roches du Paléozoïque inférieur (Figure 6; Dawes et al., 2000). En particulier, *Hall Land* et *Washington Land*, situés de part et d'autre du Fjord, comprennent des roches du Cambrien supérieur au Silurien inférieur. Une phase de subsidence suivie d'une transgression a conduit à la mise en place d'une plateforme carbonatée au-dessus du socle proterozoïque. Cette plateforme est composée d’une séquence transgressive siliciclastique (grès, mudstone), d’une rampe carbonatée progradante (roche carbonatées : grainstone dolomitisé, packstone, wackestone), ainsi que d’une plateforme intérieure (roches carbonatées : mudstone, wackestones, dolomies, mudstones, grainstones). On observe également plusieurs failles normales, dont trois traversent le fjord et le glacier Petermann. La faille *Faith Gletscher* est la plus importante, avec un déplacement vertical de 365 m.

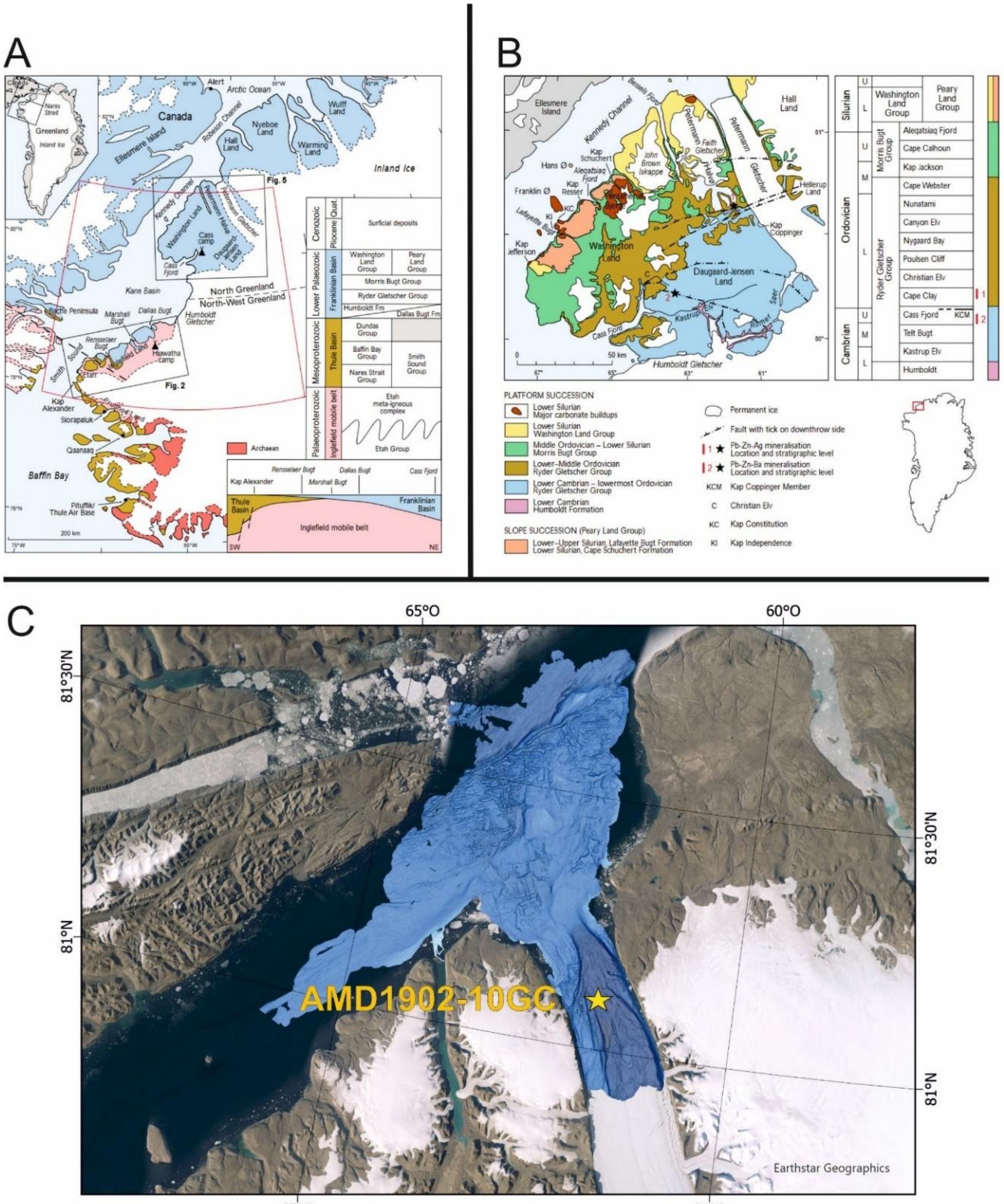

Figure 6. Carte géologique du détroit de Nares (**A**) et du fjord Petermann (**B**). Modifiée d'après Dawes et al. (2000). **C.** Carte bathymétrique du Fjord Petermann avec l'emplacement de la carotte AMD1902-10GC (étoile jaune) étudiée dans le premier chapitre. Les données bathymétriques proviennent de Jakobsson et al. (2018).

Les études bathymétriques (Jakobsson et al., 2018; Tinto et al., 2015) dans le fjord ont révélé une morphologie avec plusieurs bassins délimités par des seuils (Figure 7). Un premier seuil à l'entrée du fjord, à une profondeur d'environ 400 m, donne ensuite sur un bassin au sud, entre 800 et 1000 m de profondeur, délimité par un seuil intérieur (≥570 m). Après ce seuil, un bassin intérieur (≥840 m) continue jusqu'à la zone d'ancrage du glacier, à environ 410-480 m de profondeur et où la glace fait environ 600 m d'épaisseur.

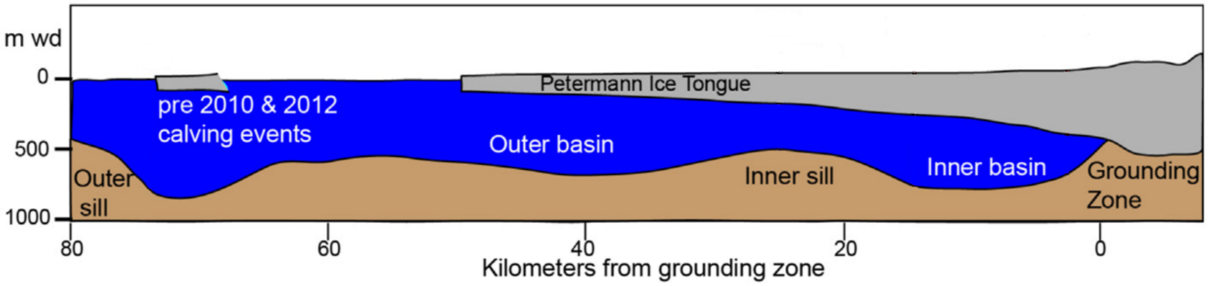

Figure 7. Schéma de la morphologie du fjord Petermann d'après Jennings et al. (2022).

La déglaciation du fjord Petermann s'est faite en plusieurs étapes, pendant la déglaciation du détroit de Nares qui a mené à l'ouverture d'un passage pour la circulation océanique entre l'océan Arctique et la baie de Baffin. Entre 10,7 et 8,4 ka, plusieurs étapes de retrait de la calotte glaciaire via le recul de la zone d'attache du glacier et la rupture de la plateforme glaciaire (Jennings et al., 2022), ont mené à l'ouverture complète du détroit de Nares à 8,4 ka. Une plateforme glaciaire était présente dans le fjord Petermann jusqu'à sa rupture vers 7,1 ka cal BP (Jennings et al., 2022). Pendant environ 5 000 ans, les températures de l'air étaient trop élevées, entre 0,8 et 2,9°C au-dessus des niveaux préindustriels, pour permettre le maintien de cette plateforme (Lecavalier et al., 2017). La langue de glace s'est rétablie dans le Fjord vers 2,2 ka cal BP (1.9-2.3), atteignant une étendue comparable à celle observée avant 2010 autour de 0,6 ka cal BP (Reilly et al., 2019; Figure 8).

La bathymétrie dans le fjord a été modelée par les différentes étapes de déglaciation, et jusqu'à 70 m de sédiments glaciogéniques ont été déposés après le retrait de la calotte glaciaire (Hogan et al., 2020). Différents facies sédimentaires ont été décrits par Hogan et al. 2020 (surfaces rocheuses, dépôts de till sous glaciaire, écoulements gravitaires) dont le principal est constitué de sédiments déposés par les panaches d'eau de fonte et par les icebergs.

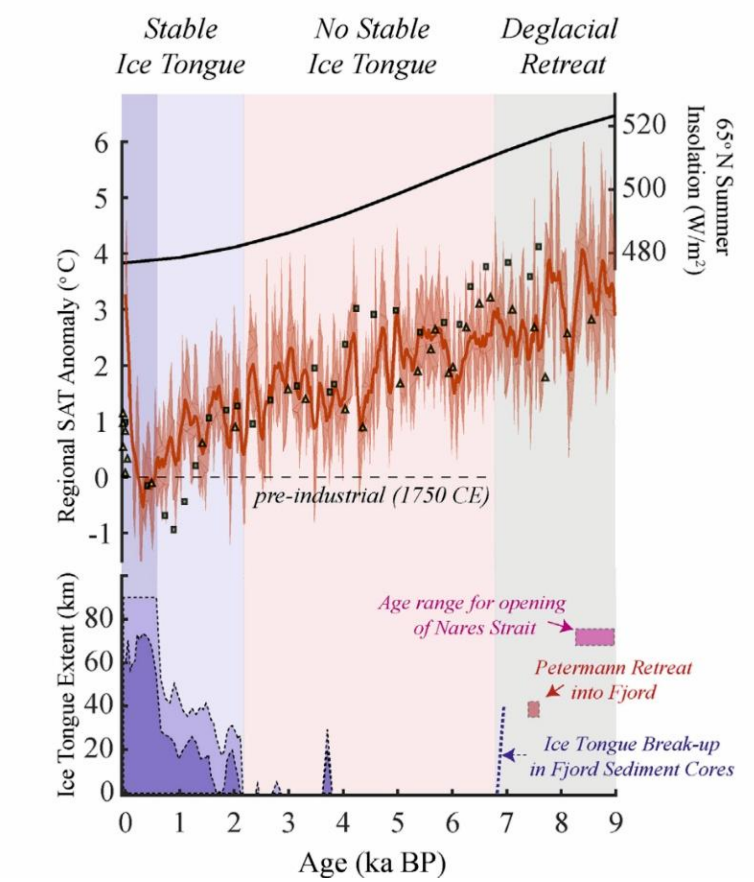

Figure 8. Variations de la langue de glace Petermann au cours des derniers 9000 ans. Modifiée d'après Reilly et al. (2019). L'ombrage indique les intervalles de temps de la déglaciation (gris), de l'absence de langue glaciaire stable et des conditions marines saisonnières ouvertes dans le fjord (rouge), du rétablissement de la langue glaciaire (bleu clair) et d'une langue glaciaire avec des étendues stables comme l'enregistrement historique 1876-2010 (bleu foncé). Les données d'insolation à 65°N indiquent la tendance à la diminution à long terme de l'insolation dans l'hémisphère Nord (Laskar et al., 2004). Les estimations de l'anomalie régionale de la température de l'air en surface (SAT) sont reconstituées à partir de la carotte de glace Agassiz par rapport au niveau pré-industriel de 1750 CE (Lecavalier et al., 2017).

Les eaux de surface du Fjord (0-50 m) sont composées des eaux polaires (*Polar Water*, PW), froides et peu salées, provenant de l'océan Arctique par le détroit de Nares. Les eaux atlantique (*Atlantic Water*, AW), plus chaudes et plus salées, proviennent de la mer de

Lincoln au nord du détroit de Nares et circulent dans le fjord à environ 450 m de profondeur, jusque sous la langue de glace, où elles remontent plus en surface (Jennings et al., 2022). Les eaux de surface sous la langue de glace sont un mélange d'eaux de fonte et de ruissellement de surface de la langue de glace. Les eaux atlantiques remontent vers la surface sous la langue de glace, entrainant sa fonte, qui libère des débris transportés et déposés par la glace (*Ice-Rafted Debris* IRD) près de la zone d'ancrage du glacier (e.g. Münchow et al., 2016; Washam et al., 2019). Les panaches d'eau de fonte circulent ensuite vers l'embouchure du fjord en déposant des sédiments fins.

7.2 Plateau continental du nord-est du Groenland et Young Sound

La calotte glaciaire du Groenland est la deuxième plus importante calotte glaciaire sur Terre après l'Antarctique. De ce fait, le nord-est du Groenland, notamment le plateau continental, est une région clé pour l'étude de la variabilité et la fonte de la calotte glaciaire , ainsi que de la glace de mer. Le plateau continental nord-est du Groenland s'étend sur plus de 300 km depuis les côtes, en mer du Groenland au sud du détroit de Fram, constituant ainsi le plateau continental le plus important du Groenland (Figure 9B). Il est caractérisé par un système de fosses, dont les deux principales sont *Westwind Trough* (WT) et *Norske/Belgica Trough* (NBT) (Arndt et al., 2015). Il est principalement recouvert de sédiments glaciaires déposés au Pléistocène. À l'ouest du plateau continental, des glaciers majeurs tels que le glacier de *Nioghalvfjerdsfjorden* (Glacier de 79°), *Zachariae Isstrøm*, *Storstrømmenet L. Bistrup Bræ* drainent 20% de la calotte glaciaire du Groenland (Zwally et al., 2012).

Le détroit de Fram, large de 500 km, est une zone d'échange majeure entre les océans Arctique et Nord Atlantique, de masses d'eaux profondes (Klenke & Schenke, 2002; Figure 9 A et B). En particulier, le courant est-groenlandais (*East Greenland Current*, EGC) circule depuis le détroit de Fram vers le sud, en longeant le plateau continental, transportant les eaux de fonte (douces) des glaciers. Les eaux polaires de surface (0-50 m), froides et peu salées, proviennent de l'Arctique et des eaux de fonte locales. Les eaux polaires, froides et plus salées (*Polar Water*, PW) circulent à 50-150 m de profondeur, par-dessus les eaux atlantiques

(*Arctic Atlantic Water*, AAW), plus chaudes et plus salées, qui s'écoulent à >150 m, provenant de l'océan Arctique (Rudels et al., 2005). Les eaux de retour de l'Atlantique (*Return Atlantic Water*, RAW), relativement chaudes, transportées par le courant de retour de l'Atlantique, font partie de la branche occidentale du courant du Spitzberg occidental qui s'écoule de l'océan Atlantique Nord vers le nord est du Groenland. Le courant de retour de l'Atlantique s'écoule vers le sud le long de la côte du Groenland en se mélangeant avec les eaux polaires froides de EGC. Ce mélange augmente la densité de la masse d'eau qui constitue ensuite les eaux de débordement du détroit du Danemark. La polynie des eaux du nord-est est délimitée par la *Norske Øer Ice Barrier* (NØIB). Plusieurs études ont documenté l'évolution de la calotte glaciaire groenlandaise au cours de l'Holocène dans cette région (ex. Hansen et al., 2022; López-Quirós et al., 2024; Pados-Dibattista et al., 2022).

Le continent adjacent à ce plateau continental est composé de roches cristallines du socle paléoprotérozoïque, de sédiments protérozoïques, de dolérites mésoprotérozoïque et de dolomies ordoviciennes (Higgins, 2015).

Le système Young Sound-Tyrolerfjord (YST) est un fjord profond de la côte est du Groenland (Figure 9C), d'environ 90 km de long, de 2-7 km de large et de 100 m de profondeur en moyenne, 360 m au maximum (Rysgaard et al., 2003). Deux seuils, interne et externe, délimitent le fjord. Le seuil externe (~45 m de profondeur) limite les échanges d'eau entre le fjord et le plateau continental (Bendtsen et al., 2007), qui s'étend jusqu'à 150 km depuis la côte. Le fjord est alimenté en eau douce par de nombreux réseaux fluviaux tels que *Tyroler River*, *Zackenberg River* et *Lerbugt River*, ainsi que par des glaciers à terminaison marine, qui le connectent à la calotte glaciaire du Groenland. Le courant principal influençant ce système est l'EGC qui transporte les eaux froides de l'Arctique, la glace de mer, ainsi que les apports fluviaux terrestres et les eaux de fonte des glaciers du continent. Généralement, la glace de mer dans le fjord est présente d'octobre-novembre à juin (Glud et al., 2007; Ribeiro et al., 2017; Sejr et al., 2011). La polynie *Sirius Water* se forme à l'extérieur du fjord, sur la plateforme continentale, pendant l'hiver.

Au cours des glaciations passées, la calotte glaciaire s'étendait sur le plateau continental comme en témoignent les dépressions *Westwind Trough* et *Norske Trough*, anciennes zones d'ancrage de glaciers, ainsi que les moraines localisées autour (Arndt et al., 2017, 2015). Les linéations glaciaires dans la dépression *Westwind Trough* sont les témoins d'un courant glaciaire actif lors du dernier maximum glaciaire (Evans et al., 2009; Winkelmann et al., 2010). L'étendue maximale de la calotte glaciaire du Groenland s'est produit entre 21 et 16 ^{14}C kyr (Arndt et al., 2017; Stein et al., 1996). La phase initiale de déglaciation coïncide avec l'arrivée des eaux chaudes de l'Atlantique dans le détroit de Fram, mais de manière générale, la rupture de la calotte glaciaire du Groenland serait due à plusieurs facteurs tels que la température, l'élévation du niveau de la mer, le réchauffement de l'océan, la bathymétrie et les conditions de glace de mer (Funder et al., 2011). Le recul de la calotte glaciaire du Groenland a eu lieu jusqu'au Dryas récent, au cours duquel une légère réavancée a probablement eu lieu (Arndt et al., 2017). Un recul rapide s'est ensuite produit, jusqu'à l'étendue minimale de la calotte (Stein et al., 1996) à l'Holocène (7.7-4.5 ka cal BP), 80 km dans les terres au-delà de la limite actuelle (Bennike and Weidick, 2001). Depuis 9.1-9.7 cal ka BP le plateau continental est libre de glace (Bennike and Björck, 2002).

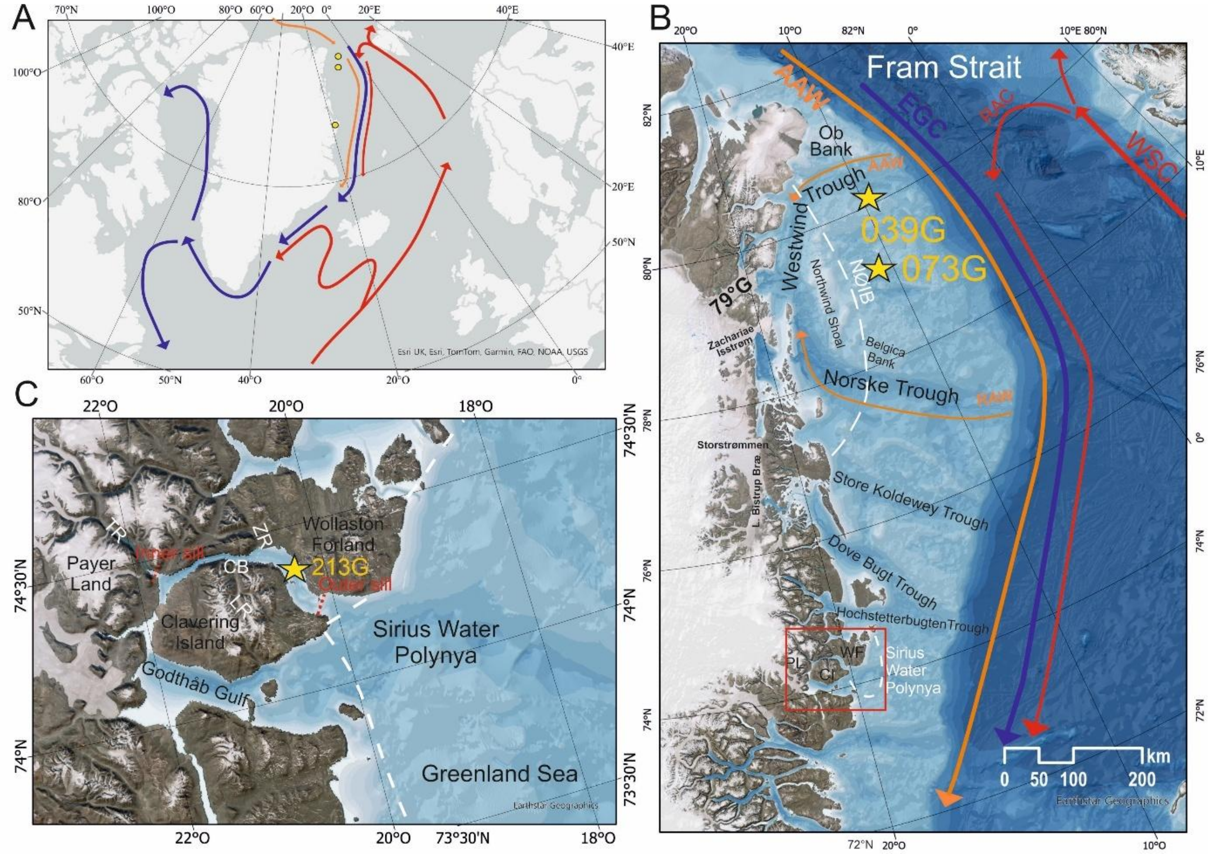

Figure 9. Cartes de la zone d'étude du chapitre 2. **A.** Circulation océanique globale dans le nord de l'océan Atlantique Nord. Flèche rouge : courant chaud. Flèche bleue : courant froid. Flèche orange : courant intermédiaire. Les points jaunes indiquent la localisation des carottes étudiées dans ce chapitre. **B.** Plateforme continentale du nord est du Groenland. Les flèches indiquent les courants océaniques. AAW - Arctic Atlantic Water, EGC - Eastern Greenland Current, RAC - Return Atlantic Current. Les traits en pointillés indiquent les polynies. NØIB: Norske Øer Ice Barrier, SWP: Sirius Water Polynya. Le rectangle rouge indique l'emprise de la carte C. Les étoiles jaunes indiquent les carottes étudiées dans ce chapitre. **C.** Système de Young Sound-Tyrolerfjord. Les lignes rouges en pointillés indiquent les seuils internes et externes du fjord. ZR (Zackenberg River), LR (Louise River), TR (Tyroler River) et CB (Clay Bay) indiquent les affluents majeurs. Les étoiles jaunes indiquent les carottes étudiées dans ce chapitre.

7.3 Grand Lake

Grand Lake est un lac de 54 km de long et de moins de 3 km de large situé au Labrador au Canada (Figure 10A). Profond de 245 m, il présente une morphologie similaire aux fjords avec des versants abrupts, incisés dans les roches métamorphiques et ignées de la province géologique de Grenville du bouclier canadien du Paléoprotérozoïque inférieur (Figure 10B). Les rivières Naskaupi et Beaver sont ses principaux affluents, apportant plus de 70 km^3/an d'eau douce au lac (Kamula et al., 2017). Grand Lake est relié à Little Lake au sud, lac soumis à la marée, qui est lui-même relié au Lac Melville, un lac estuarien, qui se jette ensuite dans la mer du Labrador.

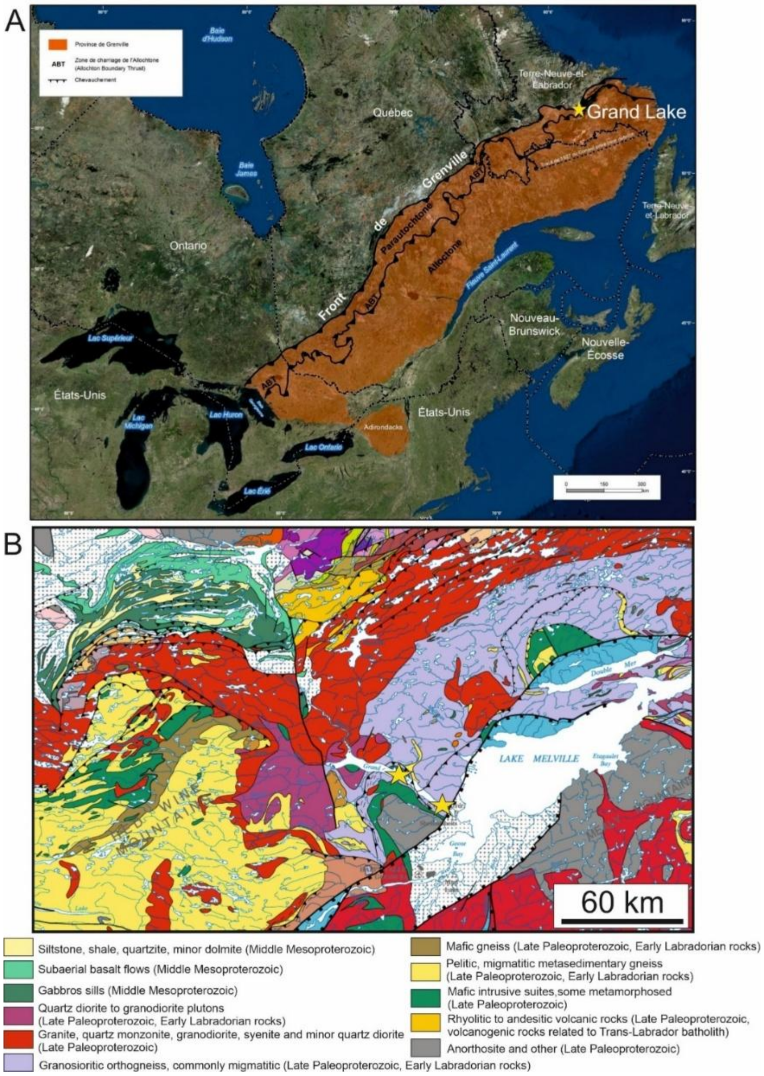

Figure 10. A. Carte de la province de Grenville au Canada et de son extension jusque dans la région des Adirondacks aux États-Unis (carte du ministère des Ressources naturelles et des Forêts du Québec). **B.** Carte géologique du Labrador aux alentours de Grand Lake. Modifiée d'après Wardle et al. (1997). Les étoiles jaunes représentent la localisation des carottes.

Au cours de la dernière glaciation, Grand Lake a été recouvert par l'inlandsis Laurentidien (LIS ; Figure 11). Le retrait de LIS a été marqué de plusieurs interruptions lors de périodes de brusques refroidissements. Notamment, lors de son retrait pendant la dernière déglaciation, la marge de LIS s'est stabilisée au sud-est de Grand Lake et a déposé la moraine de Sebaskachu, récemment datée à 8,4 ± 0,6 ka (Couette et al., 2023). La déglaciation du bassin de Grand Lake s'est poursuivie jusqu'à 7,9 ka (Couette et al., 2023) et la partie Québec-Labrador de LIS s'est finalement retirée vers 6,5-6,0 ka cal BP (Occhietti et al., 2011). Pendant la déglaciation, la limite marine se situait jusqu'à 150 m au-dessus du niveau de la mer actuel (Fitzhugh, 1973; King, 1985), inondant les vallées fluviales en amont de Grand Lake. Pendant cette période, Grand Lake a formé un fjord glaciomarin relié au lac Melville. Le fjord a été isolé de la mer vers ~3 ka, en raison du rebond isostatique résultant du retrait de LIS, qui a provoqué l'élévation de la moraine à l'embouchure du lac. Les différentes phases de retrait de LIS ont donc marqué le bassin de Grand Lake, particulièrement la géomorphologie (linéations, roches sculptées par les glaciers), la stratigraphie et la sédimentation (dépôts glaciaires, marins, fluviaux, deltaïques, puis lacustres). Le retrait de LIS a sculpté la morphologie du lac et on y retrouve des dépôts glaciaires, des linéations et des roches sculptées par les glaciers. La sédimentation reflète les différentes phases successives de retrait de LIS et les différents environnements de dépôts associés à ses différentes phases : sédimentation glaciomarine, littorale, fluvioglaciaire, fluviale, deltaïque puis lacustre (Fitzhugh, 1973; Fulton and Ferguson, 1986; Gagnon-Poiré, 2023; Klassen and Thompson, 1993; Syvitski and Lee, 1997; Trottier et al., 2020; Vilks et al., 1987). La récente étude hydroacoustique de Trottier et al. (2020) a permis d'identifier trois secteurs différents dans le lac, avec des deltas aux sorties des rivières Naskaupi et Beaver, le bassin central profond (~245 m) et plat et la section aval, moins profonde avec des crêtes morainiques et un chenal central relié à l'exutoire du lac.

Figure 11. Carte de l'étendue de la calotte de glace Laurentidienne (Laurentide Ice Sheet) à environ 8,45 ka et de la localisation de Grand Lake (étoile jaune). Les lignes rouges indiquent les positions des moraines associées au recul de LIS, notamment la moraine Sebaskachu au sud-est de Grand Lake. D'après Trottier et al. (2020).

Au cours de la déglaciation, l'environnement de dépôt sédimentaire marin de Grand Lake a progressivement laissé place à un environnement de dépôt lacustre. Les rivières Naskaupi et Beaver, ainsi que d'autres rivières plus petites, sont les principales sources de sédiments du lac. Grand Lake est caractérisé par un climat boréal avec des étés frais et des hiver froids. En raison d'un contraste saisonnier élevé, le lac subit d'importantes variations saisonnières (recouvert de glace ou en eau libre), induisant différents processus de sédimentation, tels que des écoulements hypopycnaux en période de stratification, des écoulements de sédiments générés par les deltas fluviaux libres de glace pendant la période de fonte et des écoulements hyperpycnaux lors de précipitations (Gagnon-Poiré, 2023; Kury et al., 2025). Les laminations observées dans les sédiments de Grand Lake sont des varves clastiques (Figure 12), c'est-à-dire des dépôts annuels composés de deux (parfois trois) couches distinctes. Chaque varve représente une année hydrologique (Gagnon-Poiré et al., 2021). Une couche d'argile est associée au dépôt des particules dans un environnement non turbulent, lorsque le lac est recouvert de glace en automne et en hiver. Grand Lake est dimictique, ce qui signifie que les conditions suboxiques à anoxiques résultant de la stratification verticale induite par les contrastes de température en été et en hiver permettent la préservation des varves clastiques au fond du lac, tandis que la stratification devient négligeable à l'automne et au printemps, permettant une circulation verticale deux fois par an et introduisant une quantité limitée d'oxygène au fond du lac (Gagnon-Poiré, 2023 ; Kury et al., 2025).

Figure 12. Photographie des varves des 20 premiers cm de la carotte de surface GL23-20-Up1.

8. METHODOLOGIE

La méthodologie est globalement similaire d'un chapitre à l'autre.

8.1 Échantillonnages des carottes sédimentaires

Les carottes AMD1902-10GC et AMD1902-07GC ont été prélevées respectivement dans le Fjord Petermann et dans le chenal de Robeson dans le détroit de Nares, au nord-ouest du Groenland lors du Leg 2b de l'expédition à bord du NGCC Amundsen (Figure 13) en 2019.

Figure 13. Déploiement du carottier à gravité géant à bord du NGCC Amundsen dans le détroit de Nares lors du Leg 3 de l'expédition 2023. Photo de Daniel Amirault, Amundsen Science.

Les carottes DA17-NG-ST03-039G, -ST07-073G et -ST18-213G ont été prélevées sur la marge nord-est du Groenland lors de la mission NorthGreen à bord du N/R Dana en 2017 (Figure 14).

Figure 14. N/R Dana dans Young Sound lors de l'expédition NorthGreen2017. Photo de Claus Persson, Capitaine du Dana (DTU-AQUA).

Les carottes étudiées dans le troisième chapitre ont été échantillonnées à Grand Lake au Labrador en 2017 et 2023. La carotte GL17-13A-V a été récoltée lors d'une campagne de terrain en 2017, à l'aide d'un carottier à vibrations.

Du 15 au 30 mars 2023, une autre campagne de terrain a eu lieu, avec une plateforme de carottage Uwitec (Figure 15), pouvant être déployée sur la surface gelée du lac. L'équipe était composée de trois personnes de l'ISMER dont Bruno Cayouette (technicien) et Quentin Beauvais (agent de recherche, co-chef de mission), trois personnes de l'INRS-ETE dont Arnaud De Coninck (agent de recherche, co-chef de mission), Marie-Eugénie Jamba et Milena Souza Kury (étudiantes au doctorat), de Richard Niederreiter (fondateur de Uwitec et concepteur de la plateforme utilisée) ainsi que de Dave Blake (guide originaire de North West River). Le matériel a été transporté par camion depuis Rimouski, puis déposé en hélicoptère sur la surface du lac. La plateforme a été déployée à l'endroit exact du site sélectionné au préalable. Sur ce site, plusieurs endroits ont été échantillonnés : deux carottes de surface ont été prélevées avec un carottier gravitaire à percussion à 1 m d'écart l'une de l'autre (GL23-20-Up1 ; -Up2), puis deux autres puits (A et B) ont été échantillonnés pour récupérer des séquences longues à l'aide du carottier à piston Uwitec. Aux puits A et B, des sections de 2 m chacune ont été prélevées les unes à la suite des autres pour récupérer un total de 8 m de sédiment dans le puit A et 20 m dans le puit B, avec un chevauchement en profondeur de 50 cm entre les deux puits pour obtenir une séquence continue sur les huit premiers mètres.

Du fait de l'isolement et l'éloignement du lac, le trajet aller-retour a pris quatre jours complets. L'assemblage et le démontage de la plateforme ont pris quatre jours. Six jours ont pu être consacrés aux opérations de carottage, une journée a été perdue à cause d'une forte tempête de neige et une autre journée a été consacrée à la rencontre de la communauté Innue des premières nations de Sheshatshiu afin de présenter notre campagne de terrain.

Tableau 1.Tableau récapitulatif des carottes étudiées dans cette thèse. Les carottes pour lesquelles les enregistrements avaient déjà été établis dans de précédentes études ne sont pas indiquées dans ce tableau.

Carotte	**Site**	**Coordonnées (°N/°E)**	**Profondeur d'eau (m)**	**Longueur (cm)**	**Instrument de carottage**	**Chapitre rattaché**
AMD1902-10GC	Fjord Petermann (Détroit de Nares)	81.102/ -61.746	1085	272.3	Carottier à gravité	Chapitre 1
DA17-NG-ST03-039G	Plateau continental NE du Groenland	80.033/ -8.917	391	320	Carottier à gravité	Chapitre 2
DA17-NG-ST07-073G	Plateau continental NE du Groenland	79.067/ -11.9	385	410	Carottier à gravité	Chapitre 2
DA17-NG-ST18-213G	Young Sound (Groenland)	74.333/ -20.333	168	310	Carottier à gravité	Chapitre 2
GL17-13	Grand Lake	53.561/ -60.235	75	332	Carottier à vibrations	Chapitre 3

GL23-20-Up1	Grand Lake	53.698/ -60.546	245	118	Carottier gravitaire à percussion	Chapitre 3
GL23-20A (toutes sections)	Grand Lake	53.698/ -60.546	245	788	Carottier à piston	Chapitre 3
GL23-20B (toutes sections)	Grand Lake	53.698/ -60.546	245	1996	Carottier à piston	Chapitre 3
HU2008-029-049PC	Détroit de Lancaster	74.026/ -77.125	914	868	Carottier à piston	Projet parallèle à la thèse (Jennings et al., 2025; Kelleher et al., 2022)
HU2008-029-049TWC	Détroit de Lancaster	74.026/ -77.125	185	868	Carottier à piston	

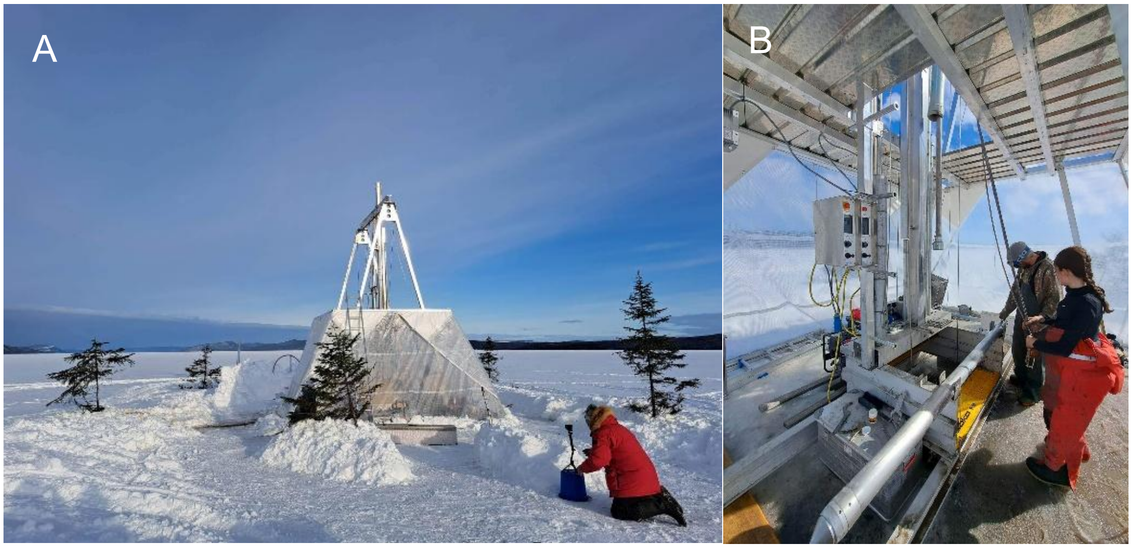

Figure 15. Photos de la campagne d'échantillonnage à Grand Lake au Labrador. **A.** Plateforme de carottage sur le lac vue de l'extérieur. Les arbres servent de signalisation pour les personnes qui circulent sur le lac. **B.** Déploiement du carottier à percussion avec Bruno Cayouette, vue de l'intérieur de la tente (photo de Quentin Beauvais).

8.2 Mesures des propriétés physiques et chimiques continues

Les carottes entières ont été scannées avec un système de tomographie à rayons X (X-CT) de GEOTEK à l'ISMER permettant d'obtenir des images numériques à rayons X en niveaux de gris pour détecter les changements de densité et identifier les différentes structures sédimentaires (St-Onge et al., 2007). Des mesures de susceptibilité magnétique volumétrique en champ faible (k_{LF}), de densité humide, de vélocité des ondes P, ont été conduites sur les carottes entières à l'aide d'un banc constitué de plusieurs capteurs (*multi-sensor core logger*, MSCL) à l'ISMER également (Figure 16).

Les carottes sont ensuite ouvertes en demi-section (archive et travail), puis décrites visuellement (couleur, granulométrie, structures, déformation) à l'aide de croquis. Les demi-sections sont également soumises à des analyses sur le banc MSCL : k_{LF} est mesurée à l'aide d'un capteur M2SEI de Bartington Instruments (pas de 1 cm) ; la composition chimique élémentaire est mesurée avec un analyseur portable de fluorescence X (pXRF) Olympus Innov-X DELTA (pas de 1 cm) ; une photographie numérique est réalisée avec un système d'imagerie GEOTEK Geoscan IV ; la réflectance spectrale diffuse est mesurée avec un spectrophotomètre Minolta CM-2600d (pas de 1 cm).

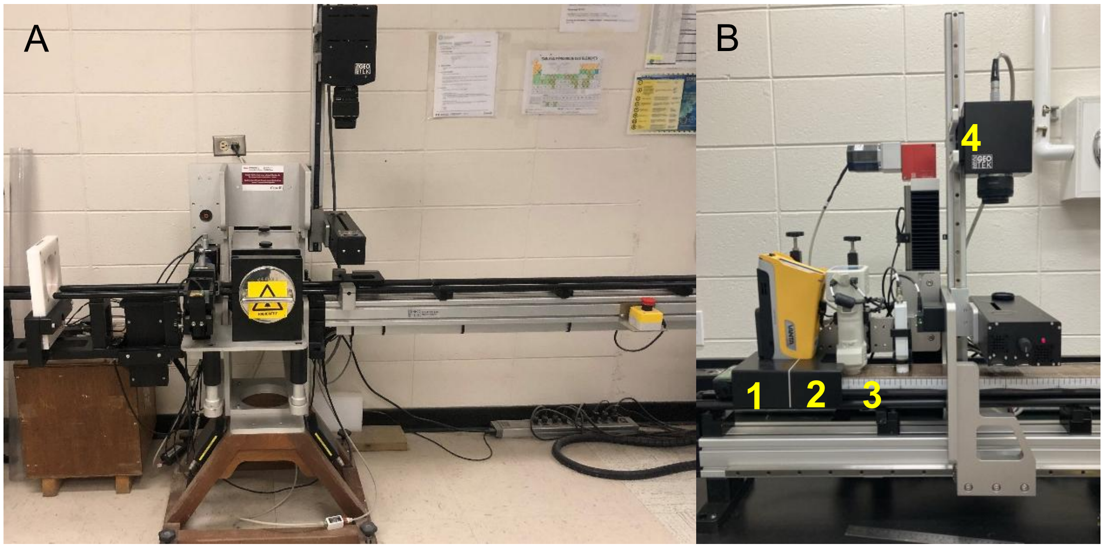

Figure 16. Photos du banc MSCL de GEOTEK à l'ISMER. **A.** Banc utilisé pour les carottes entières et ouvertes. **B.** Montage avec le pistolet XRF (1), le spectrophotomètre (2), la susceptibilité magnétique (3) et le système d'imagerie digitale (4) pour les mesures sur les demi-sections ouvertes.

Des mesures de XRF ont aussi été conduites à l'INRS-ETE (Québec, Canada) et au département de géoscience d'Aarhus (Danemark) à l'aide d'un ITRAX. Certaines mesures d'images numériques des structures internes des carottes ont été réalisées à l'INRS à l'aide d'un CT-scan. Ces mesures sont précisées dans le chapitre 3, pour les carottes concernées.

8.3 Mesures paléomagnétiques continues

Des mesures paléomagnétiques continues ont été effectuées sur toutes les carottes : AMD1902-10GC (chapitre 1), DA17-NG-ST03-039G, -ST07-073G, -ST18-213G (chapitre 2), GL23-20-Up1, GL23-20A-I-Un à -IV-Un, sections A et B, GL23-20B-I-Un à -X-Un, sections A et B (chapitre 3), ainsi que sur les carottes HU2008029-049CC dans le cadre d'une autre étude (Jennings et al., 2025; Kelleher et al., 2022) et AMD1902-07GC (non incluse dans la thèse).

Des u-channels ont été sous-échantillonnés dans les demi-sections des carottes (Figure 17) en utilisant des tubes en plastique de 4 cm² et jusqu'à 1,50 m de long (Weeks et al., 1993). Ces u-channels ont servi pour faire des mesures de différentes aimantations (pas de 1 cm) avec un magnétomètre cryogénique de 2G Enterprises 755SRM-1.65 à l'ISMER. L'aimantation rémanente naturelle (NRM) a été mesurée en démagnétisant étape par étape les sédiments de 0 à 100 mT (5 mT d'intervalle de 0 à 80 et 10 mT de 80 à 100 mT), en champ alternatif. L'aimantation rémanente anhystérétique (ARM) a ensuite été induite en appliquant un champ magnétique alternatif de démagnétisation (jusqu'à 100 mT), couplé à un champ magnétique continu de même ordre de grandeur que celui du champ magnétique terrestre (50 µT), puis mesurée en démagnétisant de la même manière que la NRM. Deux aimantations isothermales sont ensuite induites à 300 mT (IRM) et 900 mT (aimantation rémanente isothermale à saturation, SIRM) avec un magnétiseur à impulsion (*pulse magnetizer*), puis démagnétisées et mesurées de 0 à 80 mT (intervalle de 5 mT) pour l'IRM et à 0, 10, 30 et 50 mT pour la SIRM. Ces différentes aimantations induites en laboratoire serviront à normaliser la NRM afin d'obtenir le signal de paléointensité relative enregistré dans les sédiments (e.g. Tauxe, 1993; Tauxe et al., 1995; Tauxe & Wu, 1990; Valet &

Meynadier, 1998). En même temps que l'intensité de chaque aimantation, des mesures de déviation angulaire maximale (*maximum angular deviation*, MAD), de champ de destruction médian (*median destructive field*, MDF), d'inclinaison et de déclinaison sont faites. Les valeurs de MAD<5° indiquent des mesures fiables et de bonnes qualité (Stoner et St-Onge, 2007). La MDF est un indicateur de minéralogie magnétique (Stoner et St-Onge, 2007).

Après les mesures, les données sont vérifiées et les erreurs telles que les *flux jumps* sont corrigés avec le logiciel UPmag opéré dans MATLAB (Xuan and Channell, 2009). La macro Excel de Mazaud (2005) est utilisée pour calculer l'aimantation rémanente caractéristique (ChRM) avec les étapes de démagnétisation sélectionnées.

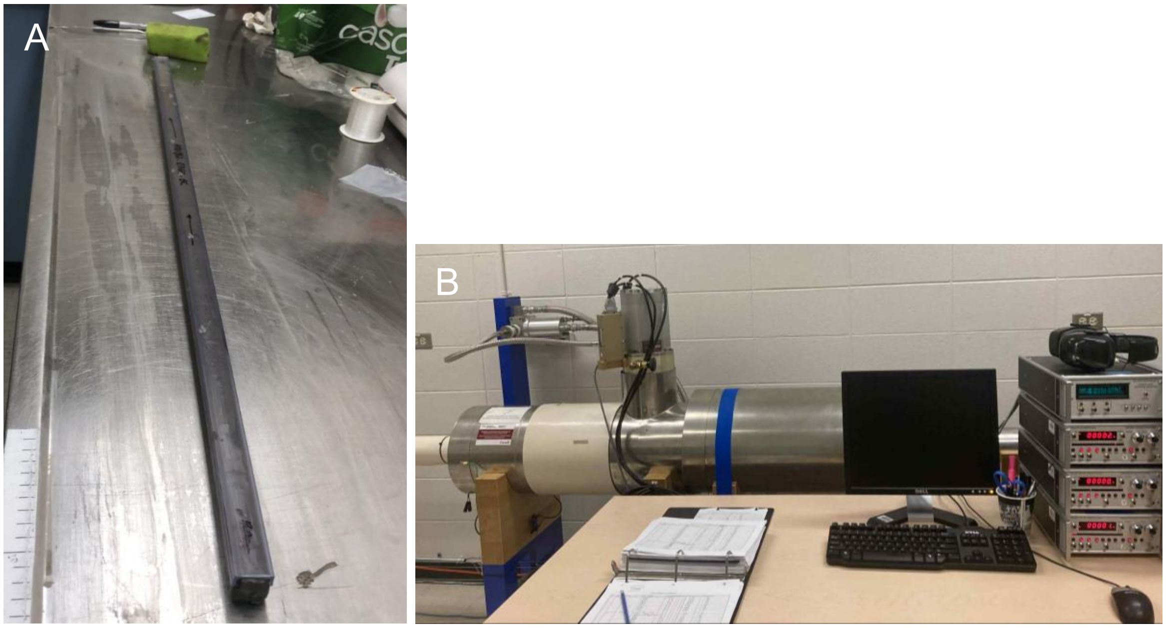

Figure 17. A. U-channel sous-échantillonné dans une carotte de sédiments. **B.** Magnétomètre cryogénique 755SRM-1.65 de 2G Enterprises à l'ISMER.

8.4 Mesures de magnétisme environnemental

Des mesures de magnétisme environnemental ont été réalisées afin de caractériser la minéralogie et la granulométrie magnétiques dans le but d'attester de la qualité des reconstitutions paléomagnétiques. Plusieurs critères ont été établis pour cela (Stoner et St-Onge, 2007; Tauxe, 1993). Les minéraux doivent être ferrimagnétiques et de faible coercivité (intensité du champ magnétique nécessaire pour annuler l'aimantation d'un minéral après qu'il ait atteint saturation; Thompson et Oldfield, 1986) tels que la magnétite ou la titanomagnétite. La granulométrie magnétique doit être à monodomaine ou pseudo-monodomaine (dans un état de type *vortex ;* Roberts et al., 2017). Enfin, la concentration magnétique ne doit pas varier de plus d'un ordre de grandeur. Ces caractéristiques sont associées à des aimantations stables et fortes, permettant aux sédiments de fournir des enregistrements fiables du champ magnétique.

Ces analyses ont été faites en partie à l'ISMER avec un magnétomètre à gradient alternatif (AGM, Figure 18) et en partie à l'IPGP (Paris, France) avec un magnétomètre à échantillon vibrant (VSM ; Figure 19). La mesure des boucles d'hystérésis consiste en l'application d'un champ cyclique (augmentation puis diminution) afin de mesurer la saturation, la coercivité et la rémanence des minéraux (force de coercivité Hc, force de coercivité rémanente Hcr, aimantation de saturation Ms et rémanence de saturation Mrs), valeurs propres à chaque minéralogie magnétique. La boucle d'hystérésis livre les informations sur l'échantillon global (*bulk*), ce qui est généralement suffisant pour les études paléomagnétiques. Les diagrammes de FORC (courbes d'inversion de premier ordre) permettent d'avoir une estimation plus précise des distributions des coercivités et des champs d'interaction (Harrison et Feinberg, 2008). Ils sont constitués d'une multitude de courbes d'hystérésis et permettent de visualiser directement la coercivité, la granulométrie et l'intensité de l'aimantation des grains magnétiques. Les courbes d'acquisition d'IRM permettent aussi de mesurer la saturation des minéraux et ces valeurs peuvent ensuite être utilisées en tant que ratio avec d'autres paramètres (Stoner et St-Onge, 2007) afin de déterminer la coercivité et la minéralogie des particules magnétiques présentes dans le sédiment.

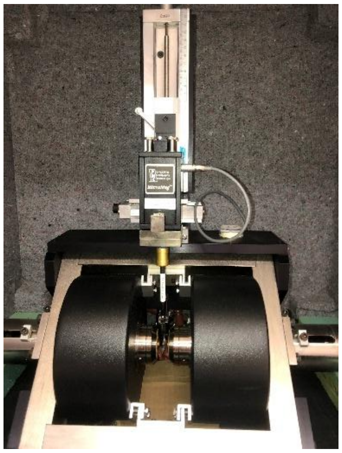

Figure 18. Photo de l'intérieur de l'AGM à l'ISMER. Le sédiment est placé sur la sonde.

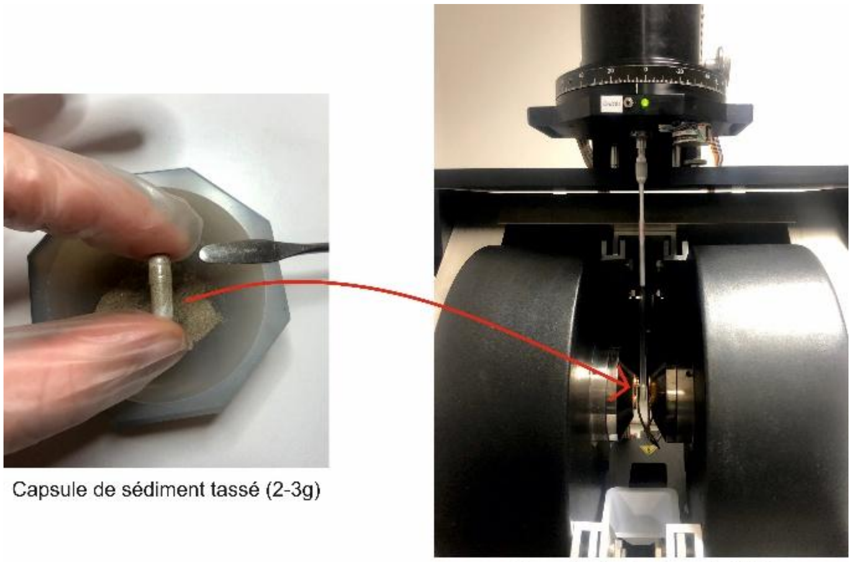

Capsule de sédiment tassé (2-3g)

Capsule placée dans le VSM

Figure 19. Montage pour les mesures de magnétisme environnemental sur le magnétomètre à échantillon vibrant (VSM) à l’IPGP. Une capsule (à gauche) est remplie de sédiment bien tassé (2-3 g), puis placée dans le VSM à droite, tenue grâce à une paille en plastique pour les mesures de boucles d’hystérésis, FORC, acquisition d’IRM, entre autres.

La susceptibilité magnétique en fonction de la température a été mesurée avec un susceptibilimètre AGICO KLY-3 à l’IPGP (Figure 20). Lors de cette mesure, on peut observer notamment la température à laquelle les minéraux présents dans le sédiment perdent leur aimantation (température de Curie), qui est propre à chaque minéral (580°C pour la magnétite) et permet donc leur identification.

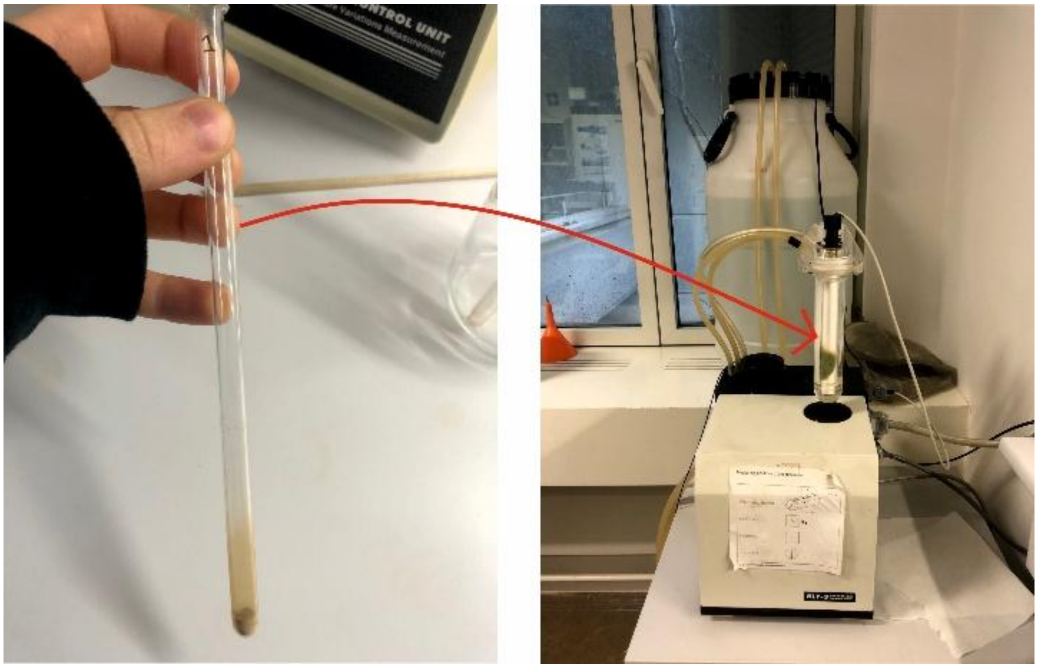

Figure 20. Acquisition de courbes de susceptibilité magnétique en fonction de la température avec un susceptibilimètre AGICO KLY-3 à l'IPGP. Le sédiment est pesé et déposé dans un tube (à gauche) qui est ensuite placé dans le susceptibilimètre (à droite) dans lequel il va être chauffé.

8.5 Granulométrie

Les mesures de granulométrie ont été faites à l'ISMER avec un analyseur granulométrique à diffraction laser Malvern PANalytical Mastersizer3000 (Figure 21) et à l'INRS-ETE à Québec avec un granulomètre laser Horiba pour les carottes de Grand Lake. La distribution de granulométrie a été calculée à l'aide du logiciel GRADISTAT (version v.9.1 ; Blott and Pye, 2001), opéré dans Excel. Ce logiciel permet d'obtenir notamment les pourcentages de sable, silt et argile, ainsi que des paramètres statistiques tels que D_{50} (valeur médiane de la distribution granulométrique) et D_{90} (valeur du diamètre des particules en dessous duquel 90 % de la population granulométrique d'un échantillon se situe). Les résultats de granulométrie sont notamment utilisés pour identifier des couches de sédiments déposées rapidement (par exemple, des turbidites), des IRD, ainsi que les zones où la granulométrie est favorable aux reconstitutions paléomagnétiques (argiles et silts).

Figure 21. Granulomètre Malvern PANalytical Mastersizer 3000 de l'ISMER.

8.6 Établissement du signal de paléointensité relative

Tel qu'expliqué précédemment, la NRM des sédiments porte le signal du champ paléomagnétique, mais ce signal est également fonction de la granulométrie, de la concentration et de la minéralogie magnétiques des sédiments. Les aimantations ARM et IRM induites en laboratoire ne dépendent pas du champ géomagnétique, mais seulement des propriétés magnétiques du sédiment. Celles-ci sont donc utilisées pour normaliser la NRM et obtenir le signal de RPI, qui représente les variations paléomagnétiques du champ. Deux méthodes de normalisation sont utilisées. La méthode pseudo-Thellier (Tauxe et al., 1995), dite « de la pente », qui se base sur la méthode Thellier utilisée pour mesurer l'aimantation absolue dans les roches volcaniques et les laves (Thellier and Thellier, 1959), consiste à tracer la pente entre la NRM et son normalisateur, et utiliser cela comme signal de RPI. La méthode du ratio consiste à diviser les valeurs de NRM par celles du normalisateur, sur des étapes de démagnétisation choisies (e.g. Channell et al., 2000; Stoner et al., 2000; Stoner & St-Onge, 2007). Habituellement, plusieurs normalisateurs potentiels sont essayés et les deux méthodes sont comparées (Valet et Meynadier, 1998), avec des indicateurs statistiques (coefficient de corrélation, coefficient de détermination).

8.7 Chronologies

Le cadre chronologique des sédiments de chaque chapitre a été établi en combinant plusieurs méthodes de datation parmi la mesure de désintégration du radiocarbone (^{14}C), du plomb (^{210}Pb), la mesure du pic d'activité du césium (^{137}Cs), le comptage de varves et la comparaison des variations paléomagnétiques.

La méthode de datation au ^{14}C est la plus utilisée pour les sédiments récents (jusqu'à 55 ka BP). Elle consiste à mesurer, à l'aide d'un spectromètre de masse par accélérateur (AMS ; Figure 22), le contenu en carbone dans les organismes carbonatés déposés dans les sédiments marins (coquilles, foraminifères benthiques et planctoniques) pour déterminer le temps écoulé depuis leur mort. Dans le cas des sédiments des zones polaires, où les carbonates biogéniques sont rarement bien préservés, le système MICADAS (*mini radiocarbon dating system*) permet de dater des échantillons contenant peu de matériel carbonaté. Cette méthode de datation peut également être appliquée sur des macrorestes végétaux que l'on trouve dans des environnements sédimentaires lacustres.

Figure 22. Parc instrumental des spectromètres de masse par accélération (AMS) au laboratoire Ion Beam Physics de l'ETH de Zürich. Photo ETH Zürich.

La méthode de datation au ^{14}C repose sur sa désintégration radioactive dans l'atmosphère, et sur l'équilibre isotopique entre l'océan et l'atmosphère, grâce aux échanges à l'interface air-océan (Figure 23). Cependant, du fait de la circulation océanique, les masses d'eau circulant en profondeur ne sont pas en contact avec l'atmosphère pendant plusieurs centaines d'années parfois, et la teneur en carbone des carbonates marins n'est pas la même que dans l'atmosphère. L'âge réservoir marin est en moyenne de 550 ans selon la courbe de calibration la plus récente Marine20 (Heaton et al., 2020) et une correction locale (ΔR) doit être appliquée selon le site d'étude. La courbe de calibration IntCal20 (Reimer et al., 2020) est utilisée pour les échantillons terrestres de l'hémisphère Nord. Dans chacun des chapitres, la courbe de calibration et le ΔR ont été sélectionnés selon les conditions environnementales des lieux d'étude.

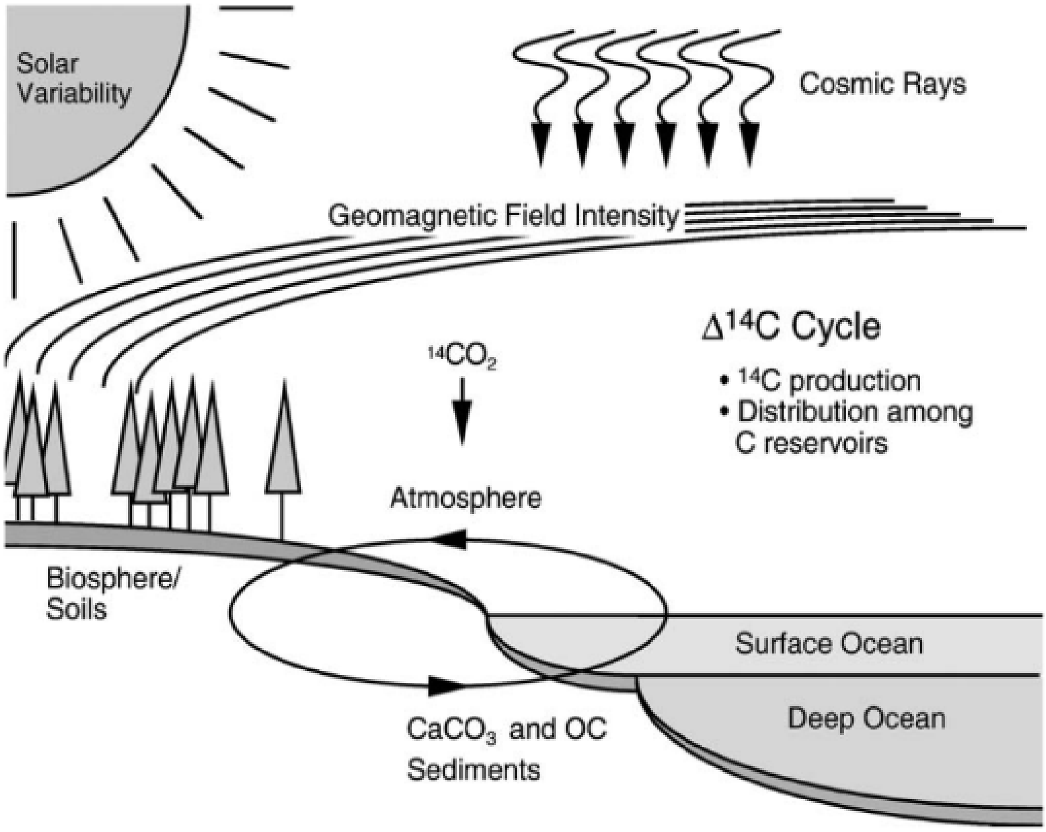

Figure 23. Schéma du cycle du ^{14}C représentant la production de ^{14}C cosmogénique dans l'atmosphère par les rayons cosmiques et la distribution du ^{14}C dans le cycle global du carbone. D'après Hughen (2007).

La mesure de la désintégration du ^{210}Pb, par spectrométrie alpha ou gamma, permet de calculer des taux d'accumulation de sédiments pour les sédiments récents (derniers 150 ans) au sommet des carottes. Dans cette thèse, les sommets des carottes ont été échantillonnés tous les cm sur une profondeur de 20 à 30 cm, puis soumis à plusieurs digestions successives avec différents acides (HNO_3, HCl, HF, H_3BO_4, H_2O_2), avant d'être analysés par spectrométrie alpha au laboratoire des isotopes radioactifs du Geotop (UQAM, Montréal), en collaboration avec Antonin Prijac et Nicole Sanderson (Figure 24). À partir des résultats, une courbe de désintégration du ^{210}Pb a été établie, permettant le calcul des taux d'accumulation de sédiments.

Les échantillons des carottes GL23-20-Up1 ont été encapsulés , puis analysés par spectrométrie gamma à l'INRS-ETE à Québec, afin d'obtenir le couplage ^{210}Pb–^{137}Cs. La mesure de l'activité du ^{137}Cs permet d'identifier le début des essais nucléaires dans les années 1950, les pics correspondant au maximum des essais nucléaires atmosphériques en 1963-1964, et parfois l'accident nucléaire de Tchernobyl en 1986. Ces dates permettent ensuite de valider les résultats obtenus avec le ^{210}Pb et le comptage des varves. Ces analyses ont été réalisées sur les carottes de Grand Lake, dont la surface était particulièrement bien conservée grâce à l'utilisation d'un carottier de surface à piston garantissant une récupération optimale des sédiments superficiels.

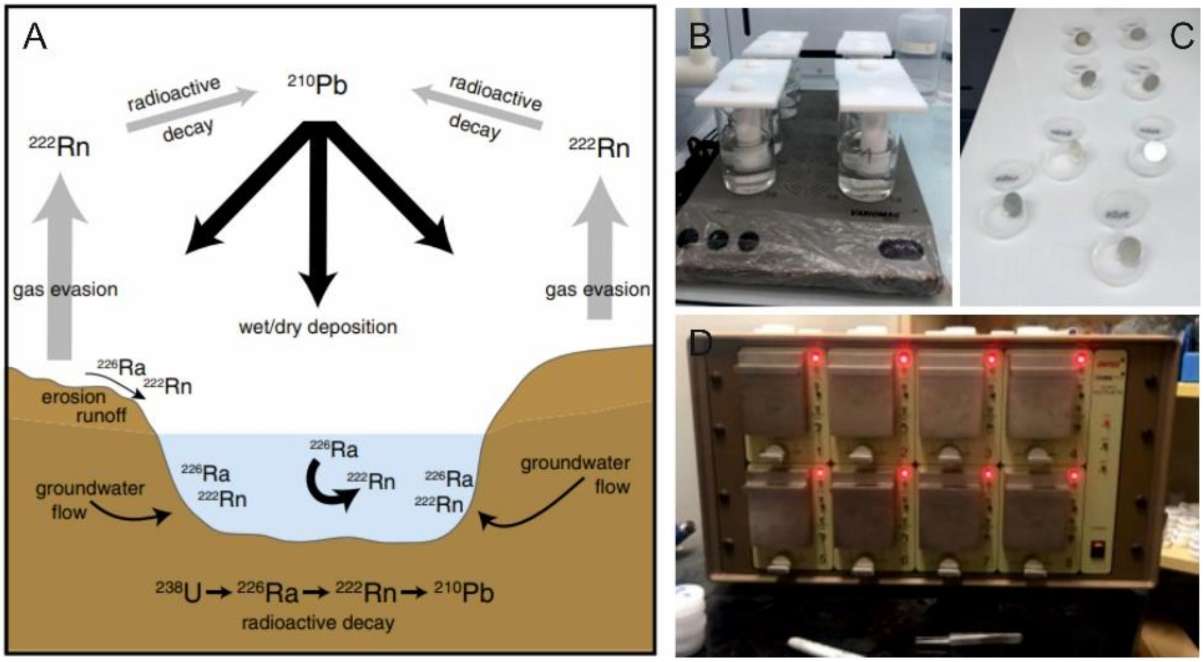

Figure 24. A. Schéma du cycle du ^{210}Pb dans l'environnement (Swarzenski, 2014). **B-D.** Analyses au GEOTOP à l'UQAM. **B.** Digestion par différents acides sur des plaques chauffantes. **C.** Disques à sécher. **D.** Compteur alpha.

Le comptage des varves a été utilisé comme méthode de datation pour les sédiments de Grand Lake du chapitre 3. Le comptage des varves est fait avec le logiciel *PeakCounter* (Marshall et al., 2012) en se basant sur les images à haute résolution des carottes couplées à des profils µXRF (Sr, Fe) mesurés avec l'ITRAX permettant la différentiation des varves (Figure 25). Pour la carotte GL17-13, le comptage a été réalisé par Antoine Gagnon-Poiré et Clarence Gagnon en utilisant le logiciel *Analyse Image* (Francus and Nobert, 2007; Gagnon-Poiré, 2023; Lapointe et al., 2025).

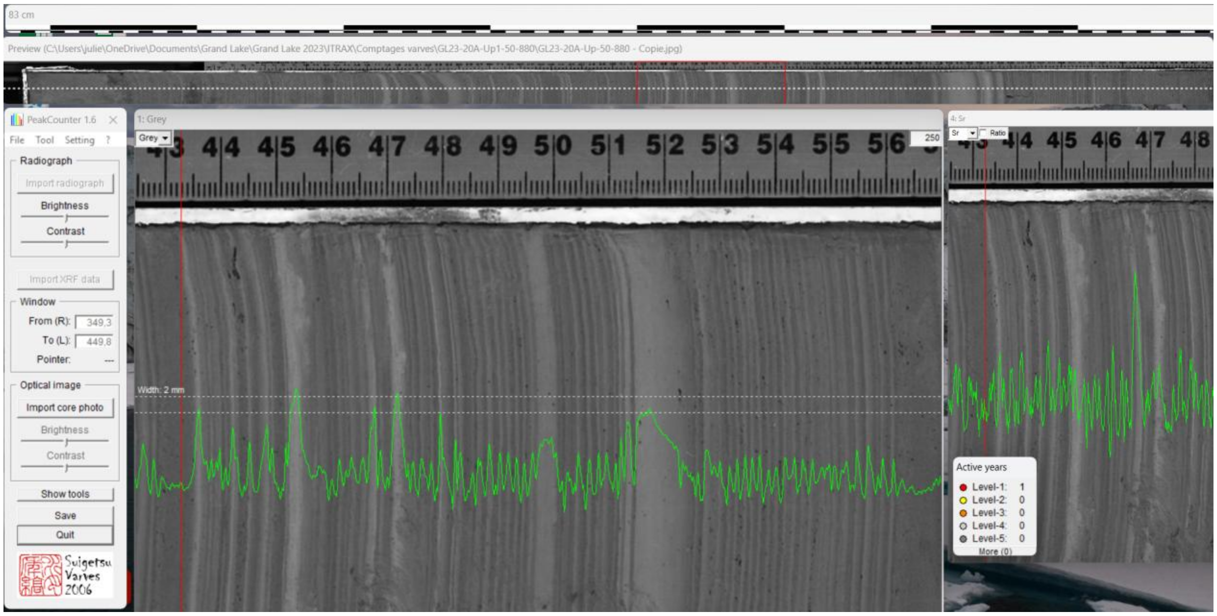

Preview (C:\Users\julie\OneDrive\Documents\Grand Lake\Grand Lake 2023\ITRAX\Comptages varves\GL23-20A-Up1-50-880\GL23-20A-Up-50-880 - Copie.jpg)

From (R): 349,3
To (L): 449,8
Pointer: ---

Active years
Level-1: 1
Level-2: 0
Level-3: 0
Level-4: 0
Level-5: 0
More (0)

Figure 25. Exemple d'identification et de comptage de varves avec le logiciel Pak Counter. Le profil µXRF de Sr et le profil de niveaux de gris sont superposés à l'image haute résolution de la carotte GL23-20-Up1.

Les variations paléomagnétiques (inclinaison, déclinaison, RPI) décrivent des similarités à l'échelle régionale, voire globale, et peuvent donc être utilisées comme méthode de datation en comparant à des enregistrements de référence déjà datés ou à des modèles géomagnétiques. Un des enregistrements utilisés est l'enregistrement GREENICE (Reilly et al., 2023; Stoner et al., 2007), basé sur des carottes sédimentaires du détroit du Danemark (sud est du Groenland), qui présentent des forts taux de sédimentation (1-15 m/ka), et qui sont très bien datées avec une combinaison de ^{14}C, paléomagnétisme et tephras (28 couches de tephras identifiées et 71 âges ^{14}C utilisés dans le stack). De nombreux modèles numériques géomagnétiques couvrent les variations de l'Holocène : CALSxk (Brown et al., 2015; Constable et al., 2016; Korte and Constable, 2011, 2005), pfm9k.x (Nilsson et al., 2022, 2014). Les variations plus récentes sont basées sur des observations et des mesures directes sur le terrain : IGRF (*International Geomagnetic Reference Field*) (1990-2025), gufm1 (1590-1990 ; Jackson et al., 2000). Bien que l'Holocène soit une période pour laquelle les PSV sont bien documentées et de nombreux modèles existent, les enregistrements polaires sont parfois absents ou ne sont pas toujours pris en compte dans les modèles (Figure 26), d’où la nécessité d’étudier les PSV en Arctique. En combinant les modèles et les enregistrements régionaux bien datés, le paléomagnétisme devient un excellent outil de datation en complément des méthodes évoquées plus haut.

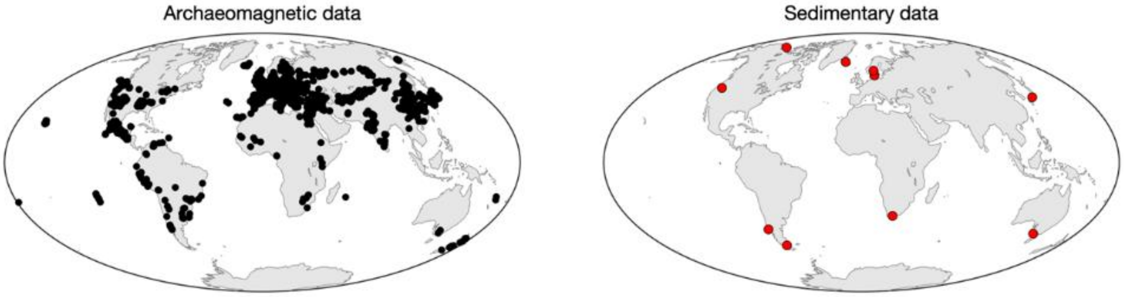

Figure 26. Figure en matériel supplémentaire de Nilsson et al., (2022), indiquant quels enregistrements sont pris en compte dans le modèle pfm9k.2. Les données archéomagnétiques des latitudes moyennes et basses sont nombreuses tandis que les données sédimentaires sont beaucoup plus rares, et que certaines régions ne sont quasiment pas représentées, dont l’Arctique.

9. ORGANISATION DE LA THESE

Cette thèse s’organise en trois chapitres, rédigés sous la forme d’articles scientifiques. Chaque chapitre correspond à un site d’étude, et incorpore des résultats de chapitres précédents à des fins de comparaison.

Le premier chapitre présente une mise à jour de la compilation des enregistrements paléomagnétiques séculaires (*stack*) enregistrées dans le fjord Petermann, situé au nord du Groenland, à partir de l’étude de Reilly et al. (2019). Cette mise à jour intègre un enregistrement supplémentaire ainsi qu’un nouveau *stack* de paléointensité relative. Les variations observées dans le stack ont permis de reconstituer les trajectoires des pôles géomagnétiques virtuels (PGV) et d’interpréter ces résultats en les reliant à la dynamique des lobes de flux géomagnétiques au cours de l’Holocène. L’article correspondant a été publié en octobre 2024.

Girard, J., Reilly, B. T., St-Onge, G., Lagroix, F., Montero-Serrano, J.-C., Stoner, J. S., & Jennings, A. E. (2024). Paleomagnetic secular variations in North Greenland around 81°N over the last 6,000 years. *Geochemistry, Geophysics, Geosystems*, 25, e2024GC011620. https://doi.org/10.1029/2024GC011620

Le deuxième chapitre présente les variations paléomagnétiques séculaires et de paléointensité relative à partir de trois carottes sédimentaires prélevées dans le nord-est du Groenland. Comme dans le premier chapitre, les résultats ont permis d'interpréter les variations des PGV en lien avec la dynamique du champ géomagnétique. Cette région, située en marge de l'influence du lobe de flux nord-américain et plus proche du lobe de flux européen, offre une perspective complémentaire sur les processus géomagnétiques à l'échelle de l'Holocène. L'article correspondant a été accepté sous réserve de modifications et la version révisée et modifiée vient d'être soumise.

Girard J., St-Onge G., Lagroix F., Seidenkrantz M-S., Pearce C., Montero-Serrano J-C., Francus P., Greenland paleomagnetic secular and relative paleointensity variations through the Holocene: influence of geomagnetic flux lobe intensity on the migration of the Virtual Geomagnetic Pole and millennial hemispheric-scale paleointensity fluctuations. Accepté sous réserve de modifications. *JGR: Solid Earth*

Le troisième chapitre porte sur l'enregistrement des variations paléomagnétiques séculaires (PSV) et de paléointensité relative (RPI) des 3 000 dernières années, à très haute résolution temporelle, dans des séquences sédimentaires varvées de Grand Lake, au Labrador (Canada). Une attention particulière est portée aux variations des 1 000 dernières années, période pour laquelle très peu d'enregistrements permettent d'établir un lien entre les fluctuations récentes du champ géomagnétique (notamment celles des 400 dernières années) et les variations observées au cours de l'Holocène. L'article correspondant sera soumis prochainement à la revue Boreas, Journal of Quaternary Science, Canadian Journal of Earth Sciences ou The Holocene.

Girard J., St-Onge G., Francus P., Reilly B., Lagroix F., Kury M., Montero-Serrano J.-C., Lajeunesse P. High resolution paleomagnetic variations of the last 2500 years recorded in varved sediment of Grand Lake (Labrador, Canada).

Les deux premiers chapitres permettront de répondre au premier objectif, soit d'étudier les variations paléomagnétiques dans l'Arctique à très haute latitude, en lien avec le cylindre tangentiel et les lobes de flux géomagnétiques. Le deuxième chapitre permettra de mettre en évidence le lien entre les variations géomagnétiques enregistrées à ces sites et les variations globales des taux de production d'isotopes cosmogéniques. Le troisième chapitre correspond au deuxième objectif, c'est-à-dire étudier les variations plus récentes à haute résolution (séculaire à multi-décennale), en lien avec le lobe de flux Nord-Américain. Par ailleurs, bien que cela ne constitue pas un objectif principal de la thèse, l'enregistrement d'un nombre élevé de couches déposées rapidement à Grand Lake, offre également l'opportunité d'explorer la relation entre les processus sédimentaires et l'acquisition de l'aimantation. Enfin, dans les trois chapitres, les enregistrements sont comparés à d'autres enregistrements de l'hémisphère Nord (Europe de l'ouest, Europe du nord, Atlantique Nord, Arctique) afin d'identifier les similarités et différences de variations régionales ou globales.

La conclusion générale synthétise les principaux résultats issus des trois chapitres de la thèse, chacun apportant des éléments de compréhension des variations paléomagnétiques séculaires et de paléointensité relative au cours de l'Holocène dans des environnements glaciomarins et lacustres du nord du Groenland et du Labrador. Elle prend la forme d'une discussion intégrée, en soulignant les apports spécifiques de chaque site étudié (le fjord Petermann, le nord-est du Groenland et Grand Lake) à la compréhension de la dynamique du champ géomagnétique au cours de l'Holocène. Elle discute également des limites méthodologiques, telles que la résolution temporelle, la conservation des sédiments superficiels et les incertitudes liées aux datations radiométriques. Enfin, elle propose plusieurs pistes de recherche futures, notamment l'amélioration des méthodes de datation radiométrique et paléomagnétique combinées, ainsi que la caractérisation approfondie de l'impact de la turbulence sur la DRM et l'utilisation d'outils paléomagnétiques pour identifier l'origine des couches déposées rapidement.

J'ai également participé à d'autres études pour lesquelles j'ai contribué aux mesures de laboratoires, à l'interprétation des données et à la relecture des articles.

Kury, M.S., Francus, P., Chassiot, L., Antoniades, D., St-Onge, G., **Girard, J.,** Lajeunesse, P., (2025). Untangling sedimentation processes in a deep fjord Lake in Labrador: A high-resolution archive of past environment dynamics at Grand Lake. The Depositional Record, 00, 1-26. Available from: https://doi.org/10.1002/dep2.70020

Jennings, A., Jenner, K., Normandeau, A., Roth, W., Andrews, J., Kelleher, R., **Girard, J.**, Reilly, B., Campbell, C., & Bennett, R. (2025). Retreat of the Boothia-Lancaster ice stream from its Last Glacial Maximum extent and its role in the origin of Baffin Bay Detrital Carbonate (BBDC) events 0, 1 and 2. Quaternary Science Reviews, 358, 109353. https://doi.org/10.1016/j.quascirev.2025.109353

Geoffroy M., Limoges A., et al. (incluant **Girard, J.**). First characterization of the marine ecosystem of Archer Fiord in the Last Ice Area of the high Arctic: a productivity paradox, under review. Arctic Science.

Au cours de mon doctorat, j'ai eu l'occasion de participer à plusieurs congrès et conférences, au cours desquels j'ai pu faire des présentations, détaillées ci-dessous, de mes travaux de recherche.

Girard J., St-Onge, G., Montero-Serrano J.-C., 2022. Rapid paleomagnetic fluctuations in the Arctic during the Holocene. Affiche lors du congrès étudiant du Geotop, 29-31 mars 2022, en ligne.

Girard J., St-Onge, G., Montero-Serrano J.-C., Seidenkrantz M.-S., Pearce C., Francus P., 2022. Rapid paleomagnetic fluctuations in the Arctic during the Holocene: preliminary results. Affiche lors de la rencontre annuelle d'ArcTrain, 13-17 mai 2022, Jouvence (QC).

Girard J., St-Onge, G., Seidenkrantz M.-S., Pearce C., 2023. Paleomagnetic variations in the Arctic from Northern Greenland records. Présentation orale Northeast Greenland Workshop, 25-27 janvier 2023, en ligne.

Girard J., St-Onge, G., Montero-Serrano J.-C., Beauvais Q., Sanderson N., Seidenkrantz M.-S., Pearce C., 2022. Paleomagnetic fluctuations in Northern Greenland during the Holocene: preliminary results. Présentation orale, 10-12 mars 2023, Chéribourg (QC).

Girard J., St-Onge G., Montero-Serrano J.-C., Francus P., Reilly B, Lagroix F., Seidenkrantz M.-S., Pearce C. 2023. Paleomagnetic fluctuations in the Arctic and Northern Canada during the Holocene: preliminary results, Biology and Paleoenvironment department Seminar, 10 avril, Palisades, oral

Girard J., Brendan Reilly, Guillaume St-Onge, France Lagroix, Jean-Carlos Montero-Serrano, Pierre Francus, 2023. Reproductibilité des variations paléomagnétiques séculaires dans l'Arctique au cours des derniers 6000 ans, Réunion des Sciences de la Terre, Rennes (France), Affiche

Girard J., St-Onge G., Reilly B., Lagroix F., Montero-Serrano J-C., Francus P., Seidenkrantz M-S., Paleomagnetic secular variations in the Arctic during the Holocene: implications for chronology and geomagnetism Geotop mars 2024, Stoneham (Québec), affiche

Girard J., Brendan Reilly, Guillaume St-Onge, France Lagroix, Anne Jennings, Joesph Stoner, 2024. Paleomagnetic secular variations inferred from High Arctic (>80oN) sediment cores suggest a potential link between North Magnetic Pole migration and intensity variations of the Earth Magnetic Field, AGU fall meeting, Washington DC, poster.

J'ai eu la chance de participer à plusieurs expéditions et campagnes de terrain. En octobre 2022, une **campagne de carottage au lac Témiscouata** a eu lieu pendant une semaine afin de préparer la **campagne de terrain à Grand Lake** (Labrador, Canada) du 15 au 30 mars 2023. Au cours de ces deux campagnes, j'ai pu me former à l'utilisation de la plateforme de carottage Uwitec, et récolter des carottes sédimentaires lacustres, dont celles de Grand Lake qui ont été utilisées pour mon chapitre 3. Du 7 septembre au 5 octobre 2023, j'ai participé au **Leg 3 de l'expédition ArcticNet 2023** dans le détroit de Nares et le nord de la baie de Baffin, pour les opérations de carottage (carottier à graviter, carottier à gravité géant, carottier boîte) à bord du NGCC Amundsen.

J'ai pu participer à l'école d'été de l'*Institute of Rock Magnetism* à Minneapolis (Minnesota, USA) en juin 2022, qui m'a permis d'acquérir des connaissances en paléomagnétisme, magnétisme environnemental, magnétisme des roches et des sédiments et des compétences en techniques de laboratoire de pointe.

J'ai effectué des analyses au laboratoire des isotopes radioactifs au Geotop à l'UQAM (Montréal, Canada) en juin 2022 avec Dr. Nicole Sanderson. Nous avons effectué différents traitements d'acides sur les sédiments au sommet de deux carottes (AMD1902-10GC et AMD1902-07GC) dans le but d'utiliser la technique du ^{210}Pb pour estimer les taux d'accumulation de sédiments récents (derniers 150-200 ans).

J'ai effectué un séjour au Lamont Doherty Earth Observatory (LDEO) au mois d'avril 2023 avec Dr. Brendan Reilly dans le but d'améliorer le traitement et l'interprétation de mes données paléomagnétiques de mon premier chapitre. J'ai également réalisé un séjour à l'Institut de Physique du Globe de Paris (IPGP) au mois de janvier 2023, sous la supervision de Dr. France Lagroix afin de réaliser des analyses de magnétisme environnemental.

J'ai participé à un atelier de *MagellanPlus Workshop series* au MARUM en Allemagne (*Bremen Core Repository*) du 2 au 13 novembre 2024, intitulé *21st Century Drilling : Building capacity in the digital domain using scientific ocean drilling legacy material*, durant lequel j'ai réalisé des mesures de propriétés physiques et chimiques sur des carottes provenant de l'expédition ODP Leg 177. J'ai également travaillé sur les données paléomagnétiques dans le but d'aider l'équipe de biostratigraphie à réviser le modèle d'âge.

CHAPITRE 1

VARIATIONS SECULAIRES PALEOMAGNETIQUES A 81°N AU NORD DU GROENLAND AU COURS DES DERNIERS 6000 ANS

1.1 RESUME EN FRANÇAIS DU PREMIER ARTICLE

Dans ce chapitre, les variations paléomagnétiques du champ ont été reconstituées à partir du vecteur paléomagnétique complet enregistré dans les sédiments du fjord Petermann (détroit de Nares, Groenland) au cours des derniers 6 000 ans. Les variations paléomagnétiques (inclinaison, déclinaison, paléointensité relative) des quatre carottes sédimentaires ont été compilées en un seul enregistrement, le *Petermann stack*, avec un modèle d'âge indépendant basé sur sept datations au radiocarbone. Les analyses de magnétisme environnemental démontrent que le signal magnétique est porté par des minéraux ferrimagnétiques de faible coercivité et qu'il est reproductible entre chaque carotte, attestant de la qualité et de la fiabilité de l'enregistrement. Les changements directionnels sont globalement cohérents avec des enregistrements en Amérique du Nord et dans le nord de l'Atlantique Nord sur des échelles de temps séculaires à millénaires. De plus, les variations d'intensité à l'échelle millénaire sont cohérentes avec les prédictions des modèles géomagnétiques. En comparant le stack à l'enregistrement de haute résolution GREENICE, un décalage est observé. Ce décalage est attribué soit à une variation de l'âge réservoir dans le fjord au cours du temps soit à un délai d'enregistrement de l'aimantation dû à une profondeur de blocage d'environ 11 cm, ou encore à une combinaison des deux phénomènes. La trajectoire du pôle géomagnétique virtuel a été reconstruite grâce aux données directionnelles et montre que la migration récente du Pôle Nord magnétique est cohérente avec les variations paléomagnétiques séculaires à l'échelle de l'Holocène. Les résultats de ce chapitre, comme d'autres études précédentes en ont fait l'hypothèse, suggèrent que les variations temporelles et spatiales de l'intensité du champ géomagnétique sont liées à la dynamique des lobes de flux géomagnétiques et ont une influence sur la trajectoire de migration du pôle géomagnétique virtuel. Cet article a été accepté pour publication dans sa version finale en septembre 2024 dans le journal *Geochemistry, Geophysiscs, Geosystems* de l'*American Geophysical Union*. En tant que première autrice, j'ai établi les objectifs et hypothèses de recherche, réalisé les analyses en laboratoires, interprété et discuté les résultats et rédigé le manuscrit. Le professeur **Brendan Reilly** en tant que deuxième auteur a apporté les résultats d'une étude précédente (Reilly et al., 2019), aidé à l'établissement des hypothèses de recherche et participé à l'interprétation et la discussion des résultats et à la révision de l'article. Le professeur **Guillaume St-Onge** en tant que troisième auteur a participé à établir les objectifs et hypothèses de recherche, à l'interprétation et à la discussion des résultats, à la révision de l'article ainsi qu'au financement des analyses. La directrice de recherche **France Lagroix** m'a accueillie à l'IPGP pour réaliser une partie des analyses, a participé à l'interprétation des résultats, à la discussion et à la révision de l'article. Le professeur **Jean-Carlos Montero-Serrano** a financé la collecte de la carotte sédimentaire AMD1902-10GC et a participé à la discussion et à la révision de l'article. Le professeur **Joseph Stoner** et la chercheuse **Anne Jennings** ont participé à l'étude qui a servi de base à celle-ci (Reilly et al., 2019), à la discussion et à la révision de l'article. Les résultats présentés dans cet article ont été présentés aux conférences suivantes : Réunion des Sciences de la Terre à Rennes (France) en 2023, congrès du Geotop à Chéribourg (Canada) en 2023 et à l'*AGU Fall meeting* à Washington D.C. (USA) en 2024.

1.2 PALEOMAGNETIC SECULAR VARIATIONS IN NORTH GREENLAND AT 81°N OVER THE LAST 6,000 YEARS

1.2.1 Abstract

We investigate full vector paleomagnetic changes recorded in high-resolution sediments of Petermann Fjord, North Greenland, deposited over the last 6 kyr, in the context of the recent rapid changes in the geomagnetic field. A Paleomagnetic Secular Variation (PSV) stack (inclination, declination, and relative paleointensity) was reconstructed using four marine sediment cores with an independent age model constrained by seven radiocarbon ages. Magnetic investigations demonstrate that the paleomagnetic signal is carried by low coercivity ferrimagnetic minerals and is well reproduced in all cores, attesting to the quality and reliability of the paleomagnetic recording of these sediments. This signal is broadly consistent in directional changes with distant records in North America and the northern North Atlantic at centennial and millennial timescales, and has millennial scale intensity variations that are consistent with model predictions. The offset between a magnetization age determined through comparison with a northern North Atlantic PSV reference curve, GREENICE, and the radiocarbon age model indicates either a reasonable lock-in depth of magnetization (~11 cm from the coretop) or centennial-scale reservoir age variation through time in the fjord. Reconstructed virtual geomagnetic pole (VGP) migration for the last 6 kyr shows that the recent migration of the magnetic North Pole is consistent with secular paleomagnetic variations on geologic timescales. Our results suggest that magnetic field intensity variations (temporal and spatial) are linked to magnetic flux lobe dynamics and influence the VGP migration.

1.2.2 Plain Language Summary

The magnetic field of the Earth is generated by convection in the outer core of the Earth. Magnetic sediments deposited on the ocean seafloor record the Earth's magnetic field and are important archives of its past fluctuations (intensity and direction). Studying the

geomagnetic field is important as it gives us information about processes in the Earth's core and can be used for correlating sediment cores together and for establishing the chronology of sedimentary sequences. In this study, we used sediment cores from Petermann Fjord (Nares Strait, Northern Greenland) to study past geomagnetic variations. Petermann Fjord is an excellent site to conduct such studies because of its close location to the North Magnetic Pole (NMP) and because of the high sediment accumulation rates that enable us to conduct studies with a high temporal resolution. We hypothesize that the NMP migration during the last millennia could have been driven by strong regional intensity features of the geomagnetic field and that the recent rapid migration of the NMP is not unusual because such amplitudes of migration happened in the past, without necessary leading to a reversal of the poles.

1.3 INTRODUCTION

The North Magnetic Pole (NMP) was directly located for the first time in 1831 in the Canadian Arctic (Ross, 1834). Direct observations from 1831 to 2007 and recent satellite observations show a clear migration of the NMP over more than 1,700 km since the early twentieth century from the Canadian Arctic into the Arctic Ocean and toward Siberia (Livermore et al., 2020; Olsen & Mandea, 2007). Recent data from the Resolute Bay observatory show an increase in the NMP migration velocity from 9 to 41 km/year during the 1970s and up to 60 km/year in 2003 (NOAA, 2021). According to the current World Magnetic Model (National Centers for Environmental Information, 2023), the 2023 North Magnetic Dip Pole is located at 146.826°E 86.146°N (National Centers for Environmental Information, 2022). NMP migration is coupled with a decrease in the geomagnetic dipole moment by 10% since the first mathematical reconstruction by Gauss (1833) (Gubbins, 2008). The modern northern Hemisphere intensity pattern is not that of a perfect dipole; rather, subarctic regions of high field intensity, called geomagnetic flux lobes, can be observed in North America, Siberia and Europe (Bloxham & Jackson, 1992; Bloxham et al., 1989; Jackson et al., 2000). The NMP migration is currently following a straight path between two of these geomagnetic flux lobes (Livermore et al., 2020). Here, we ask if this recent rapid migration of the NMP is unusual relative to pre-1831 variations and use the high-resolution (>50 cm/ka) sedimentary record of Petermann Fjord, North Greenland (~81°N), as a high Arctic geologic observatory, to answer this question.

The geomagnetic field displays unique variations in the High Arctic region (Bloxham et al., 1989; Chulliat, Hulot, & Newitt, 2010; Chulliat, Hulot, Newitt, Orgeval, 2010; Haines & Newitt, 1997; Jackson et al., 2000; Newitt et al., 2002; Olson & Aurnou, 1999; St-Onge & Stoner, 2011) and pioneer studies of the Baffin Bay sediments using PSV revealed excursions at high latitudes (Simon et al., 2012, 2016; Thouveny, 1988), which makes the Arctic a pertinent zone to study paleomagnetism. Because of the Coriolis effect and the solid inner Earth core, different flow regimes operate in the outer core, separated by a cylinder, tangent to the inner core and parallel to the rotation axis (e.g., Aurnou et al., 2003; Hollerbach & Jones, 1993; Lawrence et al., 2009). The projection of the tangent cylinder (TC) at the Earth's surface is observed in the Arctic (70°N), and presents low geomagnetic intensities (Hulot et al., 2002; Olson & Aurnou, 1999). The higher geomagnetic intensity at flux lobes arises from the convection outside the TC (Bloxham & Gubbins, 1985). Previous paleomagnetic studies in the European Arctic (Caricchi et al., 2020) and northern North Atlantic (Stoner et al., 2013) demonstrated that flux lobes and intensity variations likely play a role in the variation of the NMP migration on geologic timescales. However, expanding these observations through paleomagnetic reconstructions in the Arctic is often challenging due to complexities in chronologies that stem from lack of datable material, large uncertainties in old carbon effects, and low or variable sedimentation rates.

The sediments of Petermann Fjord have shown great potential as a high Arctic Holocene paleomagnetic site, with previous studies dedicated to establishing a chronostratigraphy to study deglaciation and floating ice tongue history (Jennings et al., 2022; Reilly et al., 2019). Here we revisit the Petermann Fjord paleomagnetic record with a new core, additional radiocarbon data, new rock magnetic data, and estimates of relative paleointensity (RPI) to establish a new full vector PSV reconstruction with an independent age model that can be evaluated against other Northern Hemisphere records and global models. The high sediment accumulation rates or SAR (~60 cm/ka) and proximity to the

NMP make this site ideal for assessing the role of the TC and geomagnetic flux lobes on the paleomagnetic variations and NMP migration (St-Onge & Stoner, 2011).

1.4 MATERIALS AND METHODS

1.4.1 Petermann Fjord Sediment cores

Petermann Fjord is a 1,100 m deep, 90 km long and 20 km wide fjord located in Nares Strait (Jakobsson et al., 2018), which is connected with the Lincoln Sea to the North and Baffin Bay to the southwest (Figure 27a). Sediments are primarily derived from Lower Paleozoic sedimentary carbonate rocks and inland, sub-ice crystalline rocks (Dawes et al., 2000), delivered primarily by suspension settling from glacier meltwater plumes and ice-rafted debris, with an increased influence of downslope transport in the fjord's deep basin (Hogan et al., 2020; Reilly et al., 2019). SAR on bathymetric highs away from downslope deposits range from 50 to 90 cm/ka and average ~60 cm/ka in the cores studied here (Reilly et al., 2019). While this study focuses on the paleomagnetic signals in these sediments, recent changes to the floating Petermann Ice Tongue have motivated a number of studies focused on the oceanography, climate, and ice sheet histories of the region (e.g., Detlef et al., 2021; Heuzé et al., 2017; Hogan et al., 2020; Jakobsson et al., 2018; Jennings et al., 2022; Reilly et al., 2019; Washam et al., 2019).

Core AMD1902-10GC (hereafter referred to as 10GC, Figure 27b and Table 2) was recovered in Petermann Fjord during the ArcticNet expedition in 2019 onboard the Canadian Coast Guard Ship Amundsen using a 3 m gravity corer. On board, the cores were cut into 1.5 m sections, and new data were generated for this study, as described below. The top of core 10GC was most likely lost during coring. However, not knowing how much was lost, we still define the top of the core at 0 cm in the following figures and text. OD1507-04GC, -41GC and -40TC (Figure 27b and Table 2) were collected in Petermann Fjord during the Petermann 2015 Expedition onboard the Swedish Icebreaker Oden (OD1507), with data and methods previously reported by Reilly et al. (2019).

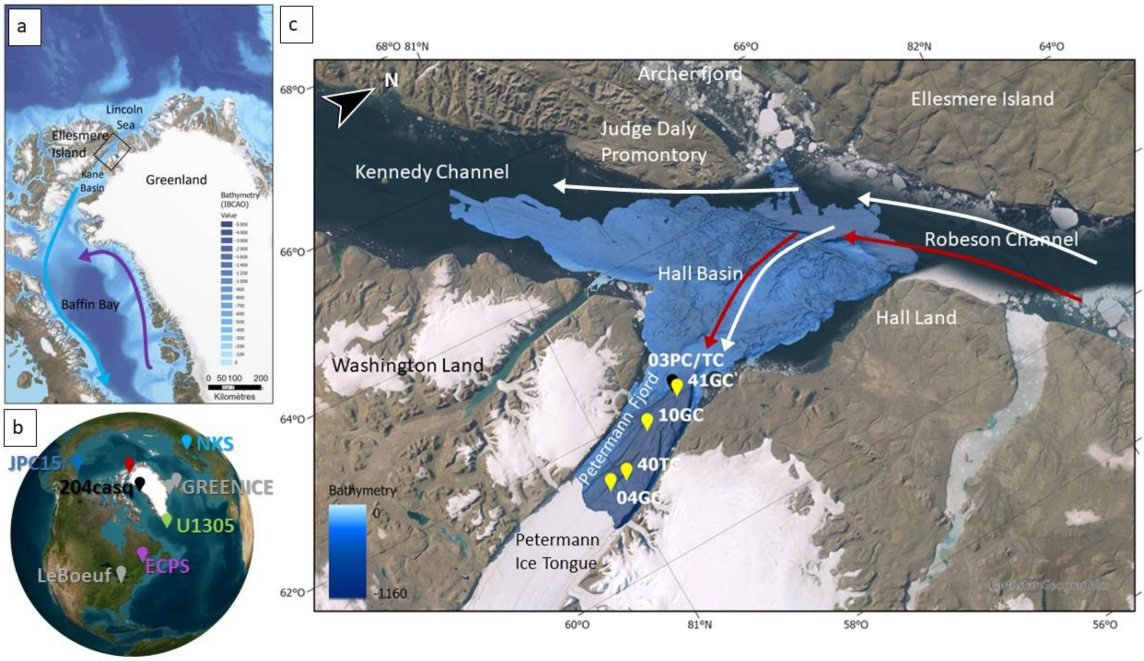

Figure 27. (a) Location of study site in Nares Strait, with bathymetric data from the International Bathymetric Chart of the Arctic Ocean (IBCAO, Jakobsson et al., 2020). Blue arrows represent the cold polar waters becoming the Baffin Current, Purple arrows represent the West Greenland Current. **(b)** Location of the comparison records mentioned in this study. **(c)** Map of the study sites in Petermann Fjord. Multibeam bathymetry of the Petermann Fjord and Hall Basin were obtained from Jakobsson et al. (2018). Black dots = cores composing the outer fjord splice; yellow dots = cores composing the stack. 10GC was collected during AMD1902 expedition, 03PC/TC, 41GC, 04GC, 40TC during OD1507 (Reilly et al., 2019). Surface Polar Waters are represented by white arrows and subsurface Atlantic Waters are represented by red arrows.

Table 2. Sediment cores used in this study.

Core	Location	Latitude (°)	Longitude (°)	Depth (mbsl)	Length (m)	References
AMD1902 -10GC	Petermann Fjord (~70 km from grounding line)	81.102	-61.746	1085	2.723	(Montero-Serrano & Brossard, 2019)
OD1507-04GC	Petermann Fjord (52 km from grounding line)	80.970	-61.253	968	4.46	(Reilly et al., 2019)
OD1507-41GC	Petermann Fjord (80 km from grounding line)	81.194	-61.977	991	4.4	

OD1507-40TC	Petermann Fjord (56 km from grounding line)	81.010	-61.271	932	3.188

1.4.2 Physical properties: X-Ray Imaging and Multi-Sensor Core Logger Analysis

The whole sections of core 10GC were scanned with a GEOTEK X-ray Computed Tomography (X-CT) system at ISMER (Québec, Canada) to obtain digital X-ray images in greyscale to detect density changes and identify different sedimentary structures (St-Onge et al., 2007). Physical and magnetic properties of core 10GC were measured at 1 cm intervals using a GEOTEK Multi Sensor Core Logger at ISMER (St-Onge et al., 2007), including P-wave velocity and wet bulk density on whole cores. Low field volumetric magnetic susceptibility (k_{LF}) was measured both on the whole core and half sections with a Bartington Instruments M2SEI point sensor at 1 cm intervals. Chemical composition was measured on the half-sections of core 10GC with an energy-dispersive Olympus Innov-X DELTA portable X-ray fluorescence (pXRF) analyzer at 1 cm intervals. Half-sections were digitally photographed with a GEOTEK Geoscan IV imaging system. Diffuse spectral reflectance measurements were conducted at 1 cm intervals using a Minolta CM-2600d spectrophotometer at ISMER. The data acquired were expressed according to the color space of the International Commission on Illumination: L* black (0) to white (100), a* green (60) to red (+60), and b* blue (60) to yellow (+60) (Debret et al., 2011; St-Onge et al., 2007).

The physical and chemical properties of cores 40TC, 41GC and 04GC were obtained by Reilly et al. (2019). While many data sets are comparable, XRF measurements were performed with an ITRAX XRF core scanner with a Mo tube and 5 s exposure time at the Oregon State University Marine and Geology Repository (USA). Accordingly, absolute values differ between the two XRF systems, and only relative comparisons are possible. In this study, we only used Ti/Ca as a proxy for the terrigenous sediment composition (Croudace & Rothwell, 2015) to correlate all sediment cores. In this system, it reflects the relative detrital input from carbonate rock erosion (detrital calcite, low Ti/Ca) versus from crystalline basement rock erosion (higher Ti/Ca) (Jennings et al., 2022; Reilly et al., 2019).

1.4.3 Grain size analysis

Grain size measurements (<2 mm fraction) on core 10GC were conducted with a Malvern-Panalytical Mastersizer 3000 laser particle size analyzer at ISMER on non-pretreated sediment samples at 10 cm intervals. Prior to the analyses, 0.5 g of sediment was deflocculated with a solution composed of 30 mL of sodium hexametaphosphate (concentration 20 g/L) and 70 mL of water and by agitating the mixture for at least 3 hr before analysis using an in-house rotator. After measurement, grain-size distribution and statistical parameters were calculated with the GRADISTAT Excel spreadsheet version 9.1 (Blott & Pye, 2001) to obtain different parameters such as the D_{90} (µm). Ice rafted debris (IRD) abundance was determined by counting the >2 mm fraction on the X-CT images in contiguous 2-cm windows (Grobe, 1987). All of these grain size parameters can help to document lithological changes in the core sediment.

1.4.4 Continuous paleomagnetic measurements

U-channels were sampled in core 10GC using square plastic tubes of 4 cm^2 and up to 1.5 m long (e.g., Weeks et al., 1993) and were then used to conduct continuous magnetic measurements at 1 cm intervals with a 2G Enterprises 755SRM-1.65 cryogenic magnetometer at ISMER. It enabled us to first measure the Natural Remanent Magnetization (NRM) and then conduct stepwise demagnetization from 0 to 80 mT at 5 mT increments and at 10 mT increments from 80 to 100 mT using an alternating field (AF). Anhysteretic remanent magnetization (ARM) was induced with a 100 mT peak AF field and a 50 µT direct current biasing field. U-channels were then stepwise demagnetized in the same way as the NRM. A pulse magnetizer was used to induce an isothermal remanent magnetization at 300 mT (IRM) and 950 mT (representing a saturation isothermal remanent magnetization [SIRM]), which were then subsequently demagnetized and measured at 5 mT increments from 0 to 80 mT for the IRM and at 0, 10, 30, and 50 mT for the SIRM.

After each measurement, data were checked, and flux jumps corrected if necessary with the UPmag MATLAB software (Xuan & Channell, 2009). The characteristic remanent magnetization was then calculated by principal component analysis (PCA; Kirschvink, 1980) with the Mazaud Excel spreadsheet (Mazaud, 2005) using the 2060 mT steps, providing declination and inclination data as well as maximum angular deviation (MAD) and median destructive field (MDF) values. Due to the response function of the magnetometer, values are smoothed over a 7–8 cm interval (Philippe et al., 2018; Weeks et al., 1993). To avoid edge effects, we do not consider the 4 cm interval at the top and bottom of each u-channel.

The MDF is the field intensity required to remove half of the initial remanence and is a measure of the unblocking field spectrum of the remanence-carrying grains assemblage of the NRM, ARM, or IRM. The k_{ARM}/k_{LF} ratio is a parameter sensitive to changes in magnetic grain size if the magnetic mineralogy is dominated by magnetite and varies inversely with magnetic grainsize (Banerjee et al., 1981; King et al., 1982).

MAD values are one of several indicators of the quality of the directional data (Kirschvink, 1980). High MAD values generally result from complex magnetization with different coercivities and/or sedimentary processes such as turbidity currents and debris flows (Lévesque et al., 2020) and therefore must be carefully used. Zijderveld diagrams (orthogonal projections; Zijderveld, 1967) document the demagnetization behavior (Figure S2 in Supporting Information).

Previously reported paleomagnetic measurements from Reilly et al. (2019) were measured on a nearly identical 2G magnetometer at the Oregon State University Paleo- and Environmental Magnetism Laboratory. A previous study has shown that both magnetometers are well intercalibrated (Velle et al., 2021).

1.4.5 Rock magnetic measurements

A susceptibility meter AGICO KLY-3 was used to measure the temperature-dependent magnetic susceptibility of seven samples of core 10GC (10, 25, 40, 50, 130, 250 cm) in air.

The intervals of interest were chosen based on continuous magnetic measurements to determine the magnetic mineralogy and granulometry of the remanence carriers. Samples were heated up to 700°C and then cooled down back to room temperature to notably detect the Curie temperature (Dunlop & Ozdemir, 2007), the temperature at which a mineral loses its permanent magnetization.

Discrete magnetic measurements on core 10GC samples were conducted on a Princeton Measurements vibrating sample magnetometer (VSM) at the Institut de Physique du Globe de Paris (IPGP, France). Hysteresis loops, FORC diagrams (First order reversal curves; Roberts et al., 2019, 2022) and IRM acquisition curves were measured for the same samples before and after heating. Dia/paramagnetic correction (70%) was applied to the hysteresis loops, which are used to identify the magnetic domain state of a mineral (e.g., Day et al., 1977). Additional hysteresis loops were made on OD1507 samples on a VSM at Western Washington University (USA). Magnetic parameters were derived from the hysteresis loops: coercive force (Hc), remanent coercive force (Hcr), saturation magnetization (Ms) and saturation remanence (Mrs). The resulting coercivity and remanence ratios (Hcr/Hc; Mrs/Ms) and the shape of the hysteresis loops are indicative of the magnetic mineralogy and grain size and enable to estimate the magnetic domains (Day et al., 1977; Dunlop, 2002). IRM acquisition curves were measured on the VSM. S-ratios were calculated according to the following equation $S - ratio = 0.5 \times (\frac{1 - IRM_{300\,mT}}{SIRM})$ (Bloemendal et al., 1988). To determine the coercivity components of the samples, IRM acquisition curves were "unmixed" (Table S3 in Supporting Information S1) using the online software MAX UnMix (Maxbauer et al., 2016). FORC measurements were processed using the FORCinel software (Harrison & Feinberg, 2008).

1.4.6 Chronology

Two intervals of 4 cm in core 10GC were sieved at 100 and 150 µm and 2 mm. Foraminifera were picked from the dry fractions 150 µm to 2 mm and 100–150 µm at the University of New Brunswick. The samples were then sent to the Alfred Wegener Institute in Bremerhaven to conduct carbon dating analyses using a Mini Carbon Dating System MICADAS. Five other radiocarbon ages from Reilly et al. (2019) were also used in the age model (Table 3).

The Marine20 ΔR value was calculated using the value ΔR = 188 ± 91 for the Canadian Artic Archipelago (Pieńkowski et al., 2022) and adding the age offset between Holocene bottom and surface waters in Nares Strait 240 ± 20 (Jennings et al., 2022), leading to a ΔR = 430 ± 95 years. As the ΔR is uncertain in the Fjord, and to account for possible local variations (in comparison to Nares Strait) in oceanographic circulation, sea ice cover, meltwater, reservoir age variation through time and the difference between planktic and benthic foraminifera, an uncertainty of ±50 years was added, leading to a final Marine20 value of ΔR = 430 ± 145 years. In Reilly et al. (2019), one of the presented age models, M2, includes a 20 cm lock-in-depth and is calculated with a ΔR = 570 years using the Marine13 calibration curve. For the Holocene, Marine20 ΔR values are about 150 years less than the Marine13 ΔR values. Therefore, the independently derived ΔR value used in the present study is consistent with the M2 ΔR value in Reilly et al. (2019). Based on studies of ocean circulation in the fjord, we consider the age offset between benthic and planktonic foraminifera to be negligible (Heuzé et al., 2017; Jakobsson et al., 2018; Jennings et al., 2020, 2022; Johnson et al., 2011; Münchow et al., 2011, 2016) and near modern mixed planktonic, mixed benthic, and species specific (Cassidulina neoteretis) return similar ages (Reilly et al., 2019). For that reason, a common value of ΔR was used for radiocarbon dates obtained from planktic and benthic foraminifera. The R package "rbacon" version 3.2.0 (Blaauw & Christen, 2011) was used to build the age models using the calibration curve Marine20 (Heaton et al., 2020) and attributing an age of 0 (±65) at 7 cm depth due to vertical compaction of the top of the core 40TC during transport after coring.

Table 3. Radiocarbon results. The age in italics was not used for the age-depth model. Radiocarbon ages were calibrated using the Marine20 (Heaton et al., 2020) calibration curve with a $\Delta R = 430 \pm 145$ yrs in the R package 'rbacon' (Blaauw & Christen, 2011).

Core	Independent depth (cm)	Correlated Equivalent Depth (cm)	Lab. number	$\delta^{13}C$ (‰)	Dated material	Uncalibrated Age	Error ^{14}C ±	Median calibrated Age (BP)	Min-max calibrated ages (BP)
03UW	52-54	40.87	ANU # 56605	-1.2	Mixed benthic foraminifera	1421	26	410	188-632
10GC	96-100	79.33	AWI#10207.1.1	-7.2	30% planktic (N. *pachyderma* s.) 70% benthic	1784	60	913	669-1213
41GC	*62-64*	*91.72*	*ANU#17240*	*-1.65*	*Mixed benthic*	*2578*	*33*	*Too old (remobilized material) Not calibrated*	
03UW	229-231	188.72	ANU#56606	-2.2	Mixed benthic	3427	27	2718	2460-3022
41GC	166-168	195.72	ANU#56603	-1.82	E. *excavatum*	3567	26	2847	2592-3150
10GC	251-253	232	AWI#10208.1.1	-4.9	30% planktic (N. *pachyderma* s.) 70% benthic	4277	66	3593	3286-3928
41GC	292-296	322.72	ANU#56604	-1.7	N. *pachyderma* (s)	5697	30	5425	5057-5771
41GC	374-376	403.72	ANU#53516	-1.4	C. *neoteretis*	7174	53	7023	6635-7391

1.5 RESULTS

1.5.1 Lithology

High-resolution digital images (Figure 28a) and visual description of the split core indicate differences between lithologic units: reddish brown clay (0–7 cm), pinkish gray clay (7–68 cm) with fine sand intervals (20–23 cm and 61–63 cm) and fine laminations (50–54 cm), homogeneous grayish brown clay (68–124 cm) with fine sand-silt intervals (75–76 cm, 108–110 cm, 117–118 cm), IRD-rich brown clay (125–146 cm), brown clay with pinkish gray clay laminations (146–184 cm), and IRD-rich light gray clay (185–269 cm). Rock fragments (cm-scale grains) can be seen on the X-CT images as well as the laminations in the top part of the core (0–50 cm). Point source k_{LF} (Figure 28a) shows variations around 50 x 10^{-5} SI, and a transition around 180 cm depth toward slightly lower values (~30 x 10^{-5} SI). The same transition is observed in the a* profile, with higher amplitude variations in the 0–180 cm interval and a decrease in the average value and the amplitude variations at the bottom of the core (180–257 cm). The Ti/Ca ratio revealed higher amplitude variations in the 0–180 cm interval and lower amplitude variations in the bottom of the core (180–257 cm). The grain size is homogeneous throughout the entire core: <20% clay, <20% sand and ~60%–70% silt, with 20 µm < D (90) < 30 µm and peaks >40 µm at the top (20 cm) and bottom (250 cm) of the core. There is a low number of >2 mm clasts (0–2 clasts) or IRD in the top 70 cm of the core, with increasing concentrations toward the bottom, up to 6 clasts. Statistics results from GRADISTAT treatment are presented in Supporting Information S1 (Table S1).

1.5.2 Continuous paleomagnetic measurements

k_{ARM}/k (Figure 28a) presents a similar transition at 180 cm toward higher values as well as a long term trend toward lower values up the core, consistent with a finer magnetic mineralogy in the bottom part of the core (180–250 cm).

In the top 65 cm of the core, MDFNRM values display variations between 35 and 55 mT, possibly indicating the presence of higher coercivity magnetic minerals (Dankers, 1981; Stoner & St-Onge, 2007), whereas the lower values in the rest of the core (~30 mT) are characteristic of ferrimagnetic, low coercivity minerals such as magnetite (Dankers, 1981). MDFARM and MDFIRM, which are indicators of the coercivity of the magnetic assemblages responding to ARM and IRM, respectively (Stoner & St-Onge, 2007) are both lower than the MDFNRM values and show similar variations in the top part of the core 0–65 cm, which reinforces the hypothesis of higher coercivity grains in that interval, activated by the IRM.

Overall, the physical and magnetic properties of this core indicate a change in the magnetic mineralogy at ~65 cm (MDF) and another change at 190 cm in the lithology (Ti/Ca, a*, k_{LF}, k_{ARM}/k_{LF}). Based on the precedent results, the core can be split into three lithologic units:

- 0–65 cm: pink-gray clay, k_{LF} ~ 50 x 10^{-5} SI, a* ~ 5, high amplitude variations of Ti/Ca, low IRD content, higher MDF between 35 and 65 mT, stable kARM/kLF (5–13);

- 65–190 cm: brown clay with color variations from pink to gray, IRD enrichment, higher variations of k_{LF} (40-70 x 10^{-5} SI), Ti/Ca, stable MDF close to 30 mT, a* ~ 4.5, stable k_{ARM}/k_{LF} (8–13);
- 190–270 cm: light gray clay, high IRD content, stable Ti/Ca (0.01–0.02), lower k_{LF} (20–40 x 10^{-5} SI) and a* (3.5), stable MDF close to 30 mT, higher k_{ARM}/k_{LF} (8–18).

This is coherent with units 1A, 1B, and 1C described in previous studies in Petermann Fjord (Jennings et al., 2022; Reilly et al., 2019). As in Reilly et al. (2019), unit 1A refers to the unit from 0 to 65 cm, 1B from 65 to 190 cm and 1C from 190 to 270 cm.

It is possible that a coercivity transition between units 1A and 1B is related to an oxidic/suboxidic transition. Above this redox change, magnetite could have undergone changes such as maghemitization or maghemite coating. However, in 10GC, redox sensitive elements such as Mn and Fe do not display the variations expected at the redox boundary (Froelich et al., 1979, Figure S1 in Supporting Information S1), such as layers with peaks in Mn concentrations or down core changes in Fe concentration. Moreover, Al, which is redox independent, demonstrates an increase in the top 55 cm of core 10GC associated with the lithologic transition. Due to over penetration, the top of 10GC was lost during coring, whereas 04GC (Reilly et al., 2019) has a good recovery of the surface and shows a Mn peak at ~30 cm. This may indicate that redox could still explain this coercivity shift in 10GC, although we cannot fully rule out that the coercivity change may be associated with a provenance change related to the presence of the ice tongue. Similar magnetic mineralogic changes were observed in studies of southern Greenland with no discernible impact on the paleomagnetic signal (Stoner et al., 1995, 2013).

NRM, ARM, IRM and SIRM are characterized by a strong and stable magnetization (Figure 28b). The sediment is well demagnetized and exhibits a generally stable single component magnetization (Figure S2 in Supporting Information S1) except for an intensity increase for the 75–100 mT AF demagnetization steps at ~25 cm, which is sometimes observed during AF demagnetization (Hu et al., 1998). This magnetization was acquired parallel to the last applied field (z axis), which could reflect a spurious ARM and rule out a gyroremanent magnetization. MAD values are <5°, indicating a well resolved magnetization, and inclination values vary around the Geoentric Axial Dipole value (GAD; Figure 28b), indicating high quality directional data and reliable inclination and declination results. NRM directions are less well defined at the top of core (MAD > 5°, low inclination values), likely reflecting a coring disturbance (Montero-Serrano & Brossard, 2019). ARM values are lower at the top of the core (0–65 cm) than for the rest of the core, whereas IRM values are higher for that part of the core than for the rest of the core. Along with higher MDF values (Figure 28a), this further supports inferences of a change in magnetic minerals. The interval 70–180 cm demonstrates more variations in NRM, ARM, IRM and SIRM values than the interval 180–250 cm where the values are much more linear.

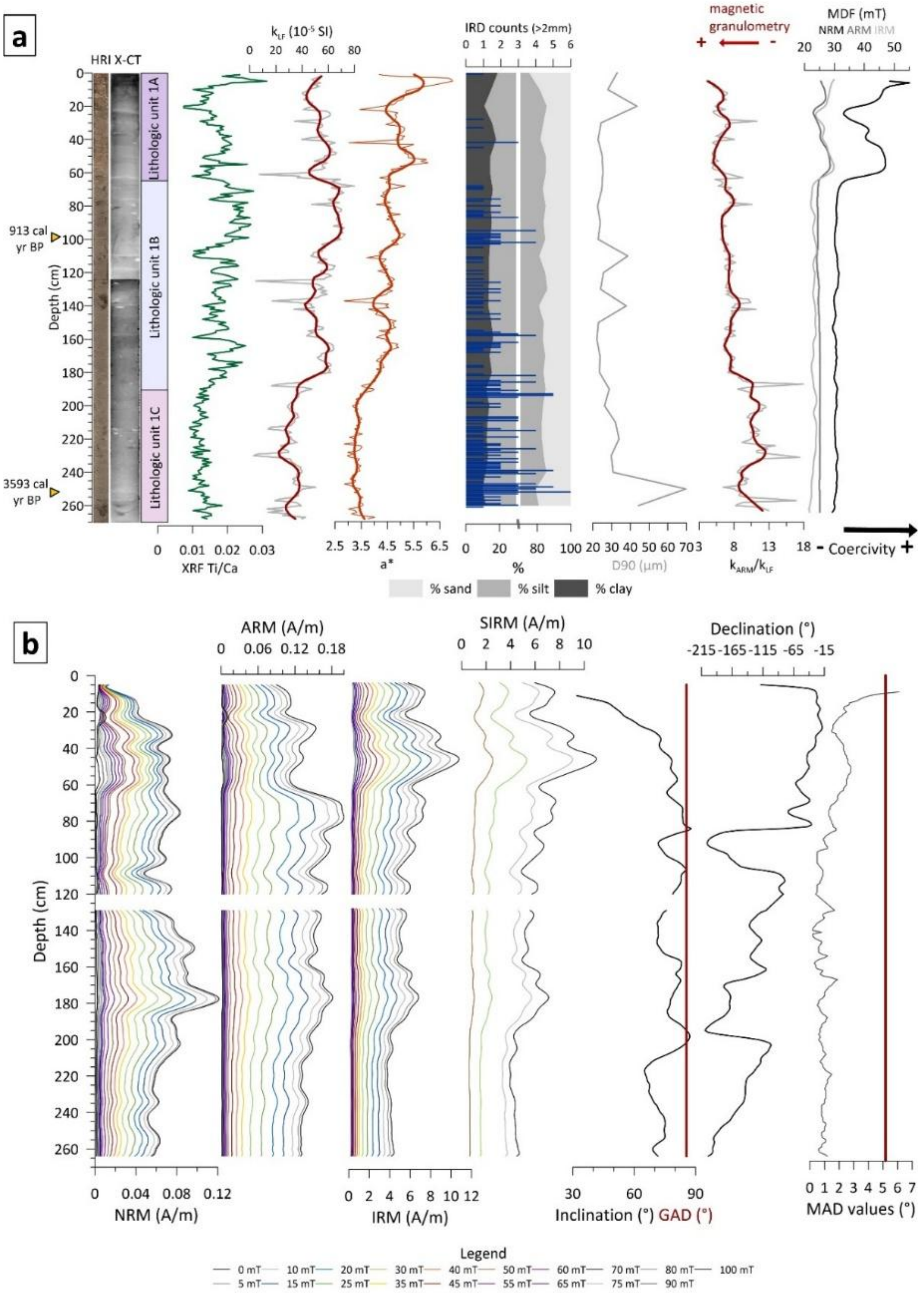
a
HRI X-CT
Lithologic unit 1A
Lithologic unit 1B
Lithologic unit 1C
913 cal yr BP
3593 cal yr BP
Depth (cm)
XRF Ti/Ca
k$_{LF}$ (10^{-5} SI)
a*
IRD counts (>2mm)
%
% sand
% silt
% clay
D90 (µm)
magnetic granulometry
+
-
k$_{ARM}$/k$_{LF}$
MDF (mT)
NRM ARM IRM
- Coercivity +
b
NRM (A/m)
ARM (A/m)
IRM (A/m)
SIRM (A/m)
Inclination (°) GAD (°)
Declination (°)
MAD values (°)
Legend
0 mT
5 mT
10 mT
15 mT
20 mT
25 mT
30 mT
35 mT
40 mT
45 mT
50 mT
55 mT
60 mT
65 mT
70 mT
75 mT
80 mT
90 mT
100 mT

Figure 28. (a) Downcore physical and magnetic properties in core AMD1902-10GC including: high-resolution core image (HRI), X-ray computed tomography (X-CT) scan image, Ti/Ca profile, magnetic susceptibility (kLF), a* red color indicator, relative abundance of the sand, silt and clay, ice rafted debris (IRD) counts based on XCT images (>2 mm clasts), grain size proxy D90 (um), kARM/kLF (magnetic grain size proxy), Median Destructive Field values (mT) of natural remanent magnetization (NRM), anhysteretic remanent magnetization (ARM) and isothermal remanent magnetization (IRM) (magnetic mineralogy indicator). **(b)** Downcore continuous paleomagnetic measurements of core AMD1902-10GC including demagnetization steps 0–100 mT, NRM (A/m), ARM (A/m), IRM 300 mT (A/m), saturation isothermal remanent magnetization (SIRM) 950 mT (A/m), characteristic remanent magnetization (ChRM) Inclination (°) and GAD value, ChRM relative Declination (°) and maximum angular deviation (MAD) values (°).

1.5.3 Magnetic Assemblage

The results of the discrete magnetic analyses are presented in Figure 29. Temperature-dependent magnetic susceptibility measurements demonstrated, on all heating curves, a clear Curie transition around 580°C, indicating the presence of magnetite in the samples (Figure 29a). To precisely determine the temperature of the transition, curve derivatives were calculated. Curie temperatures ranged from 571 to 596°C. Magnetic susceptibility drops shortly before 580°C for samples 25, 40, and 180 and significant magnetic susceptibility persists beyond 600°C, indicating the possible presence of hematite. The sample at 40 cm shows an increase in susceptibility starting around 450°C with a maximum of 525°C. Similar but smaller peaks are also present in samples at 10, 25, 50, and 130 cm. A slight bump at 300°C is visible in the heating curves of the samples at 10, 40, and 130 cm and less but still visible in a sample at 180 cm, suggesting the presence of titanomagnetite. All samples are characterized by an increase in susceptibility after cooling, indicating an increase in the magnetite content.

The shapes of the hysteresis loops (Figure 29b) are typical of low coercivity minerals such as magnetite or titanomagnetite (e.g., Tauxe et al., 1996). However, hysteresis loops are not totally linear at 300 mT and reach saturation between 0.5 and 1 T (Figure 29b), indicating the presence of higher coercivity minerals, despite the dominance of magnetite. This is supported by the S-ratio values (Bloemendal et al., 1988; Table 4). According to the hysteresis loops, all magnetization values were multiplied by a factor 10 after heating (Figure 29b). Magnetization of samples at 25 and 40 cm increased slightly less (0.058–0.3; 0.058–0.4), contrary to the sample at 250 cm for example, (0.02–0.2). Mrs and Ms values are higher after heating except for the sample at 10 cm (Table 4). Multiplication factors were slightly higher for Mrs than for Ms (Table 5).

Table 4. Hysteresis and S-ratio measurements results (heated samples in grey).

	Mrs	Ms	Hc	Hcr	IRM $_{-300mT}$	SIRM	S-ratio (Bloemendal et al.,1988)
10 cm	9.14E-03	4.96E-02	1.95E-02	4.83E-02	-3.74E-06	3.92E-06	0.9780
25 cm	8.26E-03	5.27E-02	1.60E-02	3.97E-02	-3.16E-06	3.31E-06	0.9779
40 cm	1.02E-02	5.79E-02	1.87E-02	4.61E-02	-3.72E-06	3.88E-06	0.9790
50 cm	9.27E-03	5.18E-02	1.93E-02	4.92E-02	-3.51E-06	3.65E-06	0.9807
130 cm	6.15E-03	3.81E-02	1.53E-02	3.68E-02	-2.32E-06	2.46E-06	0.9719
180 cm	7.10E-03	4.38E-02	1.60E-02	3.71E-02	-2.64E-06	2.78E-06	0.9756
250 cm	3.44E-03	2.36E-02	1.38E-02	3.58E-02	-1.48E-06	1.57E-06	0.9694
10 cm	2.52E-05	9.18E-05	1.82E-02	3.31E-02	-24.13E-06	2.40E-05	1.0018
25 cm	7.70E-02	3.11E-01	1.93E-02	3.86E-02	-8.876E-06	8.78E-06	1.0050
40 cm	1.04E-01	3.98E-01	2.20E-02	4.19E-02	-1.35E-05	1.35E-05	1.0000
50 cm	1.14E-01	5.97E-01	1.46E-02	1.55E-02	-3.70E-06	2.78E-06	1.1660
130 cm	1.19E-01	4.17E-01	2.08E-02	3.80E-02	-1.94E-05	1.94E-05	1.0012
180 cm	1.34E-01	4.82E-01	1.82E-02	3.28E-02	-1.74E-05	1.73E-05	1.0040
250 cm	7.35E-02	2.57E-01	1.92E-02	3.40E-02	-1.01E-05	9.99E-06	1.0031

Table 5. Factors of multiplication describing magnetic changes in hysteresis parameters after heating.

	Mrs	Ms	Hc	Hcr	IRM $_{-300\ mT}$	SIRM	S-ratio (Bloemendal et al.,1988)
10 cm	0.0028	0.0019	0.9333	0.6853	6.4519	6.1224	1.0243
25 cm	9.3220	5.9013	1.2063	0.9723	2.8089	2.6526	1.0277
40 cm	10.1961	6.8739	1.1765	0.9089	3.6290	3.4794	1.0215
50 cm	12.2977	11.5251	0.7565	0.3150	1.0541	0.7616	1.1889
130 cm	19.3496	10.9449	1.3595	1.0326	8.3621	7.8862	1.0301
180 cm	18.8732	11.0046	1.1375	0.8841	6.5909	6.2230	1.0291
250 cm	21.3663	10.8898	1.3913	0.9497	6.8243	6.3631	1.0348

On IRM acquisition curves and unmixing diagrams (Figure 29c), top samples (10 and 40 cm) demonstrate major coercivity component at 66.6 and 64.6 mT, whereas bottom samples (130 and 250 cm) show major coercivity component at 53.1 and 50 mT, indicating the influence of higher coercivity minerals in the top of the core. All samples illustrate the contribution of a high coercivity component, more pronounced in the 40 cm sample. S-ratio (Table 4) is comprised between 0.97 and 0.98 for the seven samples, indicating that magnetite dominates the magnetic signal despite the presence of high coercivity minerals.

FORC diagrams (Figure 29d) reveal peak central ridges >40 Am2/T2 between 0.01 and 0.05 T (Bc) for samples 10 and 40, and >60 Am2/T2 between 0.005 and 0.03 T for samples at 130 and 250 cm, characteristic of Pseudo single domain magnetite (PSD) magnetite. Sample 130 is characterized by a strong central positive ridge around the axis Bu = 0 with a main positive peak Bc ~0.03, which is characteristic of single domain (SD) particle behavior with low magnetostatic interactions between particles. This sample does not reveal stretching along the negative Bu axis, which would be a sign of superparamagnetic (SP) particles, and low magnetization in the vortex state and multi domain (MD) areas, confirming the dominance of SD particles in that sample. Samples at 10 and 40 cm are very similar and depict strong positive central ridges as well as a strong magnetization close to the 0 axis and a low magnetization in the vortex state. This enables us to assess the large dominance of SD particles with few interactions and with the probable presence of some MD and vortex states particles, but almost no SP particles, in both samples. Again, in the sample at 250 cm, the central ridge indicates that most particles are SD with some interactions; the lobes indicate vortex state particles, and the low magnetization values along the Bu axis indicate almost no MD and SP particles. Overall, the four samples have the characteristics of noninteracting SD detrital magnetite.

All samples on the King plot (King et al., 1983; Figure 29e) are located above the theoretical 0.2 μm limit, indicating small grains within the same core and between the four cores composing the stack, although magnetic susceptibility measurements were conducted on whole cores for cores 41GC, 04GC, and 40TC and split core for core 10GC. On a modified

Day plot (Day et al., 1977; Figure 29e), samples are all located within the vortex state range (Roberts et al., 2017) equivalent to the PSD (Dunlop, 2002), supporting the FORC results and confirming the relatively homogeneous magnetic grain size. All samples show lower Hcr/Hc after heating, indicating that the average population of grains is finer.

In summary, core 10GC (except for the top 70 cm) falls within the criteria for sediments likely to preserve past variation in RPI (King et al., 1983; Tauxe, 1993): the magnetic signal is strong and stable (MAD < 5°) and carried by low coercivity grains such as magnetite and/or titanomagnetite; the magnetic grain size falls within the SD and vortex state; the NRM, ARM, and IRM intensity variations are inferior to an order of magnitude; and finally, the inclination values vary around the GAD.

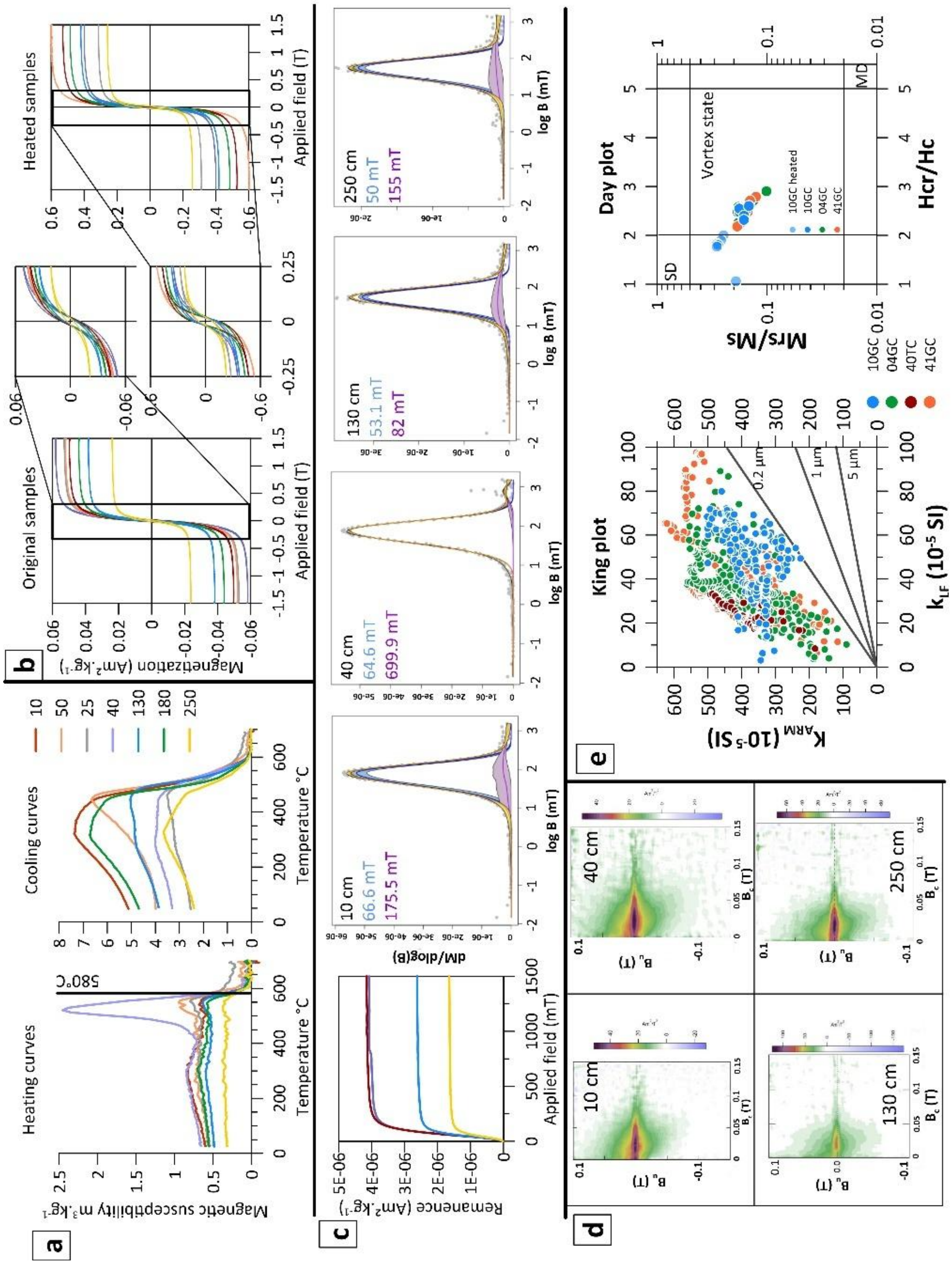

Figure 29. Rock magnetic analysis results. **(a)** Magnetic susceptibility heating and cooling thermomagnetic curves. **(b)** Hysteresis loops of samples before and after heating to 700°C. **(c)** Isothermal remanent magnetization (IRM) acquisition curves and IRM unmixing. **(d)** FORC diagrams. **(e)** Day & King plots.

1.5.4 RPI determination

The best normalizer (ARM or IRM) for RPI for core 10GC (Figure 30) was determined using both the slope (Tauxe et al., 1995; Valet & Meynadier, 1998) and ratio methods (Channell et al., 2000; Stoner et al., 2000; Tauxe & Wu, 1990). Both methods render similar results for both normalizers for the 71–265 cm interval and results that differ for the top 70 cm. The correlation coefficient (r^2) between the normalized signal and the normalizer was calculated for both ARM and IRM for the ratio method. r^2 values are non-significant but lower for the ARM than for the IRM for the whole core. Given the differences in mineralogy above and below 70 cm, r^2 was calculated for both intervals separately. For the top 70 cm, r^2 is lower for IRM than for ARM, contrary to the rest of the core where r^2 is lower for ARM than for IRM. r^2 calculated for the slope method is superior to 0.98 for 71–265 cm and comprised between 0.96 and 0.98 for the top 70 cm. ARM seems to be a better normalizer for the whole core except for the top 70 cm, but because of the uncertainty of that interval regarding RPI reliable recording, we decided not to take it into account and chose ARM as our preferred normalizer. Moreover, the slope method with ARM showed better agreement between the four cores than the slope method using IRM, and ARM shows lower r^2 with the ratio method for the four cores (Figure S4 in Supporting Information S1).

The normalized intensity derived from the slope method will be used hereafter in the stacking process and comparisons. Because of the similarity between the slope and ratio methods with both ARM and IRM, the core 10GC normalized intensity signal from 71 to 265 cm interval seems robust. Precaution should be taken when interpreting the normalized intensity for the top of the core (0–70 cm) because of the different magnetic mineralogy and differences between the 2 normalizers for the same method and differences between the 2 methods for the same normalizer. It is also the interval where the difference between the signals of the four cores is the largest (Figure 32). The discrepancy in the normalizers shows that the use of the same normalizer for the whole core cannot represent RPI very well when there are significant mineralogy variations throughout the core. However, because of the stacking process, it was important to keep consistency in the normalizers between the different cores, and we consider that it only affects the top part of the stack (0–70 cm).

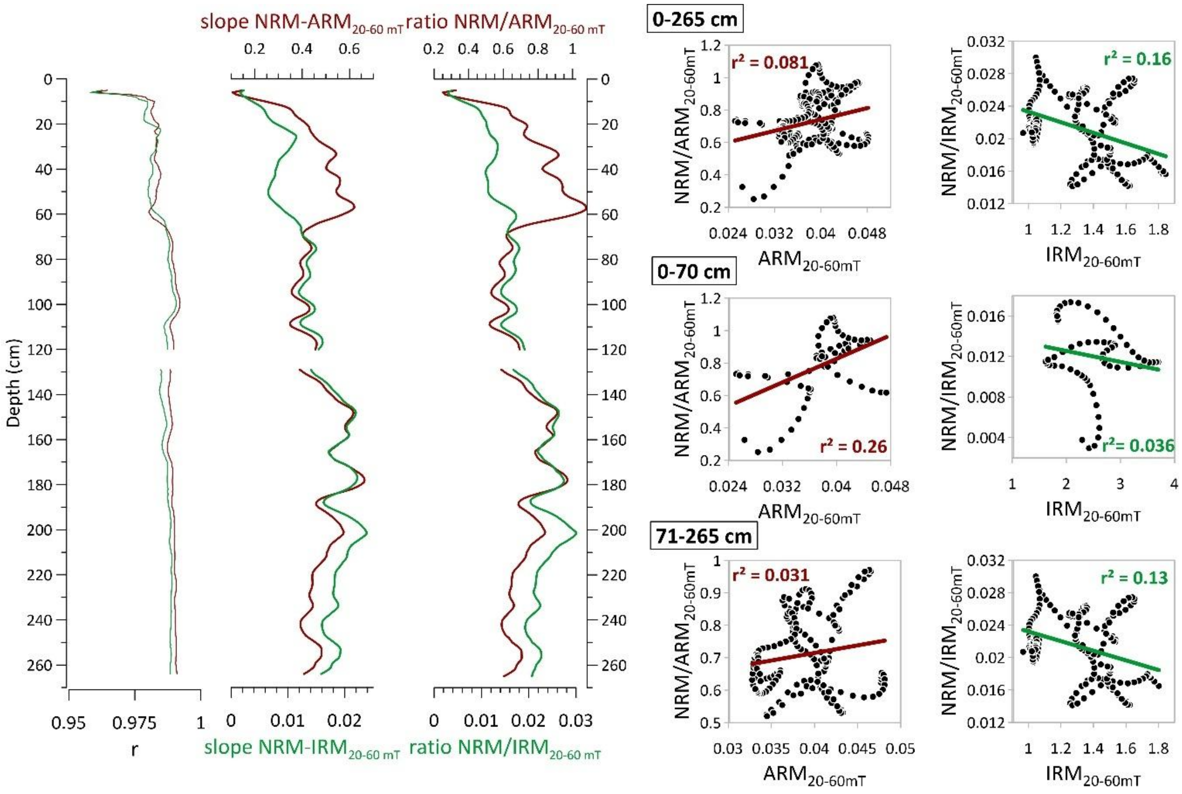

Figure 30. Determination of the 10GC relative paleointensity signal (20–60 mT). R: correlation coefficient for anhysteretic remanent magnetization (ARM) (red) and isothermal remanent magnetization (IRM) (green); profiles for slope method; profiles for ratio method. Determination coefficient r2 between the normalized signal and the normalizer for ARM (red) and IRM (green) for the whole core, core top (0–70 cm) and core bottom (71–265 cm).

1.5.5 Paleomagnetic stack

In Petermann Fjord, the Outer Fjord Splice (OFS) composed of three cores (40GC, 03PC, 03TC) places all the cores on a common depth scale, here called the Correlated Equivalent Depth (CED; Reilly et al., 2019). Using pXRF data, QAnalySeries software (QAS; Kotov & Pälike, 2018) was used to obtain the best fit between cores 10GC and the OFS. Because the cores were not measured with the same instrument, the Ti/Ca ratios were standardized using the mean and standard deviation on the depth interval 0–270 cm. This interval was chosen because of the length of core 10GC and the larger amplitude variations of the XRF signal at the bottom of the other cores. All cores being on the same depth scale are required for the stacking process. Correlation coefficients were calculated with QAS between all the Ti/Ca profiles (10GC, 40TC, 04GC, and 41GC) two by two (Table S4 in Supporting Information S1). PSV and RPI stacks were constructed following the approach of Reilly et al. (2018, 2019). Bin widths of 5 cm CED were used to calculate the Fisher mean of the directions (Fisher, 1953) with N being the number of cores contributing to the stack for each calculation, rather than the number of measurements in each bin. MAD values were converted to α95 following Khokhlov and Hulot (2016) and the uncertainty was propagated in the stacking process through 1,000 random sampling of the α95 distributions. Core 10GC declination values were rotated by 45° to match the declination of the previously created stack of the three other cores. Uncertainty was propagated suggesting a circular distribution on a sphere. Core 10GC depth conversion to the CED is presented in Figure 31 and stacking results are in Figure 32. Core 10GC Ti/ Ca profile presents a r^2 of 0.75 with the OFS Ti/Ca signal, and the Ti/Ca signals of the four cores on the same depth scale present correlation coefficients with each other varying between 0.69 and 0.94 (Figure 31b). The number of cores contributing to the stack is always >2, with the signal being the most reliable when four cores are contributing between 130 and 260 cm. All cores display similar variations. Core 10GC has the lowest value for the inclination record. The inclination displays high values >65° for the whole stack and >80° for several parts of the stack. At a very steep inclination, a small angular change can lead to large changes in declination (Reilly et al., 2019), explaining the large variability of the declination values. The declination values are therefore likely to be more reliable for the intervals where the inclination is shallower. Based on that assumption, we rotated the declination of core 10GC according to the other cores at the shallowest inclination intervals (∼190 cm), that is, by 45°. Prior to stacking, 10GC declinations values were also aligned between sections to avoid abrupt shifts at core section limits. For cores 40TC, 04GC, and 41GC, all sections were split along the same plane. In Figure 32, declination values are presented in a 0–360° range, so another 360° was added to core 10GC declination values to keep the variation amplitude between 0 and 360° and to compensate for the lack of azimuthal orientation. The low inclination at 190 cm is the most prominent feature and is well observed in the four cores. Moreover, the inclination variations in 10GC confirm the presence of two inclination features at 80 and 120 cm. Core 10GC inclination values are lower than the other cores in the intervals 190–220 cm and 240–260 cm. To minimize that difference, other XRF profile correlations were tried. Nonetheless, the initial correlation on the depth scale using the XRF profiles was used for several reasons: the correlation coefficient between the XRF profiles was higher, the alignment of the uncalibrated ages was the most linear (Figure S5 in Supporting Information S1) and more importantly, to keep the chronology independent of paleomagnetism at this point (would not have been the case with k_{LF} or PSV).

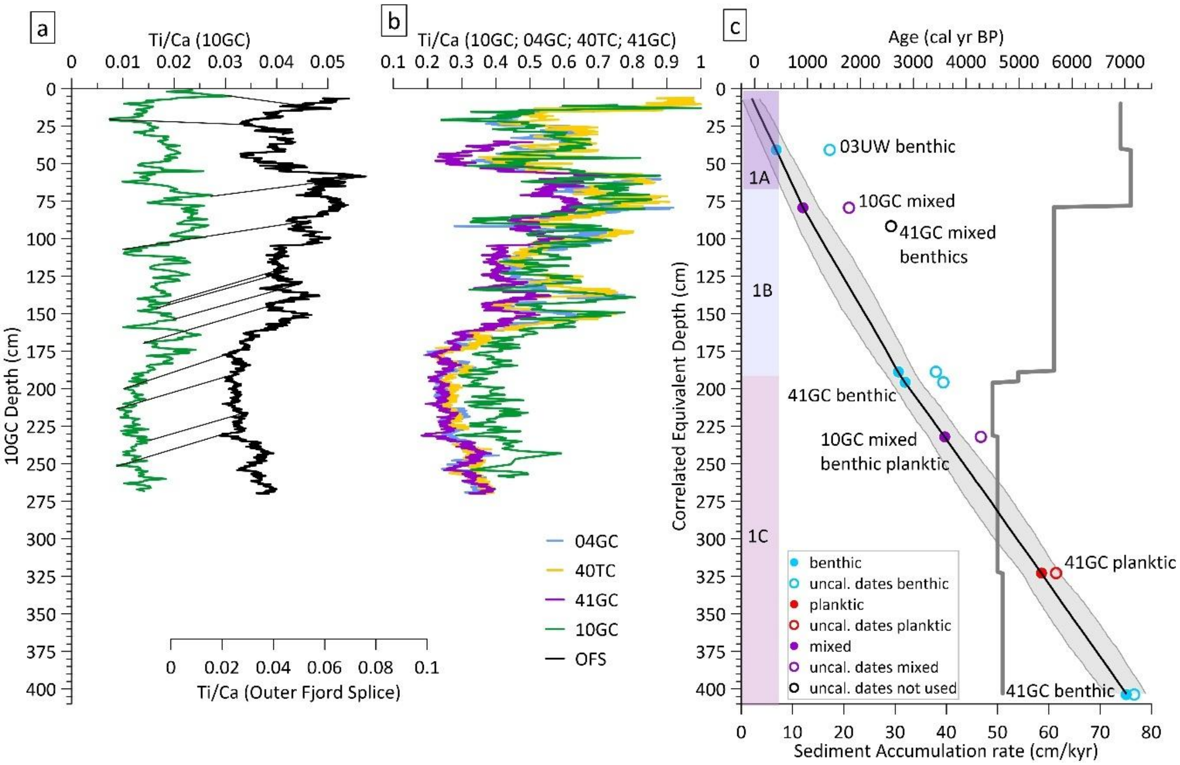

Figure 31. (a) Conversion of 10GC (independent depth, cm) to the Correlated Equivalent Depth (CED, cm) using Ti/Ca X-ray fluorescence (XRF) ratio from the outer fjord splice (OFS; 03PC, 03TC, 41GC). **(b)** Comparison of Ti/Ca XRF ratio of the four cores composing the stack (04GC, 41GC, 04TC, 10GC) on CED. **(c)** Age model and accumulation rates for Petermann stack using ^{14}C dates from cores 41GC, 03UW (Reilly et al., 2019) and 10GC (this study), Marine 20 calibration curve and ΔR = 430 ± 145 years. Red = planktic foraminifera, blue = benthic foraminifera, purple = mixed benthic and planktic, black = uncalibrated dates, white = date not used in the age model.

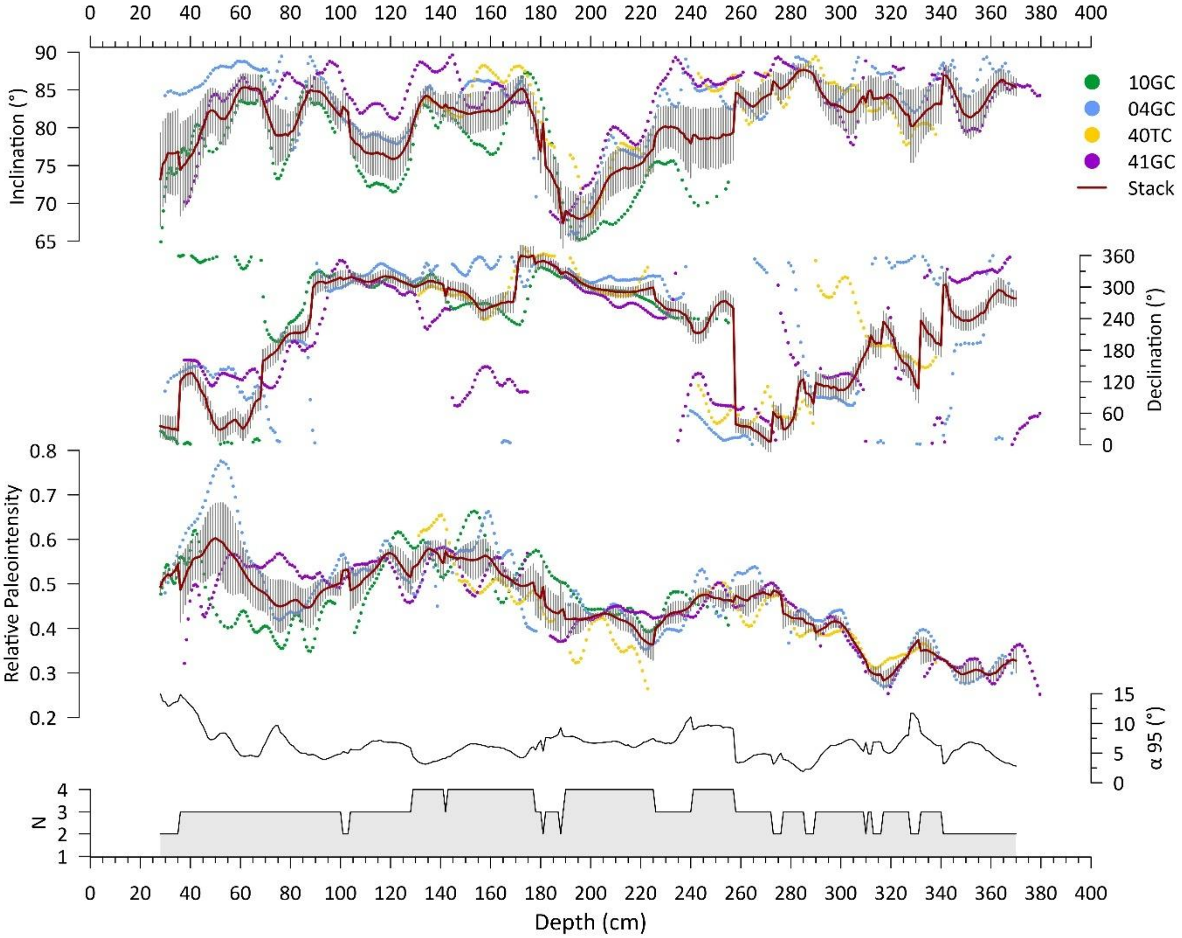

Figure 32. Petermann paleomagnetic secular variations stack: inclination, declination, relative paleointensity (RPI), angular difference (α95) and number of cores contributing to the stack (N).

1.5.6 Age model

The age model is presented in Figure 31. According to the proposed age model, the core 10GC spans the last 5 kyr, and the stack spans the last 7 kyr. Adding core 10GC to the previous stack (Reilly et al., 2019) reinforced the age model by adding two more ^{14}C dates (Figure 31). More precisely, it enabled us to refine the 200–320 cm (CED) interval, where ages were lacking, with the 10GC date (AWI#10208.1.1). Moreover, the addition of the 10GC age AWI#10207.1.1 justified the exclusion of the 41GC age ANU#17240. Indeed, that sample was considered too old because of its offset relative to a linear age-depth relationship.

For that sample, the uncalibrated age only is presented in Figure 31. The other ages are presented and discussed in Reilly et al. (2019). SAR in Petermann Fjord was calculated using the calibrated ages of the four cores on the CED and indicated three depth intervals of different SAR that correspond broadly to the three lithologic units: 75 cm/ka (0–80 cm), 60 cm/ka (80–190 cm), and 50 cm/ka (190–400 cm). SAR transitions are based on where the radiocarbon dates are located, which is likely an artifact and SAR changes more likely occurred at the lithologic boundaries.

1.5.7 PSV variations

To facilitate further comparisons with records from outside the Petermann Fjord, PSV from previously published records, all projected to the location of Petermann Fjord via their VGP paths (precise coordinates of 10GC), are displayed in Figures 33 and 34. Similar peaks and lows of inclination, declination and RPI can be seen in the different models and records. The records were chosen based on their location (Arctic, Northern Europe, northern North Atlantic, inside and outside of the TC projection surface) and their SAR and resolution (same order of magnitude as the Petermann stack). CALS10k.2 (Constable et al., 2016) and ARCH3k.1 (Donadini et al., 2009) data were obtained from the GEOMAGIA database (Brown et al., 2015).

The Petermann Fjord inclination stack shows good agreement with U1305 (Southern Greenland; Stoner et al., 2013), GREENICE (east Greenland-Iceland; Stoner et al., 2007), JPC15 (Chuckchi Sea; Lund et al., 2016) and core 204 from Baffin Bay (Caron et al., 2019) inclination record, although the shallow inclination feature at ~2.5 ka appears earlier in that record that could be consistent with age model uncertainty. Comparison with the recent global data model outputs pfm9k.2 model signals (Nilsson et al., 2022; Figure 33a) also shows significant similarities. In contrast, records like MD99-2220 from the St. Lawrence Estuary (St-Onge et al., 2003) and those from Northern Europe are fundamentally different. The shallow inclination feature is more pronounced as well at the coordinates of Petermann Fjord than at the original coordinates of the records (e.g., GREENICE; Reilly et al., 2023;

Stoner et al., 2007). The Petermann PSV stack, JPC15 Chukchi Sea record (Lund et al., 2016), and Baffin Bay record (Caron et al., 2019) are all located within the TC surface projection (70°N) but display variations similar to the records situated outside (U1305, GREENICE, north Karelian stack, Eastern Canadian stack, Lake le Boeuf). Inclination variations in the St-Lawrence Estuary (Barletta, St-Onge, Stoner, et al., 2010) at lower latitudes are similar to the variations in Northern Europe (North Karelian stack) but with a slight temporal offset. Similarities in the inclination variations can be observed between U1305, GREENICE, JPC15 and Petermann stack even though they are not all situated within the TC surface projection. The Petermann declination stack has similarities with other regional Arctic records, similar to inclination, though it is more subdued than those sites transferred to the Petermann location. The Petermann stack shows inclination similarity with the pfm9k.2 model with common key features at 1, 3.7, and 6 ka (underlined in Figure 33). The Petermann stack declination shows a decrease at 2.5 ka, which can be identified in the pfm9k.2 model, U1305, GREENICE and the North Karelian stack (Finland; Haltia-Hovi et al., 2010) and another decrease at 4.5 ka, which is less clear in individual Petermann records (Figure 32) and at other locations.

Comparison of paleointensity records shows that high intensities are observed at 0.8–1.2 ka (Eastern Canadian Stack ECS, Western Europe, U1305, models pfm9k.2 and CALS10k.2), 1.3–2.2 ka (Petermann stack, CALS10k.2, pfm9k.2, U1305) and 2–2.4 ka (Lake LeBoeuf, Western Europe, U1305, CALS10k.2, pfm9k.2). Low intensities are identified by other records for the same intervals: 0.8–1.2 ka (Petermann stack, Lake LeBoeuf, AMD2014-204casq), 1.3–2.2 ka (Western Europe, ECS, Lake LeBoeuf, AMD2014-204casq), 2–2.4 ka (Petermann stack), 4.8–5.3 ka (Petermann stack, CALS10k.2, pfm9k.2).

Correlation coefficient was calculated between the Petermann stack RPI signal and other records using the QAS software (Supporting Information S1). The Petermann RPI signal (Figure 34) has a higher correlation coefficient with the pfm9k.2 model (0.76) than with the CALS10k.2 model (0.57). It is interesting to underline that the RPI record from

U1305 has a higher correlation coefficient (0.77) with paleointensity (Virtual Axial Dipole Moment [VADM]) from European archeomagnetic data (VADM western Eurasia; Genevey et al., 2008) than with the Petermann RPI stack (0.68 for the median age, 0.287 for the min age and 0.612 for the max age).

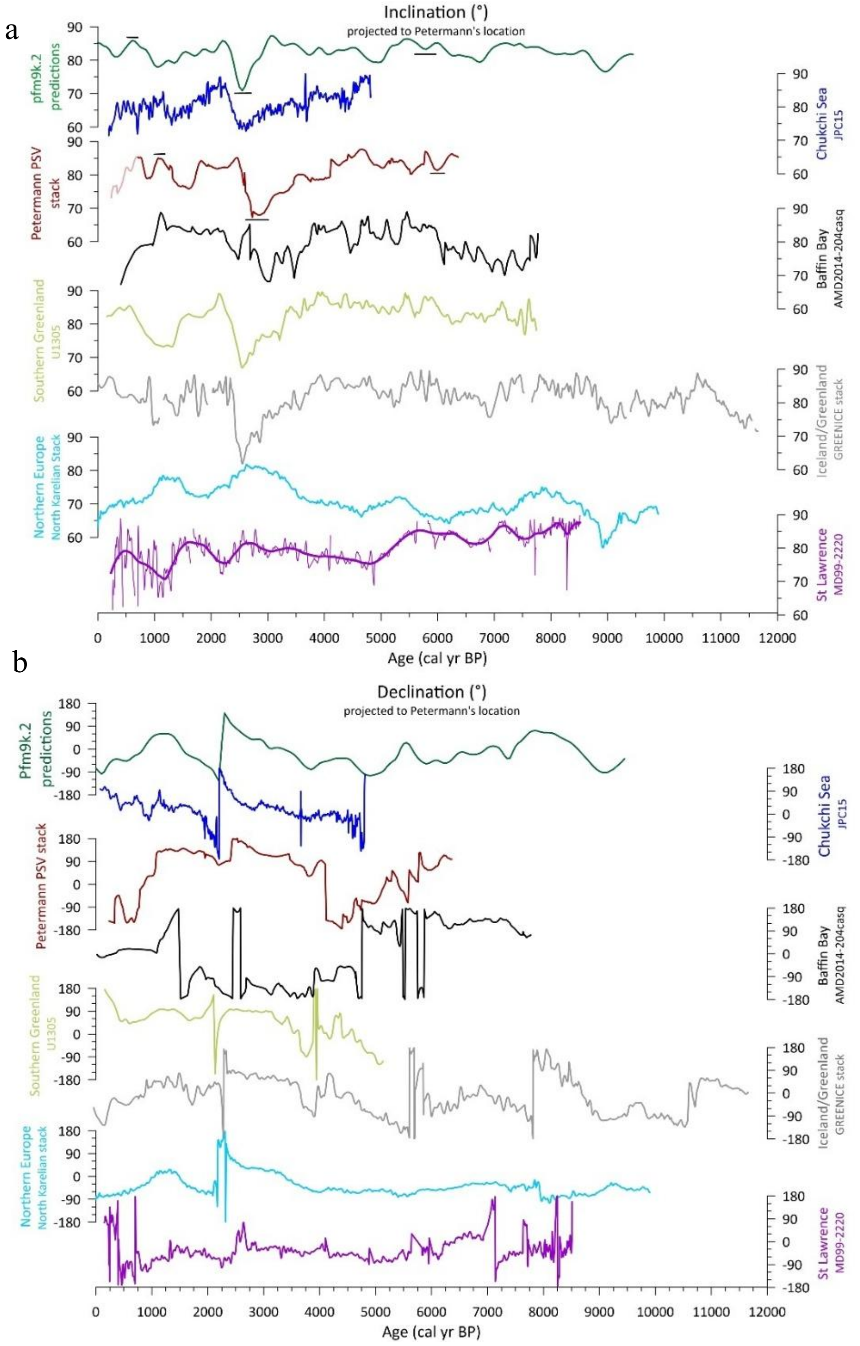

Figure 33. Comparison of inclination (a) and declination (b) profiles from different paleorecords: pfm9k.2 geomagnetic model (Nilsson et al., 2022), JPC15 (Lund et al., 2016), Petermann stack (this study), 204casq (Caron et al., 2019), U1305 (Stoner et al., 2013), GREENICE stack (Stoner et al., 2007), North Karelian stack (Haltia-Hovi et al., 2010), MD99-2220 (St-Onge et al., 2003). Key features (1, 3.7, and 6 ka) mentioned in the text are underlined in the figure.

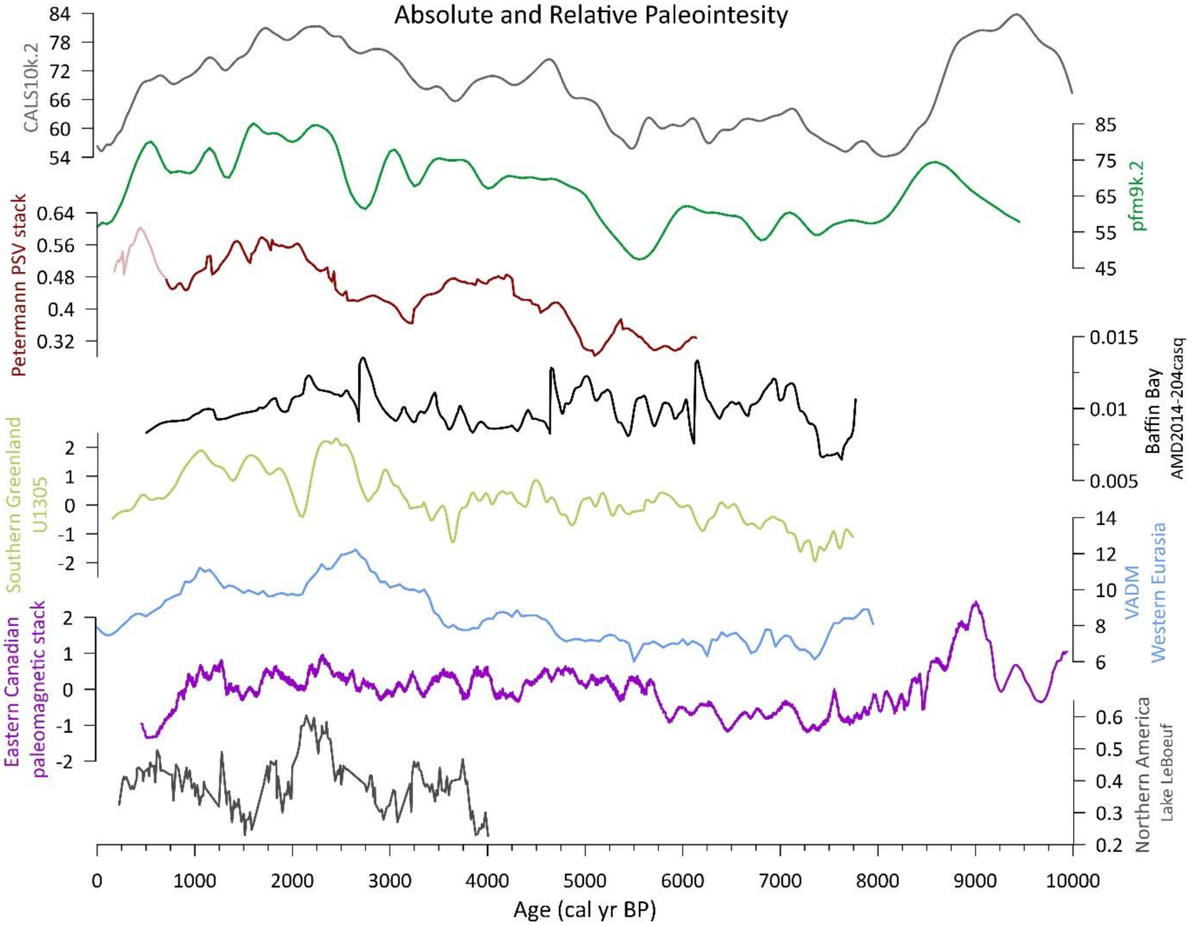

Figure 34. Comparison of absolute and relative paleointensities profiles for different paleorecords: CALS10k.2 (Constable et al., 2016) and pfm9k.2 geomagnetic models (Nilsson et al., 2022), Petermann stack (this study), 204casq (Baffin Bay relative paleointensity (RPI) record, Caron et al., 2019), U1305 (North Atlantic RPI record, Stoner et al., 2013), GREENICE stack (Northern North Atlantic RPI record, Stoner et al., 2007), North Karelian stack (lacustrine RPI record from Finnish lakes, Haltia-Hovi et al., 2010), Virtual Axial Dipole Moment, Western Eurasia (absolute paleointensity from archeological artifacts and volcanic products; Genevey et al., 2008), Eastern Canadian stack (St-Lawrence RPI record, Barletta, Channell, & Rochon, 2010), Lake LeBoeuf (lacustrine RPI record from North America, King et al., 1983).

1.6 DISCUSSION

1.6.1 Age model, magnetic lock-in depth and ΔR Variations

While there are broad similarities in the comparisons discussed in Section 1.5.6, we notice a systematic offset relative to the better understood chronologies of the region around Iceland (Hagen et al., 2020; Reilly et al., 2023; Stoner et al., 2007, 2013). For example, the Petermann Fjord record is systematically slightly older than the GREENICE record, which could be explained by either lock-in depth uncertainty or an underestimated ΔR (Figure 35).

In order to evaluate potential ΔR variation or magnetic lock-in depth, paleomagnetic tie points were chosen from the Petermann stack in comparison with the GREENICE stack (Stoner et al., 2013) to calculate the age of the magnetization. GREENICE was constructed with a large number of ^{14}C ages (44) and tephras and depicted very high SAR (>1 m/ka, up to 5 m/ka; Stoner et al., 2007). With such a high SAR, the temporal offset associated with any lock-in depth is probably very small (Reilly et al., 2023). The selected tie points (Table 5) were used to calculate the mean depth offset between the 2 curves, which was evaluated at 11 ± 3.6 cm and could be considered an estimate of the lock-in depth offset at Petermann Fjord. This value is consistent with other estimates, such as the similarly derived 12 cm estimate for site U1305 (Hagen et al., 2020; Stoner et al., 2013) and the ∼5–15 cm offset inferred from ^{10}Be data in lower accumulation rate cores (Simon et al., 2018; Suganuma et al., 2010). Using that value, the depth of the radiocarbon ages was adjusted (Table 6), and an updated age model was calculated to estimate the age of the magnetization (Figure 35b) following the approach of Stoner et al. (2013). The updated age model uses the same radiocarbon ages but with modified depth according to the offsets calculated in Tables 6 and 7.

An alternative explanation is that the offset between the magnetic age curve and the median radiocarbon age model actually represents uncertainty in the radiocarbon age model itself (specifically variation of the ΔR; Figure 35b). The age offset varies between 55 and

235 years, being lower at the top and higher toward the bottom of the core, with a mean of 181 years. The offset between the two curves is reasonable as the magnetic age curve is still comprised between the minimum and maximum of the initial age model, given the ±145 ΔR uncertainty used (Figure 35). Variation of the reservoir age is a viable hypothesis given that calibration curves are challenging to use in the Arctic because of a number of factors, such as seasonal sea ice, mixing of water masses of different ages and meltwater inputs, among others (e.g., Pearce et al., 2023). Centennial scale uncertainty in ΔR is not unexpected in this environment as the built-in Marine20 calibration curve reservoir effect is not expected to reflect larger scale variability in the polar ocean (Heaton et al., 2020), and Petermann Fjord is known to have variability in sea ice and ice-tongue extents over this time interval (Detlef et al., 2021; Jennings et al., 2022; Reilly et al., 2019).

Previous studies introduced the hypothesis of the drift of the non-dipole field (Yukutake, 1967), that is, that the main geomagnetic field PSV features drift mainly westward (Dumberry & Finlay, 2007; Korte & Constable, 2018; Nilsson et al., 2020). Other studies found that the hypothesis and the previously published data were rather unconvincing (e.g., Tauxe, 2010). Here, we observe the features in GREENICE with a delay compared to the Petermann stack, located more to the west, which would run counter to the westward drift hypothesis. Moreover, the age offset between the two records is rather constant when the literature suggests variation in the drift rate (Nilsson et al., 2020). In addition, the observed features in the Petermann stack are then observed in the Chukchi Sea (JPC15 record) and in Southern Greenland (GREENICE record, U1305; Figure 33), which lead us to rule out this hypothesis because it would mean drifting toward both eastward and westward directions.

While the uncertainty derived from calibration and ΔR uncertainty in our independent age model captures the magnetic age model derived from correlation to the very-well dated GREENICE record, it is difficult to distinguish if the systematic offset to the median radiocarbon age model is actually related to reasonable centennial scale ΔR uncertainty/variability, ~10 cm scale NRM lock-in depth, or a combination of both. These factors and timescales are challenging to assess and this level of uncertainty may be the limit to which we can resolve time in Petermann Fjord sediments.

Table 6. Paleomagnetic tie points used to modify the depth of the radiocarbon ages and to calculate the magnetic age depth model.

Tie point	Depth (cm)	Magnetic age (yr BP) based on GREENICE	Depth ^{14}C (cm)	Depth offset (cm)
D1	40	325	35	-5
D2	91	910	79	-12
I1	121	1400	109	-12
I2	133	1700	127	-6
I3	173	2260	160.5	-13
I4	196	2555	179	-17
I5	240	3560	230.5	-10
I6	352	5800	342	-10

Table 7. Calculation of the magnetic depth for the radiocarbon ages for the Petermann stack. The updated depths were used to construct the magnetic age model in the R package ‘rbacon’.

Age (cal yr BP)	CED (cm)	Magnetic depth (cm)
1421	40.87	51.87
1784	79.33	90.33
3427	188.72	199.72
3567	195.72	206.72
4277	232	243
5697	322.72	333.72
7174	403.72	414.72

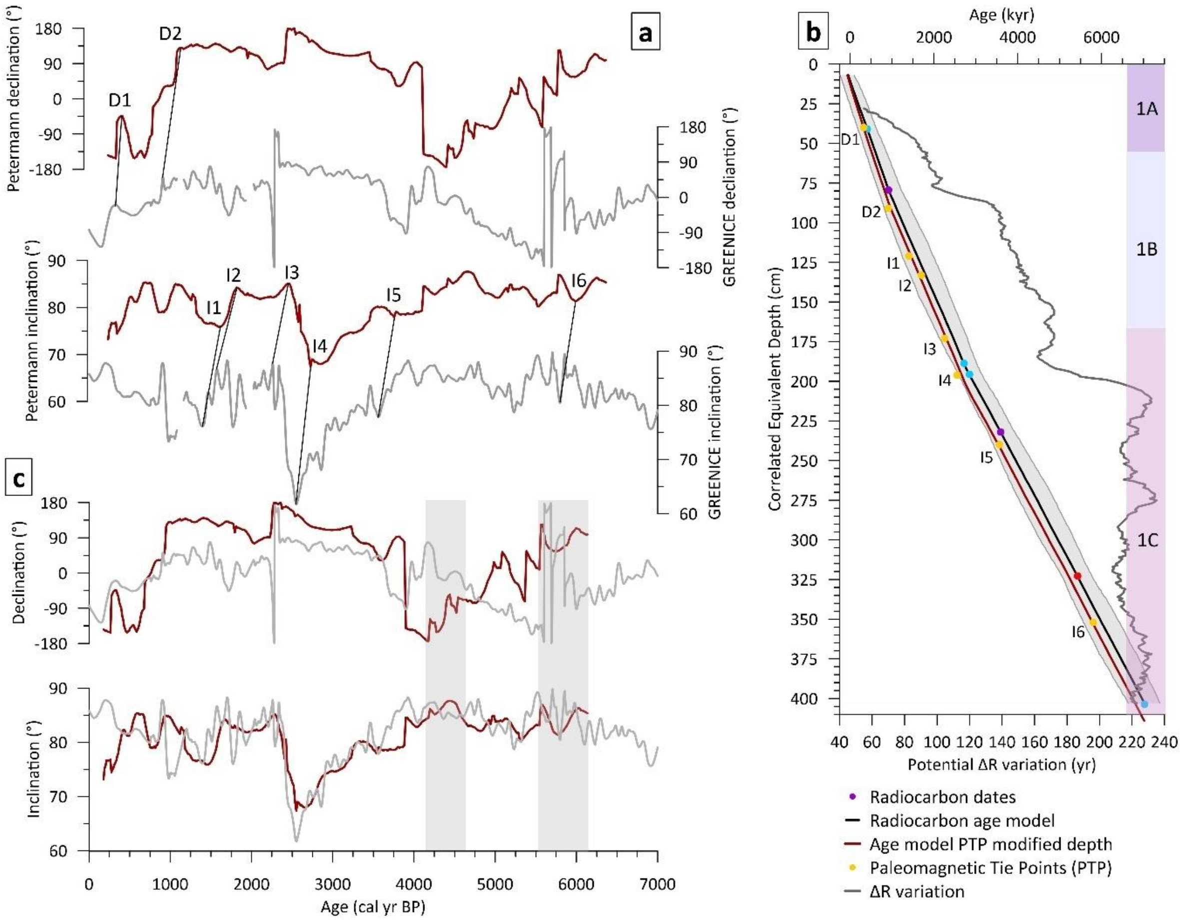

Figure 35. Construction of the magnetic age model for the Petermann stack. (a) Paleomagnetic tie points based on Petermann and GREENICE stack comparison. (b) Bayesian magnetic age-depth model for the Petermann stack. Yellow points = paleomagnetic tie points; red, blue, purple points = calibrated ^{14}C ages; red curve = magnetic age model; black curve radiocarbon age model; gray curve = ΔR variation. (c) GREENICE and Petermann Paleomagnetic Secular Variation stack comparisons based on the Bayesian magnetic age model. Gray shaded bars indicate inclination >85° where important declination changes should be interpreted carefully.

1.6.2 Paleointensity and paleomagnetic secular variations in the Arctic and the Northern North Atlantic

Because of the uncertain reliability of the top interval, we will focus on the reconstitution of the PSV and VGP for the time period 0.7–6.3 ka, where the RPI and PSV signals of the stack are robust and reliable. In Figure 34, RPI signals for the U1305 site and

Petermann stack are plotted with their magnetic age model (this study; Stoner et al., 2013), whereas other signals have an age model based on ^{14}C dates, which could explain some of the differences and offsets. Virtual Geomagnetic Poles (VGP) paleopositions (latitude, longitude) were calculated using the Mazaud Excel spreadsheet (Mazaud, 2005) from the Petermann PSV stack and are presented in Figure 36.

The directional PSV records discussed here are broadly similar and there is no clear relation between their variability and the position of these records relative to the surface projection of the TC. On the contrary, Arctic records are similar to northern North Atlantic records, whereas North American records are similar to European records, indicating that the TC is likely not the driver of these geomagnetic field feature variations. While declinations appear to be offsets between 3.7 and 6.1 ka (Figure 35c), angular (VGP or directions) differences between GREENICE and Petermann are between 0° and 25° for 0–6 ka and between 3° and 17° for the interval 3.7–6.1 ka, attesting to the similarities of these records. Because of the steep inclinations (~85°), the importance of declination is debatable. Petermann RPI signal is similar to both the projections from the pfm9k.2 model for the site location (Figure 34) and the pfm9k.2 global dipole moment (Figure 36). This is remarkable given the limited amount of data from the Arctic used to build pfm9k.2. A change in the variation is observed in the record around 3.5 ka (0.5–3.5 ka: latitude varies between 45° and 85°; 3.5–6.3 ka: latitude varies between 65° and 85°). The model from Nilsson et al. (2022) described a mode shift from a 1,300 years periodicity to a 650 years periodicity, at the same time (3.6 ka). Further studies are needed to test if there is a link between what is described by the model and what we observe in our record. The phase difference between the Europe and Petermann intensity profiles (Figure 36) is consistent with the idea of east-west hemispherical field asymmetry resulting from the intensification of geomagnetic flux lobes (Gallet et al., 2009; Nilsson et al., 2022; Stoner et al., 2013). The pfm9k.2 model describes two particular periods of strong east-west field asymmetry, the time period around 1600–300 BCE (2.3–3.6 ka BP) is observed in our RPI record as a low intensity and low latitude VGPs. Petermann intensity and Western Europe VADM seem to be out of phase, while RPI at site U1305 and VADM from western Eurasia are in phase.

Comparing current variations (International Geomagnetic Reference Field; IGRF curves; Figure 36) to the Holocene records demonstrates that the recent NMP migration (Livermore et al., 2020; NOAA, 2021) does not seem abnormal with regard to the whole Holocene, as the VGP reconstruction from the Petermann stack and U1305 record display larger amplitude variations than the IGRF curve describing the recent variations. Nonetheless, it must be kept in mind that the IGRF depicts the variation of the actual NMP (dip pole), whereas the Holocene records reconstitute the Virtual Geomagnetic Pole position (north pole for a geomagnetic dipole). Differences between our record and the ARCH3k.1 model may be explained by the bias of the model toward mid-latitude in the Northern Hemisphere. VGP latitude variations prior to 3.5 ka have a similar amplitude to the recent variations displayed by the IGRF curve, whereas the U1305 and Petermann stack curves between 0.5 and 3.5 ka show greater amplitude variations. More past VGP variation data would allow a more definitive determination of ongoing NMP changes. Moreover, given that the declination is almost always relative, it is rather difficult to ascertain that the variations we are describing are the true paleo pole positions. VGP migrated within the surface projection of the TC for most of the last 6.3 ka, except for a large swing above Europe in the time interval 2.53.4 ka, and a smaller one around 1.3–1.6 ka. Another VGP path variation outside the TC is observed around 5.5 ka from the Petermann stack and from the NBS stack (Caricchi et al., 2020) but with a slight temporal offset (5.6 ka). It fits within the change of frequencies established by Nilsson et al. (2022). The uncertainties of the variation for that event are within the projection surface of the TC. A VGP migration above Greenland, within the TC surface projection (Figure 36), is observed at 4.2–4.4 ka in the Petermann stack but not in other paleorecords.

The 2.5–3 ka time interval of VGP migration at low latitude over Europe happening at a time of high intensity over Europe is coherent to what can be observed in other records such as GREENICE (Stoner et al., 2007, 2013), U1305 (Stoner et al., 2013) and the NBS stack from the Barents Sea (Caricchi et al., 2020). These studies, among others, suggested that variations in intensity, possibly driven by either the morphology or intensity of geomagnetic flux lobes, could play a role in VGP migration as a VGP attractor (Amit et al., 2011). However, high intensities are visible in Petermann Fjord and south Greenland (U1305) at 1.5–2 ka, but according to the projections, the Petermann VGP is located above Northern Europe, although the intensity is lower in that area. This could be because declination data are not accurate. The high intensity over Europe (2.5–3 ka) is coeval with the Levantine Iron Age Anomaly (LIAA), which was an intense positive geomagnetic anomaly in the Levant and Mediterranean regions (e.g., Shaar et al., 2016, 2017) characterized by a VADM of almost twice today's axial dipole moment (Shaar et al., 2017). If that played a role in the VGP migration at that time, it is an indication that a very high intensity is required to have that influence and the intensity over the Arctic was not high enough for that. Converting the Petermann RPI values into VADM would enable comparison of the intensities and ascertain the hypothesis because relative variations are more complex to compare than absolute values, and it is hard to determine if the anomalies are positive or negative. Moreover, Livermore et al. (2020) showed that the elongation and weakening of the North American flux lobe between 1970 and 1999 was responsible for the recent NMP migration acceleration toward Siberia, indicating that the intensity and size of the flux lobes may have an impact on the migration of the NMP. According to the pfm9k.2 geomagnetic model (Nilsson et al., 2022), a decrease in the global dipole moment can coincide with local intensity anomalies. Our data could be consistent with that hypothesis, with the example of the LIAA (Figure 36), which takes place when the global dipole moment and the Petermann RPI are decreasing (pfm9k.2 model; Figure 36). It could be the same phenomenon responsible for the recent migration of the NMP toward Siberia, with the growth of the geomagnetic flux lobe in that region (Livermore et al., 2020) and the recent decrease of the dipole moment (Gubbins et al., 2006). Our work supports the link between VGP incursions to lower latitude and strong field asymmetries, and additional studies are needed to test the hypothesis of a link between the intensity oscillation periodicity derived from pfm9k.2, NMP migration and field asymmetries. As all these hypotheses are based on a record at a very high latitude, it is not enough to draw firm conclusions. This shows that despite the Petermann record's potential, we need more data, including absolute intensity and accurate declination values (cores need to be oriented during coring).

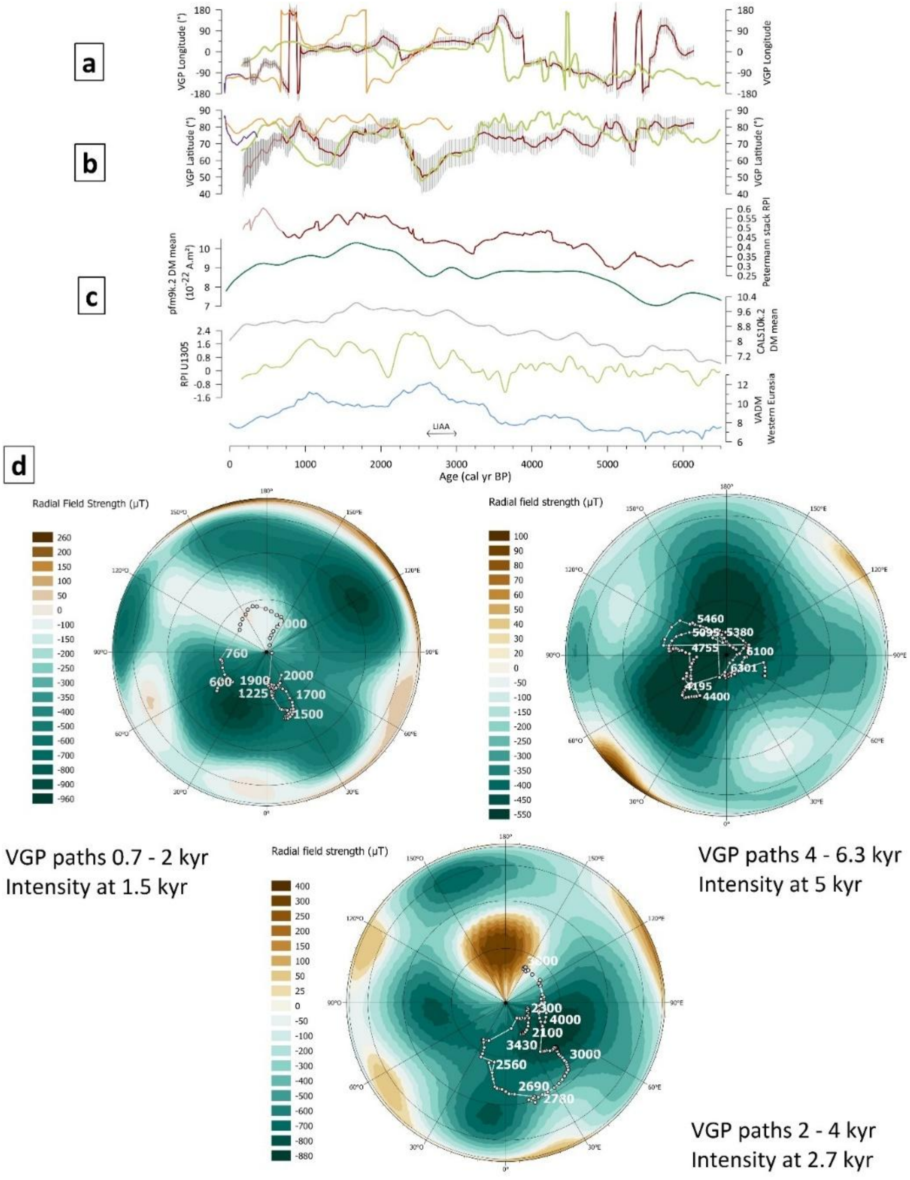

Figure 36. (**a**) Longitude variations of virtual geomagnetic poles based on the record's directional data. (**b**) Latitude variations of Virtual Geomagnetic Pole. Red = Petermann stack; purple = International Geomagnetic Reference Field; orange = ARCH3K.1; green = U1305. (**c**) Relative and absolute paleointensities curves in Petermann (red), Northern Atlantic (light green), over Europe (blue), and global dipole moment according to pfm9k.2 model (dark green, Nilsson et al., 2022) and CALS10k.2 model (gray, Constable et al., 2016). (**d**) Projection of VGP paths reconstructions based on Petermann stack directional data at time-intervals 0–2 ka; 2–4 ka; 4–6.3 ka overlaid on maps of radial field strength at Core Mantle Boundary from CALS10k.2 model respectively at 1.5, 2.7, 5 ka. The projections and maps were designed on ArcGIS.

1.7 CONCLUSIONS

This study illustrates that Petermann Fjord sediments record reproducible Holocene paleomagnetic secular variations that are similar throughout the Arctic. In particular, the shallow inclination at 2.5 ka is the most prominent feature of the last 7 kyr and is described in several records from the Arctic (Lund et al., 2016), the northern North Atlantic (Stoner et al., 2007, 2013) and geomagnetic model outputs (pfm9k.2; Nilsson et al., 2022). However, RPI variations in North Greenland are out-of-sync at millennial timescales with Southern Greenland, which looks more like European reconstructions (Stoner et al., 2013). There is good agreement between the Petermann RPI signal and local predictions and global dipole moment from the pfm9k.2 model, supporting the output of that model despite a lack of data from this region. These observations suggest that some directional PSV features that are well described and dated in several Arctic and northern North Atlantic records can be used as precise tie points to build Arctic chronologies where dating is challenging. This is consistent with findings from the very well-dated but lower resolution Lake Hajeren record from ~80°N in Svalbard (Ólafsdóttir et al., 2019). We recognize that the use of RPI at the centennial to millennial timescale, in this region, might require additional study to better understand its spatial pattern of variability.

Taken together, our results support the idea that Petermann Fjord is an excellent site to study PSV and RPI because it is located at a very high latitude with sediments characterized by high SAR capable of capturing the main millennial and secular variations of the Holocene. VGP reconstructions from this High Arctic geologic observatory display rapid NMP movements between the Eastern and Western Hemispheres, illustrating that recent variations of the historical periods are not abnormal and that such amplitudes of variations are consistent with Holocene variations and likely related to millennial scale dynamics of intensity anomalies of Northern Hemisphere Flux Lobes. Our work supports the hypothesis that magnetic field intensity variations linked to geomagnetic flux lobe variations could influence VGP migrations. Further full-vector paleomagnetic studies of high resolution and well-dated Arctic records will help improve our understanding of these dynamics, particularly conducting such studies on a larger scale to evaluate the extent of the influence of geomagnetic flux lobes.

1.8 DATA AVAILABILITY STATEMENT

Paleomagnetic data (core AMD1902-10GC and updated Petermann stack) are archived in the PANGAEA database (Girard et al., 2024a, 2024b). Maps were made using ArcGIS with IBCAO bathymetric data. Figures using Golden Software Grapher 21. The age model was made using the R Bacon package.

1.9 ACKNOWLEDGMENTS

We are grateful to the captain, officers, crew and scientists onboard both the CCGS Amundsen during the 2019 (Leg 2) ArcticNet expedition and the Swedish Icebreaker Oden during the Petermann 2015 Expedition for the recovery of the sediment cores used in this study. We also thank Quentin Beauvais (ISMER) for his help with the magnetic measurements; Dominique Lavallée (ISMER) for the grain size analysis; Nicole Sanderson (UQAM) for her help with the R package "rbacon"; Nicolas Van Nieuwenhove (UNB) for the foraminifera picking; and Arthur Bieber and Quentin Duboc (ISMER) for interesting discussions about the data. We also wish to thank the two anonymous reviewers and the editor Sonia Tikoo for their constructive comments that helped to improve the manuscripts. This research was funded by ArcticNet, the Canada Research Chair in Marine Geology from G. St-Onge, the Natural Sciences and Engineering Research Council of Canada (NSERC) through discovery grants to G. St-Onge and J.-C. Montero-Serrano, and the ISMER excellence scholarship and PBEEE-FRQNT scholarship n°334533 provided to J. Girard. J. Stoner and A. Jennings received support from the National Science Foundation Office of Polar Programs (awards 1417784 and 1418053).

1.10 REFERENCES

Amit, H., Korte, M., Aubert, J., Constable, C., & Hulot, G. (2011). The time-dependence of intense archeomagnetic flux patches. Journal of Geophysical Research, 116(B12), B12106. https://doi.org/10.1029/2011JB008538

Aurnou, J., Andreadis, S., Zhu, L., & Olson, P. (2003). Experiments on convection in Earth's core tangent cylinder. Earth and Planetary Science Letters, 212(1–2), 119–134. https://doi.org/10.1016/S0012-821X(03)00237-1

Banerjee, S. K., King, J., & Marvin, J. (1981). A rapid method for magnetic granulometry with applications to environmental studies. Geophysical Research Letters, 8(4), 333–336. https://doi.org/10.1029/GL008i004p00333

Barletta, F., St-Onge, G., Channell, J. E. T., & Rochon, A. (2010). Dating of Holocene western Canadian Arctic sediments by matching paleomagnetic secular variation to a geomagnetic field model. Quaternary Science Reviews, 29(17–18), 2315–2324. https://doi.org/10.1016/j. quascirev.2010.05.035

Barletta, F., St-Onge, G., Stoner, J. S., Lajeunesse, P., & Locat, J. (2010). A high-resolution Holocene paleomagnetic secular variation and relative paleointensity stack from eastern Canada. Earth and Planetary Science Letters, 298(1–2), 162–174. https://doi.org/10.1016/j.epsl.2010.07.038

Blaauw, M., & Christen, J. A. (2011). Flexible paleoclimate age-depth models using an autoregressive gamma process. Bayesian Analysis, 6(3), 457–474. https://doi.org/10.1214/11-BA618

Bloemendal, J., Lamb, B., & King, J. (1988). Paleoenvironmental implications of rock magnetic properties of late quaternary sediment cores from the eastern equatorial Atlantic. Paleoceanography, 3(1), 61–87. https://doi.org/10.1029/PA003i001p00061

Blott, S. J., & Pye, K. (2001). GRADISTAT: A grain size distribution and statistics package for the analysis of unconsolidated sediments. Earth Surface Processes and Landforms, 26(11), 1237–1248. https://doi.org/10.1002/esp.261

Bloxham, J., & Gubbins, D. (1985). The secular variation of Earth's magnetic field. Nature, 317(6040), 777–781. https://doi.org/10.1038/ 317777a0

Bloxham, J., Gubbins, D., & Jackson, A. (1989). Geomagnetic secular variation. Philosophical Transactions of the Royal Society of London. Series A: Mathematical, Physical and Engineering Sciences, 329(1606), 415–502.

Bloxham, J., & Jackson, A. (1992). Time-dependent mapping of the magnetic field at the core-mantle boundary. Journal of Geophysical Research, 97(B13), 19537–19563. https://doi.org/10.1029/92JB01591

Brown, M. C., Donadini, F., Korte, M., Nilsson, A., Korhonen, K., Lodge, A., et al. (2015). GEOMAGIA50.v3: 1. General structure and modifications to the archeological and volcanic database. Earth, Planets and Space, 67(1), 83. https://doi.org/10.1186/s40623-015-0232-0

Caricchi, C., Sagnotti, L., Campuzano, S. A., Lucchi, R. G., Macrì, P., Rebesco, M., & Camerlenghi, A. (2020). A refined age calibrated paleosecular variation and relative paleointensity stack for the NW Barents Sea: Implication for geomagnetic field behavior during the Holocene. Quaternary Science Reviews, 229, 106133. https://doi.org/10.1016/j.quascirev.2019.106133

Caron, M., St-Onge, G., Montero-Serrano, J.-C., Rochon, A., Georgiadis, E., Giraudeau, J., & Massé, G. (2019). Holocene chronostratigraphy of northeastern Baffin Bay based on radiocarbon and palaeomagnetic data. Boreas, 48(1), 147–165. https://doi.org/10.1111/bor.12346

Channell, J. E. T., Stoner, J. S., Hodell, D. A., & Charles, C. D. (2000). Geomagnetic paleointensity for the last 100 kyr from the sub-Antarctic South Atlantic: A tool for inter-hemispheric correlation. Earth and Planetary Science Letters, 175(1–2), 145–160. https://doi.org/10.1016/ S0012-821X(99)00285-X

Chulliat, A., Hulot, G., & Newitt, L. R. (2010). Magnetic flux expulsion from the core as a possible cause of the unusually large acceleration of the north magnetic pole during the 1990s. Journal of Geophysical Research, 115(B7), B07101. https://doi.org/10.1029/2009JB007143

Chulliat, A., Hulot, G., Newitt, L. R., & Orgeval, J.-J. (2010). What caused recent acceleration of the north magnetic pole drift? Eos, Transactions American Geophysical Union, 91(51), 501–502. https://doi.org/10.1029/2010EO510001

Constable, C., Korte, M., & Panovska, S. (2016). Persistent high paleosecular variation activity in southern hemisphere for at least 10 000 years. Earth and Planetary Science Letters, 453, 78–86. https://doi.org/10.1016/j.epsl.2016.08.015

Croudace, I. W. & Rothwell, R. G. (Eds.) (2015). Micro-XRF studies of sediment cores: Applications of a non-destructive tool for the environmental sciences (Vol. 17). Springer Netherlands. https://doi.org/10.1007/978-94-017-9849-5

Dankers, P. (1981). Relationship between median destructive field and remanent coercive forces for dispersed natural magnetite, titanomagnetite and hematite. Geophysical Journal International, 64(2), 447–461. https://doi.org/10.1111/j.1365-246X.1981.tb02676.x

Dawes, P. R., Frisch, T., Garde, A. A., Iannelli, T. R., Ineson, J. R., Jensen, S. M., et al. (2000). Kane Basin 1999: Mapping, stratigraphic studies and economic assessment of Precambrian and Lower Palaeozoic provinces in north-western Greenland. Geology of Greenland Survey Bulletin, 186, 11–28. https://doi.org/10.34194/ggub.v186.5211

Day, R., Fuller, M., & Schmidt, V. A. (1977). Hysteresis properties of titanomagnetites: Grain-size and compositional dependence. Physics of the Earth and Planetary Interiors, 13(4), 260–267. https://doi.org/10.1016/0031-9201(77)90108-X

Debret, M., Sebag, D., Desmet, M., Balsam, W., Copard, Y., Mourier, B., et al. (2011). Spectrocolorimetric interpretation of sedimentary dynamics: The new “Q7/4 diagram”. Earth-Science Reviews, 109(1–2), 1–19. https://doi.org/10.1016/j.earscirev.2011.07.002

Detlef, H., Reilly, B., Jennings, A., Mørk Jensen, M., O'Regan, M., Glasius, M., et al. (2021). Holocene sea-ice dynamics in Petermann Fjord in relation to ice tongue stability and Nares Strait ice arch formation. The Cryosphere, 15(9), 4357–4380. https://doi.org/10.5194/tc-15-4357-2021

Donadini, F., Korte, M., & Constable, C. G. (2009). Geomagnetic field for 0–3 ka: 1. New data sets for global modeling. Geochemistry, Geophysics, Geosystems, 10(6), 2008GC002295. https://doi.org/10.1029/2008GC002295

Dumberry, M., & Finlay, C. C. (2007). Eastward and westward drift of the Earth's magnetic field for the last three millennia. Earth and Planetary Science Letters, 254(1–2), 146–157. https://doi.org/10.1016/j.epsl.2006.11.026

Dunlop, D. J. (2002). Theory and application of the Day plot (Mrs/Ms versus Hcr/Hc) 1. Theoretical curves and tests using titanomagnetite data. Journal of Geophysical Research, 107(B3), EPM4-1. https://doi.org/10.1029/2001JB000486

Dunlop, D. J., & Ozdemir, O. (2007). Magnetization in rocks and minerals. In Geomagnetism, treatise on geophysics (Vol. 5, pp. 277–336). Elsevier. G. Scubert. https://doi.org/10.1016/b978-044452748-6/00093-6

Fisher, R. (1953). Dispersion on a sphere. Proceedings of the Royal Society A: Mathematical, Physical and Engineering Sciences, 217(1130), 295–305. https://doi.org/10.1098/rspa.1953.0064

Froelich, P. N., Klinkhammer, G. P., Bender, M. L., Luedtke, N. A., Heath, G. R., Cullen, D., et al. (1979). Early oxidation of organic matter in pelagic sediments of the eastern equatorial Atlantic: Suhoxic diagenesis. Geochimica et Cosmochimica Acta, 43(7), 1075–1090. https://doi.org/ 10.1016/0016-7037(79)90095-4

Gallet, Y., Hulot, G., Chulliat, A., & Genevey, A. (2009). Geomagnetic field hemispheric asymmetry and archeomagnetic jerks. Earth and Planetary Science Letters, 284(1–2), 179–186. https://doi.org/10.1016/j.epsl.2009.04.028

Gauss, C. F. (1833). Intensitas vis magneticae terrestris ad mensuram absolutam revocata.

Genevey, A., Gallet, Y., Constable, C. G., Korte, M., & Hulot, G. (2008). ArcheoInt: An upgraded compilation of geomagnetic field intensity data for the past ten millennia and its application to the recovery of the past dipole moment: Geomagnetic field intensity data compilation. Geochemistry, Geophysics, Geosystems, 9(4), n/a. https://doi.org/10.1029/2007GC001881

Girard, J., Reilly, B. T., St-Onge, G., Lagroix, F., Montero-Serrano, J.-C., Stoner, J., & Jennings, A. E. (2024a). Paleomagnetic data (inclination, declination, relative paleointensity) in sediment core AMD1902-10GC from Petermann Fjord (Nares Strait, Northern Greenland) [Dataset]. Retrieved from https://doi.pangaea.de/10.1594/PANGAEA.971852

Girard, J., Reilly, B. T., St-Onge, G., Lagroix, F., Montero-Serrano, J.-C., Stoner, J., & Jennings, A. E. (2024b). Updated paleomagnetic Petermann stack (inclination, declination, relative paleointensity, Virtual Geomagnetic Pole) from Petermann Fjord (Nares Strait, Northern Greenland) [Dataset]. Retrieved from https://doi.pangaea.de/10.1594/PANGAEA.971851

Grobe, H. (1987). A simple method for the determination of Ice-Rafted Debris in sediment cores. Polarforschung, 57, 123–126.

Gubbins, D. (2008). Geomagnetic reversals. Nature, 452(7184), 165–167. https://doi.org/10.1038/452165a

Gubbins, D., Jones, A. L., & Finlay, C. C. (2006). Fall in Earth's magnetic field is erratic. Science, 312(5775), 900–902. https://doi.org/10.1126/ science.1124855

Hagen, C. J., Reilly, B. T., Stoner, J. S., & Creveling, J. R. (2020). Dynamic time warping of palaeomagnetic secular variation data. Geophysical Journal International, 221(1), 706–721. https://doi.org/10.1093/gji/ggaa004

Haines, G. V., & Newitt, L. R. (1997). The Canadian geomagnetic reference field 1995. Journal of Geomagnetism and Geoelectricity, 49(2), 317336. https://doi.org/10.5636/jgg.49.317

Haltia-Hovi, E., Nowaczyk, N., & Saarinen, T. (2010). Holocene palaeomagnetic secular variation recorded in multiple lake sediment cores from eastern Finland. Geophysical Journal International, 180(2), 609–622. https://doi.org/10.1111/j.1365-246X.2009.04456.x

Harrison, R. J., & Feinberg, J. M. (2008). FORCinel: An improved algorithm for calculating first-order reversal curve distributions using locally weighted regression smoothing: FORCinel algorithm. Geochemistry, Geophysics, Geosystems, 9(5), n /a. https://doi.org/10.1029/ 2008GC001987

Heaton, T. J., Köhler, P., Butzin, M., Bard, E., Reimer, R. W., Austin, W. E. N., et al. (2020). Marine20—The marine radiocarbon age calibration curve (0–55,000 cal BP). Radiocarbon, 62(4), 779–820. https://doi.org/10.1017/RDC.2020.68

Heuzé, C., Wåhlin, A., Johnson, H. L., & Münchow, A. (2017). Pathways of meltwater export from Petermann Glacier, Greenland. Journal of Physical Oceanography, 47(2), 405–418. https://doi.org/10.1175/JPO-D-16-0161.1

Hogan, K. A., Jakobsson, M., Mayer, L., Reilly, B. T., Jennings, A. E., Stoner, J. S., et al. (2020). Glacial sedimentation, fluxes and erosion rates associated with ice retreat in Petermann Fjord and Nares Strait, north-west Greenland. The Cryosphere, 14(1), 261–286. https://doi.org/10. 5194/tc-14-261-2020

Hollerbach, R., & Jones, C. (1993). Influence of the Earth's inner core on geomagnetic fluctuations and reversals. Nature, 365(6446), 541–543. https://doi.org/10.1038/365541a0

Hu, S., Appel, E., Hoffmann, V., Schmahl, W. W., & Wang, S. (1998). Gyromagnetic remanence acquired by greigite (Fe3S4) during static threeaxis alternating field demagnetization: GRM acquired by greigite. Geophysical Journal International, 134(3), 831–842. https://doi.org/10. 1046/j.1365-246x.1998.00627.x

Hulot, G., Eymin, C., Langlais, B., Mandea, M., & Olsen, N. (2002). Small-scale structure of the geodynamo inferred from Oersted and Magsat satellite data. Nature, 416(6881), 620–623. https://doi.org/10.1038/416620a

Jackson, A., Jonkers, A. R. T., & Walker, M. R. (2000). Four centuries of geomagnetic secular variation from historical records. Philosophical Transactions of the Royal Society of London. Series A: Mathematical, Physical and Engineering Sciences, 358(1768), 957–990. https://doi.org/ 10.1098/rsta.2000.0569

Jakobsson, M., Hogan, K. A., Mayer, L. A., Mix, A., Jennings, A., Stoner, J., et al. (2018). The Holocene retreat dynamics and stability of Petermann Glacier in northwest Greenland. Nature Communications, 9(1), 2104. https://doi.org/10.1038/s41467-018-04573-2

Jakobsson, M., Mayer, L. A., Bringensparr, C., Castro, C. F., Mohammad, R., Johnson, P., et al. (2020). The International Bathymetric Chart of the Arctic Ocean version 4.0. Scientific Data, 7(1), 176. https://doi.org/10.1038/s41597-020-0520-9

Jennings, A. E., Reilly, B., Andrews, J., Hogan, K., Walczak, M., Jakobsson, M., et al. (2022). Modern and early Holocene ice shelf sediment facies from Petermann Fjord and northern Nares Strait, northwest Greenland. Quaternary Science Reviews, 283, 107460. https://doi.org/10. 1016/j.quascirev.2022.107460

Jennings, A. E., Seidenkrantz, M.-S., & Knudsen, K. L. (2020). Glomulina oculus, new calcareous foraminiferal species from the High Arctic: A potential indicator of a nearby marine-terminating glacier. Journal of Foraminiferal Research, 50(2), 219–234. https://doi.org/10.2113/gsjfr. 52.2.219

Johnson, H. L., Münchow, A., Falkner, K. K., & Melling, H. (2011). Ocean circulation and properties in Petermann Fjord, Greenland. Journal of Geophysical Research, 116(C1), C01003. https://doi.org/10.1029/2010JC006519

Khokhlov, A., & Hulot, G. (2016). Principal component analysis of palaeomagnetic directions: Converting a Maximum Angular Deviation (MAD) into an α95 angle. Geophysical Journal International, 204(1), 274–291. https://doi.org/10.1093/gji/ggv451

King, J. W., Banerjee, S. K., & Marvin, J. (1983). A new rock-magnetic approach to selecting sediments for geomagnetic paleointensity studies: Application to paleointensity for the last 4000 years. Journal of Geophysical Research, 88(B7), 5911–5921. https://doi.org/10.1029/ JB088iB07p05911

King, J. W., Banerjee, S. K., Marvin, J., & Özdemir, Ö. (1982). A comparison of different magnetic methods for determining the relative grain size of magnetite in natural materials: Some results from lake sediments. Earth and Planetary Science Letters, 59(2), 404–419. https://doi.org/10. 1016/0012-821X(82)90142-X

Kirschvink, J. L. (1980). The least-squares line and plane and the analysis of palaeomagnetic data. Geophysical Journal International, 62(3), 699718. https://doi.org/10.1111/j.1365-246X.1980.tb02601.x

Korte, M., & Constable, C. G. (2018). Archeomagnetic intensity spikes: Global or regional geomagnetic field features? Frontiers in Earth Science, 6, 17. https://doi.org/10.3389/feart.2018.00017

Kotov, S., & Pälike, H. (2018). QAnalySeries – A cross-platform time series tuning and analysis tool. ESS Open Archive. https://doi.org/10.1002/ essoar.10500226.1

Lawrence, K. P., Tauxe, L., Staudigel, H., Constable, C. G., Koppers, A., McIntosh, W., & Johnson, C. L. (2009). Paleomagnetic field properties at high southern latitude. Geochemistry, Geophysics, Geosystems, 10(1), Q01005. https://doi.org/10.1029/2008GC002072

Lévesque, Y., St-Onge, G., Lajeunesse, P., Desiage, P., & Brouard, E. (2020). Defining the maximum extent of the Laurentide Ice Sheet in Home Bay (eastern Arctic Canada) during the Last Glacial episode. Boreas, 49(1), 52–70. https://doi.org/10.1111/bor.12415

Livermore, P. W., Finlay, C. C., & Bayliff, M. (2020). Recent north magnetic pole acceleration towards Siberia caused by flux lobe elongation. Nature Geoscience, 13(5), 387–391. https://doi.org/10.1038/s41561-020-0570-9

Lund, S., Keigwin, L., & Darby, D. (2016). Character of Holocene paleomagnetic secular variation in the tangent cylinder: Evidence from the Chukchi Sea. Physics of the Earth and Planetary Interiors, 256, 49–58. https://doi.org/10.1016/j.pepi.2016.03.005

Maxbauer, D. P., Feinberg, J. M., & Fox, D. L. (2016). MAX UnMix: A web application for unmixing magnetic coercivity distributions. Computers & Geosciences, 95, 140–145. https://doi.org/10.1016/j.cageo.2016.07.009

Mazaud, A. (2005). User-friendly software for vector analysis of the magnetization of long sediment cores: Software for vector analysis. Geochemistry, Geophysics, Geosystems, 6(12), n/a. https://doi.org/10.1029/2005GC001036

Montero-Serrano, J.-C., & Brossard, J. (2019). Cruise report: Collecting sedimentary sequences and plankton samples in the continental margins from the eastern Canadian Arctic Archipelago. [Cruise Report] (p. 22). Münchow, A., Falkner, K. K., Melling, H., Rabe, B., & Johnson, H. L. (2011). Ocean warming of Nares Strait bottom waters off northwest Greenland. 2003-2009. Oceanography, 24(3), 114–123. https://doi.org/10.5670/oceanog.2011.62

Münchow, A., Padman, L., Washam, P., & Nicholls, K. (2016). The Ice Shelf of Petermann Gletscher, North Greenland, and its connection to the Arctic and Atlantic Oceans. Oceanography, 29(4), 84–95. https://doi.org/10.5670/oceanog.2016.101

National Centers for Environmental Information. (2022). State of the geomagnetic field 2022. https://doi.org/10.25923/8R5D-FJ70

National Centers for Environmental Information (U.S.). (2023). State of the geomagnetic field 2023. https://doi.org/10.25923/CWW1-SC35

Newitt, L. R., Mandea, M., McKee, L. A., & Orgeval, J.-J. (2002). Recent acceleration of the north magnetic pole linked to magnetic jerks. Eos, Transactions American Geophysical Union, 83(35), 381–389. https://doi.org/10.1029/2002EO000276

Nilsson, A., Suttie, N., Korte, M., Holme, R., & Hill, M. (2020). Persistent westward drift of the geomagnetic field at the core–mantle boundary linked to recurrent high-latitude weak/reverse flux patches. Geophysical Journal International, 222(2), 1423–1432. https://doi.org/10.1093/gji/ ggaa249

Nilsson, A., Suttie, N., Stoner, J. S., & Muscheler, R. (2022). Recurrent ancient geomagnetic field anomalies shed light on future evolution of the South Atlantic Anomaly. Proceedings of the National Academy of Sciences, 119(24), e2200749119. https://doi.org/10.1073/pnas.2200749119

NOAA. (2021). State of the geomagnetic field. WMM Annual Report, 13.

Ólafsdóttir, S., Reilly, B. T., Bakke, J., Stoner, J. S., Gjerde, M., & Van Der Bilt, W. G. M. (2019). Holocene paleomagnetic secular variation (PSV) near 80° N, Northwest Spitsbergen, Svalbard: Implications for evaluating High Arctic sediment chronologies. Quaternary Science Reviews, 210, 90–102. https://doi.org/10.1016/j.quascirev.2019.03.003

Olsen, N., & Mandea, M. (2007). Will the magnetic North Pole move to Siberia? Eos, Transactions American Geophysical Union, 88(29), 293. https://doi.org/10.1029/2007EO290001

Olson, P., & Aurnou, J. (1999). A polar vortex in the Earth's core. Nature, 402(6758), 170–173. https://doi.org/10.1038/46017 Pearce, C., Özdemir, K. S., Forchhammer Mathiasen, R., Detlef, H., & Olsen, J. (2023). The marine reservoir age of Greenland coastal waters. Geochronology, 5(2), 451–465. https://doi.org/10.5194/gchron-5-451-2023

Philippe, É. G. H., Valet, J., St-Onge, G., & Thevarasan, A. (2018). Are paleomagnetic records from U-channels appropriate for studies of reversals and excursions? Geochemistry, Geophysics, Geosystems, 19(11), 4130–4142. https://doi.org/10.1029/2018GC007803

Pieńkowski, A. J., Coulthard, R. D., & Furze, M. F. A. (2022). Revised marine reservoir offset (ΔR) values for molluscs and marine mammals from Arctic North America. Boreas, 52(2), 145–167. https://doi.org/10.1111/bor.12606

Reilly, B. T., Stoner, J. S., Hatfield, R. G., Abbott, M. B., Marchetti, D. W., Larsen, D. J., et al. (2018). Regionally consistent Western North America paleomagnetic directions from 15 to 35 ka: Assessing chronology and uncertainty with paleosecular variation (PSV) stratigraphy. Quaternary Science Reviews, 201, 186–205. https://doi.org/10.1016/j.quascirev.2018.10.016

Reilly, B. T., Stoner, J. S., Mix, A. C., Walczak, M. H., Jennings, A., Jakobsson, M., et al. (2019). Holocene break-up and reestablishment of the Petermann Ice Tongue, Northwest Greenland. Quaternary Science Reviews, 218, 322–342. https://doi.org/10.1016/j.quascirev.2019.06.023

Reilly, B. T., Stoner, J. S., Ólafsdóttir, S., Jennings, A., Hatfield, R., Kristjánsdóttir, G. B., & Geirsdóttir, Á. (2023). The amplitude and timescales of 0–15 ka paleomagnetic secular variation in the Northern North Atlantic. Journal of Geophysical Research: Solid Earth, 128(6), e2023JB026891. https://doi.org/10.1029/2023JB026891

Roberts, A. P., Almeida, T., Church, N. S., Harrison, R. J., Heslop, D., Li, Y., et al. (2017). Resolving the origin of pseudo-single domain magnetic behavior. Journal of Geophysical Research: Solid Earth, 122(12), 9534–9558. https://doi.org/10.1002/2017JB014860

Roberts, A. P., Heslop, D., Zhao, X., Oda, H., Egli, R., Harrison, R. J., et al. (2022). Unlocking information about fine magnetic particle assemblages from first-order reversal curve diagrams: Recent advances. Earth-Science Reviews, 227, 103950. https://doi.org/10.1016/j.earscirev. 2022.103950

Roberts, A. P., Hu, P., Harrison, R. J., Heslop, D., Muxworthy, A. R., Oda, H., et al. (2019). Domain state diagnosis in rock magnetism: Evaluation of potential alternatives to the day diagram. Journal of Geophysical Research: Solid Earth, 124(6), 5286–5314. https://doi.org/10.1029/ 2018JB017049 Ross, J. C. (1834). III. On the position of the north magnetic pole. The Royal Society, 124, 47–52. https://doi.org/10.1098/rstl.1834.0005

Shaar, R., Tauxe, L., Goguitchaichvili, A., Devidze, M., & Licheli, V. (2017). Further evidence of the Levantine Iron Age geomagnetic anomaly from Georgian pottery. Geophysical Research Letters, 44(5), 2229–2236. https://doi.org/10.1002/2016GL071494

Shaar, R., Tauxe, L., Ron, H., Ebert, Y., Zuckerman, S., Finkelstein, I., & Agnon, A. (2016). Large geomagnetic field anomalies revealed in Bronze to Iron Age archeomagnetic data from Tel Megiddo and Tel Hazor, Israel. Earth and Planetary Science Letters, 442, 173–185. https:// doi.org/10.1016/j.epsl.2016.02.038

Simon, Q., Bourlès, D. L., Thouveny, N., Horng, C.-S., Valet, J.-P., Bassinot, F., & Choy, S. (2018). Cosmogenic signature of geomagnetic reversals and excursions from the Réunion event to the Matuyama–Brunhes transition (0.7–2.14 Ma interval). Earth and Planetary Science Letters, 482, 510–524. https://doi.org/10.1016/j.epsl.2017.11.021

Simon, Q., St-Onge, G., & Hillaire-Marcel, C. (2012). Late Quaternary chronostratigraphic framework of deep Baffin Bay glaciomarine sediments from high-resolution paleomagnetic data. Geochemistry, Geophysics, Geosystems, 13(11), 2012GC004272. https://doi.org/10.1029/ 2012GC004272

Simon, Q., Thouveny, N., Bourlès, D. L., Nuttin, L., Hillaire-Marcel, C., & St-Onge, G. (2016). Authigenic 10Be/9Be ratios and 10Be-fluxes (230Thxs-normalized) in central Baffin Bay sediments during the last glacial cycle: Paleoenvironmental implications. Quaternary Science Reviews, 140, 142–162. https://doi.org/10.1016/j.quascirev.2016.03.027

Stoner, J. S., Channell, J. E. T., & Hillaire-Marcel, C. (1995). Late Pleistocene relative geomagnetic paleointensity from the deep Labrador Sea: Regional and global correlations. Earth and Planetary Science Letters, 134(3–4), 237–252. https://doi.org/10.1016/0012-821X(95)00134-X

Stoner, J. S., Channell, J. E. T., Hillaire-Marcel, C., & Kissel, C. (2000). Geomagnetic paleointensity and environmental record from Labrador Sea core MD95-2024: Global marine sediment and ice core chronostratigraphy for the last 110 kyr. Earth and Planetary Science Letters, 183(1–2), 161–177. https://doi.org/10.1016/S0012-821X(00)00272-7

Stoner, J. S., Channell, J. E. T., Mazaud, A., Strano, S. E., & Xuan, C. (2013). The influence of high-latitude flux lobes on the Holocene paleomagnetic record of IODP Site U1305 and the northern North Atlantic: Paleomagnetic Record of the N. Atlantic. Geochemistry, Geophysics, Geosystems, 14(10), 4623–4646. https://doi.org/10.1002/ggge.20272

Stoner, J. S., Jennings, A., Kristjánsdóttir, G. B., Dunhill, G., Andrews, J. T., & Hardardóttir, J. (2007). A paleomagnetic approach toward refining Holocene radiocarbon-based chronologies: Paleoceanographic records from the north Iceland (MD99-2269) and east Greenland (MD99-2322) margins: Holocene PSV and radiocarbon chronology. Paleoceanography, 22(1), n/a. https://doi.org/10.1029/2006PA001285

Stoner, J. S., & St-Onge, G. (2007). Chapter Three Magnetic stratigraphy in paleoceanography: Reversals, excursions, paleointensity, and secular variation. In C. Hillaire–Marcel & A. De Vernal (Eds.), Developments in marine geology (Vol. 1, pp. 99–138). Elsevier. https://doi.org/10. 1016/S1572-5480(07)01008-1

St-Onge, G., Mulder, T., Francus, P., & Long, B. (2007). Chapter Two Continuous physical properties of cored marine sediments. In Developments in marine geology (Vol. 1, pp. 63–98). Elsevier. https://doi.org/10.1016/S1572-5480(07)01007-X

St-Onge, G., & Stoner, J. (2011). Paleomagnetism near the north magnetic pole: A unique vantage point for understanding the dynamics of the geomagnetic field and its secular variations. Oceanography, 24(3), 42–50. https://doi.org/10.5670/oceanog.2011.53

St-Onge, G., Stoner, J. S., & Hillaire-Marcel, C. (2003). Holocene paleomagnetic records from the St. Lawrence Estuary, eastern Canada: Centennial- to millennial-scale geomagnetic modulation of cosmogenic isotopes. Earth and Planetary Science Letters, 209(1–2), 113–130. https://doi.org/10.1016/S0012-821X(03)00079-7

Suganuma, Y., Yokoyama, Y., Yamazaki, T., Kawamura, K., Horng, C.-S., & Matsuzaki, H. (2010). 10Be evidence for delayed acquisition of remanent magnetization in marine sediments: Implication for a new age for the Matuyama–Brunhes boundary. Earth and Planetary Science Letters, 296(3–4), 443–450. https://doi.org/10.1016/j.epsl.2010.05.031

Tauxe, L. (1993). Sedimentary records of relative paleointensity of the geomagnetic field: Theory and practice. Reviews of Geophysics, 31(3), 319–354. https://doi.org/10.1029/93RG01771

Tauxe, L. (2010). Essentials of paleomagnetism. University of Columbia Press. https://doi.org/10.1525/9780520946378

Tauxe, L., Mullender, T. A. T., & Pick, T. (1996). Potbellies, wasp-waists, and superparamagnetism in magnetic hysteresis. Journal of Geophysical Research, 101(B1), 571–583. https://doi.org/10.1029/95JB03041

Tauxe, L., Pick, T., & Kok, Y. S. (1995). Relative paleointenisty in sediments: A pseudo-Thellier approach. Geophysical Research Letters, 22(21), 2885–2888. https://doi.org/10.1029/95GL03166

Tauxe, L., & Wu, G. (1990). Normalized remanence in sediments of the western equatorial Pacific: Relative paleointensity of the geomagnetic field? Journal of Geophysical Research, 95(B8), 12337–12350. https://doi.org/10.1029/JB095iB08p12337

Thouveny, N. (1988). High-resolution palaeomagnetic study of Late Pleistocene sediments from Baffin Bay: First results. Canadian Journal of Earth Sciences, 25(6), 833–843. https://doi.org/10.1139/e88-082

Valet, J.-P., & Meynadier, L. (1998). A comparison of different techniques for relative paleointensity. Geophysical Research Letters, 25(1), 8992. https://doi.org/10.1029/97GL03489

Velle, J. H., Walczak, M. H., Reilly, B., St-Onge, G., Stoner, J. S., Fallon, S., et al. (2021). High resolution inclination records from the Gulf of Alaska, IODP Expedition 341 Sites U1418 and U1419. Geophysical Journal International, 229(1), 345–358. https://doi.org/10.1093/gji/ ggab479

Washam, P., Nicholls, K. W., Münchow, A., & Padman, L. (2019). Summer surface melt thins Petermann Gletscher Ice Shelf by enhancing channelized basal melt. Journal of Glaciology, 65(252), 662–674. https://doi.org/10.1017/jog.2019.43

Weeks, R., Laj, C., Endignoux, L., Fuller, M., Roberts, A., Manganne, R., et al. (1993). Improvements in long-core measurement techniques: Applications in palaeomagnetism and palaeoceanography. Geophysical Journal International, 114(3), 651–662. https://doi.org/10.1111/j. 1365-246X.1993.tb06994.x

Xuan, C., & Channell, J. E. T. (2009). UPmag: MATLAB software for viewing and processing u channel or other pass-through paleomagnetic data. Geochemistry, Geophysics, Geosystems, 10(10), Q10Y07. https://doi.org/10.1029/2009GC002584

Yukutake, T. (1967). Dominion Observatory, Ottawa, Canada (p. 14). (Received February 18, 1967).

Zijderveld, J. (1967). AC demagnetisation of rocks: Analysis of results. In Methods in paleomagnetism.

1.11 SUPPORTING INFORMATION (FIGURES AND TABLES)

Data presented here contain: XRF point source (MSCL) data of core 10GC to support the mineralogy variation at the top of core; Zijdeverld diagrams for 10GC to support the quality of the demagnetization process (measured on cryogenic magnetometer 2G Enterprise, and processed with the Mazaud Excel spreadsheet); plots of rock magnetic parameters (measured on Vibrating Sample Magnetometer); details of the RPI determination process for already published cores. Supplementary tables contain: grainsize analysis results; correlation coefficient of different RPI records comparisons and details of unmixing of IRM acquisition on 10GC samples realized with MaxUnmix software and correlation coefficients between Ti/Ca XRF profiles for the establishment of the Correlated Equivalent Depth (calculated on QAnalySeries). Figures were made using Golden Software Grapher.

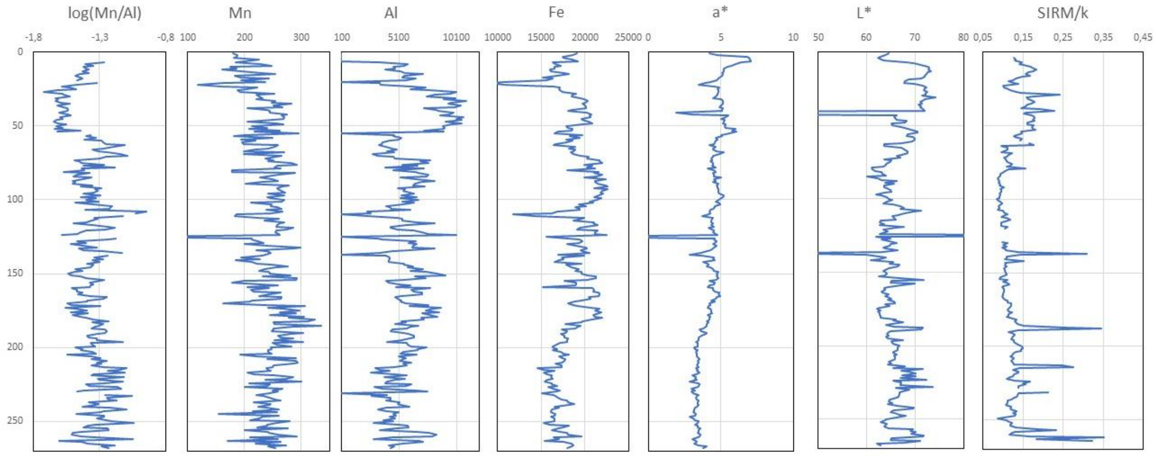

Figure S1. 10GC MSCL data.

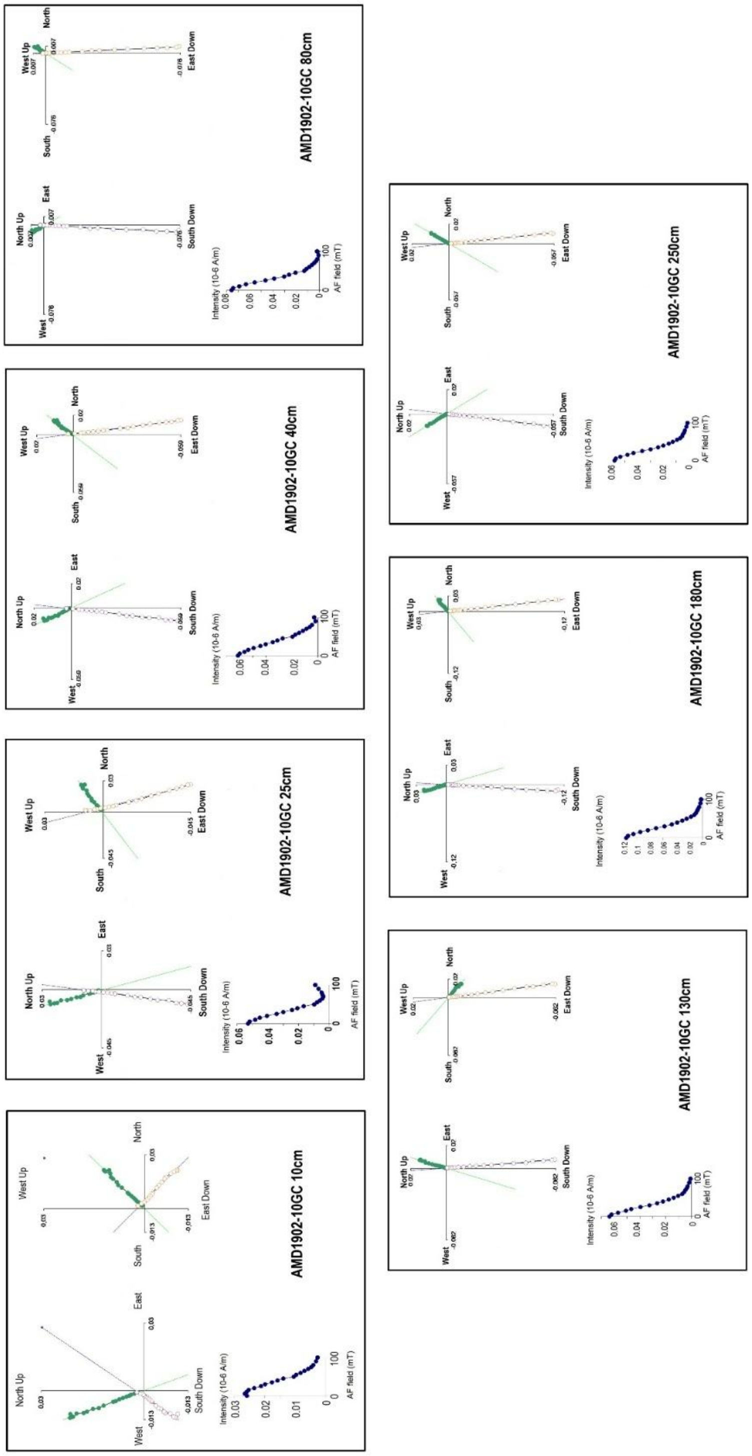

Figure S2. Zijdeverld diagrams for 10GC demagnetization process during NRM measurements

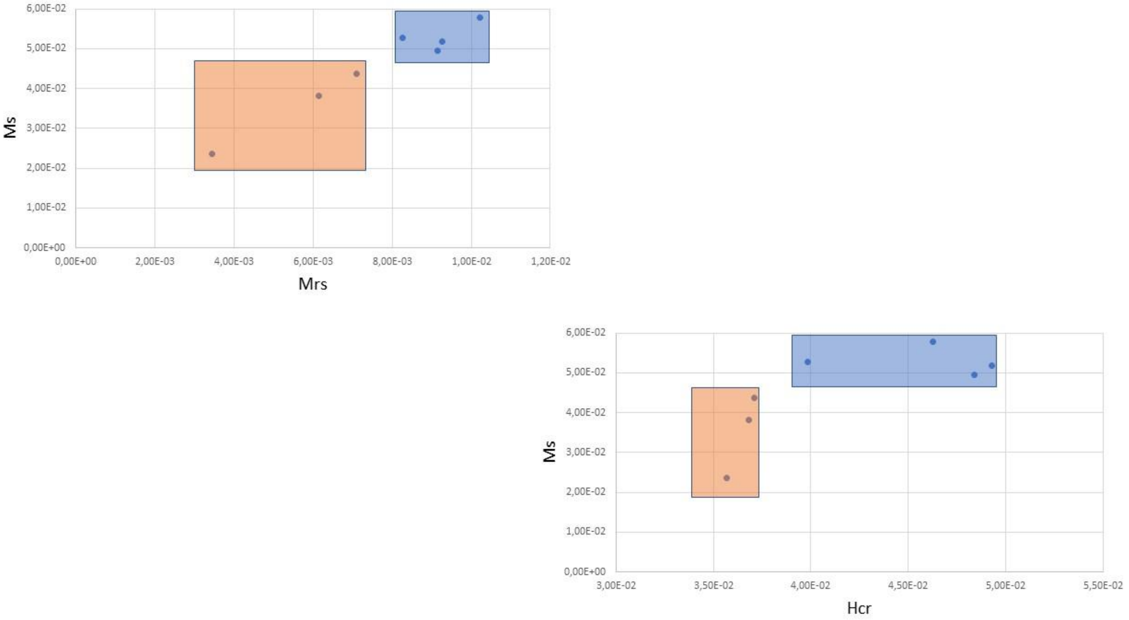

Figure S3. Rock magnetic measurements bi-plots.

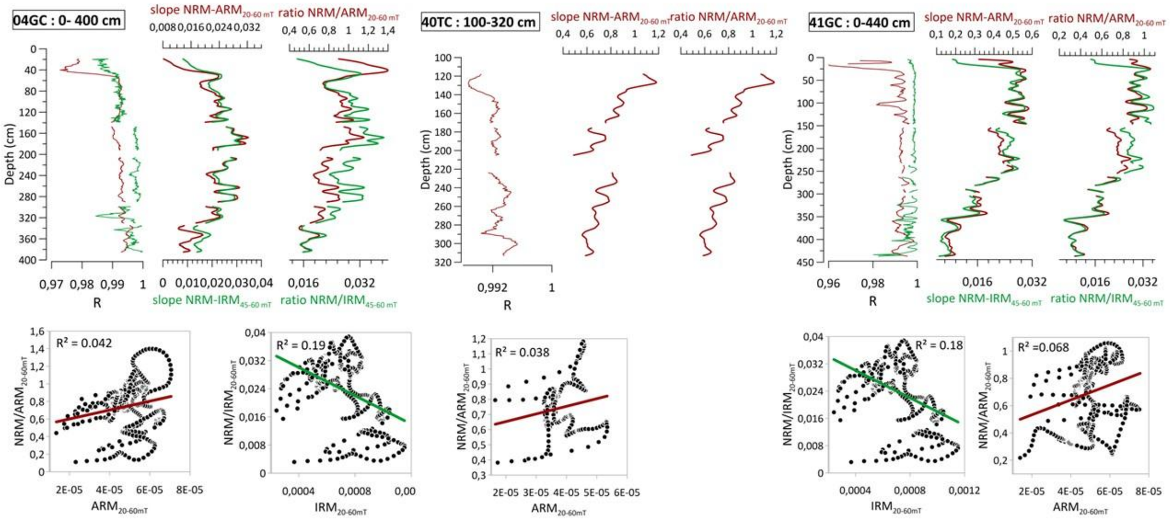

Figure S4. Determination of the RPI signal for 40TC, 04GC, 41GC. R: correlation coefficient for ARM (red) and IRM (green); profil for slope method; profil for ratio method. Determination coefficient r² between the normalized signal and the normalizer for ARM and IRM.

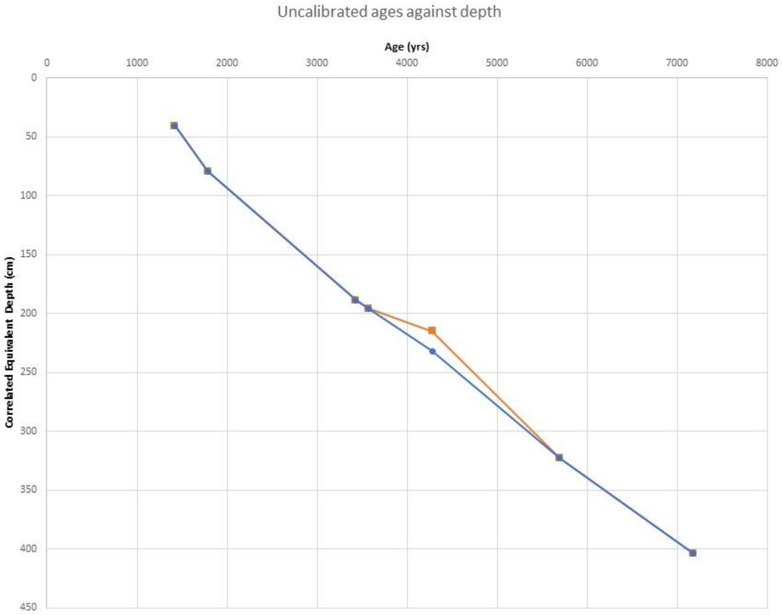

Figure S5. Alignment of the uncalibrated ages versus the depth (CED, cm) depending on the different correlation of 10GC to the OFS. The blue curve represents the preferred correlation (used in this study), based on the XRF data with the higher r². The orange curve represents the test that was made to better correlate 10GC inclination features with other records of the stack. This lead to modify the depth of one age (4177 yrs BP) which results in a less linear alignment of the uncalibrated ages.

Table S1. Grainsize sample statistics after GRADISTAT treatment (Folk and Warm method)

Sample	Sample type	Textural group	Sediment name	Mean (mm)	Sorting (mm)	Skewness (mm)	Kurtosis (mm)
0-1cm	Trimodal, Very Poorly Sorted	Slightly Gravelly Mud	Slightly Very Fine Gravelly Fine Silt	6	5.2	0.16	1.59
10-11 cm	Bimodal, Poorly Sorted	Slightly Gravelly Mud	Slightly Very Fine Gravelly Fine Silt	6.53	3.31	-0.06	1.09
20-21 cm	Polymodal, Poorly Sorted	Mud	Coarse Silt	9.95	3.52	-0.14	0.91
30-31 cm	Trimodal, Poorly Sorted	Mud	Fine Silt	6.19	3.13	-0.09	1.05
40-41 cm	Trimodal, Poorly Sorted	Mud	Fine Silt	5.66	3.19	-0.102	1.02
50-51 cm	Trimodal, Poorly Sorted	Mud	Medium Silt	6.54	3.08	-0.11	1.01

60-61 cm	Trimodal, Poorly Sorted	Mud	Medium Silt	6.64	3.10	-0.12	1.01
70-71 cm	Trimodal, Poorly Sorted	Mud	Fine Silt	6.13	3.17	-0.08	1.04
80-81 cm	Bimodal, Poorly Sorted	Mud	Fine Silt	5.97	2.96	-0.07	1.07
90-91 cm	Bimodal, Poorly Sorted	Mud	Fine Silt	5.97	3.01	-0.05	1.09
100-101 cm	Bimodal, Poorly Sorted	Mud	Fine Silt	6.08	2.98	-0.074	1.07
110-111 cm	Trimodal, Poorly Sorted	Mud	Fine Silt	7.33	3.6	0.03	1.1
120-121 cm	Bimodal, Poorly Sorted	Mud	Fine Silt	6.42	3.07	-0.04	1.08
130-131 cm	Bimodal, Poorly Sorted	Mud	Fine Silt	6.25	2.97	-0.042	1.07
140-141 cm	Bimodal, Poorly Sorted	Mud	Fine Silt	7.33	3.6	0.03	1.15
150-151 cm	Bimodal, Poorly Sorted	Mud	Fine Silt	5.91	3.03	-0.06	1.09
160-161 cm	Bimodal, Poorly Sorted	Mud	Fine Silt	5.68	3.04	-0.07	1.1
170-171 cm	Bimodal, Poorly Sorted	Mud	Fine Silt	6.26	2.99	-0.07	1.06
180-181 cm	Bimodal, Poorly Sorted	Mud	Fine Silt	6	3.08	-0.07	1.07
190-191 cm	Bimodal, Poorly Sorted	Mud	Fine Silt	6.9	3.07	0.01	1.07
200-201 cm	Bimodal, Poorly Sorted	Mud	Fine Silt	6.41	3.11	-0.03	1.08
210-211 cm	Bimodal, Poorly Sorted	Mud	Fine Silt	6.96	3.3	0.04	1.1
220-221 cm	Trimodal, Poorly Sorted	Mud	Fine Silt	7.35	3.36	0.02	1.1
230-231 cm	Bimodal, Poorly Sorted	Mud	Fine Silt	6.88	3.2	-0.01	1.1
240-241 cm	Trimodal, Poorly Sorted	Mud	Fine Silt	7.36	3.12	-0.02	1.04
250-251 cm	Polymodal, Poorly Sorted	Sandy Mud	Very Fine Sandy Fine Silt	10.25	3.98	0.1	1.03
260-261 cm	Trimodal, Poorly Sorted	Mud	Fine Silt	7.96	3.7	0.08	1.13

Table S2. Correlation coeficient of the RPI signals calculated with QAS

RPI R^2	CALS10k.2 prediction	Pfm9k.2 prediction	U1305	VADM West. Eurasia
Petermann stack	0.57	0.76	0.68	0.48
U1305				0.77

Tableau S3. Unmixing of IRM acquisition on 10GC samples

	10 cm		40 cm		130 cm		250 cm	
Component	1	2	1	2	1	2	1	2
Bh (log units)	1.82	2.24	1.81	2.84	1.72	1.91	1.70	2.19
Dp	0.28	0.61	0.29	0.26	0.26	0.13	0.27	0.91
skewness	0.8	1	0.85	0.8	0.85	1	0.85	0.9
Smoothing factor	0.55		0.55		0.55		0.55	
Residual Sum Square	$2.01 \,.\, 10^{-12}$		$2.8 \,.\, 10^{-12}$				$3.7 \,.\, 10^{-13}$	
Relative proportion	1	0.03	0.99	0.07	1	0.05	0.98	0.04

Table S4. Correlation coefficients between Ti/Ca XRF profiles for the establishment of the Correlated Equivalent Depth

	10GC	04GC	41GC	40TC
10GC	-	0.784	0.788	0.687
04GC	-	-	0.924	0.937
41GC	-	-	-	0.899

CHAPITRE 2

DES ENREGISTREMENTS PALEOMAGNETIQUES DU NORD EST DU GROENLAND INDIQUENT L'INFLUENCE DES LOBES DE FLUX GEOMAGNETIQUES SUR LA MIGRATION DU POLE GEOMAGNETIQUE VIRTUEL AU COURS DE L'HOLOCENE

2.1 RESUME EN FRANÇAIS DU DEUXIEME ARTICLE

Ce chapitre porte sur les variations paléomagnétiques séculaires enregistrées dans les sédiments du plateau continental nord-est du Groenland. Des analyses paléomagnétiques et de magnétisme environnemental ont été effectuées sur trois carottes de sédiments marines provenant du plateau continental du nord-est du Groenland et de Young Sound, à l'ouest du détroit de Fram. Cette étude démontre que le signal paléomagnétique enregistré dans les carottes sédimentaires est caractérisé par une aimantation forte et stable à composante unique portée par des particules ferrimagnétiques monodomaines (ou à l'état de vortex), de faible coercivité. Ceci atteste de la qualité des données et de la fiabilité des enregistrements de paléointensité relative (RPI) et des variations séculaires paléomagnétiques (PSV). La comparaison avec d'autres archives, ainsi qu'avec les projections de modèles de champ géomagnétique, a révélé de grandes similitudes entre les enregistrements, en particulier avec ceux du Nord de l'Europe (Finlande et Suède) et du nord de l'Atlantique Nord, et dans une moindre mesure avec ceux du nord du Groenland. La comparaison des nouveaux enregistrements de RPI avec les modèles du champ géomagnétique global et le taux de production d'isotopes cosmogéniques met en évidence le caractère global des variations géomagnétiques du nord-est du plateau continental du Groenland. La trajectoire du pôle géomagnétique virtuel (VGP) a également été reconstituée pour les 8 derniers ka à l'aide de données directionnelles (inclinaison et déclinaison) et comparées à l'intensité du champ géomagnétique à la limite entre le noyau et le manteau sur le même intervalle de temps. Ceci a permis de montrer qu'en période de forte intensité, les lobes de flux géomagnétiques pourraient avoir un effet sur les migrations du VGP. Les résultats de cette étude impliquent que les PSV de l'Arctique supérieur sont très probablement influencées par des changements hémisphériques à l'échelle millénaire. Cet article a été accepté sous réserve de modifications pour publication dans la revue *Journal of Geophysical Research : Solid Earth* de l'*AGU*. En tant que première autrice, j'ai établi les objectifs et hypothèses de recherche, réalisé les analyses en laboratoire, interprété et discuté les résultats et rédigé l'article. En tant que deuxième auteur, le professeur **Guillaume St-Onge** a financé les analyses, participé à l'interprétation des résultats, à la discussion et à la révision de l'article. Les professeur.e.s **Christof Pearce** et **Marit-Solveig Seidenkrantz** ont récolté les carottes sédimentaires, financé les analyses, et participé à la discussion et à la révision de l'article. La directrice de recherche **France Lagroix** m'a accueillie à l'IPGP pour réaliser une partie des analyses, a participé à l'interprétation des résultats, à la discussion et à la révision de l'article. La professeure **Katrine Juul Andresen** a participé à la collecte des échantillons et à la révision de l'article. Les professeurs **Jean-Carlos Montero-Serrano** et **Pierre Francus** ont participé à la révision de l'article. Les résultats présentés dans ce chapitre ont été présentés aux conférences suivantes : Northeast Greenland Workshop en 2023 et congrès du Geotop en 2024.

2.2 NORTHEASTERN GREENLAND PALEOMAGNETIC RECORDS INDICATE THE INFLUENCE OF GEOMAGNETIC FLUX LOBES ON THE VIRTUAL GEOMAGNETIC POLE MIGRATION DURING THE HOLOCENE

2.2.1 Abstract

Paleomagnetic and rock magnetic analyses were conducted on sediment cores from the northeastern Greenland Shelf and Young Sound along the western edge of Fram Strait. The paleomagnetic signal in all three sediment cores is characterized by a strong and stable single component magnetization carried by low coercivity ferrimagnetic single domain or vortex state grains, attesting to the quality of the recorded relative paleointensity (RPI) and paleomagnetic secular variation (PSV) signals. Comparison with other archives from the northern North Atlantic, northern Greenland, and northern Europe and with geomagnetic field model outputs indicates broad similarities between the records, particularly with Finnish, Swedish and southern Greenland records. Comparison of the new RPI records with global geomagnetic field models and cosmogenic isotopes production rates highlights the global character of the geomagnetic variations from the northeastern Greenland Shelf. Virtual geomagnetic pole (VGP) paths for the last 8 kyr compared to geomagnetic field strength maps at the core-mantle boundary over the same time interval illustrate that, at times of high intensity, geomagnetic flux lobes could have an effect on VGP migration. We suggest that High Arctic PSV is most likely driven by millennial-scale hemispheric geomagnetic flux lobe geometry changes.

2.2.2 Plain Language Summary

Magnetic particles on the bottom of the ocean align with the ambient geomagnetic field and record its intensity and direction at time of deposition. We use sediment cores from the northeastern Greenland Shelf to study geomagnetic field behavior over the past 8,000 years, in particular the relation between high geomagnetic intensity zones (geomagnetic flux lobes)

and migration of the north magnetic pole. Our study supports the hypothesis that high intensity geomagnetic flux lobes can influence the migration of the north magnetic pole.

2.3 INTRODUCTION

The Earth's magnetic field has existed for 4 billion years (Tarduno et al., 2020). It is generated by liquid iron convection in the outer core and can be approximated by a geocentric axial dipole (GAD) when averaged on timescales ~10,000 years or even possibly on millennial timescales (Merrill & McFadden, 2003; Nilsson et al., 2024; St-Onge et al., 2003). However, on shorter timescales, non-dipolar components influence paleomagnetic secular variation (PSV, e.g. Merrill & McFadden, 2003; Valet, 2003; Panovska et al., 2019). In particular, spectacular recent changes are evident such as rapid migration of the north magnetic pole (NMP) over the 20th century and fluctuations of two non-dipolar features identified as "geomagnetic flux lobes", located in North America and Siberia (Livermore et al., 2020; Olsen & Mandea, 2007). Although it is difficult to compare direct observations and measurements of the last 400 years with paleointensity and paleodirection observations from sediment records on longer time scales, sediment archives provide a unique way to study continuous paleomagnetic variations to comprehend the geomagnetic field. Studies in the Arctic offer a unique vantage point for paleomagnetic studies (St-Onge & Stoner, 2011), especially about the NMP, but face the challenge of establishing a precise chronology due to scarcity of datable material (carbonate dissolution in corrosive bottom waters; e.g. Jutterström & Anderson, 2005) and reservoir age uncertainties (Heaton et al., 2020) caused by "old" radiocarbon input from glaciers and permafrost melting and sea ice transport (Ingolf Eide & Martin, 1975). Numerous studies have documented Arctic PSV, however few describe PSV on the northeastern coast and shelf of Greenland at very high latitude (>75°N).

Here we investigate the northeast Greenland region, specifically the shelf and one fjord, for millennial-scale PSV and RPI variations and to understand the coupling between different geomagnetic field components. This is important for reconstructing hemispheric-scale geomagnetic field behavior and the influence of geomagnetic flux lobe intensity on NMP migration during the Holocene. It also provides a mean to link to other studies from western Greenland (Girard et al., 2024; Reilly et al., 2019), the North Atlantic (e.g., Reilly et al., 2023; Stoner et al., 2013), northern Europe (e.g., Haltia-Hovi et al., 2010; Snowball et al., 2007) and Svalbard (Sagnotti et al., 2011; Caricchi et al., 2020, 2022).

2.4 MATERIAL AND METHODS

2.4.1 Northeast Greenland Shelf sediment cores and setting

Sediment cores DA17-NG-ST03-039G (80.0333°; -8.91667°) and DA17-NG-ST07-073G (79.0667°; -11.9°) (hereinafter 039G and 073G) were collected during the NorthGreen2017 Expedition (Seidenkrantz et al., 2018) onboard the R/V Dana on the NE Greenland Shelf (Fig. 37) southwest of Fram Strait while core DA17-NG-ST18-213G (74.333°; -20.333°) (hereinafter 213G) was retrieved in the outer part of the Young Sound fjord (Supporting information; Table S5, Figure S6).

Core 039G (3.2 m length) was sampled in a depression (~391 meters below sea level or mbsl) at the edge of Westwind Trough on the outer northeast Greenland Shelf, while core 073G (4.1 m length) was collected from the middle of the shelf in a depression (385 mbsl) in the inter-trough area between Westwind Trough and Norske/Belgica Trough. Both cores have been investigated previously for paleoenvironmental and paleoceanographic purposes (Hansen et al., 2022, 2023; Pados-Dibattista et al., 2022). The Greenland coast close to these sites is composed of Paleoproterozoic crystalline basement rocks (orthogneiss), with Proterozoic sediments (sand and siltstones), Mesoproterozoic dolorites, and Ordovician dolomites (Higgins, 2015).

Core 213G (3.1 m length) was collected in Young Sound (at ~168 mbsl), a deep silled fjord on the east coast of Greenland, with ~90 km length and 2-7 km width. The Young Sound-Tyrolerfjord (YST) system is shallower and wider at the mouth than in its interior (100 m on average, down to 360 m; Ribeiro et al., 2017; Rysgaard et al., 2018) due to differential glacial bedrock erosion. The shallow sill marks the terminus of the YST system and limits sea water exchange between the fjord interior and the shelf, which extends to 150 km from the Greenland coast. The fjord catchment is surrounded by land-terminating glaciers and large river systems.

Fram Strait is a major gateway for deep-water and sea-ice exchange between the Arctic and North Atlantic Oceans (Fig. 37), where the East Greenland Current (EGC) circulates southward, along the Greenland Shelf (Johannessen, 1986), transporting riverine input and glacial meltwater from marine terminating glaciers (Bendtsen et al., 2014). It is composed of Polar surface waters (0-50 m, cold, relatively fresh water), originating from the Arctic Ocean, with local meltwater contributions. Below are the Polar waters (PW, 50-150 m, cold, more saline), which are underlain by Atlantic water masses: Arctic Atlantic water, (AAW) is a relatively warm and saline water mass that has circulated in the Arctic Ocean at >150 m depth (Rudels et al., 2005). Return Atlantic Water (RAW), transported by the Return Atlantic Current (RAC), which is part of the western branch of the West Spitsbergen Current (WSC), that flows from the North Atlantic Ocean toward NE Greenland, and then joins the EGC and flows southward along the Greenland Coast.

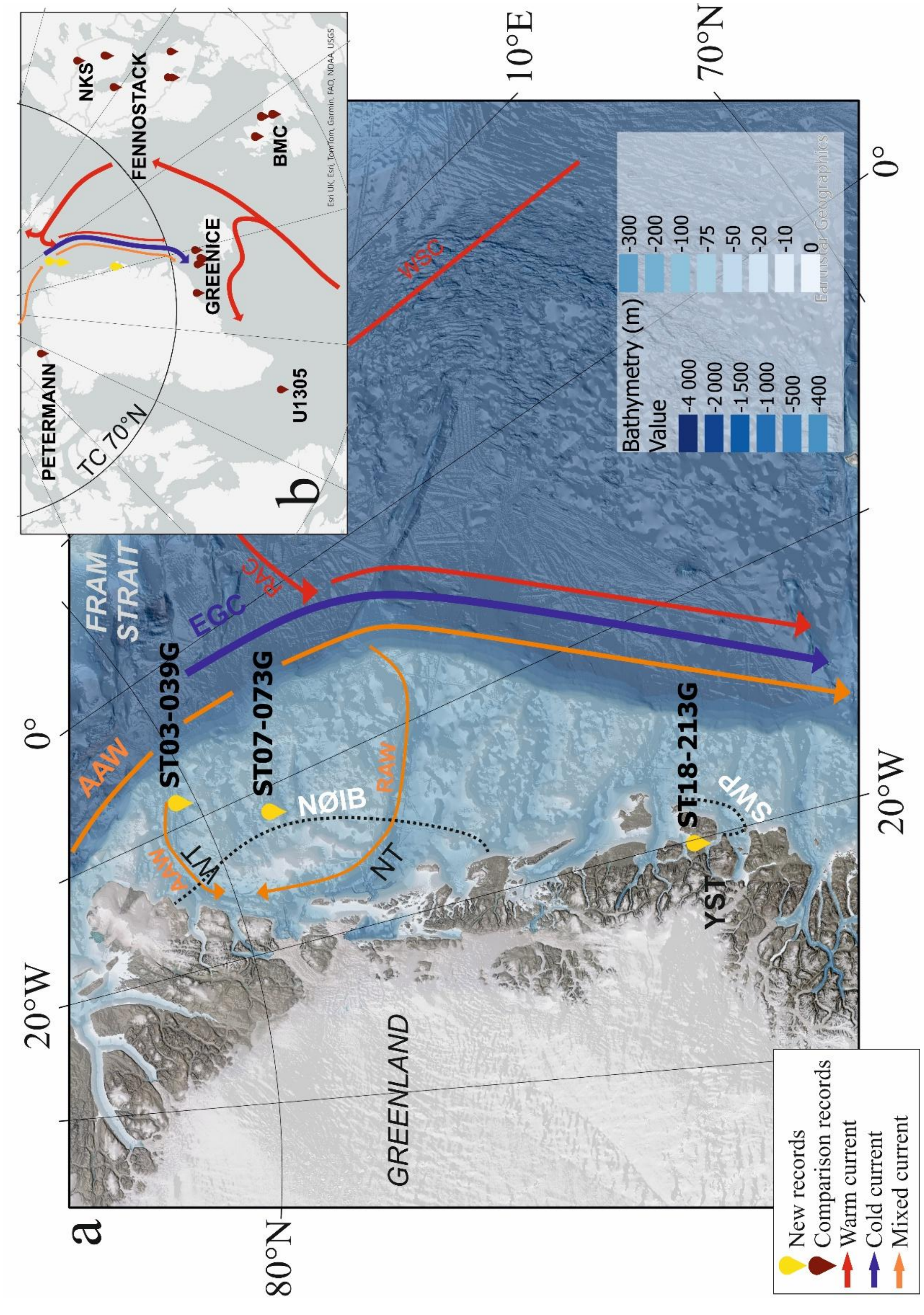
a
b
80°N
20°W
0°
10°E
70°N
20°W
0°
GREENLAND
FRAM STRAIT
EGC
RAC
WSC
AAW
RAW
NØIB
WT
NT
YST
SWP
ST03-039G
ST07-073G
ST18-213G
PETERMANN
TC 70°N
U1305
GREENICE
FENNOSTACK
NKS
BMC
Esri UK, Esri, TomTom, Garmin, FAO, NOAA, USGS
Bathymetry (m)
Value
-4 000
-2 000
-1 500
-1 000
-500
-400
-300
-200
-100
-75
-50
-20
-10
0
Earthstar Geographics
New records
Comparison records
Warm current
Cold current
Mixed current

Figure 37. (a) Map of the sampling sites and surface currents: AAW - Arctic Atlantic Water, EGC - Eastern Greenland Current, RAC - Return Atlantic Current. NØIB: Norske Øer Ice Barrier, SWP: Sirius Water Polynya. NT: Norske Trough; WT: Westwind Trough; YST: Young Sound Tyrolerfjord. Bathymetry data from General Bathymetric Chart of the Ocean, 2023 version (GEBCO Compilation Group, 2023). Map were made using ArcGIS and CorelDraw software. (b) General location of the study area and cores used in this study: Petermann Stack (Girard et al., 2024), Fennostack (Snowball et al., 2007), U1305 (Stoner et al., 2013), GREENICE15k (Reilly et al., 2023), North Karelian Stack (NKS; Haltia-Hovi et al., 2010), British master curve (BMC; Turner & Thompson, 1981). TC 70°N indicates the surface projection of the tangent cylinder.

2.4.2 Physical and geochemical properties: X-ray fluorescence and imaging

Cores were cut into 1 m sections onboard and subsequently split into halves and described using the Munsell color chart (archive and working) in the laboratory at the Department of Geosciences, Aarhus University (Denmark). Low-field magnetic susceptibility (k_{LF}) measurement (2 mm resolution), analysis of bulk geochemical composition (30 kV, 30 mA, 200 µm), and radiographic image (60 kV, 45 mA, 200 µm) were measured with an Itrax X-ray fluorescence (XRF) core scanner (Cox Analytical) on the archive halves of the core, with a Molybdenum tube (step size: 200 µm; exposure time: 10 s; voltage: 30 kV, current: 30 mA). XRF elements were normalized by the total counts of all elements measured and the following proxies were used. Zr/Rb is used as a grain size proxy and is commonly higher at turbidites base, Ti/Ca is a provenance proxy (terrestrial or marine) and Ca/Fe is used to discriminate between turbidite or pelagic sedimentation (Croudace & Rothwell, 2015).

2.4.3 Grain size analysis

Grain size measurements (<2 mm fraction) were conducted with a Malvern-Panalytical Mastersizer 3000 laser particle size analyzer at the *Institut des sciences de la mer* (ISMER) on bulk sediments at 10 cm intervals (5 cm intervals in sand layers). Before analysis, 0.5 g of wet sediment sample for each chosen interval was deflocculated with a solution composed of 30 ml of sodium hexametaphosphate (concentration 20 g/l) and 70 ml of water, by agitating the mixture for at least 3 hours with an inhouse rotator. After measurement, grain-size distributions were calculated with the GRADISTAT Excel spreadsheet version 9.1 (Blott

& Pye, 2001) to obtain different statistical parameters (Folk and Wark method), to document sediment lithological changes (sand, silt and clay percentages, median grain size D_{50} and D_{90}).

2.4.4 Continuous paleomagnetic analysis

Continuous subsections were sampled from the working halves of the cores using u-channels, with a cross section of 4 cm², up to 1 m long and were then used to conduct continuous magnetic measurements at 1 cm intervals with a 2G Enterprises 755SRM-1.65 cryogenic magnetometer at ISMER. The natural remanent magnetization (NRM) was measured by demagnetizing the sediment from 0 to 80 mT at 5 mT steps, and from 80 to 100 mT at 10 mT steps until less than 10% of the initial remanent magnetization remained. The direction of the characteristic remanent magnetization (ChRM) was then calculated by principal component analysis (Kirschvink, 1980) with the Excel routine from Mazaud (2005), using 15-60 mT demagnetization steps. An anhysteretic remanent magnetization (ARM) was induced with a 100 mT peak field and a 50 µT direct current bias field. Stepwise demagnetization was conducted identically as the NRM. An isothermal remanent magnetization was induced with a pulse magnetizer at 300 mT (IRM) and 950 mT (saturation isothermal remanent magnetization, SIRM). Seventeen demagnetization steps (0 to 80 mT, 5 mT increments) were used for the IRM and 4 steps (0, 10, 30 and 50 mT) for the SIRM.

After the measurements, data were first checked and flux jumps corrected if necessary with the UPmag software (Xuan & Channell, 2009). The Mazaud (2005) Excel spreadsheet provided declination and inclination data, maximum angular deviation (MAD) and median destructive field (MDF) values (field intensity required to remove half of the initial remanence), through principal component analysis and using an unanchored origin. MDFNRM represents the coercivity of the remanence-carrying grains assemblage and is an indicator of the magnetic mineralogy. The MDFARM indicates the mineral coercivity of the magnetic mineral assemblages responding to ARM and reflects magnetic mineralogy and grain sizes (Stoner & St-Onge, 2007). MAD values <5° reflect high quality data and reliable inclination and declination results. High MAD values generally show complex magnetization with different coercivities and must be used carefully. Zijderveld diagrams (orthogonal projections; Zijderveld, 1967) enable checking on the demagnetization process and selection of ChRM steps. kARM/kLF is sensitive to downcore magnetic grain size and mineralogy variations (Banerjee et al., 1981; King et al., 1982) if the magnetic mineralogy is dominated by magnetite and varies inversely with magnetic grainsize (Stoner & St-Onge, 2007). Measurements are acquired every centimeter, but the magnetometer used at ISMER is characterized by a smoothing window of 7-8 cm (Philippe et al., 2018). To avoid biases resulting from this response function, the 4 cm intervals at the top and bottom of each u-channel were excluded.

2.4.5 Rock magnetic measurements

An AGICO KLY-3/CS-3 susceptibility meter was used at the Institut de Physique du globe de Paris (IPGP), to measure the temperature-dependent magnetic susceptibility of representatives samples (039G: 55, 95, 150, 185, 240, 270 and 300 cm; 073G: 15, 40, 60, 150, 228, 330, 356, 370 and 390 cm; 213G: 10, 40, 70, 115, 126, 145, 152 and 210 cm). The samples were heated to 700°C and then cooled to room temperature, in an air-atmosphere. This enables Curie temperature identification (Dunlop and Ozdemir, 2007). Chemical alteration often occurs during heating and it can be challenging to differentiate between original and newly formed magnetic minerals. To assess mineralogical changes that occurred during heating, hysteresis loop measurements were conducted on the bulk sediment before heating and on the altered sediment after heating.

Hysteresis loops, remanent coercive force (Hcr), remanence curves, first order reversal curve (FORC) diagrams (Pike et al., 1999) and IRM acquisition curves were acquired on a Princeton Measurements corporation vibrating sample magnetometer (VSM) on the same samples, before and after heating. The maximum field applied for all experiments was +/-1.5 T. The linear high field slope over the 1.05 T to 1.5 T field range of the hysteresis loop was calculated to estimate the high field susceptibility. The following magnetic parameters were derived from the high-field slope corrected hysteresis loops: coercive force (Hc), saturation magnetization (Ms) and saturation remanence (Mrs). The S-ratio was calculated according to the Bloemendal et al., (1988) equation S-ratio = 0.5 × (1- 〖IRM〗_(-300 mT)/SIRM) using parameters derived from back-field remanence curves. The online software MAX unMix (Maxbauer et al., 2016) was used to identify the coercivity distribution of the main magnetic carriers contributing to the IRM acquisition curves. FORC diagrams, processed with the FORCinel software (Harrison & Feinberg, 2008), allow identification of the domain state and coercivities of the magnetic minerals present in the samples (Roberts et al., 2019, 2022).

2.4.6 Chronology

Age-depth models for the three sediment cores are based on radiocarbon dating. Acceleration mass spectrometry (AMS) ^{14}C dating was performed at the Aarhus AMS centre (Aarhus University, Denmark), and for smaller samples, at the Laboratory of Ion Beam Physics, Eidgenössische Technische Hochschule (ETH, Zürich, Switzerland). Previous studies (Hansen et al., 2022; Pados-Dibattista et al., 2022) determined age models for cores 039G and 073G using the OxCal v4.4 software (Ramsey, 2008; Ramsey & Lee, 2013). All ages were calibrated with the calibration curve Marine20 (Heaton et al., 2020) to account for the reservoir effect, using a local reservoir age correction of ΔR = 0 ± 50 years (Hansen et al., 2022). The core 213G Bayesian age model is based on 10 radiocarbon ages (Table 8) and was built with the R package "Bacon" using Marine20 and ΔR = -50 ± 50 years (Pearce et al., 2023).

Table 8. Radiocarbon ages for core 213G.

AMS lab sample code	Core depth (middle, cm)	Material	^{14}C date (BP)	Uncertainty (+/- 1σ)	Calibrated date (+/- 2σ, cal a BP)	Modelled median date (cal a BP)
AAR-29838	21.5	Bivalve	1791	36	1051-1400	1187
AAR-27557	31.5	Bivalve shell fragment (unidentified)	2072	32	1345-1700	1487
AAR-27558	45	Bivalve (*Ennucula tenuis*)	2358	23	1684-2070	1853
AAR-27559	57	Bivalve (*Ennucula tenuis*)	2657	23	2033-2436	2229
AAR-28087	81.5	Bivalve (*Axinopsida orbiculata*)	3463	47	3002-3436	3175
ETH-126104.1.1	140.5*	Benthic foraminifera (*E. clavatum* and *C. reniforme*)	4889	201	4525-5555	5029
ETH-126105.1.1	170.5	Benthic foraminifera (*E. clavatum* and *C. reniforme*)	5670	116	5609-6226	5966
AAR-27560	225	Bivalve (*Yoldiella intermedia*)	7723	33	7870-8240	8031
ETH-126106.2.1	271.5	Benthic foraminifera (*E. clavatum* and *C. reniforme*)	8771	181	8792-9841	9825
AAR-30050	285.5	Benthic foraminifera (mixed species)	10138	68	10800-11395	10973

*The age at 140.5 cm was not used in the age-depth model (see section 2.5.5), because it is located in a rapidly deposited layer.

2.5 RESULTS

2.5.1 Lithology

Core 039G consists of homogenous sediment, with brown clayey silt and small pebbles at the bottom of the core (Hansen et al., 2022). Lower (higher) Ti/Ca (and Zr/Rb) values occur in the lowermost 20 cm (300-320 cm) with a slight increase (decrease) to stable values in the rest of the core (Fig. 38a). Clay, silt, and sand contents are stable throughout the core, except for a small sand percentage increase at 250 cm. Zones I to IV identified by Hansen et al. (2022) based on foraminiferal data are indicated in Fig. 38a.

Core 073G is composed of clayey silt (Pados-Dibattista et al., 2022) with increased clay content from 0 to 360 cm. The lowermost 50 cm is coarser, with higher sand content and higher D50. In the rest of the core, sand, silt and clay percentages are stable except for two sand percentages peaks at 220 cm and 300 cm. All proxies presented are stable except for the bottom part of the core, where Ti/Ca, Zr/Rb, and kLF variations are observed. As for core 039G, the five zones identified based on the foraminiferal assemblages (Pados-Dibattista et al., 2022) are shown in Fig. 38a.

Core 213G consists of homogeneous clay of stable grain size with a number of black spots, interrupted by two prominent sand layers (higher sand percentage and D_{50}) between 125-160 cm and 200-220 cm (Fig. 38a). A transition in kLF is observed around 130 cm to lower values towards the top of the core. Ti/Ca also displays a transition at 130 cm, with values increasing towards core top. Ti/Ca, Zr/Rb and kLF variations are noted in the sand layers (Fig. 38a).

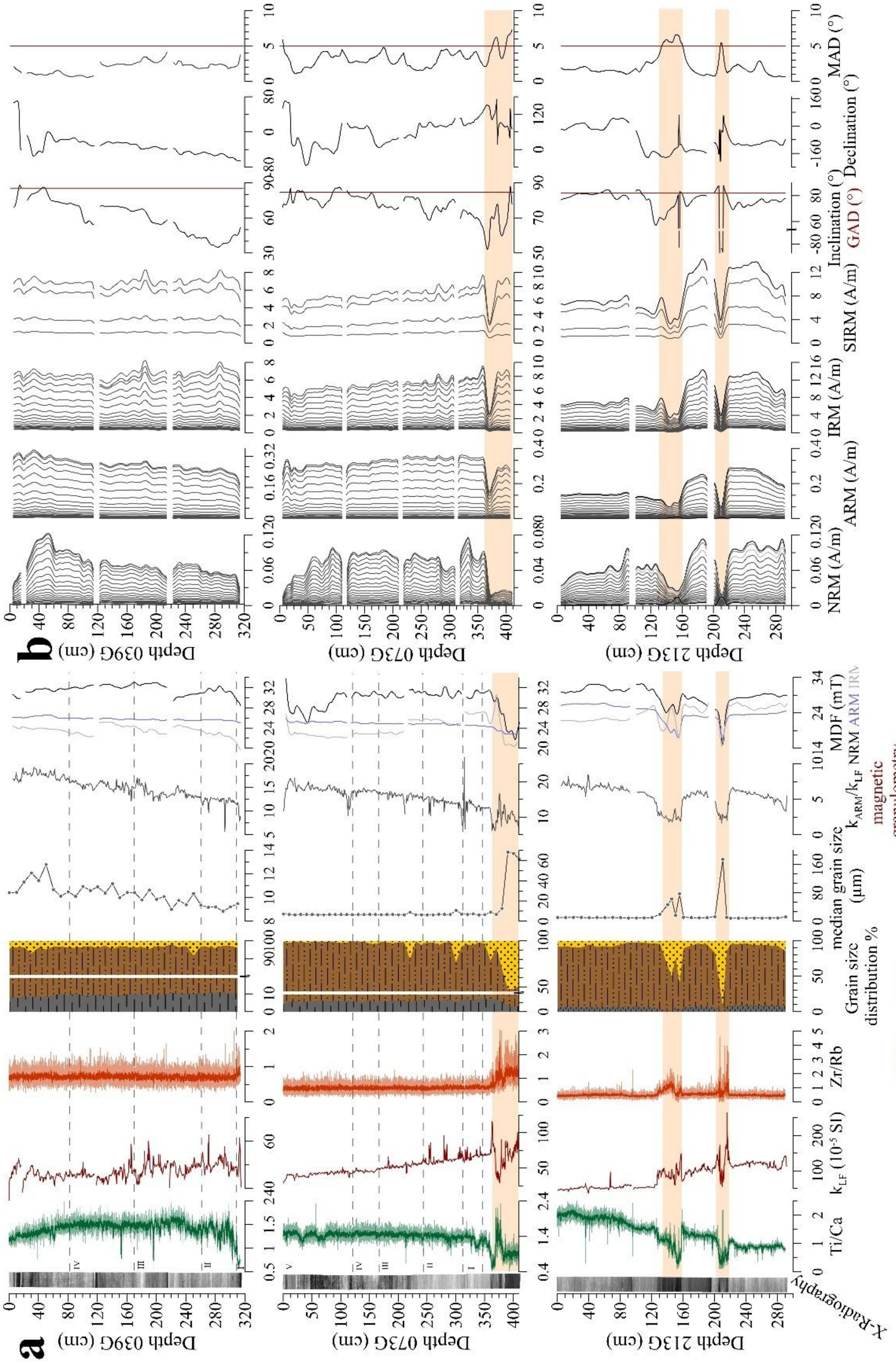
a
b
Depth 039G (cm)
Depth 073G (cm)
Depth 213G (cm)
X-Radiography
Ti/Ca
k_{LF} (10^{-5} SI)
Zr/Rb
Grain size distribution %
median grain size (µm)
k_{ARM}/k_{LF}
magnetic granulometry
+
-
MDF (mT)
NRM ARM IRM
NRM (A/m)
ARM (A/m)
IRM (A/m)
SIRM (A/m)
Inclination (°)
GAD (°)
Declination (°)
MAD (°)
Sand
Silt
Clay
I
II
III
IV
V

Figure 38. (a) Physical and geochemical continuous properties of cores 039G, 073G, and 213G. From left to right: X-radiography, Ti/Ca, low-field magnetic susceptibility (k_{LF}), Zr/Rb, grain size (sand, silt, clay) composition (%), median grain size (µm), k_{ARM}/k_{LF}, MDF (mT). **(b)** Continuous magnetic properties of cores 039G, 073G and 213G. From left to right: NRM, ARM, IRM and SIRM intensities (A/m), inclination and GAD value (°), declination (°) and MAD values (°). Beige horizontal bars in (a) and (b) indicate sand layers.

2.5.2 Continuous magnetic properties

Low-field magnetic susceptibility (k_{LF}) values are stable in core 039G (~50×10-5 SI) indicating a relative constant mineralogy (Fig. 38a). k_{ARM}/k_{LF} decreases downcore in 039G, due to the k_{LF} increase at the bottom of the core, probably associated with the coarser magnetic mineral grain size (Hansen et al., 2022). Core 073G has much larger amplitude k_{LF} variations than core 039G, especially in the sand layer. At the top, k_{LF} has low values of 30×10-5 SI which increases gradually to ~80×10-5 SI then rise sharply to a peak of 150×10-5 SI at the top of the sand layer. Core 213G has a declining k_{LF} trend toward the top with variations around 100×10-5 SI to 125 cm and around 50×10-5 SI to the core top. Sand layers (125-160 cm; 197-210 cm) have higher amplitude variations. k_{ARM}/k_{LF} variations are similar to k_{LF}, with larger variations in sand layers (cores 073G and 213G).

All cores have stable NRM, ARM, IRM, and SIRM intensity variations (except for sand layers) (Fig. 38b). Sand layers have low intensities and remagnetization for the last demagnetization steps (60-100 mT) in core 213G. The rest of the sediment in the three cores demagnetizes clearly, i.e. magnetization intensity decreases during AF demagnetization and a single component magnetization tending toward the origin of the projection plot (Supporting information, Figs. S2 & S3).

Inclination values vary around the GAD value except at the bottom of core 039G (220-320 cm) where values are lower (30-60°) than the GAD value (85°N), which corresponds to the k_{ARM}/k_{LF} decrease, and the probable coarser magnetic mineralogy (Hansen et al., 2022). Core 213G inclination has negative values in the sand layers. MAD values are less than 5°, even for the 039G low inclination interval, except for the sand layers (core 213G: 135-160 cm and 209-211 cm; core 073G: 377-387 cm and 400-410 cm).

MDF_{NRM} values are between 28 and 33 mT for the three cores, which are characteristic of low coercivity ferrimagnetic minerals such as magnetite. The bottom of core 073G and two layers in core 213G (125-158 cm; 200-218 cm) have lower values (16-28 mT), corresponding to coarser grain sizes.

Magnetic minerals in the three cores record the geomagnetic field effectively except for the coarser layers in cores 073G (370-410 cm) and 213G (125-160 cm; 200-220 cm), which are excluded from further paleomagnetic reconstructions. Larger grains are not reliable paleomagnetic field recorders (e.g., Tauxe, 1993), and are often associated with rapidly deposited layers (RDL), which have lower inclinations and unreliable ChRM directions (e.g. St-Onge et al., 2004).

2.5.3 Rock magnetic properties

All magnetic susceptibility heating curves (Fig. 39a) for core 039G samples increase with temperature, with abrupt increases just below 300°C, until reaching a peak at around 525°C before decreasing sharply at the Curie temperature of magnetite (580°C). The sample at 55 cm is the only one that lacks the sharp increase at 300°C, with only two slight bumps at 300 and 525°C, and the decrease at ~580°C. The cooling curves (Fig. 39b) have similar shapes, with a bump at ~350°C, which indicates the presence of titanomagnetite. Core 073G samples have similar behavior to those from core 039G, with the sharp increase at 300°C and peak at 525°C (especially for sample 370) and Curie temperature at 580°C, except for sample 15. Heating curves have more diverse shapes in core 073G than for core 039G. Cooling curves have similar shapes, with a bump at around 350-400°C. Susceptibilities over the lower temperature range are higher during cooling than heating (except for the maximum peak during heating), which suggests neo-formation of strongly susceptible minerals during heating. Again, samples in core 213G have a similar pattern during heating, except for samples 210 and 290. Sample 210 denotes a constant increase as opposed to the other samples, which can be explained by sand composition. Heating curve derivatives were calculated to identify more precisely the Curie temperature. They have 563-580°C values for core 039G, 554-578°C for core 073G and 571-580°C for core 213G indicates the presence of magnetite or titanomagnetite. Samples 228 in core 073G, 240 in core 039G and 115 in core 213G upon heating to 700°C have persistent susceptibility values that are greater than other samples. The same processing (subtraction of oven signal) and experimental conditions (heating and cooling rates) were applied uniformly to all samples. FORC and IRM acquisition curves results for sample 240 (039G) are described below. The mineral assemblage differs with respect to sample 150 (073G) and 70 (213G) having an overall higher coercivity. Samples 55 in core 039G and 15 in core 073G have a small magnetization decrease in heating curves at around 350°C which could be associated with greigite alteration. For all three cores, heating curves are not completely reversible, indicating that ferrimagnetic minerals are altered during heating.

Hysteresis loops (Fig. 39c) have typical shapes of low coercivity minerals such as magnetite or titanomagnetite (e.g., Tauxe et al., 1996) and reach saturation between 0.5 and 1 T (well below Hmax applied of 1.5 T), indicating the presence of moderately higher coercivity minerals. S-ratios are between 0.95 and 1 for all except sand samples (210 cm in 213G and 390 cm in 073G) which have S-ratio >1 (Supporting information; Table S8) because of noise measurement du to the nature of the sample. In any case, the rapidly deposited layers were excluded from the age models and paleomagnetic reconstructions. Hysteresis loops and derived parameters for samples after heating are presented in the supporting information (Fig. S9, Table S8). They show systematically S-ratios closer to 1 and saturation magnetization values that are one order of magnitude higher after heating. The alteration incurred upon heating results in an increased concentration of a strong ferrimagnetic phase. Maghemite being known to be thermally metastable and of the same cubic spinel crystal structure as magnetite is the most probable mineral phase to be reduced to magnetite during heating. While the experiments were carried in the air, the presence of organic matter and/or interstitial water could favor the reducing conditions required for the maghemite to magnetite conversion. The post-heating minerals are not present when measuring the NRM and thus do not impact the PSV and RPI reconstructions.

FORC diagrams (Fig. 39d) were produced for one sample per core, avoiding sand intervals. They all depict strong positive central ridges along Bu=0 mT axis, characteristic of stable single domain (SD) particles, with Bc = 15-35 mT (039G), Bc =10-40 mT (073G) and Bc = 5-20 mT (213G) revealing micro coercivities characteristic of magnetite. Stretching along the vertical axis, with lower intensities suggests smaller contribution of vortex state (Roberts et al., 2017). FORC diagrams show dominance of magnetite SD particles with contribution of particles in the vortex state.

IRM acquisition curve measurements and coercivity unmixing (Fig. 39e,f) were performed for the same samples as FORC analyses. The three samples present coercivities between 47 and 56 mT, with higher coercivity contributions for cores 073G and 213G. Based on IRM acquisition curves, saturation was reached before 0.5 T, confirming the dominance of low coercivity minerals in these samples.

The King plot (Fig. 39g; King et al., 1983) displays fine grains (<0.2 µm) and indicates that cores 039G and 073G have similar magnetic grain size, whereas core 213G seems to differ. Difference in magnetic mineralogy and grain size could reflect a difference in sedimentary sources and inputs between core 213G, which is located in a fjord closer to land, and cores 039G and 073G which are located further offshore on the Northeast Greenland Shelf.

In summary, the rock magnetic analyses indicate that all three sediment cores (except sand layers) meet the criteria for PSV and RPI reliability (Tauxe, 1993; Thompson, 1984). The magnetic signal is strong, stable and carried by low coercivity minerals such as magnetite or titanomagnetite, SD to vortex state grains, directional data are well defined (MAD <5° and inclination varies around GAD values) and magnetization intensity (NRM, ARM, IRM and SIRM) variations are less than one order of magnitude.

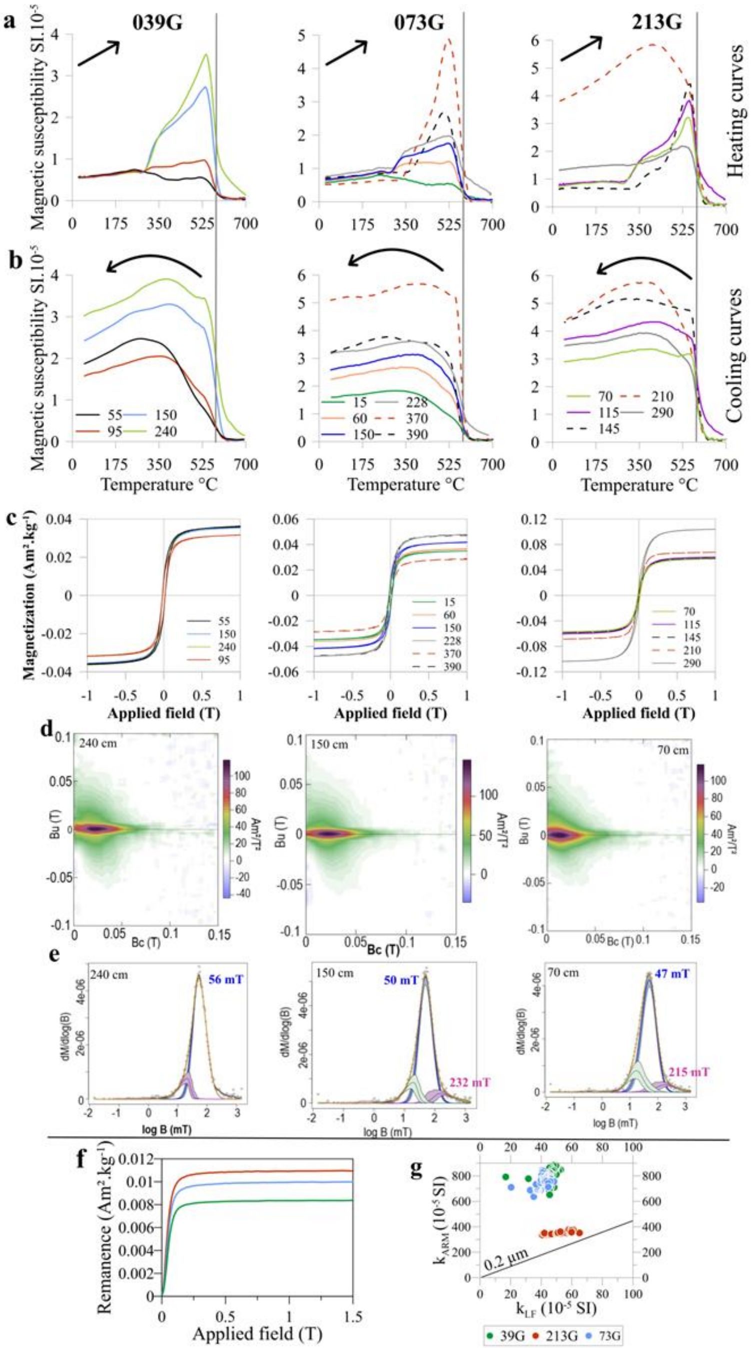

Figure 39. Rock magnetic results. (**a**) Temperature-dependent magnetic susceptibility measurements; heating curves up to 700°C. (**b**). Cooling curves down to room temperature. (**c**) Hysteresis loops. (**d**) FORC diagrams. (**e**) IRM acquisition curves unmixing. (**f**) IRM acquisition curves. (**g**) King plot. For a, b, c, d, e, left to right: cores 039G, 073G and 213G. Dotted lines in panels a, b and c represent sand samples.

2.5.4 Relative paleointensity determination

To estimate the normalized paleointensity profiles for the three cores, both ratio and slope methods (pseudo-Thellier; Tauxe et al., 1995; Valet & Meynadier, 1998) were attempted (Supporting information; Fig. S11) using the ChRM. For cores 073G and 039G, both methods yield similar profiles for ARM and IRM with low r^2 values (<0.15) between normalized NRM profiles and the normalizers (r^2ARM slightly higher for core 073G), whereas results for core 213G are more different. The slope method gives similar profiles for both ARM and IRM, while ARM and IRM profiles are more different for the ratio method, with r^2IRM being higher (0.54). The ARM ratio profile is more like the profiles obtained with the slope method. For that reason, ARM is considered a better normalizer for core 213G and the profile obtained with the slope method is used to represent the normalized paleointensity curve. ARM is used as the normalizer for the two other cores, because they have low r^2, with similar and comparable normalized intensities values. Sand layers are excluded from these calculations and are not considered in the subsequent paleomagnetic reconstructions.

2.5.5 Age depth model and identification of rapidly deposited layers

The chronology for cores 039G and 073G is presented in previous studies (Hansen et al., 2022; Pados-Dibattista et al., 2022; Supporting information Table S6, Table S7, Fig. S12, Fig. S13), we focus here on the age model for core 213G (Fig. 40). Sand layers are identified based on grain size parameters (median and D90), k_{ARM}/k_{LF}, Ti/Ca, Ca/Fe and Zr/Rb (Fig. 40). They are considered as RDL and were identified at 205-218 cm (RDL 1) and 135-158 cm (RDL 2) core depths. From the subbottom profiler data, it is further evident that larger mass flow deposits occur in the vicinity of the core (Supporting information; Fig. S6). XRF data have higher resolution (0.2 mm) than other data (magnetic data averaged on 8 cm, grain size analyses every 5 to 10 cm), so RDL identification relies mainly on the XRF data. In both cases, the base of RDL was identified because of abrupt changes, especially in XRF parameters. Both layers show gradual transition to hemipelagic sedimentation values at the top, therefore the top limit of a RDL is more difficult to determine. The top limit was fixed at the depth where the values of the different parameters (grain size, XRF, and magnetic parameters) are halfway back to normal for surrounding sediments, considering that above this limit hemipelagic sedimentation starts again. RDL 1 has negative inclination values at its base, which could be an indicator of turbidite deposition (St-Onge et al., 2004). For RDL 2, there is no negative value at the base of the layer, rather in the middle. For both RDLs, kARM/kLF decreases abruptly at the bottom of the layer and increases progressively toward the top of the layer. An abrupt grain size increase at the bottom of the layer and a progressive decrease toward the top is also observed. The sharp increase of XRF proxies at the base of each layer indicates that these layers could be turbidites. These RDL were excluded from the age model, because they represent instantaneous deposits. The presented paleomagnetic secular and relative paleointensity variation records presented here, therefore represent an event-free stratigraphy.

The resulting age model indicates that core 213G spans the last 10,900 years, corresponding to most of the Holocene Epoch. Sample ETH-126104.1.1 (140.5 cm, benthic foraminifera) located in RDL 2, was not used in the age model because. Based on the modelled median ages, sediment accumulation rates (SAR) were calculated and vary between 10 and 40 cm/kyr. The SAR increase toward the top probably reflects the lower ice cover during deglaciation. The low SAR at the top might be biased because it is uncertain how much sediment was lost during coring.

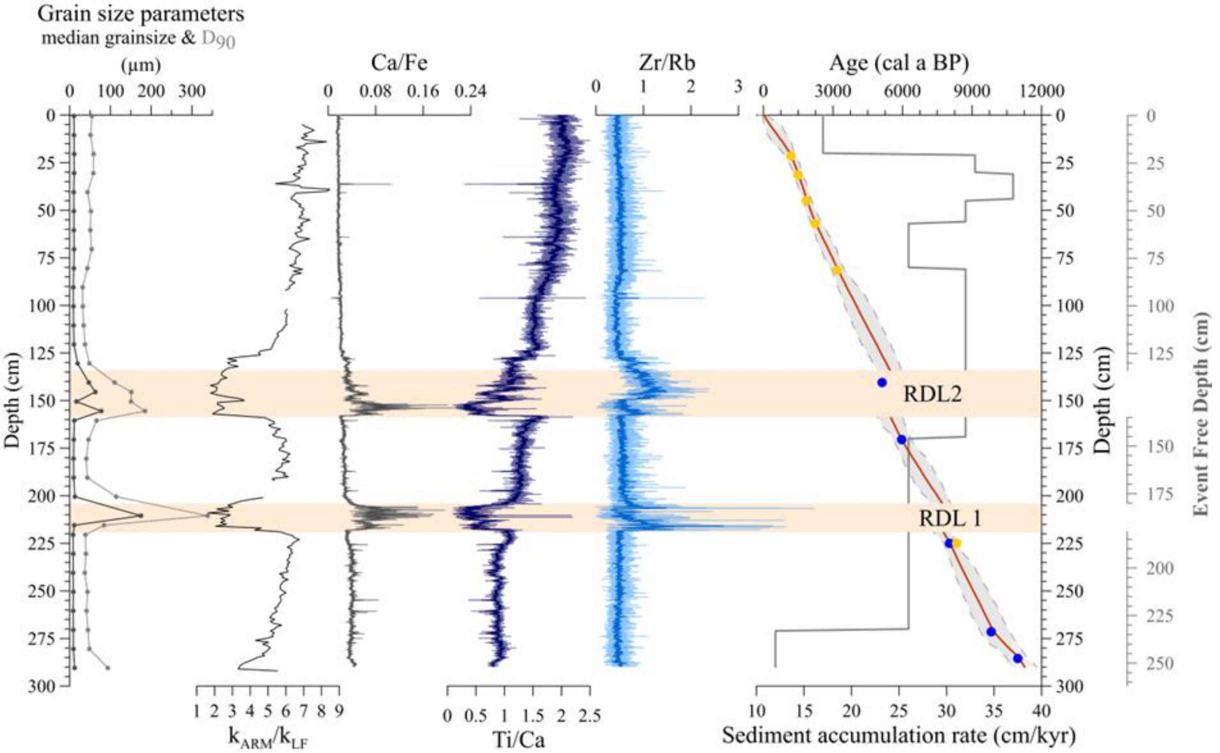

Figure 40. Core 213G age depth model. Horizontal beige bars represent the identified rapidly deposited layers (RDL). Left to right: grain size parameters median grain size (black) and D_{90} (grey) ; k_{ARM}/k_{LF}; Ca/Fe; Ti/Ca; Zr/Rb; Bayesian age-depth model. Grey curve = sediment accumulation rate (SAR, cm/kyr). Red curve = median modelled age. Dashed grey lines = min/max modelled ages. Yellow dots = ages obtained from shells. Blue dots = ages obtained from foraminifera. The age at 140.5 cm in RDL 2 is not used in the age-depth model. The Event Free Depth refers to the depth scale used to build the age-depth model, without the RDL, corresponding to an event-free stratigraphy (grey axis).

Cores 039G and 073G age models cover, respectively 3.9-13.3 ka and the last 9.4 kyr with SAR of 4-40 cm/kyr and 27-60 cm/kyr (Hansen et al., 2022; Pados-Dibattista et al., 2022). Hansen et al. (2022) indicated that, due to the ambiguity of the three ages at the top of core 039G, they focused on sediment below these ages for their paleo-reconstructions. However, paleomagnetism is used here to ascertain the age at the top of core 039G. Based on comparison of inclination, declination and RPI with the geomagnetic model CALS10k.2 (Constable et al., 2016), the North Karelian stack (Haltia-Hovi et al., 2010), FENNOSTACK (Snowball et al., 2007), GREENICE (Reilly et al., 2023) and core 073G (this study), we propose to include sample ETH-106022 (37.5 cm, radiocarbon date 2775 ± 70 cal a BP) in the age model (Supporting information, Fig. S12). Including this sample makes the age model more linear than with the other samples at the core top (Fig. S10b). Another point at the sediment surface (0 cm, -67 yr cal. BP) was added to the new age model, although it is possible that a few cm at the top of the gravity core was disturbed, lost, or compressed during coring.

2.5.6 Paleomagnetic secular and relative paleointensity variations

PSV and RPI comparisons among different records are presented in Fig. 41. Because of the lack of azimuthal orientation during coring, relative declination values were rotated to a mean of 0: the mean declination for the whole core was subtracted from each individual declination value, to obtain a mean of 0° for the entire core. At a very steep inclination, a small angular change can lead to large changes in declination (Reilly et al., 2019), explaining the large variability of the declination values, which must be interpreted carefully. In the case that record present similar feature, we calculated Pearson correlation coefficient (PCC) and associated p-values in R to support comparison between records.

All three cores from this study record inclination maxima at 2.5-3 ka, 1-1.5 ka (less visible in 213G) and 4.3-4.5 ka (073G and 213G) and inclination minima at around 7 ka and 9.9-10 ka in 039G and 073G (Fig. 41a). Cores 039G and 073G have similar variations (peaks at 6.5 ka, 8 ka, and an increase between 8-10 ka) with a high (PCC) of $r=0.82$ ($p\text{-value}<0.01$) even though core 039G inclination is globally lower than for core 073G, likely due to the presence of coarser grain size (21% of coarse silts and sands for core 073G and 37% for core 039G) . Because of the low SAR at the bottom of core 039G, RPI and PSV records have low amplitude variations between 11 and 13 ka. A declination peak around 3 ka and following minimum are common to all three records (Fig. 41b). This feature is described in other records, such as the North Karelian Stack (Haltia-Hovi et al 2010) and in other studies (Caricchi et al., 2020; 2022), which supports our interpretations that this feature is probably real, even though it does not represent a major directional swing. They all display lower amplitude variations for the 5-12 ka interval than for the 0-5 ka interval. The RPI decrease during the last 3 kyr is present in the three records, even though core 073G presents higher amplitude variations (Fig. 41c). The RPI peak at around 9 ka in core 073G is not present in the other two records. For the interval 10-12 ka, both cores 039G and 213G increase from 10-11ka and start decreasing around 11ka. That variation is small in core 039G because of the low SAR in that part of the core (Supporting Information; Fig. S12). Overall RPI records from the three cores correlate well (r=0.63 for 39G and 073G , r=0.57 for 039G and 213G and r=0.50 for 213G and 073G; p-values <0.01).

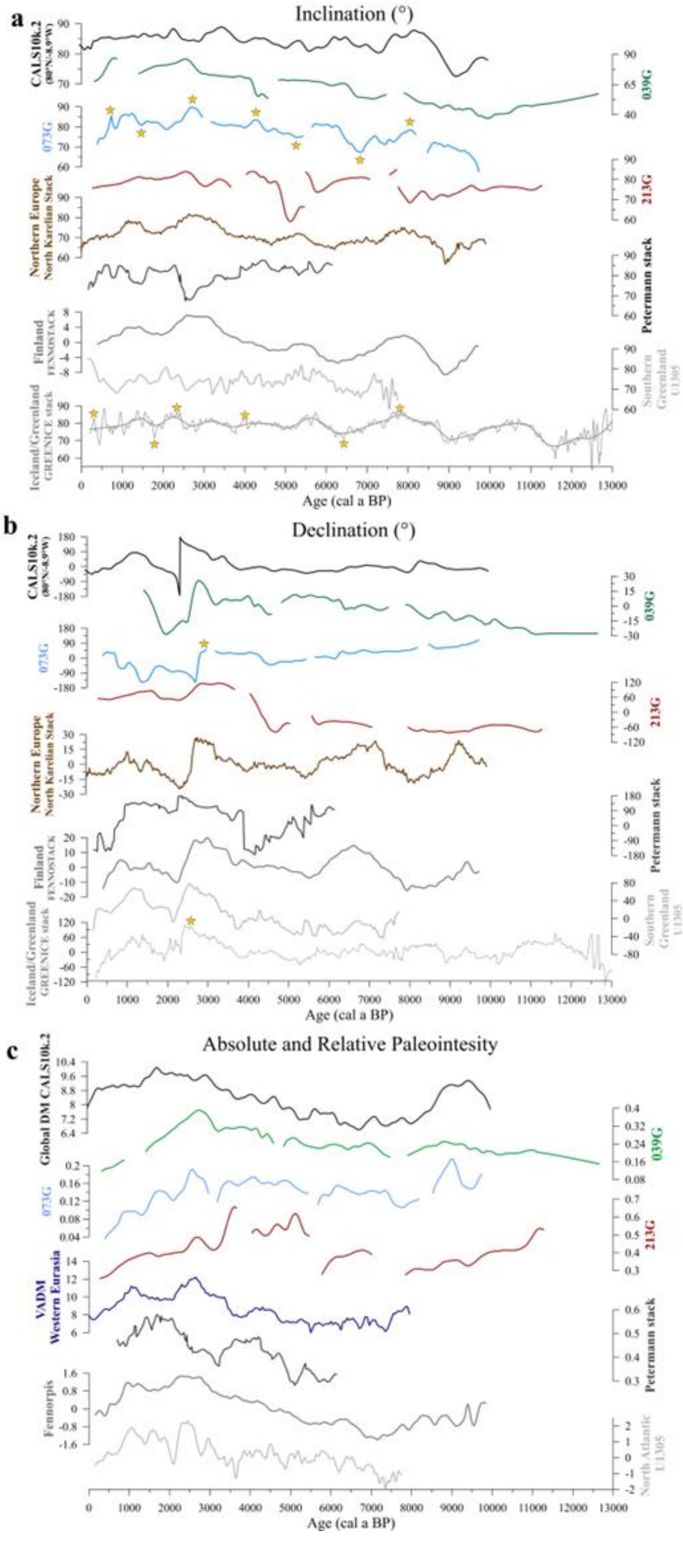
a
Inclination (°)
CALS10k.2 (80°N/-8.9°W)
039G
073G
213G
Northern Europe North Karelian Stack
Petermann stack
Finland FENNOSTACK
Southern Greenland U1305
Iceland/Greenland GREENICE stack
Age (cal a BP)
b
Declination (°)
CALS10k.2 (80°N/-8.9°W)
039G
073G
213G
Northern Europe North Karelian Stack
Petermann stack
Finland FENNOSTACK
Southern Greenland U1305
Iceland/Greenland GREENICE stack
Age (cal a BP)
c
Absolute and Relative Paleointesity
Global DM CALS10k.2
039G
073G
213G
VADM Western Eurasia
Petermann stack
Fennorpis
North Atlantic U1305
Age (cal a BP)
0 1000 2000 3000 4000 5000 6000 7000 8000 9000 10000 11000 12000 13000

Figure 41. Inclination, declination and relative paleointensity (RPI) comparisons. CALS10k.2 geomagnetic field model projected to the location of core 073G. Data include cores 039G (green), 073G (blue), and 213G (red), along with reference records from the North Karelian Stack, FENNOSTACK, U1305, and GREENICE Stack. Absolute paleointensity data from western Eurasia (VADM) are also included, based on archeological artefacts and volcanic products (Genevey et al., 2008). Yellow stars represent the features indicated in Fig. 42. The declination change in CALS10k.2 record does not reflect a real change, only a scaling choice according to the declination averaging to 0° and covering a maximum variation range of 360°.

2.6 DISCUSSION

2.6.1 PSV and RPI variations

The core 039G, 073G, and 213G records are compared to northern North Atlantic records (GREENICE15k, U1305; Stoner et al., 2013), northern Europe records (Finland and Sweden: FENNOSTACK, North Karelian Stack, NKS), the Petermann PSV and RPI stack (Girard et al., 2024; Reilly et al., 2019) and Western Eurasia virtual axial dipole moment (VADM) compilation from absolute paleointensity data from archeological artefacts and volcanic products (Genevey et al., 2008) in Fig. 41. The CALS10k.2 geomagnetic model curve shown is the model projection at the location of core 073G obtained using the GEOMAGIA database (Brown et al., 2015). Core 039G is presented with the updated age model from this study. The FENNOSTACK curves represent relative inclination and declination values, due to the geographical spread of cores used in the stack (Snowball et al., 2007).

Some observed variations are common to all records (northern North Atlantic to northern Europe) such as the 2.5-3 ka declination maximum which is visible in south Greenland (U1305), Finland (FENNOSTACK and NKS) and eastern Greenland (cores 039G, 073G and 213G). Other features are only common to regional records (declination maxima at around 6.5 ka and 9.5 ka in both Finland records). Lower SAR in cores 039G, 073G, and 213G could prevent the recording of rapid variations, or fluctuations may be caused by geomagnetic features with different intensities (global higher intensity for variations common to all records). The 2.5-3 ka declination maximum is observed during a high-inclination interval (>80°), which means it must be interpreted carefully, as small angular changes at very steep inclination can lead to large declination changes. This declination maxima seems to be common to the seven sediment records presented in Fig. 41b. It is also described in studies from the Barents Sea (Caricchi et al., 2020; 2022), but not in the CALS10k.2 geomagnetic model (declination decreases), which illustrates the importance of considering Arctic records to build geomagnetic models, to better constrain geomagnetic variations around the globe. The two inclination peaks at around 1-1.5 ka and 2.5-3 ka in cores 073G and 039G (and in core 213G with lower amplitude) are also observed in both northern European records (NKS and FENNOSTACK). Core 073G and 039G inclination records are similar to the Fennostack (r=0.71 and r=0.73 respectively, p-values<0.01) and NKS (r = 0.66 and r = 0.71 respectively, p-values<0.01). Core 073G depicts the same inclination high (low) as the Petermann stack at 1 ka (2 ka), but the records are different over the 2.5-3.5 ka interval. During this interval, a third flux lobe appears over Europe leading to strong intensity differences (Fig. 45c), which could influence the paleomagnetic directional variations.

Over the last 4 kyr, the 073G record has much larger amplitude declination variations than other reference records such as U1305 (-80; 80), NKS (-30; 30) or Fennostack (-20; 20). This can be explained by the high inclination values recorded by core 073G. For the rest of the record (10-5 ka), declination values are on a similar scale as the GREENICE record. Declinations in core 073G are similar to the GREENICE variations for the 9-5 ka interval, as well as for the last 5 kyr, but with a time offset (Fig. 42). The larger declination variations amplitude for the 0-5 ka interval compared to 5-12 ka are also evident in the CALS10k.2 model, but not by the Finnish and North Atlantic records. This could be explained by the lower SAR toward the bottom of cores 039G, 073G, and 213G. Finland records are both lacustrine and have high sedimentation rates, as does the GREENICE15k record (SAR >100 cm/kyr). Northern North Atlantic records also have lower declination variations. It could be that during that time, northern North Atlantic records were influenced by the same geomagnetic features, and that northern Europe variations originate from a different flux feature. The same similarities are observed in the RPI reconstructions: a similar global intensity decrease is observed during the last 3 kyr with two peaks which are well defined in 073G, FENNORPIS and western Eurasia VADM. Like declination, RPI amplitude variation is not constant, with lower amplitude before 5 ka, except for a peak in 073G at ~9 ka, which is also observed in the CALS10k.2 model.

When comparing core 073G inclination to the GREENICE15k smoothed signal (Fig. 42), we observe an offset of about 330 ± 60 yr across the Holocene ($r = 0.46$ on their own age model and $r = 0.57$ after applying a 330 year offset to 073G; p-values<0.01). Both records are from the same longitude which allows us to rule out the non-dipole or westward drift. This difference must be related to either ΔR changes through time and/or to the magnetic grain realignment after deposition during compaction and dewatering that leads to delayed magnetization acquisition by the sediment: post-depositional remanent magnetization (pDRM(Kent, 1973; Roberts et al., 2013; Verosub, 1977). The 073G record looks older than GREENICE15k (similar features observed in 073G before GREENICE15k), which could be consistent with the pDRM hypothesis: magnetic particles continue to orientate after deposition, which results in paleomagnetic recording in older surrounding sediments. When the sediment is dated using conventional radiocarbon methods, then paleomagnetic features appear older than they are. It is not possible here to disentangle the influence of the two phenomena, especially since data smoothing du to the response function of the magnetometer also contributes to this uncertainty. However, we can estimate the maximum ΔR variation value through time (supporting information; Fig. S14). In this region, the reservoir age could be impacted by water mass changes (proportion of PW or AAW/RAW in EGC) and freshwater runoff (Nioghalvfjerdsfjorden Glacier ice tongue extent; Pados-Dibattista et al., 2022). Increased meltwater mixing into the subsurface or bottom waters, as well as a lower Atlantic Water influx could cause the reservoir age to be higher.

Fig. 43 focuses on the last 5 kyr, during which core 073G record has higher amplitude variations and is similar to the GREENICE15k and NKS records. Inclination variations (Fig. 43a) are similar in the three records , synchronous in NKS and 073G (peaks at 1-1.5 ka, 2.5-

3 ka; low at around 2 ka and 4 ka, r=0.66, p-value<0.01) with a ~500 year offset with GREENICE15k (r=0.46, p-value<0.01). NKS and core 073G also have common declination variations (Fig. 43b), in particular the peak at 2.5-2.7 ka, also visible in GREENICE15k. That declination change looks more important in 073G and GREENICE than in NKS, probably because of the steep inclination values.

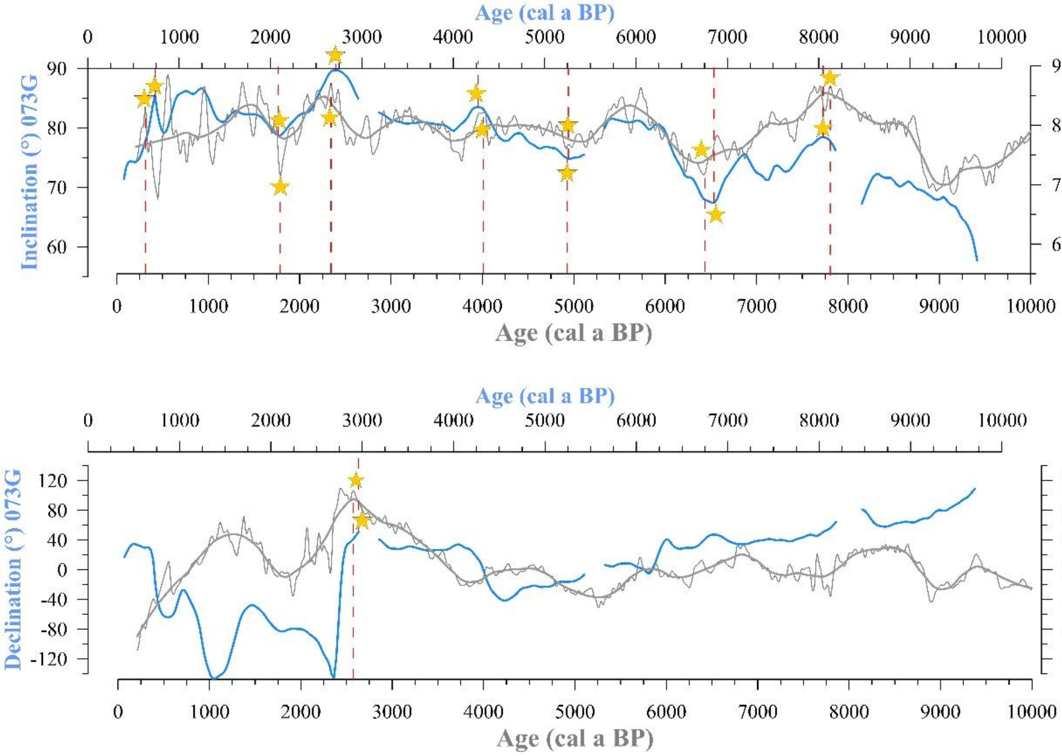

Figure 42. Comparison of inclination and declination records from core 073G (blue) and GREENICE15k (grey) record. Records are on their independent age models. The x-axis (age) is offset by 300 years to illustrate the match between the two records. Dashed red lines and yellow stars indicate similar features in both records on their independent age models. The features chosen are the tops of peaks and middle of troughs.

RPI from cores 073G and 039G record similar features: low intensity at 8 ka, then gradually increasing until 2.5-3 ka and then decreasing (Fig. 41c). This demonstrates the reproducibility of RPI recording between sites, with comparable environmental conditions, and use of the same normalizer. Intensity peak in 073G at 1, 2 and 9 ka are not visible in 039G record, which could be explained by the lower SAR at the top and bottom of this core.

Fig. 43c presents intensity variations (absolute and relative) in Europe (VADM western Eurasia), Northeastern Greenland (core 073G) and Northern North Atlantic (U1305), compared to smoothed cosmogenic isotope production rates including the average Northern Hemisphere ^{10}Be production rate and average global ^{14}C production rate (Nilsson et al., 2024). Production rates of these cosmogenic isotopes are inversely linked to geomagnetic field intensity, as well as the Sun's (e.g. Elsasser et al., 1956; Johnson, 1938). Intensity highs (lows) in core 073G correspond to low (high) ^{14}C and ^{10}Be production rates smoothed signals (±50 to 200 years), at 1, 1.5-2 and 2.5 cal ka BP (0.5, 1-1.5, ~2-2.5 cal ka BP). The RPI curve has PCC of $r = -0.7$ with ^{14}C, and $r = -0.58$ (p-values <0.01) with ^{10}Be production rate smoothed curves for the last 3 kyr. This corroborates the relationship between geomagnetic field intensity and the production rate of cosmogenic isotopes such as ^{10}Be and ^{14}C at millennial timescales (St-Onge et al., 2003), which also confirms a geomagnetic origin for this RPI record. 073G intensity highs at 1 and 2.5 ka are also visible both in western Eurasia and site U1305 records.

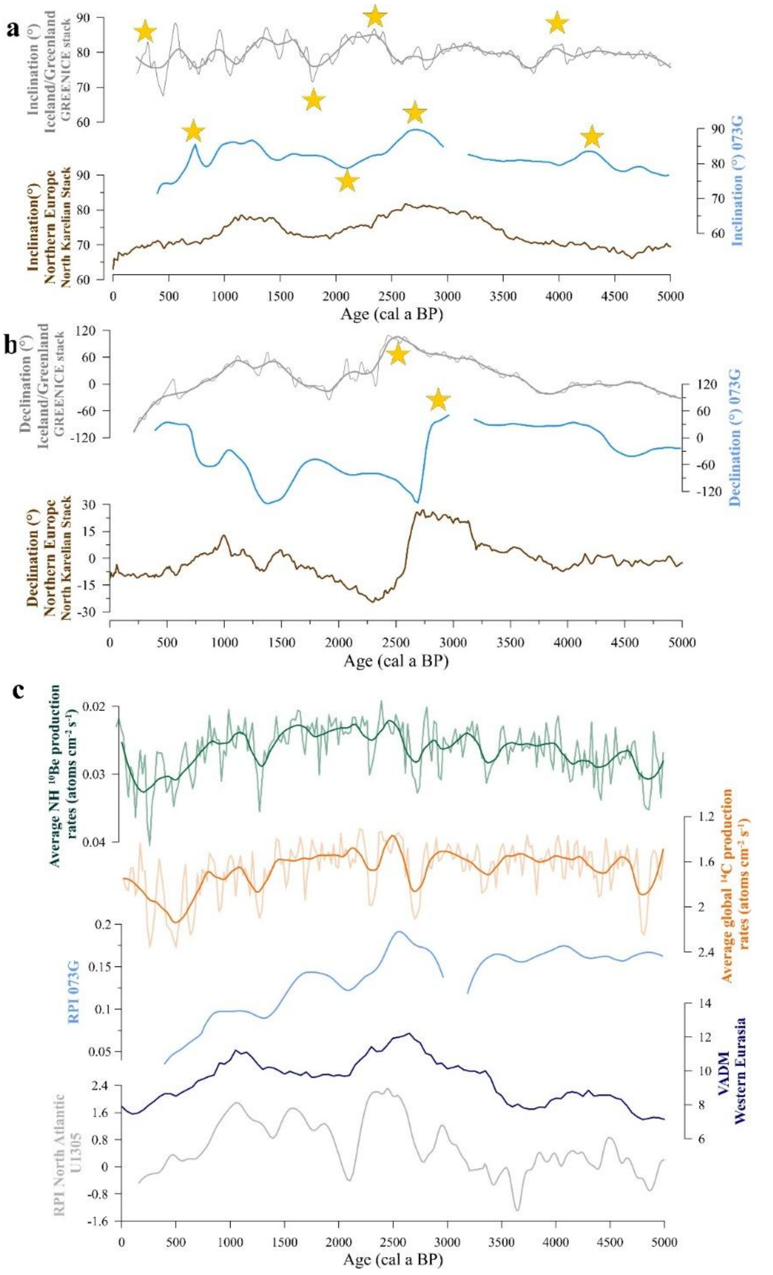

Figure 43. Comparison of inclination (a) and declination (b) records for GREENICE15k (grey), the North Karelian Stack (brown), and core 073G (blue) for the last 5 kyr. Comparison of paleointensities and cosmogenic isotope production rates for the last 5 kyr: average Northern Hemisphere ^{10}Be production rate (green), average global ^{14}C production rate (orange) (Nilsson et al., 2024), core 073G RPI record (blue), VADM Western Eurasia (dark blue), and U1305 RPI record (grey). Core 073G is plotted on its own independent chronology. Yellow stars indicate the same features as in Fig. 41 and 42.

Our new results confirm a link between geomagnetic field intensity and cosmogenic isotope production rates in the High Arctic, which indicates that High Arctic intensity records are similar beyond the regional scale, and potentially at hemispherical scale. Our data support previous observations from the northwestern Barents Sea (Sagnotti et al., 2011), that geomagnetic field behavior within the inner core tangent cylinder was not different (St-Onge and Stoner, 2011) than at lower northern latitudes over the last 5 kyr.

2.6.2 Virtual Geomagnetic Poles path

Virtual Geomagnetic Pole (VGP) path reconstructions were made here for core 073G. This core has the most similarities with published reference records, and it probably has the highest temporal resolution of PSV variations among our three records. VGP latitudes and longitudes were calculated with our directional data using the Excel spreadsheet from Mazaud (2005). Due to lower inclination values and increasing declination values toward the end of the record, the VGP projections focus on the last 8 kyr (Figs. S10, 8 & 9).

VGP latitude for core 073G is similar to the Petermann stack and U1305 for the 0-2 ka and 4-8 ka intervals (Supporting information; Fig. S15). However they have different variations for the 2-4 ka interval because core 073G does not contain the swing toward low European latitudes observed in the Petermann stack and U1305 records (Supporting information; Fig. S15). If we compare with the Petermann stack and U1305 on their magnetic age model, we observe an offset, with particular paleomagnetic features recorded before in core 073G and after in the Petermann stack and U1305, which supports the lock-in delay hypothesis, or ΔR variation in time. NKS and core 073G are the only records not characterized by the low latitude feature at 2.7 ka. Even though not all records contain that feature, they all record eastward VGP migration (Fig. 44). NKS and core 073G both record a low latitude feature at ~7.0 ka with a slight time offset (~200 years younger in 073G). During 0-2 ka time interval, VGP reconstructions for the five records display larger variations than during other time intervals, such as 6-8 ka. The core 073G VGP record migrates both toward the east and west (Fig. 44) as previously observed (Caricchi et al., 2022; Stoner et al., 2013).

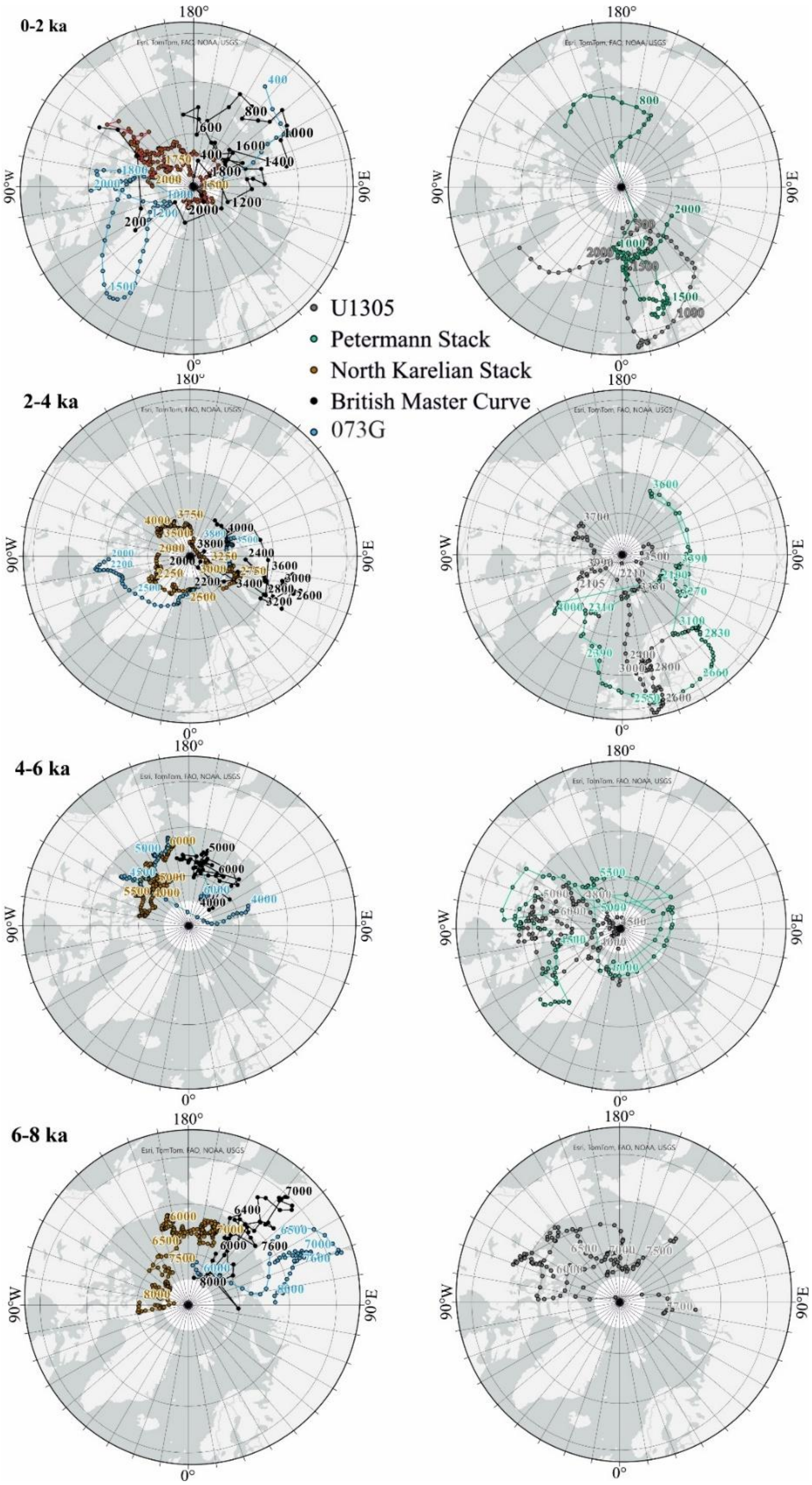

Figure 44. VGP projections from the different records for 0-2 ka, 2-4 ka, 4-6 ka, 6-8 ka time intervals.

In Fig. 45 we present the core 073G VGP record projected at 2 kyr intervals onto the radial field strength (µT) at the core-mantle boundary (CMB) from the CALS10k.2 geomagnetic model (Constable et al., 2016), at different times: 1.05 (Fig. 45a), 1.5 (Fig. 45b), 2.6 (Fig. 45c), 4 (Fig. 45d), 4.5 (Fig. 45e), 5.4 (Fig. 45f) and 6.6 cal ka BP (Fig. 45g). At 1.5 ka, the VGP was located above a geomagnetic flux lobe, at 1.05, 4.5, 5.4 and 6.6 ka VGP was located between two flux lobes and at 2.6 and 4 ka, VGP was located between three flux lobes. VGP appear to have greater migrations at times of higher geomagnetic global intensity (Fig. 45a-c), especially over the last 6 kyr. Our results support findings from recent studies from the Barents Sea (Caricchi et al., 2022) that demonstrate higher rates of VGP change over the 0.6-3 ka interval, which is also when the radial field intensity at the CMB is higher according to the CALS10k.2 model projections, compared to the 8-10 ka interval for example. VGP location above or between two geomagnetic flux lobes occurred at times of higher geomagnetic field intensity (>700 µT at 1.05 cal ka BP; >800 µT at 1.5 cal ka BP; 700-800 µT at 2.6 cal ka BP), suggesting as in previous studies (Caricchi et al., 2022; Girard et al., 2024), that intensity variations could be a factor in VGP migrations. Other records (Fig. 44) do not describe the same migration in relation to intensity variations. It is important to consider that most VGP reconstructions are based on relative declination values, which can lead to differences between records, even though most declination values average to a mean of zero.

By opposition to the Petermann Stack, core 073G from the northeastern Greenland Shelf records variations similar to the Northern European records, as well as GREENICE15k, indicating that PSV in northern Europe and on the northeastern Greenland margin might be driven by a similar local geomagnetic feature. This is particularly true for the last 4 kyr, which is also the time interval with higher geomagnetic field intensities (Fig. 45a-d). PSV signals from Nares Strait and the Barents Sea indicate VGP migration toward European mid-latitudes at times of lower RPI at the core location, which have been interpreted as influenced by the Levantine Iron Age Anomaly (Caricchi et al., 2022; Girard et al., 2024). Our results do not depict this variation toward lower latitude and show an intensity peak at that time, but all three records show eastward VGP migration (described as clockwise by Caricchi et al., 2022). This time interval is characterized by the appearance of a third geomagnetic flux lobe in Europe in addition to the Canadian and Siberian ones (Fig. 45c), and a low intensity zone in the Arctic Ocean toward the Chukchi Sea. These high intensity contrasts might make it difficult to disentangle their respective influence.

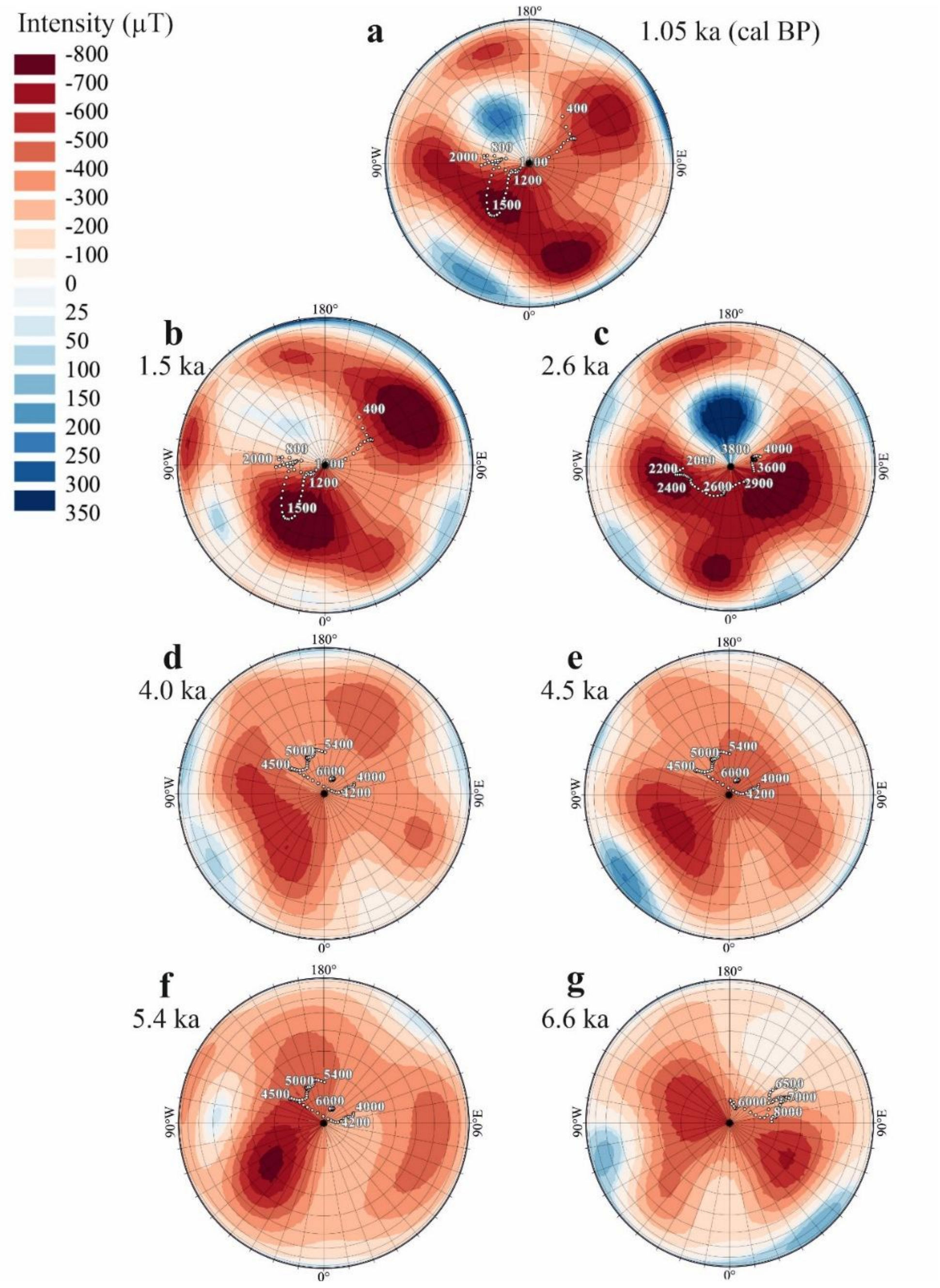

Figure 45. VGP positions reconstructed from core 073G at different time intervals: 0-2 ka (a, b), 2-4 ka (c), 4-6 ka (d, e, f), 6-8 ka (g), projected onto the radial field strength (intensity μT) at the core mantle boundary at 1.05 (a), 1.5 (b), 2.6 (c), 4.0 (d), 4.5 (e), 5.4 (f), and 6.6 (g) cal ka BP. The radial field strength is from the CALS10k.2 model (Constable et al., 2016).

2.7 CONCLUSIONS

We reconstructed PSV and RPI variations along the northeastern Greenland margin during the Holocene using three sediment cores, providing insights into regional geomagnetic field behavior. All records are characterized by similar inclination, declination and RPI features. Comparison with reference records from the North Atlantic, Finland, and Sweden, and the CALS10k.2 geomagnetic field model, highlights directional similarities between core 073G, GREENICE15k and records from Finland and Sweden, especially over the last 5 kyr. This suggests that PSV in Northeastern Greenland and Northern Europe were driven by similar millennial-scale hemispheric geomagnetic features. Correspondence between RPI and cosmogenic isotope production rates supports the geomagnetic origin of the RPI signal and its modulation of isotope production on millennial timescales. We also investigated a link between VGP migration, geomagnetic field intensity and geomagnetic flux lobe behavior. Our results, consistent with previous studies, suggest that geomagnetic flux lobes could influence VGP migration, especially at times of high field intensity. Finally, our study also illustrates that the geomagnetic field behavior in the High Arctic over the last 5 kyr was similar to that in the northern North Atlantic and to Europe.

2.8 ACKNOWLEDGMENTS

Juliette Girard received excellence scholarships from ISMER and the Programme de Bourses d'Excellence pour les Étudiants Étrangers of the Fonds de Recherche du Québec - Nature et Technologies (n°334533). Guillaume St-Onge, Jean-Carlos Montero-Serrano and Pierre Francus research is supported by discovery and northern supplement grants from the Natural Sciences and Engineering Research Council of Canada (NSERC). The research of Marit-Solveig Seidenkrantz and Christof Pearce is supported by the Independent Research Fund Denmark (grant no. 0135–00165 B (GreenShelf project), the European Union's Horizon 2020 research and innovation program under Grant Agreement No. 869383 (ECOTIP), and the European Union's Horizon Europe research and innovation program under Grant Agreement No. 101136480 (SEA-Quester). The expedition was funded by the

Danish Centre for Marine Research, the Natural Science and Engineering Research Council of Canada and the Independent Research Fund Denmark (G-Ice Project (grant no. 7014-00113 B/FNU). We thank the captain, crew and scientists of the R/V Dana during the NorthGreen2017 Expedition, with sampling permission from the Government of Greenland. We are thankful to Quentin Beauvais (ISMER) and Yohan Guyodo (IPGP) for their help with paleomagnetic measurements, Dominique Lavallée (ISMER) for grain size analysis, and to Quentin Duboc (ISMER) for discussions on lithologies. Lasse Nygaard Eriksen (Aarhus U.) aided in samples collection for radiocarbon ages. We are thankful to Prof. Stefanie Brachfled, to Prof. Andrew Roberts, to an anonymous reviewer and to the editor Dr. Mark Dekkers for their comments that greatly improved our manuscript.

2.9 OPEN RESEARCH

Paleomagnetic data presented in that study (PSV and RPI) are available in the PANGAEA repository, in three datasets, one for each core (Girard et al., 2025).

2.10 CONFLICT-OF-INTEREST STATEMENT

The authors have no conflicts of interest to disclose.

2.11 REFERENCES

Banerjee, S. K., King, J., & Marvin, J. (1981). A rapid method for magnetic granulometry with applications to environmental studies. Geophysical Research Letters, 8(4), 333–336. https://doi.org/10.1029/GL008i004p00333

Bendtsen, J., Mortensen, J., & Rysgaard, S. (2014). Seasonal surface layer dynamics and sensitivity to runoff in a high Arctic fjord (Young Sound/Tyrolerfjord, 74°N). Journal of Geophysical Research: Oceans, 119(9), 6461–6478. https://doi.org/10.1002/2014JC010077

Bloemendal, J., Lamb, B., & King, J. (1988). Paleoenvironmental implications of rock magnetic properties of late Quaternary sediment cores from the eastern Equatorial Atlantic. Paleoceanography, 3(1), 61–87. https://doi.org/10.1029/PA003i001p00061

Blott, S. J., & Pye, K. (2001). GRADISTAT: A grain size distribution and statistics package for the analysis of unconsolidated sediments. Earth Surface Processes and Landforms, 26(11), 1237–1248. https://doi.org/10.1002/esp.261

Brown, M. C., Donadini, F., Korte, M., Nilsson, A., Korhonen, K., Lodge, A., Lengyel, S. N., & Constable, C. G. (2015). GEOMAGIA50.v3: 1. general structure and modifications to the archeological and volcanic database. Earth, Planets and Space, 67(1), 83. https://doi.org/10.1186/s40623-015-0232-0

Caricchi, C., Campuzano, S. A., Sagnotti, L., Macrì, P., & Lucchi, R. G. (2022). Reconstruction of the Virtual Geomagnetic Pole (VGP) path at high latitude for the last 22 kyr: The role of radial field flux patches as VGP attractor. Earth and Planetary Science Letters, 595, 117762. https://doi.org/10.1016/j.epsl.2022.117762

Caricchi, C., Sagnotti, L., Campuzano, S. A., Lucchi, R. G., Macrì, P., Rebesco, M., & Camerlenghi, A. (2020). A refined age calibrated paleosecular variation and relative paleointensity stack for the NW Barents Sea: Implication for geomagnetic field behavior during the Holocene. Quaternary Science Reviews, 229, 106133. https://doi.org/10.1016/j.quascirev.2019.106133

Constable, C., Korte, M., & Panovska, S. (2016). Persistent high paleosecular variation activity in southern hemisphere for at least 10 000 years. Earth and Planetary Science Letters, 453, 78–86. https://doi.org/10.1016/j.epsl.2016.08.015

Croudace, I. W., & Rothwell, R. G. (Eds.). (2015). Micro-XRF Studies of Sediment Cores: Applications of a non-destructive tool for the environmental sciences (Vol. 17). Springer Netherlands. https://doi.org/10.1007/978-94-017-9849-5

Dunlop, D. J., & Ozdemir, O. (2007). Magnetization in rocks and minerals. In Geomagnetism, Treatise on Geophysics (Elsevier, Vol. 5, pp. 277–336). G. Scubert.

Elsasser, W., Ney, E. P., & Winckler, J. R. (1956). Cosmic-Ray Intensity and Geomagnetism. Nature, 178(4544), 1226–1227. https://doi.org/10.1038/1781226a0

GEBCO Compilation Group. (2023). GEBCO 2023 Grid [Dataset]. https://doi.org/doi:10.5285/f98b053b-0cbc-6c23-e053-6c86abc0af7b

Genevey, A., Gallet, Y., Constable, C. G., Korte, M., & Hulot, G. (2008). ArcheoInt: An upgraded compilation of geomagnetic field intensity data for the past ten millennia and its application to the recovery of the past dipole moment: Geomagnetic Field Intensity Data Compilation. Geochemistry, Geophysics, Geosystems, 9(4). https://doi.org/10.1029/2007GC001881

Girard, J., Reilly, B. T., St-Onge, G., Lagroix, F., Montero-Serrano, J., Stoner, J. S., & Jennings, A. E. (2024). Paleomagnetic Secular Variations in North Greenland Around 81°N Over the Last 6,000 Years. Geochemistry, Geophysics, Geosystems, 25(10), e2024GC011620. https://doi.org/10.1029/2024GC011620

Girard, J., St-Onge, G., Pearce, C., Seidenkrantz, M.-S., Lagroix, F., Montero-Serrano, J.-C., Francus, P., & Andresen, K. J. (2025). Holocene paleomagnetic data (inclination, declination, relative paleointensity and virtual geomagnetic pole positions) from three marine sediment cores collected on the North East Greenland Shelf during Expedition NorthGreen2017 [Dataset]. https://doi.org/10.1594/PANGAEA.983315

Haltia-Hovi, E., Nowaczyk, N., & Saarinen, T. (2010). Holocene palaeomagnetic secular variation recorded in multiple lake sediment cores from eastern Finland. Geophysical Journal International, 180(2), 609–622. https://doi.org/10.1111/j.1365-246X.2009.04456.x

Hansen, K. E., Lorenzen, J., Davies, J., Wacker, L., Pearce, C., & Seidenkrantz, M.-S. (2022). Deglacial to Mid Holocene environmental conditions on the northeastern Greenland shelf, western Fram Strait. Quaternary Science Reviews, 293, 107704. https://doi.org/10.1016/j.quascirev.2022.107704

Hansen, K. E., Pearce, C., & Seidenkrantz, M.-S. (2023). Response of Arctic benthic foraminiferal traits to past environmental changes. Scientific Reports, 13(1), 22135. https://doi.org/10.1038/s41598-023-47603-w

Harrison, R. J., & Feinberg, J. M. (2008). FORCinel: An improved algorithm for calculating first-order reversal curve distributions using locally weighted regression smoothing: FORCINEL ALGORITHM. Geochemistry, Geophysics, Geosystems, 9(5). https://doi.org/10.1029/2008GC001987

Heaton, T. J., Köhler, P., Butzin, M., Bard, E., Reimer, R. W., Austin, W. E. N., Bronk Ramsey, C., Grootes, P. M., Hughen, K. A., Kromer, B., Reimer, P. J., Adkins, J., Burke, A., Cook, M. S., Olsen, J., & Skinner, L. C. (2020). Marine20—The Marine Radiocarbon Age Calibration Curve (0–55,000 cal BP). Radiocarbon, 62(4), 779–820. https://doi.org/10.1017/RDC.2020.68

Higgins, A. K. (2015). Descriptive text to the Geological map of Greenland, 1:500 000, Lambert Land, Sheet 9. GEUS.

Ingolf Eide, L., & Martin, S. (1975). The formation of Brine Drainage Features in Young Sea Ice. Journal of Glaciology, 14, 137–154. https://doi.org/doi:10.3189/S0022143000013460

Johannessen, O. M. (1986). Brief Overview of the Physical Oceanography. In The Nordic Seas (pp. 103–128). Springer, New York, NY. https://doi.org/10.1007/978-1-4615-8035-5_4

Johnson, T. H. (1938). Cosmic-Ray Intensity and Geomagnetic Effects. Reviews of Modern Physics, 10(4), 193–244. https://doi.org/10.1103/RevModPhys.10.193

Jutterström, S., & Anderson, L. G. (2005). The saturation of calcite and aragonite in the Arctic Ocean. Marine Chemistry, 94(1), 101–110. https://doi.org/10.1016/j.marchem.2004.08.010

Kent, D. V. (1973). Post-depositional Remanent Magnetisation in Deep-sea Sediment. Nature, 246(5427), 32–34. https://doi.org/10.1038/246032a0

King, J., Banerjee, S. K., Marvin, J., & Özdemir, Ö. (1982). A comparison of different magnetic methods for determining the relative grain size of magnetite in natural materials: Some results from lake sediments. Earth and Planetary Science Letters, 59(2), 404–419. https://doi.org/10.1016/0012-821X(82)90142-X

King, J. W., Banerjee, S. K., & Marvin, J. (1983). A new rock-magnetic approach to selecting sediments for geomagnetic paleointensity studies: Application to paleointensity for the last 4000 years. Journal of Geophysical Research: Solid Earth, 88(B7), 5911–5921. https://doi.org/10.1029/JB088iB07p05911

Kirschvink, J. L. (1980). The least-squares line and plane and the analysis of palaeomagnetic data. Geophysical Journal International, 62(3), 699–718. https://doi.org/10.1111/j.1365-246X.1980.tb02601.x

Livermore, P. W., Finlay, C. C., & Bayliff, M. (2020). Recent north magnetic pole acceleration towards Siberia caused by flux lobe elongation. Nature Geoscience, 13(5), 387–391. https://doi.org/10.1038/s41561-020-0570-9

Maxbauer, D. P., Feinberg, J. M., & Fox, D. L. (2016). MAX UnMix: A web application for unmixing magnetic coercivity distributions. Computers & Geosciences, 95, 140–145. https://doi.org/10.1016/j.cageo.2016.07.009

Mazaud, A. (2005). User-friendly software for vector analysis of the magnetization of long sediment cores: Software for vector analysis. Geochemistry, Geophysics, Geosystems, 6(12). https://doi.org/10.1029/2005GC001036

Merrill, R. T., & McFadden, P. L. (2003). The geomagnetic axial dipole field assumption. Physics of the Earth and Planetary Interiors, 139(3–4), 171–185. https://doi.org/10.1016/j.pepi.2003.07.016

Nilsson, A., Nguyen, L., Panovska, S., Herbst, K., Zheng, M., Suttie, N., & Muscheler, R. (2024). Holocene solar activity inferred from global and hemispherical cosmic-ray proxy records. Nature Geoscience, 17(7), 654–659. https://doi.org/10.1038/s41561-024-01467-5

Olsen, N., & Mandea, M. (2007). Will the magnetic North Pole move to Siberia? Eos, Transactions American Geophysical Union, 88(29), 293–293. https://doi.org/10.1029/2007EO290001

Pados-Dibattista, T., Pearce, C., Detlef, H., Bendtsen, J., & Seidenkrantz, M.-S. (2022). Holocene palaeoceanography of the Northeast Greenland shelf. Climate of the Past, 18(1), 103–127. https://doi.org/10.5194/cp-18-103-2022

Panovska, S., Korte, M., & Constable, C. G. (2019). One Hundred Thousand Years of Geomagnetic Field Evolution. Reviews of Geophysics, 57(4), 1289–1337. https://doi.org/10.1029/2019RG000656

Pearce, C., Özdemir, K. S., Forchhammer Mathiasen, R., Detlef, H., & Olsen, J. (2023). The marine reservoir age of Greenland coastal waters. Geochronology, 5(2), 451–465. https://doi.org/10.5194/gchron-5-451-2023

Philippe, É. G. H., Valet, J., St-Onge, G., & Thevarasan, A. (2018). Are Paleomagnetic Records From U-Channels Appropriate for Studies of Reversals and Excursions? Geochemistry, Geophysics, Geosystems, 19(11), 4130–4142. https://doi.org/10.1029/2018GC007803

Pike, C. R., Roberts, A. P., & Verosub, K. L. (1999). Characterizing interactions in fine magnetic particle systems using first order reversal curves. Journal of Applied Physics, 85(9), 6660–6667. https://doi.org/10.1063/1.370176

Ramsey, C. B. (2008). Deposition models for chronological records. Quaternary Science Reviews, 27(1–2), 42–60. https://doi.org/10.1016/j.quascirev.2007.01.019

Ramsey, C. B., & Lee, S. (2013). Recent and Planned Developments of the Program OxCal. Radiocarbon, 55(2), 720–730. https://doi.org/10.1017/s0033822200057878

Reilly, B. T., Stoner, J. S., Mix, A. C., Walczak, M. H., Jennings, A., Jakobsson, M., Dyke, L., Glueder, A., Nicholls, K., Hogan, K. A., Mayer, L. A., Hatfield, R. G., Albert, S., Marcott, S., Fallon, S., & Cheseby, M. (2019). Holocene break-up and reestablishment of the Petermann Ice Tongue, Northwest Greenland. Quaternary Science Reviews, 218, 322–342. https://doi.org/10.1016/j.quascirev.2019.06.023

Reilly, B. T., Stoner, J. S., Ólafsdóttir, S., Jennings, A., Hatfield, R., Kristjánsdóttir, G. B., & Geirsdóttir, Á. (2023). The Amplitude and Timescales of 0–15 ka Paleomagnetic Secular Variation in the Northern North Atlantic. Journal of Geophysical Research: Solid Earth, 128(6), e2023JB026891. https://doi.org/10.1029/2023JB026891

Ribeiro, S., Sejr, M. K., Limoges, A., Heikkilä, M., Andersen, T. J., Tallberg, P., Weckström, K., Husum, K., Forwick, M., Dalsgaard, T., Massé, G., Seidenkrantz, M.-S., & Rysgaard, S. (2017). Sea ice and primary production proxies in surface sediments from a High Arctic Greenland fjord: Spatial distribution and implications for palaeoenvironmental studies. Ambio, 46(S1), 106–118. https://doi.org/10.1007/s13280-016-0894-2

Roberts, A. P., Almeida, T., Church, N. S., Harrison, R. J., Heslop, D., Li, Y., Li, J., Muxworthy, A. R., Williams, W., & Zhao, X. (2017). Resolving the Origin of Pseudo-Single Domain Magnetic Behavior. Journal of Geophysical Research: Solid Earth, 122, 9534–9558. https://doi.org/10.1002/2017JB014860

Roberts, A. P., Heslop, D., Zhao, X., Oda, H., Egli, R., Harrison, R. J., Hu, P., Muxworthy, A. R., & Sato, T. (2022). Unlocking information about fine magnetic particle assemblages from first-order reversal curve diagrams: Recent advances. Earth-Science Reviews, 227, 103950. https://doi.org/10.1016/j.earscirev.2022.103950

Roberts, A. P., Hu, P., Harrison, R. J., Heslop, D., Muxworthy, A. R., Oda, H., Sato, T., Tauxe, L., & Zhao, X. (2019). Domain State Diagnosis in Rock Magnetism: Evaluation of Potential Alternatives to the Day Diagram. Journal of Geophysical Research: Solid Earth, 124(6), 5286–5314. https://doi.org/10.1029/2018JB017049

Roberts, A. P., Tauxe, L., & Heslop, D. (2013). Magnetic paleointensity stratigraphy and high-resolution Quaternary geochronology: Successes and future challenges. Quaternary Science Reviews, 61, 1–16. https://doi.org/10.1016/j.quascirev.2012.10.036

Rudels, B., Björk, G., Nilsson, J., Winsor, P., Lake, I., & Nohr, C. (2005). The interaction between waters from the Arctic Ocean and the Nordic Seas north of Fram Strait and along the East Greenland Current: Results from the Arctic Ocean-02 Oden expedition. Journal of Marine Systems, 55(1–2), 1–30. https://doi.org/10.1016/j.jmarsys.2004.06.008

Rysgaard, S., Bendtsen, J., Mortensen, J., & Sejr, M. K. (2018). High geothermal heat flux in close proximity to the Northeast Greenland Ice Stream. Scientific Reports, 8(1), 1344. https://doi.org/10.1038/s41598-018-19244-x

Sagnotti, L., Macrì, P., Lucchi, R., Rebesco, M., & Camerlenghi, A. (2011). A Holocene paleosecular variation record from the northwestern Barents Sea continental margin: Holocene PSV from NW Barents Sea. Geochemistry, Geophysics, Geosystems, 12(11). https://doi.org/10.1029/2011GC003810

Seidenkrantz, M.-S., Andersen, J. R., Andresen, K. J., Bendtsen, J., Brice, C., Ellegard, M., Eriksen, L. N., & Gariboldi, K. (2018). NorthGreen2017, a marine research expedition to NE Greenland onboard R/V Dana—Cruise report [Cruise report]. Danish Center for Marine Research.

Snowball, I., Zillén, L., Ojala, A., Saarinen, T., & Sandgren, P. (2007). FENNOSTACK and FENNORPIS: Varve dated Holocene palaeomagnetic secular variation and relative palaeointensity stacks for Fennoscandia. Earth and Planetary Science Letters, 255(1–2), 106–116. https://doi.org/10.1016/j.epsl.2006.12.009

Stoner, J. S., Channell, J. E. T., Mazaud, A., Strano, S. E., & Xuan, C. (2013). The influence of high-latitude flux lobes on the Holocene paleomagnetic record of IODP Site U1305 and the northern North Atlantic: Paleomagnetic Record of the N. Atlantic. Geochemistry, Geophysics, Geosystems, 14(10), 4623–4646. https://doi.org/10.1002/ggge.20272

Stoner, J. S., & St-Onge, G. (2007). Chapter Three Magnetic Stratigraphy in Paleoceanography: Reversals, Excursions, Paleointensity, and Secular Variation. In C. Hillaire–Marcel & A. De Vernal (Eds.), Developments in Marine Geology (Vol. 1, pp. 99–138). Elsevier. https://doi.org/10.1016/S1572-5480(07)01008-1

St-Onge, G., Mulder, T., Piper, D. J. W., Hillaire-Marcel, C., & Stoner, J. S. (2004). Earthquake and flood-induced turbidites in the Saguenay Fjord (Québec): A Holocene paleoseismicity record. Quaternary Science Reviews, 23(3–4), 283–294. https://doi.org/10.1016/j.quascirev.2003.03.001

St-Onge, G., & Stoner, J. (2011). Paleomagnetism Near the North Magnetic Pole: A Unique Vantage Point for Understanding the Dynamics of the Geomagnetic Field and Its Secular Variations. Oceanography, 24(3), 42–50. https://doi.org/10.5670/oceanog.2011.53

St-Onge, G., Stoner, J. S., & Hillaire-Marcel, C. (2003). Holocene paleomagnetic records from the St. Lawrence Estuary, eastern Canada: Centennial- to millennial-scale geomagnetic modulation of cosmogenic isotopes. Earth and Planetary Science Letters, 209(1–2), 113–130. https://doi.org/10.1016/S0012-821X(03)00079-7

Tarduno, J. A., Cottrell, R. D., Bono, R. K., Oda, H., Davis, W. J., Fayek, M., Erve, O. V. 'T, Nimmo, F., Huang, W., Thern, E. R., Fearn, S., Mitra, G., Smirnov, A. V., & Blackman, E. G. (2020). Paleomagnetism indicates that primary magnetite in zircon records a strong Hadean geodynamo. Proceedings of the National Academy of Sciences, 117(5), 2309–2318. https://doi.org/10.1073/pnas.1916553117

Tauxe, L. (1993). Sedimentary records of relative paleointensity of the geomagnetic field: Theory and practice. Reviews of Geophysics, 31(3), 319–354. https://doi.org/10.1029/93RG01771

Tauxe, L., Mullender, T. A. T., & Pick, T. (1996). Potbellies, wasp-waists, and superparamagnetism in magnetic hysteresis. Journal of Geophysical Research: Solid Earth, 101(B1), 571–583. https://doi.org/10.1029/95JB03041

Tauxe, L., Pick, T., & Kok, Y. S. (1995). Relative paleointenisty in sediments: A pseudo-Thellier approach. Geophysical Research Letters, 22(21), 2885–2888. https://doi.org/10.1029/95GL03166

Thompson. (1984). A global review of paleomagnetic results from wet lake sediments. In Lake sediments and environmental history: Studies in palaeolimnology and palaeoecology in honour of Winifred Tutin (E. Y. Haworth, J. W. G. Lund, pp. 145–164). University of Minnesota Press.

Turner, G. M., & Thompson, R. (1981). Lake sediment record of the geomagnetic secular variation in Britain during Holocene times. Geophysical Journal International, 65(3), 703–725. https://doi.org/10.1111/j.1365-246X.1981.tb04879.x

Valet, J.-P. (2003). Time variations in geomagnetic intensity: TIME VARIATIONS IN GEOMAGNETIC INTENSITY. Reviews of Geophysics, 41(1). https://doi.org/10.1029/2001RG000104

Valet, J.-P., & Meynadier, L. (1998). A comparison of different techniques for relative paleointensity. Geophysical Research Letters, 25(1), 89–92. https://doi.org/10.1029/97GL03489

Verosub, K. L. (1977). Depositional and postdepositional processes in the magnetization of sediments. Reviews of Geophysics, 15(2), 129–143. https://doi.org/10.1029/RG015i002p00129

Xuan, C., & Channell, J. E. T. (2009). UPmag: MATLAB software for viewing and processing u channel or other pass-through paleomagnetic data. Geochemistry, Geophysics, Geosystems, 10(10). https://doi.org/10.1029/2009GC002584

Zijderveld, J. (1967). AC demagnetisation of rocks: Analysis of results. Methods in Paleomagnetism.

SUPPORTING INFORMATION (FIGURES AND TABLES)

Figures were made using Golden Software Grapher, CorelDraw, S&P Global Kingdom, QGIS, Adobe Illustrator and Microsoft Excel. Data presented here supports the quality of the paleomagnetic measurements and relative paleointensity determination, as well as the location of the sediment cores, nature of the subbottom and depositional context of each core and age-depth models previously published for cores 039G and 073G.

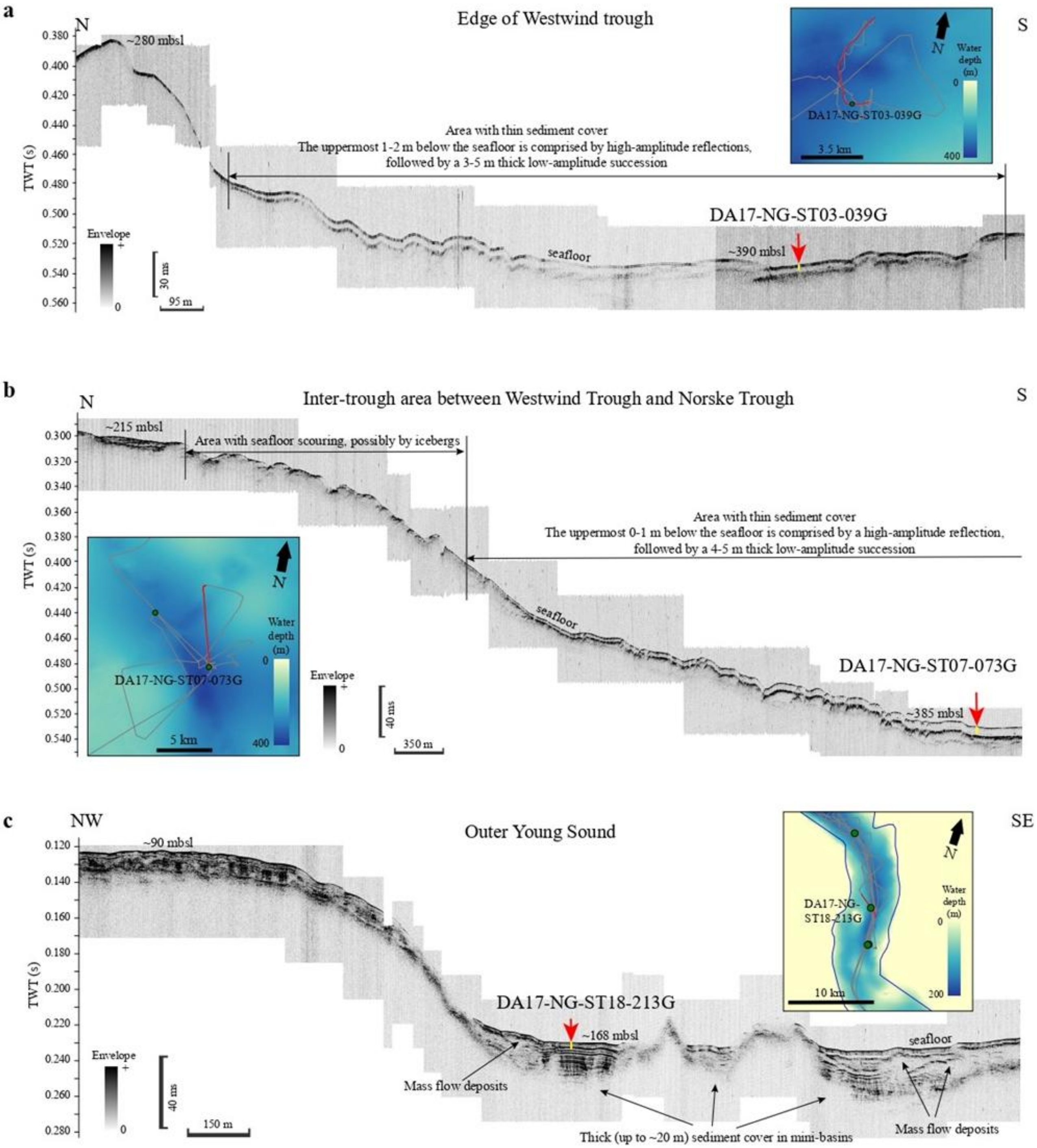
a
N
Edge of Westwind trough
S
~280 mbsl
Area with thin sediment cover
The uppermost 1-2 m below the seafloor is comprised by high-amplitude reflections, followed by a 3-5 m thick low-amplitude succession
DA17-NG-ST03-039G
~390 mbsl
seafloor
TWT (s)
0.380
0.400
0.420
0.440
0.460
0.480
0.500
0.520
0.540
0.560
Envelope
+
0
30 ms
95 m
N
Water depth (m)
0
400
DA17-NG-ST03-039G
3.5 km
b
N
Inter-trough area between Westwind Trough and Norske Trough
S
~215 mbsl
Area with seafloor scouring, possibly by icebergs
Area with thin sediment cover
The uppermost 0-1 m below the seafloor is comprised by a high-amplitude reflection, followed by a 4-5 m thick low-amplitude succession
seafloor
DA17-NG-ST07-073G
~385 mbsl
TWT (s)
0.300
0.320
0.340
0.360
0.380
0.400
0.420
0.440
0.460
0.480
0.500
0.520
0.540
N
Water depth (m)
0
400
DA17-NG-ST07-073G
5 km
Envelope
+
0
40 ms
350 m
c
NW
Outer Young Sound
SE
~90 mbsl
DA17-NG-ST18-213G
~168 mbsl
seafloor
Mass flow deposits
Thick (up to ~20 m) sediment cover in mini-basins
Mass flow deposits
TWT (s)
0.120
0.140
0.160
0.180
0.200
0.220
0.240
0.260
0.280
Envelope
+
0
40 ms
150 m
N
Water depth (m)
0
200
DA17-NG-ST18-213G
10 km

Figure S6. Subbottom profiles at the three coring locations showing the depositional context for each core. Vertical axis show two-way-travel-time (TWT) in seconds. Inset maps show the ship track and subbottom profiles (grey lines) around the coring stations (green dots) with the red lines highlighting the profiles shown in the figure. Bathymetry data from International Bathymetric Chart of the Arctic Ocean (IBCAO), version 5 (Jakobson et al., 2024). a) Core DA17-NG-ST03-039G is situated at the edge of the Westwind Through in a local depression. The core penetrated a sedimentary drape succession characterized by low amplitude to transparent reflections likely representing pelagic sedimentation. b) Core DA17-NG-ST07-073G is situated in a local depression in the inter-trough area between the Westwind and Norske Trough. Like core 039G, core 073G was taken in a local depocenter for a low-amplitude pelagic succession. Further uphill, the subbottom profiler data show indications of seafloor scouring – potentially by icebergs. c) Core DA17-NG-ST18-213G was retrieved in the outer parts of Young Sound centrally in the fjord, in a local mini basin with a thick hemipelagic sedimentary succession characterized by parallel high-amplitude continuous reflections. Buried mass flow deposits appear as transparent mounded structures.

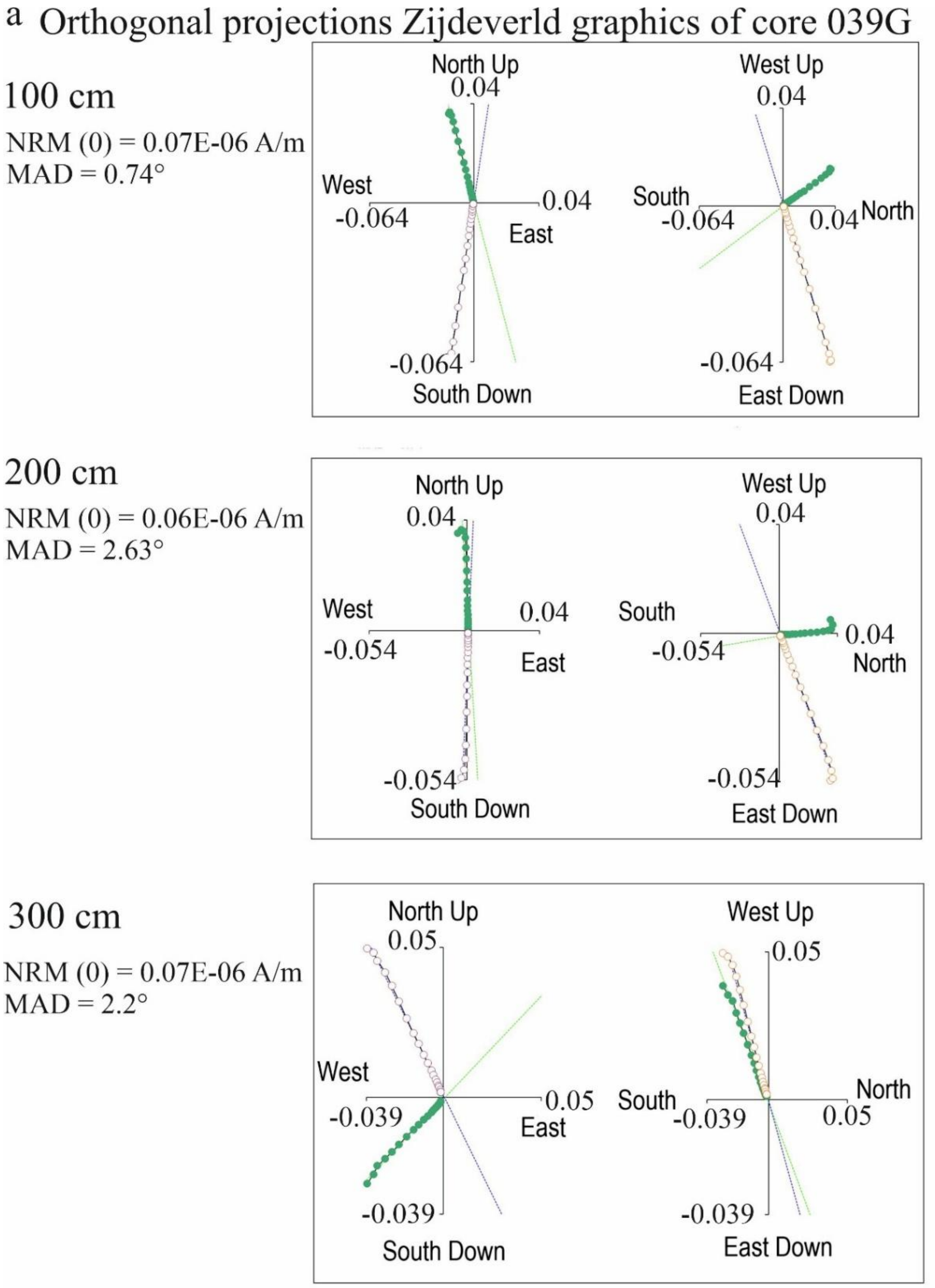

Figure S7 : Zijderveld graphs (Zijderveld, 1967), orthogonal projection of demagnetization for cores 039G (a), 073G (b) and 213G (c).

b Orthogonal projections Zijdeverld graphics of core 073G

100 cm

NRM (0) = 0.06E-06A/m
MAD = 3.59°

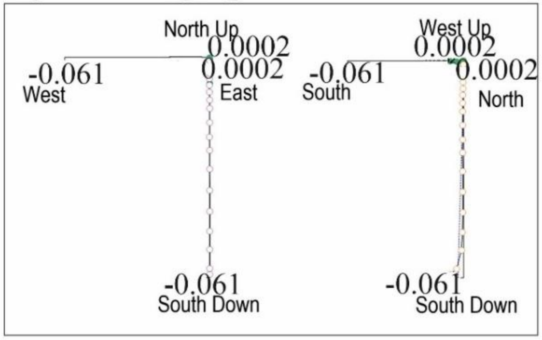

200 cm

NRM (0) = 0.06E-06 A/m
MAD= 2.4°

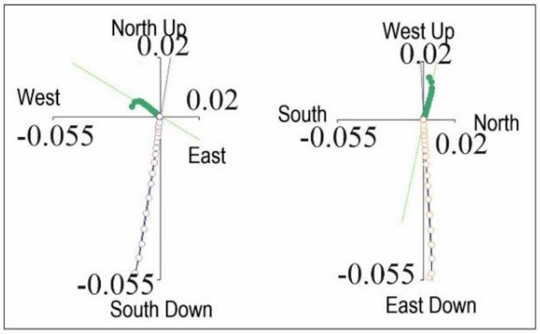

300 cm

NRM (0) = 0.04E-06 A/m
MAD = 3.83°

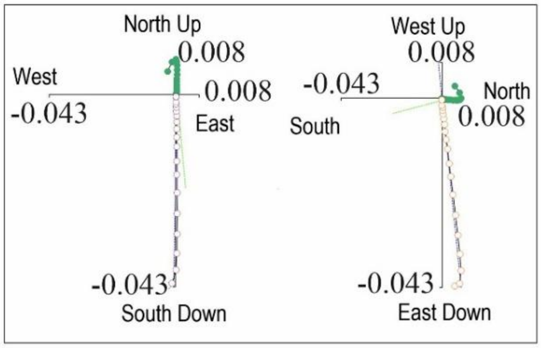

400 cm

NRM (0) = 0.02E-06 A/m
MAD = 6.26°

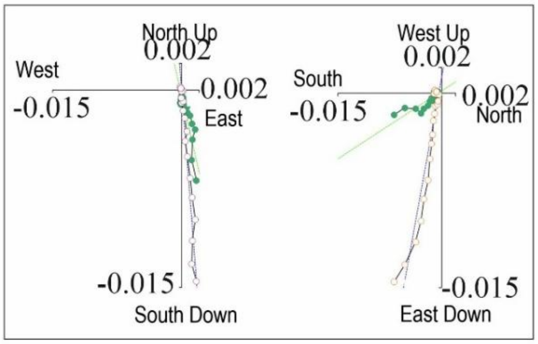

Figure S7 (continued) : Zijderveld graphs (Zijderveld, 1967), orthogonal projection of demagnetization for cores 039G (a), 073G (b) and 213G (c).

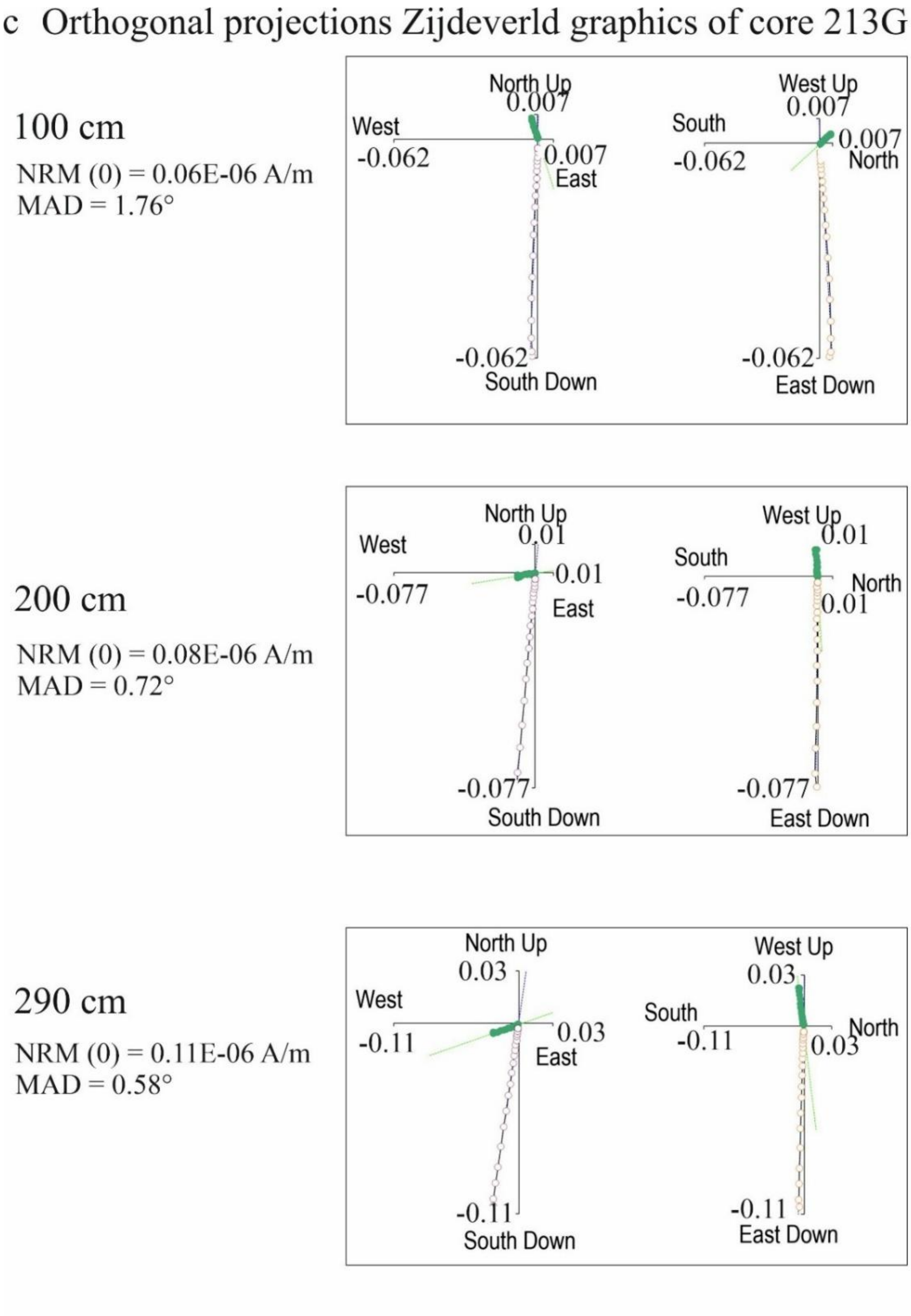

Figure S7 (continued) : Zijderveld graphs (Zijderveld, 1967), orthogonal projection of demagnetization for cores 039G (a), 073G (b) and 213G (c).

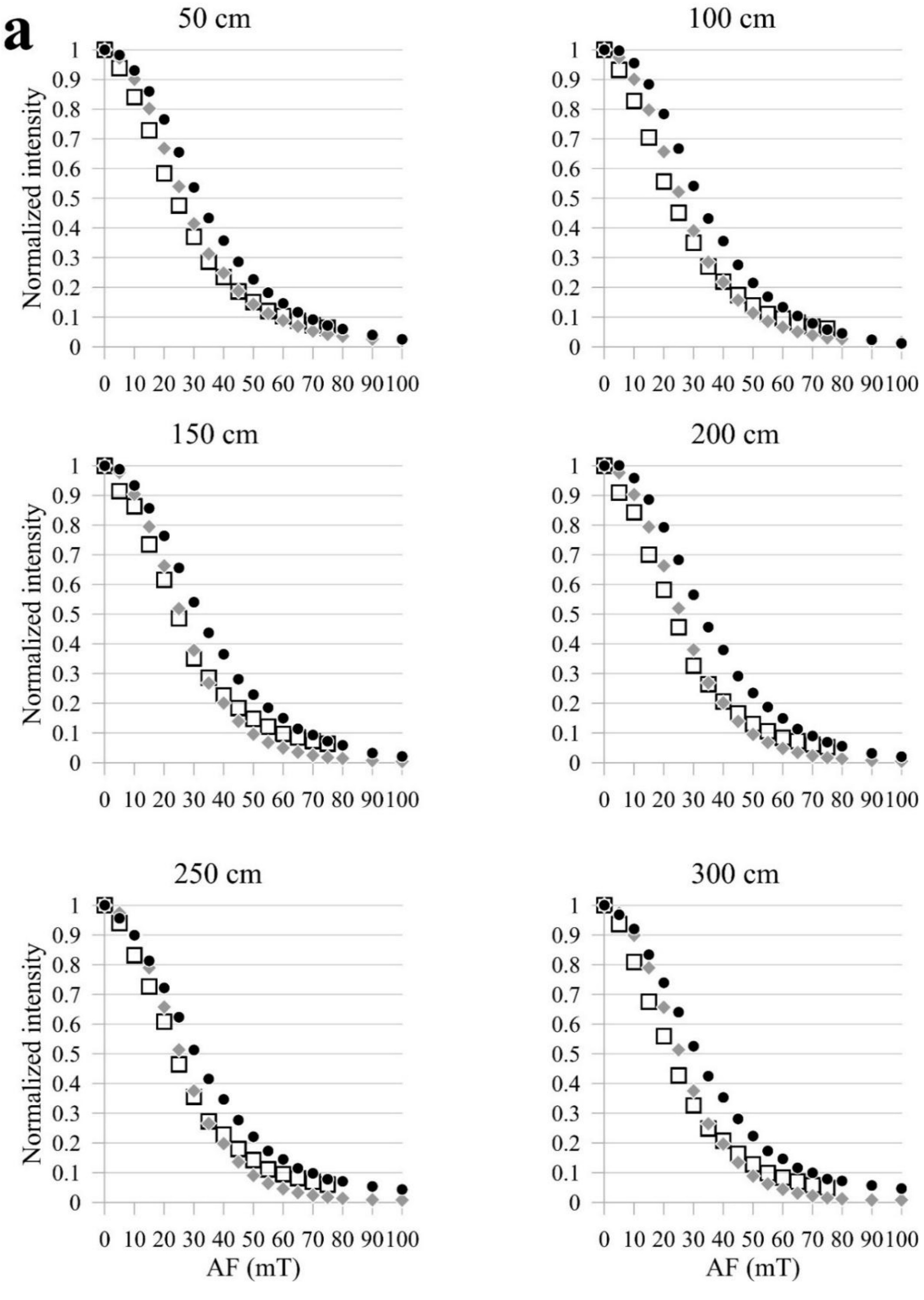

Figure S8: demagnetization graphs for core 039G (a), 073G (b) and 213G (c), black dots = NRM, grey diamond =ARM, white squares = IRM.

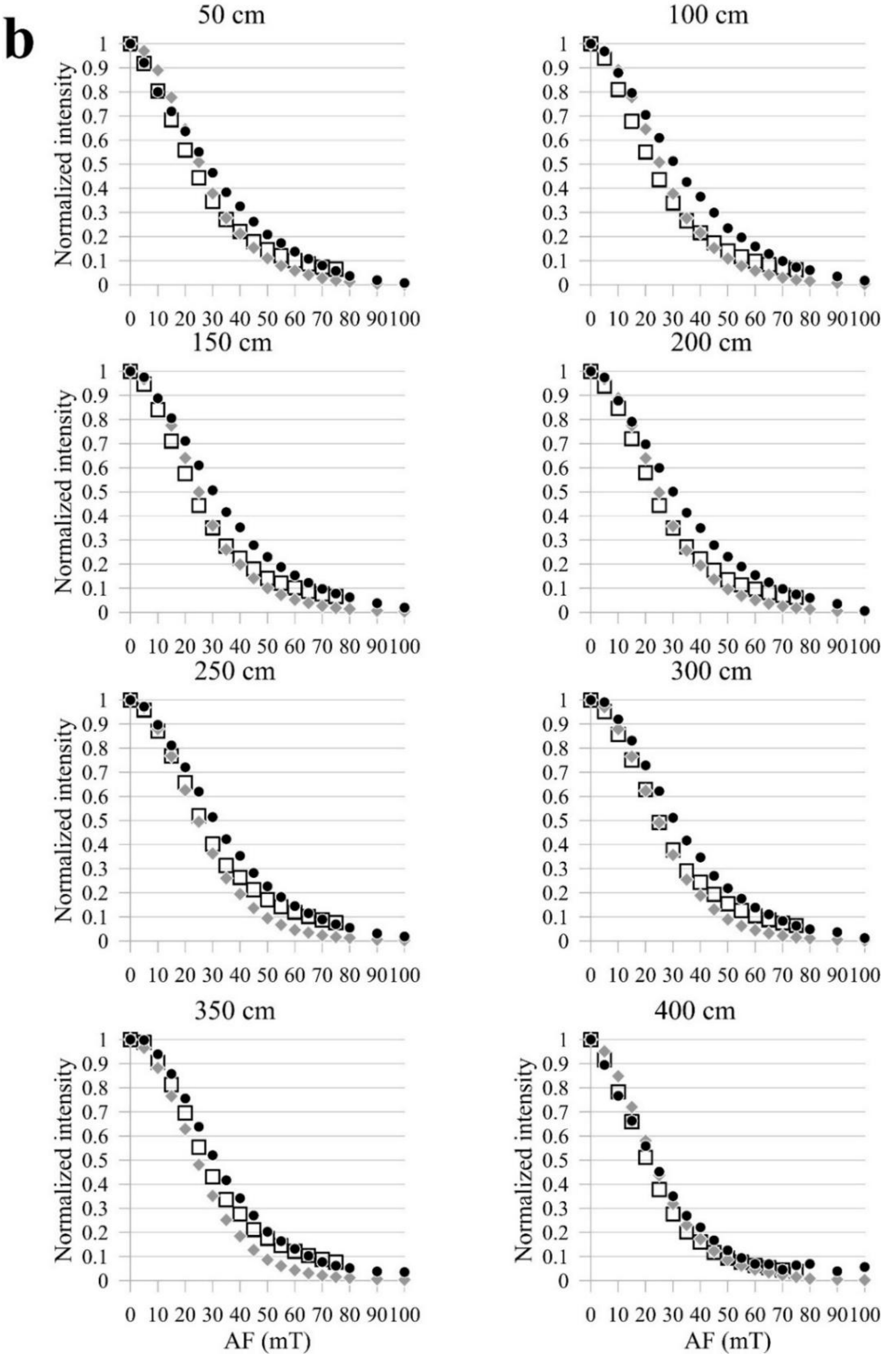

Figure S8 (continued): demagnetization graphs for core 039G (a), 073G (b) and 213G (c), black dots = NRM, grey diamond =ARM, white squares = IRM.

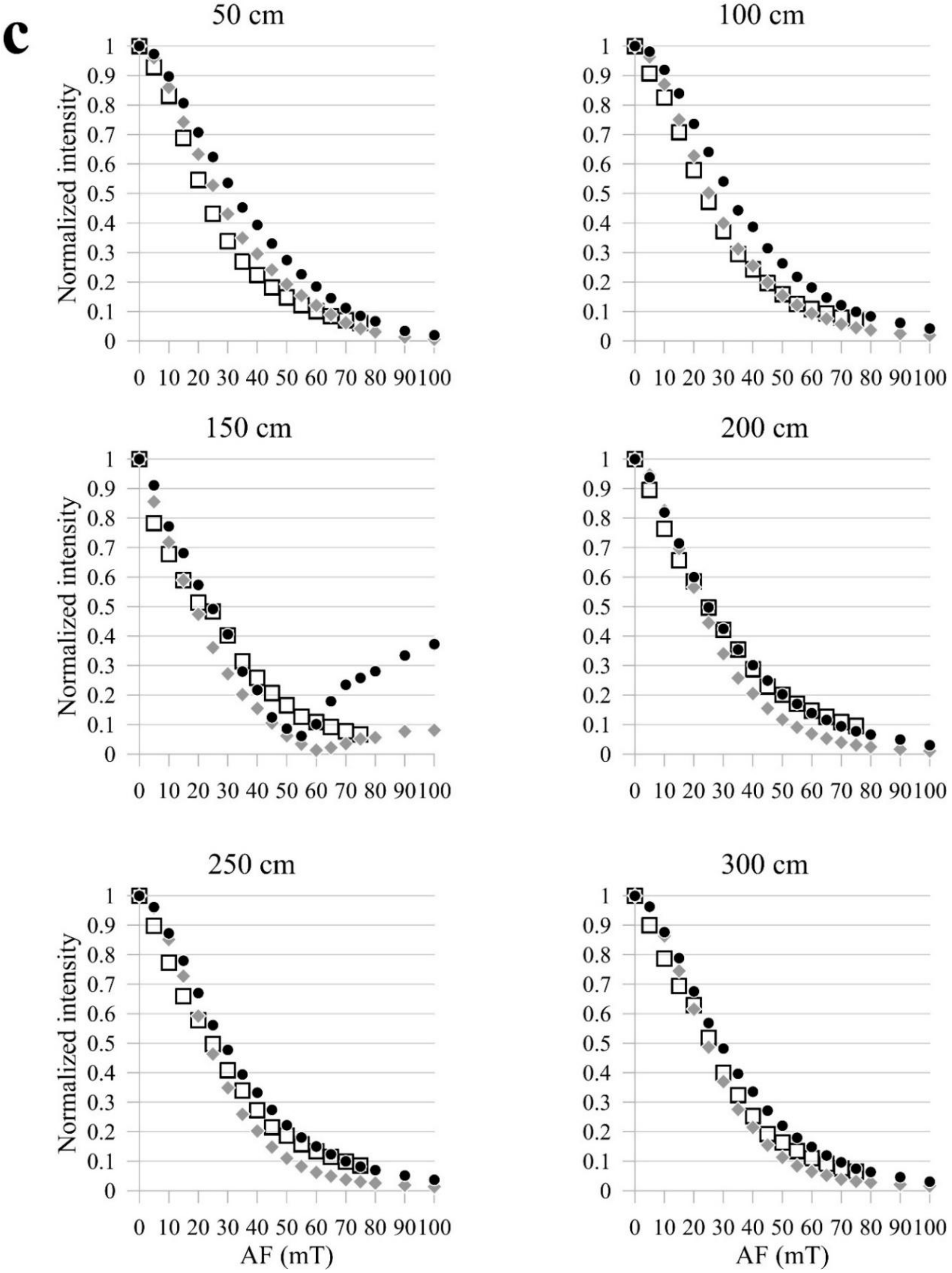

Figure S8 (continued): demagnetization graphs for core 39G (a), 073G (b) and 213G (c), black dots = NRM, grey diamond =ARM, white squares = IRM.

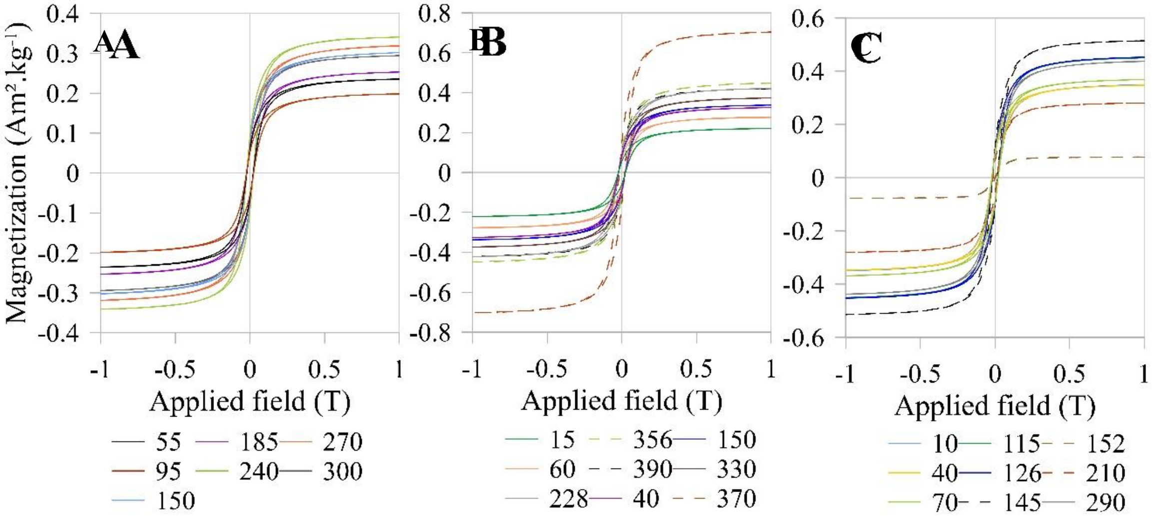

Figure S9. Hysteresis loops for discrete samples from cores 039G (A), 073G (B) and 213G (C), after being heated up to 700°C and cooled down to room temperature.

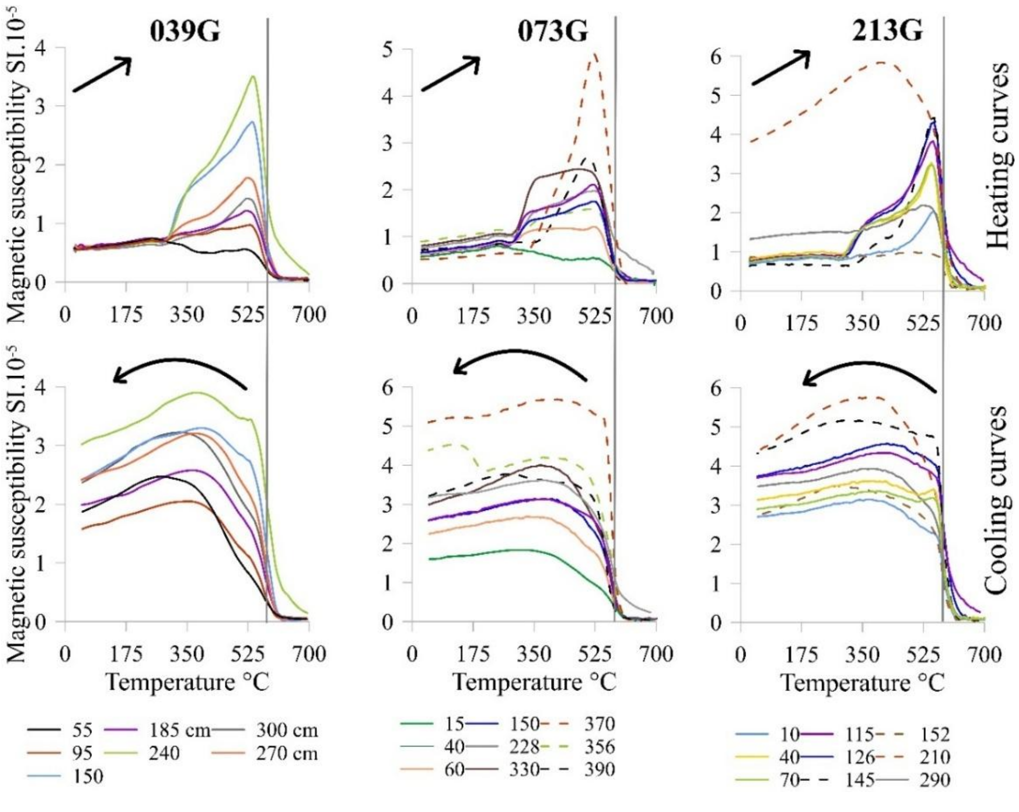

Figure S10. Temperature-dependent magnetic susceptibility measurements; heating curves up to 700°C, cooling curves down to room temperature, measured in an air-atmosphere.

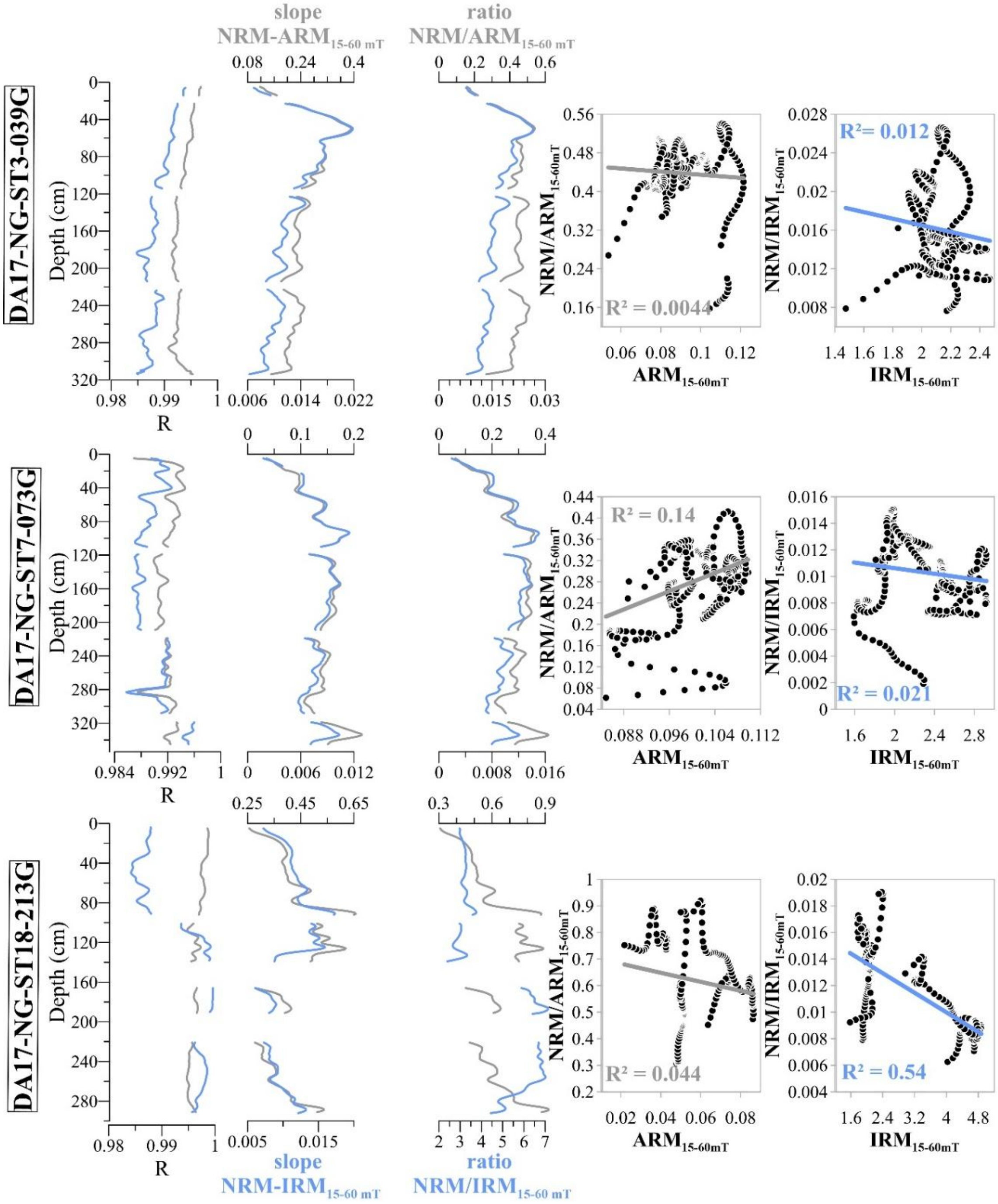

Figure S11. Normalized intensities determination. Blue curves represent IRM and grey curves represent ARM. Left to right: R coefficient for slope method; slope method curves for ARM and IRM 15-60 mT; ratio method curves for ARM and IRM 15-60 mT; r² for ratio methods ARM and IRM. Sand layers were excluded from the normalization process.

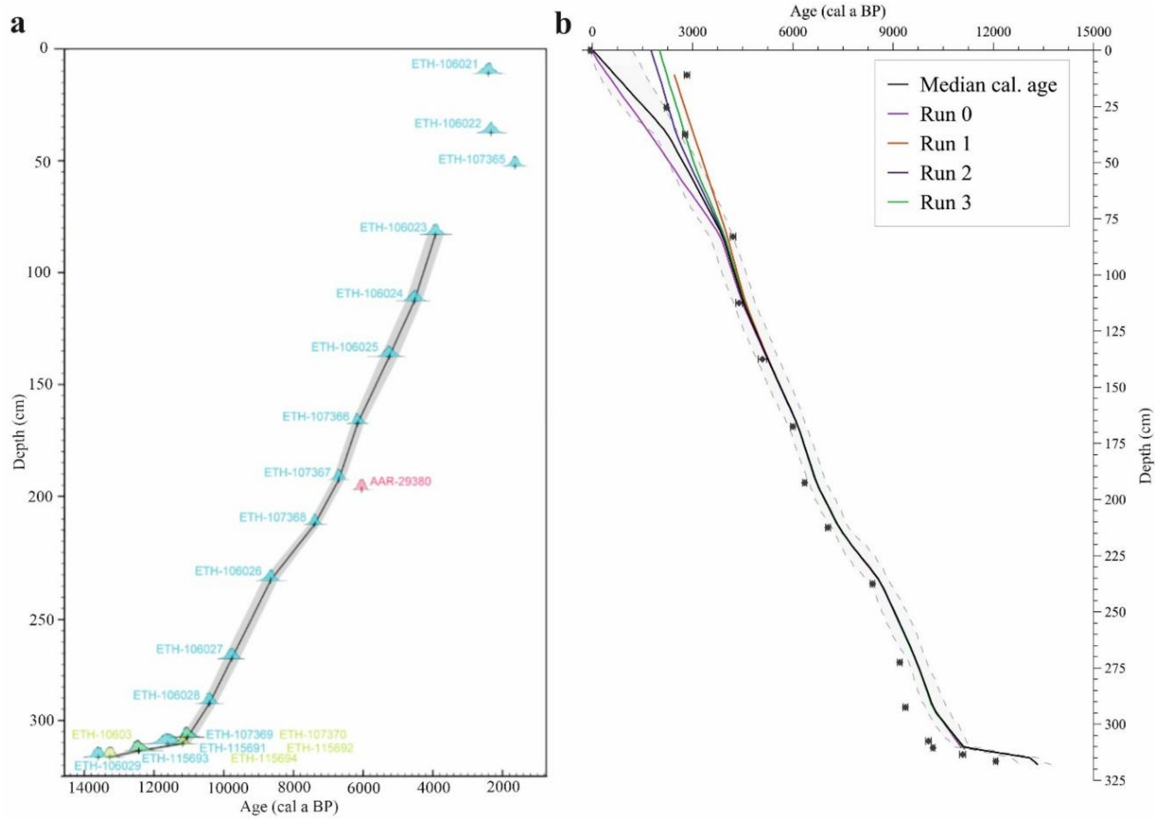

Figure S12. (a) initial age-depth model of core 039G, modified from Hansen et al. (2022). (b) modified age-depth model (this study). Black line represents the age-depth model used in that study. Other colored lines represent the different options tested with R Bacon package (all median age). Bacon run 0: 3 top samples excluded, year of collection (2017 AD =-67 yr cal. BP) included at sediment surface; Bacon run 1: sample ETH-106021 included; Bacon run 2: sample ETH-106022 included; Bacon run 3: sample ETH-107365 included; final age-depth model: sample ETH-106022 and year of collection included. Grey diamonds indicate the unmodelled radiocarbon dates (Table S6).

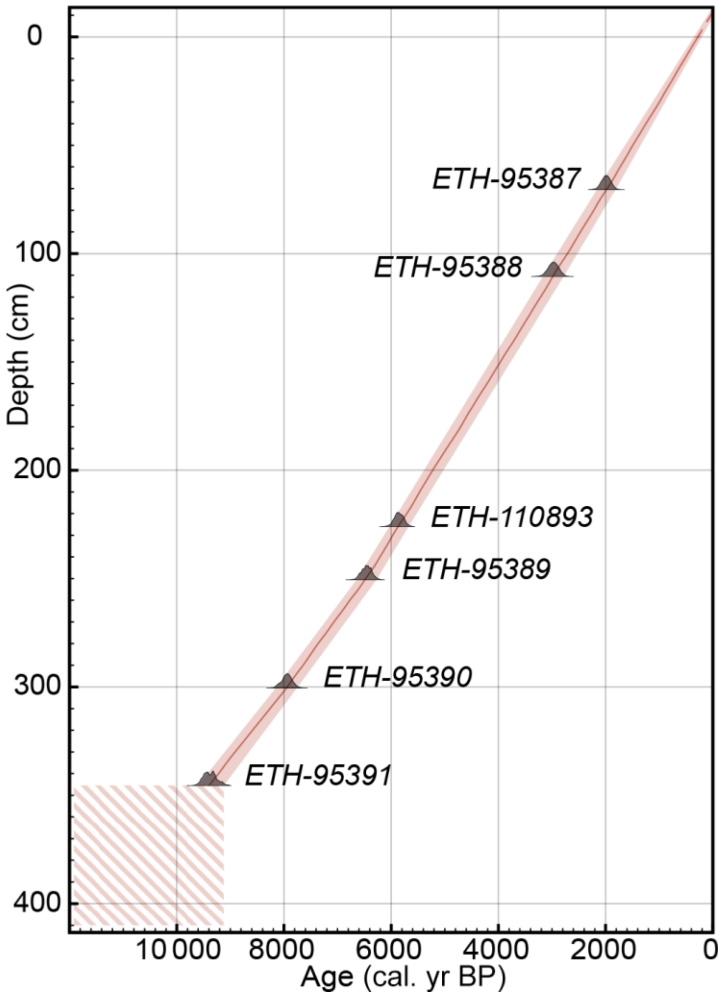

Figure S13. Age model of core DA17-NG-ST07-73G as published in Pados-Dibattista et al., (2022). It is based on six AMS ^{14}C dates and on the comparison with Rumohr core DA17-NG-ST7-72R. The shaded area around the line illustrates the 2-sigma uncertainty range of the model. The hatched box in the bottom of the core indicates an interval containing many reworked microfossils, which is therefore still of uncertain age.

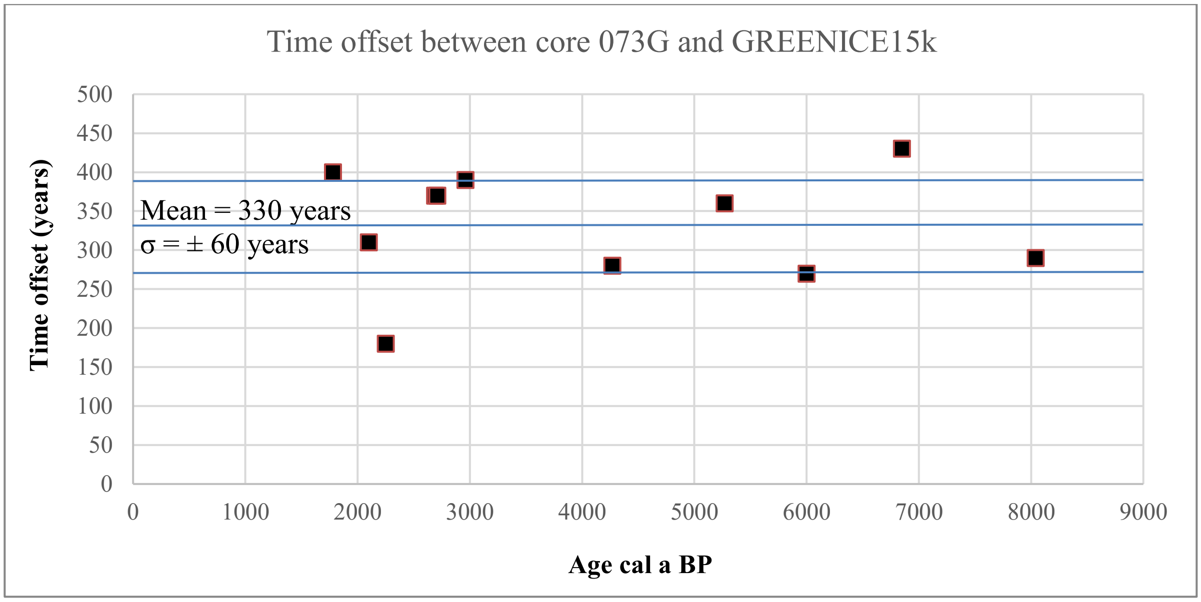

Figure S14. Estimation of the maximum value of ΔR variation through time for core 073G. The values were calculated using inclination and declinations tie-points between core 073G and GREENICE15k record (Reilly et al., 2023). The offset could be due to ΔR variation, pDRM or a mix between the two phenomena. Here we estimate the maximum ΔR value if the lock-in depth were = 0 cm. Blue lines represent the mean and the standard deviation.

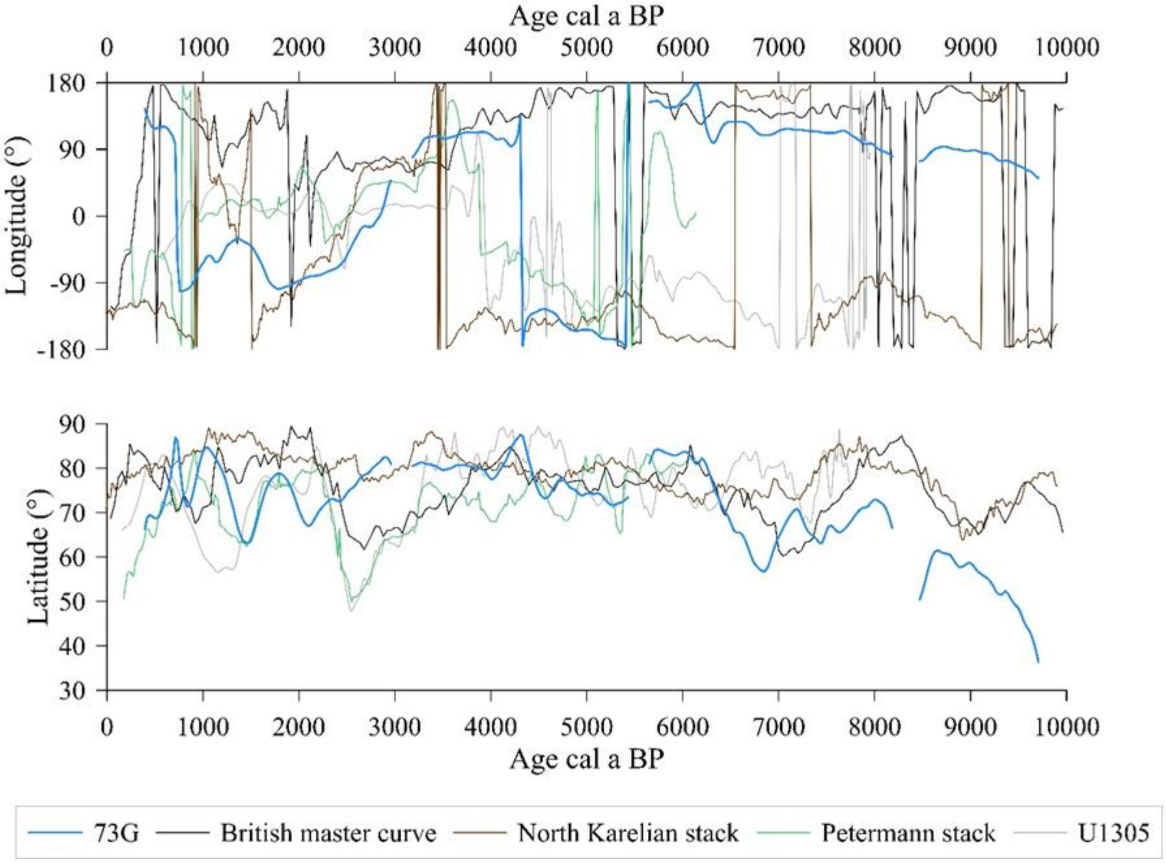

Figure S15. VGP latitude and longitude (°) reconstructions from core 073G (blue), the British master curve (black), North Karelian Stack (light brown), Petermann Stack (green) and U1305 record (grey).

Table S5. Characteristics of the collected sediment cores.

Core	Location	Latitude (°N)	Longitude (°E)	Depth (mbsl)	Length (m)	References
DA17NG-ST03-039G	Northeast Greenland Shelf	80.0333	-8.91667	390.6	3.20	(Hansen et al.. 2022; Seidenkrantz et al., 2018)
DA17NG-ST07-073G	Northeast Greenland Shelf	79.0667	-11.9	385	4.10	(Pados-Dibattista et al., 2022; Seidenkrantz et al., 2018)
DA17NG-ST18-213G	Young Sound	74.333	-20.333	168.1	3.10	(Seidenkrantz et al., 2018)

Table S6: Overview of the radiocarbon ages of core DA17-NG-ST03-039G from Hansen et al., (2022). Modelled median calibrated ages from sample depths marked with * are used in the age depth model. Samples were small (<300µg) and thus not leached. Age in the yellow line was validated with PSV reconstitution and is used in this study.

Sample depth midpoint (cm)	Lab. ID	Material	^{14}C age (yr. BP)	Unmodelled calibrated age range (cal yr. BP). 2σ	Modelled median age (cal. yr. BP)
11	ETH-106021	Mixed benthic foraminifera	2830±80	2159-2673	n.a.
37.5	ETH-106022	Mixed benthic foraminifera	2775±70	2101-2601	n.a./2220
52.5	ETH-107365	Mixed benthic foraminifera	2220±60	1439-1838	n.a.
83*	ETH-106023^{+}	Mixed benthic foraminifera	4210±80	3857-4380	3922
112.5*	ETH-106024^{+}	Mixed benthic foraminifera	4390±100	4040-4677	4523
137.5*	ETH-106025^{+}	Mixed benthic foraminifera	5090±130	4876-5552	5253
167.5*	ETH-107366	Mixed benthic foraminifera	6000±70	6000-6421	6160
192.5*	ETH-107367	Mixed benthic foraminifera	6355±60	6396-6805	6697
197	AAR-29380	Undefined shell fragment	5825±29	5892-6198	n.a.
212.5*	ETH-107368	Mixed benthic foraminifera	7050±70	7173-7537	7391
237.5*	ETH-106026	Mixed benthic foraminifera	8385±70	8524-8994	8659
272.5*	ETH-106027	Mixed benthic foraminifera	9200±70	9529-10065	9772
292.5*	ETH-106028	Mixed benthic foraminifera	9635±70	10151-10587	10413
307.5	ETH-107369	Mixed benthic foraminifera	10120±70	10765-11243	n.a.
307.5*	ETH-107370	Mixed planktonic foraminifera	10055±80	10680-11195	11039

310.5	ETH-115691	Mixed benthic foraminifera	10480±70	11256-11807	n.a.
310.5*	ETH-115692	Mixed planktonic foraminifera	10190±60	10880-11340	11188
313.5	ETH-115693	Mixed benthic foraminifera	11080±90	12121-12677	n.a.
313.5*	ETH-115694	Mixed planktonic foraminifera	11080±90	12121-12677	12435
316.5	ETH-106029	Mixed benthic foraminifera	12255±80	13358-13842	n.a.
316.5*	ETH-106030	Mixed planktonic foraminifera	12070±60	13202-13584	13291

Table S7. Overview of the ages used in 073G age-depth model from Pados-Dibattista et al., (2022). All dates were calibrated using the Marine20 calibration curve and ΔR = 0 ± 50 years.

Lab. ID	Depth (cm)	Material	Radiocarbon age (yr BP)	Error	Median calibrated age cal yr BP (2σ)	Median modelled age cal yr BP (2σ)
ETH-95387	70.5	Mixed benthic foraminifera	2475	60	1952 (2200-1705)	1989 (2161-1817)
ETH-95388	110.5	Mixed benthic foraminifera	3275	70	2935 (3190-2715)	2972 (3165-2783)
ETH-110893	226	Worm tube living	5645	30	5835 (6029-5622)	5857 (6031-5678)
ETH-95389	250.5	Mixed benthic foraminifera	6015	70	6241 (6468-5994)	6458 (6643-6275)
ETH-95390	300.5	Mixed benthic foraminifera	7595	70	7870 (8097-7654)	7942 (8151-7761)
ETH-95391	345.5	Mixed benthic foraminifera	9015	70	9536 (9823-9295)	9383 (9602-9125)

Table S8. Parameters derived from hysteresis loops, isothermal remanent magnetization values and S-ratios of discrete samples in cores 039G, 073G and 213G.

Core	Sample	Mrs ($Am^2.kg^{-1}$)	Ms ($Am^2.kg^{-1}$)	Hc (T)	Hcr (T)	Hcr/Hc	Mrs/Ms	IRM -300mT ($Am^2.kg^{-1}$)	SIRM ($Am^2.kg^{-1}$)	S-ratio
039G	55-56 cm	8.47E-03	3.59E-02	1.79E-02	3.64E-02	2.0342	0.2361	-2.90E-06	3.03E-06	-0.9570
	95-96 cm	7.39E-03	3.16E-02	1.82E-02	3.65E-02	2.0051	0.2341	-2.63E-06	2.75E-06	-0.9551
	150-151 cm	7.92E-03	3.55E-02	1.80E-02	3.64E-02	2.0266	0.2234	-2.78E-06	2.90E-06	-0.9574
	185-186 cm	8.10E-03	0.0351	1.79E-02	3.64E-02	2.0371	0.2310	-2.94E-06	3.07E-06	-0.9592
	240-241 cm	8.07E-03	3.62E-02	1.78E-02	3.71E-02	2.0807	0.2229	-2.84E-06	2.95E-06	-0.9632
	270-271 cm	7.38E-03	3.60E-02	1.69E-02	3.60E-02	2.1254	0.2051	-2.77E-06	2.88E-06	-0.9634
	300-301cm	8.54E-03	3.81E-02	1.79E-02	3.76E-02	2.1035	0.2240	-2.93E-06	3.04E-06	-0.9646
073G	15-16 cm	9.26E-03	3.48E-02	1.84E-02	3.59E-02	1.9507	0.2658	-3.11E-06	3.28E-06	-0.9484
	40-41 cm	9.17E-03	3.56E-02	0.0179	3.54E-02	1.9785	0.2578	-3.00E-06	3.16E-06	-0.9499
	59-60 cm	9.36E-03	3.65E-02	1.80E-02	3.57E-02	1.9840	0.2563	-3.11E-06	3.27E-06	-0.9501
	150-151 cm	1.02E-02	4.16E-02	1.74E-02	3.53E-02	2.0312	0.2440	-3.49E-06	3.65E-06	-0.9558
	228-229 cm	1.13E-02	4.77E-02	1.76E-02	3.60E-02	2.0465	0.2371	-4.01E-06	4.17E-06	-0.9633
	330-331 cm	1.22E-02	5.56E-02	1.67E-02	3.44E-02	2.0667	0.2202	-4.11E-06	4.37E-06	-0.9397
	356-357 cm	1.31E-02	5.93E-02	1.68E-02	3.52E-02	2.1008	0.2204	-4.85E-06	5.00E-06	-0.9702
	370-371 cm	5.62E-03	2.85E-02	1.54E-02	3.40E-02	2.2001	0.1977	-2.16E-06	2.24E-06	-0.9617
	372-373 cm	1.94E-03	1.27E-02	1.10E-02	1.86E-02	1.6935	0.1532	-6.85E-07	6.59E-07	-1.0397
	390-391 cm	7.50E-03	4.75E-02	1.06E-02	2.17E-02	2.0386	0.1578	-2.80E-06	2.73E-06	-1.0244
213G	10-11 cm	9.02E-03	4.91E-02	1.40E-02	3.18E-02	2.2724	0.1839	-2.96E-06	3.06E-06	-0.9685
	40-41 cm	1.10E-02	5.79E-02	1.42E-02	3.21E-02	2.2685	0.1898	-3.40E-06	3.50E-06	-0.9728
	70-71 cm	1.07E-02	5.72E-02	1.41E-02	3.20E-02	2.2638	0.1866	-3.34E-06	3.44E-06	-0.9706
	115-116 cm	9.65E-03	6.03E-02	1.36E-02	3.28E-02	2.4099	0.1599	-3.17E-06	3.27E-06	-0.9707
	126-127 cm	8.94E-03	6.17E-02	1.28E-02	3.26E-02	2.5355	0.1448	-2.86E-06	2.94E-06	-0.9716
	145-146 cm	5.73E-03	5.85E-02	9.04E-03	2.81E-02	3.1081	0.0980	-1.98E-06	2.02E-06	-0.9776
	152-153 cm	4.30E-03	7.50E-02	5.65E-03	2.37E-02	4.2006	0.0574	-1.50E-06	1.55E-06	-0.9666
	210-211 cm	3.38E-03	6.83E-02	3.73E-03	1.12E-02	2.9932	0.0495	-9.92E-07	9.15E-07	-1.0840
	290-291 cm	1.33E-02	1.04E-01	1.23E-02	3.34E-02	2.7205	0.1283	-4.94E-06	5.05E-06	-0.9793

Table S9. Parameters derived from hysteresis loops, isothermal remanent magnetization values and S-ratios of discrete samples in cores 039G, 073G and 213G, after being heated up to 700°C and cooled down to room temperature.

Core	Sample	Mrs (Am².kg^{-1})	Ms (Am².kg^{-1})	Hc (T)	Hcr (T)	Hcr/Hc	Mrs/Ms	IRM -300mT (Am².kg^{-1})	SIRM (Am².kg^{-1})	S-ratio
039G	55-56 cm	5.97E-02	2.36E-01	2.13E-02	3.69E-02	1.7308	0.2530	-8.27E-06	8.41E-06	-0.9839
	95-96 cm	5.22E-02	1.99E-01	2.40E-02	4.44E-02	1.8491	0.2630	-8.63E-06	8.78E-06	-0.9822
	150-151 cm	8.33E-02	3.02E-01	2.27E-02	4.0E-02	1.7641	0.2756	-12.9E-06	1.31E-05	-0.9860
	185-186 cm	6.62E-02	0.2533	2.39E-02	4.43E-02	1.8583	0.2612	-1.28E-05	1.29E-05	-0.99
	240-241 cm	9.31E-02	3.40E-01	2.20E-02	3.89E-02	1.7660	0.2739	-1.71E-05	1.72E-05	-0.9941
	270-271 cm	8.32E-02	3.19E-01	2.29E-02	4.21E-02	1.8388	0.2609	-1.34E-05	1.36E-05	-0.9889
	300-301cm	7.74E-02	2.95E-01	2.95E-01	3.92E-02	1.8160	0.2628	-1.32E-05	1.33E-05	-0.9941
073G	15-16 cm	5.61E-02	2.21E-01	2.37E-02	4.53E-02	1.9124	0.2542	-9.66E-06	9.77E-06	-0.9881
	40-41 cm	8.42E-02	3.62E-01	2.31E-02	4.31E-02	1.8682	0.2584	-1.46E-05	1.47E-05	-0.9919
	59-60 cm	7.21E-02	2.77E-01	2.33E-02	3.98E-02	1.7064	0.2605	-11.074E-06	1.11E-05	-1.0004
	150-151 cm	8.62E-02	3.37E-01	2.36E-02	4.47E-02	1.8949	0.2559	-1.45E-05	1.47E-05	-0.9884
	228-229 cm	9.83E-02	4.22E-01	2.17E-02	4.27E-02	1.9697	0.2332	-1.81E-05	1.83E-05	-0.9919
	330-331 cm	9.84E-02	3.74E-01	2.28E-02	4.18E-02	1.8338	0.2633	-16.05E-06	1.61E-05	-0.9967
	356-357 cm	1.16E-01	4.48E-01	2.30E-02	4.23E-02	1.84	0.2590	-2.04E-05	2.04E-05	-0.9972
	370-371 cm	1.53E-01	7.03E-01	1.80E-02	3.46E-02	1.9229	0.2173	-2.54E-05	2.51E-05	-1.0106
	372-373 cm	6.59E-01	3.22E-01	1.26E-02	1.04E-02	0.8207	0.2046	-9.79E-06	9.0E-06	-1.0879
	390-391 cm	1.07E-01	4.21E-01	2.14E-02	4.19E-02	1.9565	0.2540	-1.79E-05	1.88E-05	-0.9505
213G	10-11 cm	8.73E-02	3.49E-01	2.19E-02	4.22E-02	1.9289	0.25	-14.9E-06	1.51E-05	-0.9874
	40-41 cm	8.9E-02	3.48E-01	2.15E-02	4.03E-02	1.8778	0.2560	-1.6475E-05	1.665E-05	-0.9895
	70-71 cm	9.52E-02	3.69E-01	2.14E-02	3.98E-02	1.8562	0.2581	-1.67E-05	1.69E-05	-0.9919
	115-116 cm	1.02E-01	4.5E-01	1.94E-02	3.77E-02	1.9428	0.2262	-1.69E-05	1.69E-05	-0.9989
	126-127 cm	1.04E-01	4.53E-01	1.98E-02	3.81E-02	1.9221	0.2285	-1.90E-05	1.92E-05	-0.9936
	145-146 cm	1.13E-01	5.14E-01	1.74E-02	3.35E-02	1.9323	0.2194	2.00E-05	2.0E-05	-0.9986
	152-153 cm	4.24E-03	7.72E-02	3.69E-03	9.76E-03	2.6448	0.0550	-4.44E-07	4.11E-07	-1.0816
	210-211 cm	5.85E-02	2.81E-01	1.34E-02	2.52E-02	1.881	0.2084	-1.23E-05	1.22E-05	-1.0047
	290-291 cm	9.26E-02	4.38E-01	1.98E-02	4.10E-02	2.0738	0.2117	-1.79E-05	1.8E-05	-0.9956

Table S10. Parameters used for the unmixing of the IRM curves in the MaxUnmix software.

Sample	Component	Coercivity	Dispersion	Relative Proportion	Skewness	RSS
039G 240 cm	1 (blue)	1.75	0.23	0.98	1	2×10^{-13}
	2 (pink)	1.18	0.22	0.17	0.9	
073G 150 cm	1 (blue)	1.69	0.22	0.97	1	2.2×10^{-13}
	2 (pink)	2.16	0.33	0.07	1	
	3 (green)	1.17	0.2	0.13	0.95	
213G 70 cm	1 (blue)	1.68	0.27	1	1	1.75×10^{-13}
	2 (pink)	2.41	0.17	0.05	1	
	3 (green)	1.07	0.26	0.1	1	

References

Hansen, K. E., Lorenzen, J., Davies, J., Wacker, L., Pearce, C., & Seidenkrantz, M.-S. (2022). Deglacial to Mid Holocene environmental conditions on the northeastern Greenland shelf, western Fram Strait. *Quaternary Science Reviews*, *293*, 107704. https://doi.org/10.1016/j.quascirev.2022.107704

Jakobsson, M., Mohammad, R., Karlsson, M. et al. The International Bathymetric Chart of the Arctic Ocean Version 5.0. Sci Data 11, 1420 (2024). https://doi.org/10.1038/s41597-024-04278-w.

Pados-Dibattista, T., Pearce, C., Detlef, H., Bendtsen, J., & Seidenkrantz, M.-S. (2022). Holocene palaeoceanography of the Northeast Greenland shelf. *Climate of the Past*, *18*(1), 103–127. https://doi.org/10.5194/cp-18-103-2022

CHAPITRE 3

VARIATIONS PALEOMAGNETIQUES A HAUTE RESOLUTION AU COURS DES DERNIERS 2500 ANS ENREGISTREES DANS LES SEDIMENTS VARVES DE GRAND LAKE, LABRADOR, CANADA

3.1 RESUME EN FRANÇAIS DU TROISIEME CHAPITRE

Deux campagnes de terrain menées à Grand Lake, au Labrador (Canada), ont permis de prélever plusieurs carottes sédimentaires varvées, notamment la carotte GL17-13, longue de 3,3 m, située à l'extrémité ouest du lac, et la séquence composite GL23-20, longue de 20 m, prélevée dans la partie centrale la plus profonde du lac. Des mesures paléomagnétiques continues et des mesures de magnétisme environnemental discrètes ont été effectuées sur toutes les carottes afin de reconstituer les variations séculaires paléomagnétiques (PSV) et les variations de paléointensité relative (RPI). Le signal paléomagnétique de la carotte GL23-20 est interrompu par 75 couches déposées rapidement (RDL), ce qui perturbe trop le signal pour permettre des reconstitutions paléomagnétiques fiables. Cependant, la surface de la séquence composite (80 cm) est bien préservée et fournit un enregistrement des 350 dernières années. La carotte GL17-13 enregistre des variations à haute résolution pour les 2 500 dernières années. Combinées, ces deux carottes fournissent un enregistrement paléomagnétique des variations séculaires récentes, en particulier des 1 000 dernières années, une période pour laquelle il existe très peu d'enregistrements permettant d'établir un lien entre les fluctuations récentes du champ géomagnétique (400 dernières années) et les variations observées pendant l'Holocène. Bien que le signal GL23-20 soit perturbé, il décrit une tendance globale similaire à celle de l'enregistrement GL17-13. Les PSV présentent des similitudes avec les enregistrements de l'est du Canada (MD99-2220) et du sud du Groenland (GREENICE15k), ainsi qu'avec les modèles IGRF et GUFM pour les variations des 400 dernières années. Les variations de RPI sont très similaires à celles de la carotte MD99-2220.

L’étude des propriétés magnétiques des RDL montre que l’amplitude de variation de l’inclinaison au sein des événements est reliée à l’épaisseur des couches et donc à l’intensité de l’événement et de la turbulence. Nos résultats soulignent le potentiel des sédiments de Grand Lake en tant que site d'étude des variations paléomagnétiques à haute résolution. Nous recommandons, pour les travaux futurs, de prélever des carottes orientées selon la déclinaison et d'échantillonner des cubes plutôt que des u-channels afin d'augmenter la résolution, particulièrement pour les variations du dernier millénaire. De plus, les similitudes entre les carottes MD99-2220 et GL17-13 suggèrent que les enregistrements paléomagnétiques varvés pourraient être utilisés pour construire un modèle d'âge magnétique pour MD99-2220 afin d'estimer les variations de ΔR dans la région. A partir de ce chapitre, un article portant sur les variations paléomagnétiques séculaires et de paléointensité relative de la carotte GL17-13 et de la carotte de surface GL23-20-Up1 sera soumis à une revue pour publication, incluant les personnes ayant contribué au projet. Une seconde étude portant sur l’influence de la turbulence et des RDL sur l’acquisition de la rémanence détritique des sédiments pourra également être soumise pour publication.

En tant que première autrice j’ai établi les objectifs, questions et hypothèses de recherche, participé à la campagne de terrain à Grand Lake en 2023, réalisé les analyses de laboratoire, interprété et discuté les résultats et écrit le manuscrit. **Guillaume St-Onge** a supervisé le projet, financé la campagne de terrain ainsi que les analyses et participé à établir les objectifs de recherche, à l’interprétation des résultats, à la discussion et à la révision du manuscrit. **Brendan Reilly** a participé à l’interprétation des résultats et à la discussion. **France Lagroix** a participé à l’interprétation des résultats. **Milena Souza Kury** a participé à la campagne de terrain et a contribué aux résultats d’une précédente étude sur laquelle se base en partie ce manuscrit (Kury et al., 2025). **Jean-Carlos Montero-Serrano** a participé à la discussion et à la révision du manuscrit. **Patrick Lajeunesse** a fourni les données bathymétriques provenant d’une campagne de terrain et d’une étude précédentes (Trottier et al., 2020). **Pierre Francus** a financé la campagne de terrain et les analyses de laboratoire, participé à la supervision du projet, à l’interprétation des résultats, à la discussion et à la révision du manuscrit.

3.2 HIGH-RESOLUTION PALEOMAGNETIC VARIATIONS FOR THE LAST 2,500 YEARS RECORDED IN VARVED SEDIMENTS FROM GRAND LAKE, LABRADOR, CANADA

3.2.1 Abstract

Two field campaigns conducted at Grand Lake in Labrador, Canada, enabled to retrieve several varved sediment cores including the 3.3-m long core GL17-13 at the outlet of the lake, and the 20-m long sequence GL23-20 retrieved in the deepest middle part of the lake. Continuous paleomagnetic and discrete rock magnetic measurements were conducted on all cores to reconstruct the paleomagnetic secular variations (PSV) and relative paleointensity (RPI) variations. Core GL23-20 paleomagnetic signal is interrupted by 75 rapidly deposited layers (RDL) and the signal was deemed too disrupted for paleomagnetic reconstructions. However, the surface of the composite sequence (80 cm) is well preserved and provides a record of the last 350 years. Core GL17-13 is an undisturbed varved sequence that records high-resolution variations for the last 2,500 years. Altogether, these cores provide a paleomagnetic record of recent secular variations, particularly for the last 1,000 years, a period for which there are very few records that can establish a link between recent fluctuations in the geomagnetic field (last 400 years) and variations observed during the Holocene. The PSV signal presents similarities with records from Eastern Canada (MD99-2220), Southern Greenland (GREENICE15k), and corroborates the IGRF and GUFM model outputs for the last 400 years. The RPI signal is very similar to the RPI signal of core MD99-2220. Even though GL23-20 signal is disturbed, it describes a general trend that support core GL17-13 record. The magnetic properties of RDL were also studied in details and reveal results similar to previous studies. In particular, the dependence of inclination shallowing on turbulence is highlighted by a logarithmic relationship between variation in inclination amplitude and RDL thickness. Our results highlight the potential of Grand Lake as a high-resolution paleomagnetic variations study site in areas not affected by mass wasting events such as the location of core GL17-13 at the outlet of the lake. We recommend retrieving declination-oriented cores and sampling with cubes instead of u-channels in the surface core to increase the resolution and fully benefit from the varved chronology. Moreover, the

similarities between core MD99-2220 and GL17-13 with the cosmogenic isotope records suggest that the varved paleomagnetic record could be used to build a magnetic age model for core MD99-2220 to estimate changes in ΔR in the region during the Holocene.

3.3 INTRODUCTION

The North Magnetic Pole (NMP) was first physically located in 1831 by James Clark Ross (Ross, 1834), in Nunavut (Canada). A few direct observations since 1831, and then satellite observations, revealed a migration of more than 1,700 km of the NMP from the Canadian Arctic towards Siberia, through the Arctic Ocean since the early 20th century. Based on the current World Magnetic Model, the 2025 location of the NMP is 85.762°N;139.298°E, and it has moved at an average speed of 41 km/yr (National Centers for Environmental Information, 2023). The weakening of the geomagnetic dipole moment of about 10% per century since the first measurement by Gauss (1833) was observed (Gubbins, 2008). Recent studies have associated that rapid NMP migration with the presence of high intensity geomagnetic flux lobes (Livermore et al., 2020) in the northern hemisphere, and some have hypothesized that it could also have been the case during the Holocene (e.g., Caricchi et al., 2022; Girard et al., 2024; Stoner et al., 2013).

Sediment cores are commonly used as a way of reconstructing the past geomagnetic field, and unlike lavas or archeomagnetic artefacts, they provide continuous records. However, uncertainties associated with chronology or sediment accumulation rates (SAR) persist. To investigate rapid geomagnetic variations in the past, there is a need for high-resolution records. These allow to observe decadal- to centennial-scale changes, help minimize issues associated with radiocarbon (^{14}C) dating, and reduce the smoothing effects of the post-depositional remanent magnetization (pDRM). Only a few sedimentary records match these resolution requirements, such as the GREENICE15k Stack from the North Iceland and Southeast Greenland Shelf (Reilly et al., 2023). Grand Lake (Labrador, Canada) has the potential to record high-resolution paleomagnetic fluctuations, as it contains varved and laminated sediments. These features result from pronounced seasonal variations in the region (ice cover during winter and significant spring discharge), which control the different sediment inputs into the Lake. Varves represent annual sedimentation, with each varve corresponding to one year and comprising distinct sedimentary layers (Zolitschka et al., 2015). Given the challenges of establishing a reliable chronology in the adjacent Labrador Sea (e.g., Stoner et al., 2000), Grand Lake offers a valuable alternative for studying past geomagnetic variations in the region. This is particularly relevant for the first few millennia, which are sometimes difficult to recover in marine sediments due to the coring process often affecting the top of the sequence.

Grand Lake has been the subject of hydrological (Gagnon-Poiré, 2023; Gagnon-Poiré et al., 2021; Lapointe et al., 2025), deglaciation, hydroacoustic, (Trottier et al., 2020), sedimentary and environmental studies (Milena S. Kury et al., 2025). Varved sequences have a great potential for paleoenvironmental studies, but can often be complex due to rapid seasonal variations in sedimentation processes. In particular for paleomagnetism, previous studies highlighted the difference of magnetic mineralogy between winter and summer beds (Philippe et al., 2023).

In this study, we reconstruct the paleomagnetic secular variations (PSV) and relative paleointensity (RPI) for the last 2,500 years, from lacustrine varved and laminated sediment cores, including a 20 m composite sequence, allowing us to determine local variations, as well as a more global signal, and particularly to reconstruct a record for the last 1,000 years. In addition, we address the issue of the numerous rapidly deposited layers (RDL) present in the core, and their impact on the detrital remanent magnetization recording process.

3.4 SETTING

Grand Lake is a 54 km long, <3 km large and 245 m deep fjord-lake located in Labrador, Canada, 15 m above sea level (Figure 46). The main tributaries of Grand Lake are the Naskaupi and the Beaver Rivers, located at the head of the lake (Figure 46). The Naskaupi River is the second largest river in Labrador, after the Churchill River, and brings a large quantity (70 km^3 per year) of fresh water into the lake (Kamula et al., 2017). Grand Lake is connected to Little Lake (tidal lake) at the southeast, connected itself to Lake Melville, which then discharges into the Labrador Sea. Situated in the Grenville province of the Canadian Shield, Grand Lake is surrounded by Late Paleoproterozoic metamorphic and igneous rocks (Wardle et al., 1997). Sedimentary rocks are present in the north of the Naskaupi River watershed. The lake is located on the Grenville front and thus several thrusts or reverse faults run across the lake.

3.4.1 Deglaciation

During the last glaciation, Grand Lake was covered by the Laurentide Ice Sheet (LIS). When it retreated, its margin stabilized southeast of Grand Lake and deposited the Sebaskachu moraine, recently dated at 8.4 ± 0.6 ka (Couette et al., 2023). During deglaciation, the marine limit was up to 150 m above the modern sea level, inundating fluvial valleys upstream Grand Lake. During that time, Grand Lake formed a glaciomarine fjord connected to Lake Melville. The fjord was isolated from the sea around ~3.2 ka (Fitzhugh, 1973), due to isostatic rebound resulting from the LIS retreat, which caused the elevation of the moraine at the mouth of the Lake. The lake geomorphology is thus characterized by glacial deposits and lineations and glacially sculpted bedrocks. The hydroacoustic study by Trottier et al. (2020) enabled to identify three different sectors in the lake: deltas at the Naskaupi and Beaver rivers outputs, the deep (~245 m) flat central basin and the downstream section, shallower with moraine ridges and a central channel connected to the lake outlet. Gullies were observed on the subaquatic part of the abrupt cliffs and mountains that surround the lake.

3.4.2 Sedimentation

Grand Lake gradually changed from marine conditions to freshwater conditions during the deglaciation. The main sediment input in the lake comes from the main tributaries Naskaupi and Beaver Rivers, as well as smaller rivers around the lake. Due to seasonal contrast between cool and humid summers and cold winters (Gagnon-Poiré et al., 2021), Grand Lake experiences large seasonal variations, inducing different climate influenced sedimentation : hyperpycnal flow are triggered during rainfall; hypopycnal flow during seasonal stratification transports fine sediments to the outlet of the lake; seasonal stratification induce laminations (Trottier et al., 2020; Gagnon-Poiré et al., 2021; Gagnon-Poiré, 2023). In particular, laminations in Grand Lake are clastic varves (Zolitschka et al., 2015), composed of 2 to 3 distinct layers (Kury et al., 2025; Lapointe et al., 2025). A clay cap is associated with particles settling in a non-turbulent environment when the lake is covered with ice in autumn and winter. Grand Lake is dimictic, meaning that summer and winter induced suboxic to anoxic conditions at the lake's bottom allow clastic varve preservation, while vertical temperature contrast becomes negligible during fall and spring, allowing vertical circulation twice a year and introducing limited oxygen to the lake's bottom (Gagnon-Poiré, 2023;Kury et al., 2025).

3.5 MATERIAL AND METHODS

3.5.1 Sediment cores

Core GL17-13A-V (hereafter GL17-13) was collected during winter 2017 depth using a Rossfelder corp. underwater vibracorer at 75 m water depth in Grand Lake near the Lake outlet (Figure 46). The top of the core was not well preserved and about 10 cm were missing.

In March 2023, a two-week field campaign enabled to recover a long composite sequence of cores at site 20 (Figure 46) with a UWITEC coring platform. GL23-20-Up1 was collected using a UWITEC piston corer. Hole A was drilled with a UWITEC percussion corer recovering two-meter-long sections. To compensate for sediment loss between core sections, hole B was drilled one meter away from hole A, with a depth offset of 50 cm. Four sections of two meters each were retrieved from hole A and 10 sections of two meters each were retrieved from hole B. A composite sequence of more than 20 m, was built using cores from holes A and B and surface core Up1 (Table 9, Kury et al., 2025) based on CT scan images.

Table 9. Characteristics of the sediment cores collected.

Core	Latitude (°)	Longitude (°)	Water depth (m)	Core length (cm)	References
GL17-13A-V	53.561	-60.235	75	332	(Gagnon-Poiré, 2023; Lapointe et al., 2025)
GL23-20 composite sequence	53.682	-60.502	245	2066	(Kury et al., 2025)

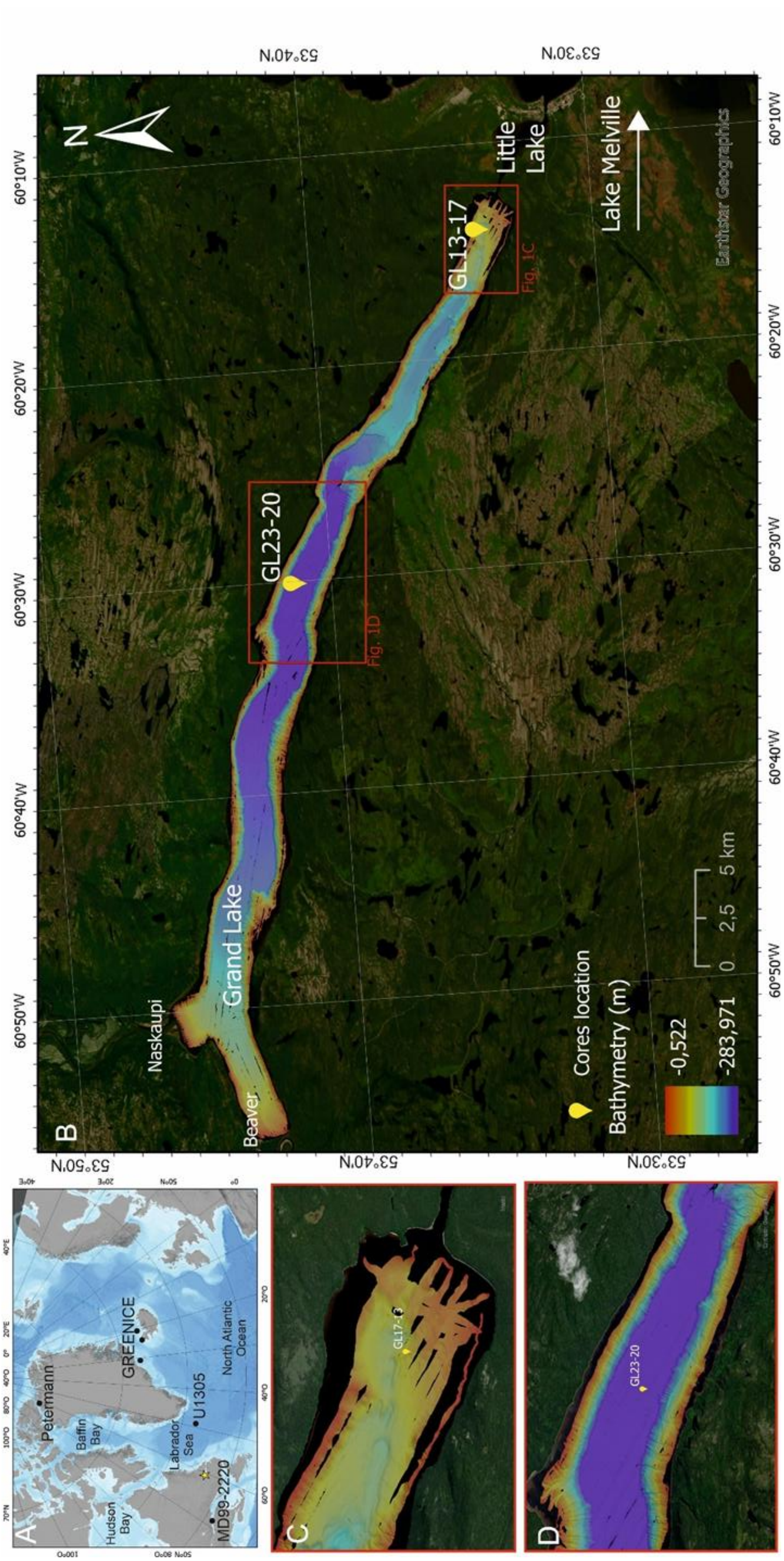
A
Hudson Bay
Baffin Bay
Petermann
GREENICE
Labrador Sea
U1305
North Atlantic Ocean
MD99-2220
B
Beaver
Naskaupi
Grand Lake
GL23-20
GL13-17
Little Lake
Lake Melville
Fig. 1D
Fig. 1C
N
Cores location
Bathymetry (m)
-0,522
-283,971
0 2,5 5 km
Earthstar Geographics
60°50'W
60°40'W
60°30'W
60°20'W
60°10'W
53°50'N
53°40'N
53°30'N
C
GL17-1
D
GL23-20

Figure 46. Map of the study location. **A.** Location of Grand Lake in Labrador. Yellow star represents the location of the cores in Grand Lake. Black dots indicate location of comparison records. **B.** Map of Grand Lake and location of the cores collected in 2023 and 2017. **C.** Zoom on GL17-13 core location and bathymetry at the site. **D.** Zoom on GL23-20 core location and bathymetry at the site. The figure was made using ArcGIS and CorelDraw. The bathymetry data is from Trottier et al., (2020).

3.5.2 Physical and geochemical properties

3.5.2.1 GL17-13 sediment core

Core GL17-13 was cut into three sections (I, II, III) and then opened and described. A high-resolution line-scan camera mounted on an ITRAX core scanner was used to photograph the sections at INRS-ETE (Quebec). X-ray fluorescence (XRF) analysis was conducted using the ITRAX core scanner at 100 µm resolution on the three sections (30 kV, 30 mA) to determine major and minor elements composition in sediments (Croudace, 2006).

3.5.2.2 GL23-20 composite sequence

Cores composing the GL23-20 composite sequence were cut into two one-meter sections in the field. P-wave velocity, density and magnetic susceptibility were measured on whole cores using the GEOTEK Multi Sensor Core Logger (MSCL) at ISMER. Cores were cut in halves and opened. Texture, grain size and color were described on the archive halves using the Munsell color chart. Archive halves were line scanned immediately after opening using a GEOTEK Geoscan V imaging system mounted on a GEOTEK MSCL. Diffuse spectral reflectance measurements were conducted at 1 cm intervals using a Minolta CM-2600d spectrophotometer at ISMER. The data acquired were expressed according to the color space of the International Commission on Illumination: L* black (0) to white (100), and a* green (-60) to red (+60) (Debret et al., 2011; St-Onge et al., 2007).

Micro X-ray fluorescence (µ-XRF) analysis was conducted on archive halves of GL23-20 cores, at 100-500 µm resolution using an ITRAX scanner with a molybdenum tube (30 kV, 50 mA) at INRS-ETE. Prior to scanning, the core surfaces were cleaned parallel to the stratigraphy. A polytetrafluoroethylene wrap was applied to the sediment core to avoid dehydration and re-adjusting of the detector (Löwemark et al., 2019). Element spectra were re-evaluated using the software Q-Spec (Croudace et al., 2006) to ensure the removal of background noise and spectral peak overlap, as well as correct peak identification. Initial element intensities are expressed as counts per second. In this study we use the Ca/Fe ratio which is a biogenic carbonate to detrital clay ratio (Croudace & Rothwell, 2015; Rothwell et al., 2006).

Grain size analyses were conducted with a Horiba Laser diffraction analyzer (range: 0.011–3000 µm) at INRS-ETE. Prior to the analyses, organic matter (OM) was removed by adding 30% H_2O_2 at 60°C (Vaasma, 2008). Samples were then rinsed and agitated in a 3% hexametaphosphate solution. Afterwards, grain-size distribution (GSD) was calculated with the Excel GRADISTAT v.9.0 spreadsheet (Blott and Pye, 2001) using the statistical parameters of Folk & Ward.

3.5.3 Continuous paleomagnetic analysis

Continuous subsections were sampled from the working halves using u-channels, with a cross section of 4 cm² and up to 1.5 m long (e.g., Weeks et al., 1993) and were then used to conduct continuous magnetic measurements at 1 cm intervals with a 2G Enterprises 755SRM-1.65 cryogenic magnetometer at ISMER. The natural remanent magnetization (NRM) was measured by demagnetizing the sediment from 0 to 80 mT with increment steps of 5 mT, and from 80 to 100 mT at 10 mT increment steps until a remanent magnetization of 10% the initial remanent magnetization was reached. Anhysteretic remanent magnetization (ARM) was induced with a 100 mT peak field and a 50 µT direct current bias field. Stepwise demagnetization was conducted identically as the NRM. An isothermal remanent magnetization was induced with a pulse magnetizer at 300 mT (IRM) and 950 mT (saturation isothermal remanent magnetization, SIRM). They were measured with 17 demagnetization steps (5 mT increments from 0 to 80 mT) for the IRM and 4 demagnetization steps (0, 10, 30 and 50 mT) for the SIRM. After the measurements, data were first checked and flux jumps corrected if necessary with the UPmag software (Xuan and Channell, 2009). The Mazaud (2005) excel spreadsheet provided declination and inclination data, the maximum angular deviation (MAD) and median destructive field (MDF) values (field intensity required to remove half of the initial remanence). MDF_{NRM} represents the coercivity of the remanence-carrying grain assemblage and is an indicator of magnetic mineralogy. The MDF_{ARM} indicates the mineral coercivity of the magnetic assemblages responding to ARM and reflects magnetic mineralogy and grain sizes (Stoner and St-Onge, 2007). MAD values <5° reflect high quality data and reliable inclination and declination results. High MAD values generally show complex magnetization with different coercivities and must be used carefully for paleomagnetic reconstructions. Zijderveld diagrams (orthogonal projections; Zijderveld, 1967) enable to check on the demagnetization process and to select the ChRM steps. k_{ARM}/k_{LF} is a parameter sensitive to downcore magnetic grain size and mineralogy variations (Banerjee et al., 1981; King et al., 1982). If the magnetic mineralogy is dominated by magnetite, it varies inversely with the magnetic grain size (Stoner and St-Onge, 2007). Due to the response function of the magnetometer, values are smoothed over 7-8 cm (Philippe et al., 2018; Stoner and St-Onge, 2007; Weeks et al., 1993). To avoid biases resulting from this response function, the 4 cm intervals at the top and bottom of each u-channel were excluded. The characteristic remanent magnetization (ChRM) directions were calculated by principal component analysis (Kirschvink, 1980) with the Excel routine from Mazaud (2005), using the 20 to 60 mT demagnetization steps.

3.5.4 Rock magnetic measurements

An AGICO KLY-3 susceptibility meter was used at IPGP to measure the temperature-dependent magnetic susceptibility of some samples (10, 30, 86, 127, 185, 203, 250 and 271 cm of core GL17-13). The samples were heated up to 700°C and then cooled down to room temperature, in air-atmosphere. It enables to identify the Curie temperature (Dunlop and Ozdemir, 2007). The measurements were mass-normalized.

Hysteresis loops, remanence curves, IRM acquisition curves and first order reversal curve (FORC) diagrams were acquired on a Princeton Measurements vibrating sample magnetometer (VSM) at IPGP for core GL17-13. Dia/paramagnetic correction (70%) was applied to the hysteresis loops from which magnetic parameters were derived: coercive force (Hc), remanent coercive force (Hcr), saturation magnetization (Ms) and saturation remanence (Mrs). S-ratio was calculated according to the Bloemendal et al. (1988) equation $S\text{-}ratio = 0.5 \times (1- \frac{IRM_{-300\,mT}}{SIRM})$ using parameters derived from back-field remanence curves. These parameters and hysteresis loops are used to estimate the domain state of the samples (Day et al., 1977). The online software MAX unMix (Maxbauer et al., 2016) was used to identify the coercivity distribution of the main magnetic carriers contributing to the IRM acquisition curves, for samples 86, 127, 203 and 250 cm). The FORC diagram (sample at 87 cm), processed with the FORCinel software (Harrison and Feinberg, 2008), allows to identify the domain state and coercivities of the magnetic minerals present in the sample (Roberts et al., 2019, 2022).

Hysteresis loops and parameters associated (Hc, Hcr, Ms, Mrs) for the composite core GL23-20 were acquired using an alternating gradient field magnetometer (AGM) at ISMER. The resulting coercivity and remanence ratios (Hcr/Hc; Mrs/Ms) are used in the Day plot to estimate the magnetic domains (Day et al., 1977; Dunlop, 2002).

3.5.5 Chronology

The chronology of core GL17-13 was established by Lapointe et al., (2025) for the top meters of the core and includes varve counting (top 200 cm), AMS radiocarbon dating on wood fragments and ^{137}Cs activity measurements (Table 10). They used core GL20-13B for the top part of the chronology because it was not disturbed. Lapointe et al. (2025) indicated that the base of the varve sequence is situated at 190.9 cm (594 CE/1356 cal yr BP), and the two ^{14}C ages were calibrated using Calib 7.1 (Stuiver et al., 2018) with the IntCal20 calibration curve (Reimer et al., 2020), at 192 cm (492 CE/1458 BP) and 214 cm (359 CE/1591 BP). The ages defined in Lapointe et al. (2025) were used to build the age model for that study (Figure 47) with rBacon (Blaauw and Christen, 2011). However, GL17-13 is 332 cm long and the absence of age constraint at the bottom of the core increases the age uncertainty towards the bottom of the core. Over the whole core, the mean sediment accumulation rate is 125 cm/kyr.

Table 10. Overview of the methods used for establishing the chronology of core GL17-13.

Core	Depth (cm)	Dating method	Material	^{14}C age (yr) ± error (yr)	Median cal age (yr) CE	BP
GL20-13B	0	Varve counting	Varves		2019	-69
GL20-13B	5	^{137}Cs activity	Sediment		1963-1964	-13
GL17-13A-V	190.9	Varve counting	Varves		594	1356
GL17-13A-V	192	Radiocarbon dating (UCIAMS-205590)	Wood fragment	1560±15	492	1458
GL17-13A-V	214	Radiocarbon dating (UCIAMS-205582)	Wood fragment	1710±15	359	1591

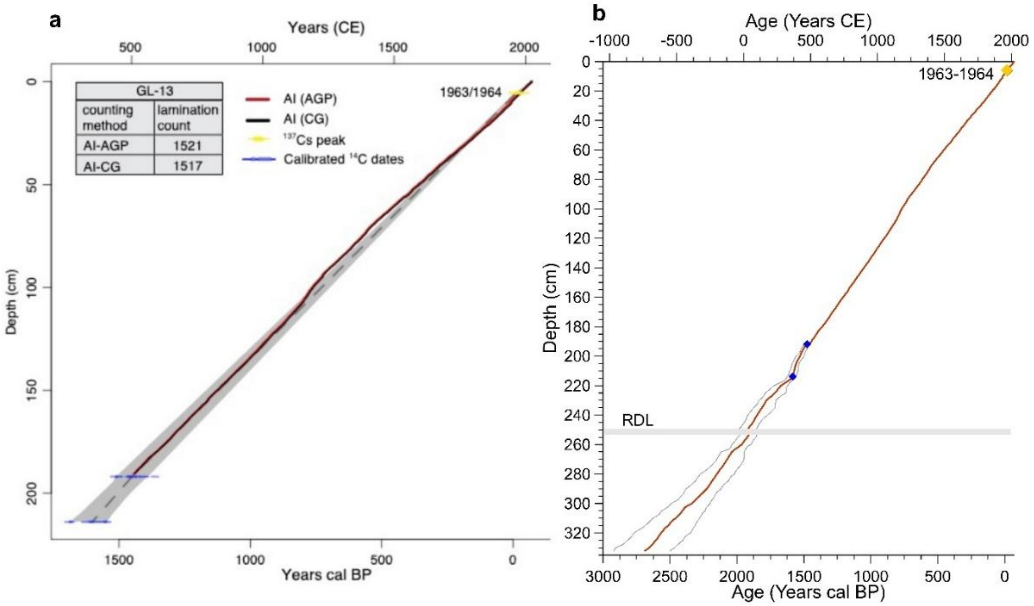

Figure 47. Age model for core GL17-13 . **A.** Age model from Lapointe et al. (2025) based on two individual lamination counts (A.G.P. and C.G.) from thin section using Image Analysis (IA) and from ^{137}Cs and AMS ^{14}C dating. Age-depth model was performed with the ClamR software version 2.2 (Blaauw 2010) using a linear interpolation for the site GL-13 with 95% confidence interval . **B.** Age model from this study, based on Lapointe et al. (2025) for the top 220 cm. The package 'bacon' in R studio was used to extrapolate the age model down to 333 cm, including an RDL (pale yellow bar). Because there are no more constraints at the base of the core, there is a large uncertainty towards the bottom of the core, that must be interpreted carefully.

The chronology of the composite core GL23-20 was established in a previous study by Kury et al. (2025) using a combination of radiocarbon dating on macro organic remains and bulk sediment samples, ^{137}Cs and ^{210}Pb analyses, and varve counting. We detail hereafter, the methodology used in Kury et al. (2025). We use the same age model (Figure 48).

Macro organic remains were collected along with bulk sediment samples at ISMER during core opening. Samples were then graphitized at the *Laboratoire de Radiochronologie* of the *Centre d'Études nordiques* in Québec and then sent for AMS dating to the University of California, Irvine. Additional samples were sent to the Radiocarbon Laboratory of the University of Ottawa. A shell located at 1810 cm depth was sent to the Alfred Wegener Institute for radiocarbon dating with the MIni radioCArbon DAting System (MICADAS).

Ages were calibrated with the Marine20 (shell, marine sample) or IntCal20 (terrestrial samples) calibration curves (Heaton et al., 2023, 2020; Reimer et al., 2020) using the CALIB 8.2 software.

Surface sediments were sampled for ^{137}Cs and ^{210}Pb, using both alpha spectrometry and gamma spectroscopy. Core GL23-20-Up1 was sampled at 1 cm intervals for the top 15 cm, and at 20, 25, and 30 cm. Samples were sent at the *Laboratoire de Géochronologie* of the *Geotop, Université du Québec à Montréal* for ^{210}Pb alpha-counting. Samples were spiked with ^{209}Po, digested with acids (HNO_3, HCl, HF, H_3BO_4, H_2O_2) then centrifuged and plated in discs for counting with alpha spectrometry. Gamma counting was performed on samples from depths 7.25–16.7 cm at the *Institut National de la Recherche Scientifique* in Québec, to assess ^{137}Cs and ^{210}Pb activities. ^{137}Cs was used to identify the 1963–64 nuclear activity peak (Pennington et al., 1976; Ritchie & McHenry, 1990). Alpha-counted ^{210}Pb profile was used to estimate sediment accumulation rates, and along with the gamma-counted ^{210}Pb profile enabled to corroborate the 1963 peak.

The previous analyses were used to calculate the age-depth model of the composite core. The tofu function in R (rbacon package, Blaauw & Christen, 2011) was used with the known surface (0 cm, 2023 CE), ^{137}Cs peak dates and non-calibrated ^{14}C ages. Rapidly deposited layers (RDL) were indicated using the 'slump' function and ages within the RDL were not used. Two iterations were made using $\Delta R = -400$ years and $\Delta R = 0$ for the shell. The latter was chosen for the final age model.

For the surface core GL23-20-Up1, varve counting was used to supplement the methods listed above. Manual varve counting was performed twice with OriginPro (version 8.5; OriginLab, USA), using the superposition of Fe and Sr chemical profiles from μ-XRF as guides for varve differentiation (Zolitschka et al., 2015) along with the high-resolution ITRAX image. The analysis covered the upper 23 cm, where varves were interrupted by a thick clay layer. The error estimation was based on the difference between the two counts.

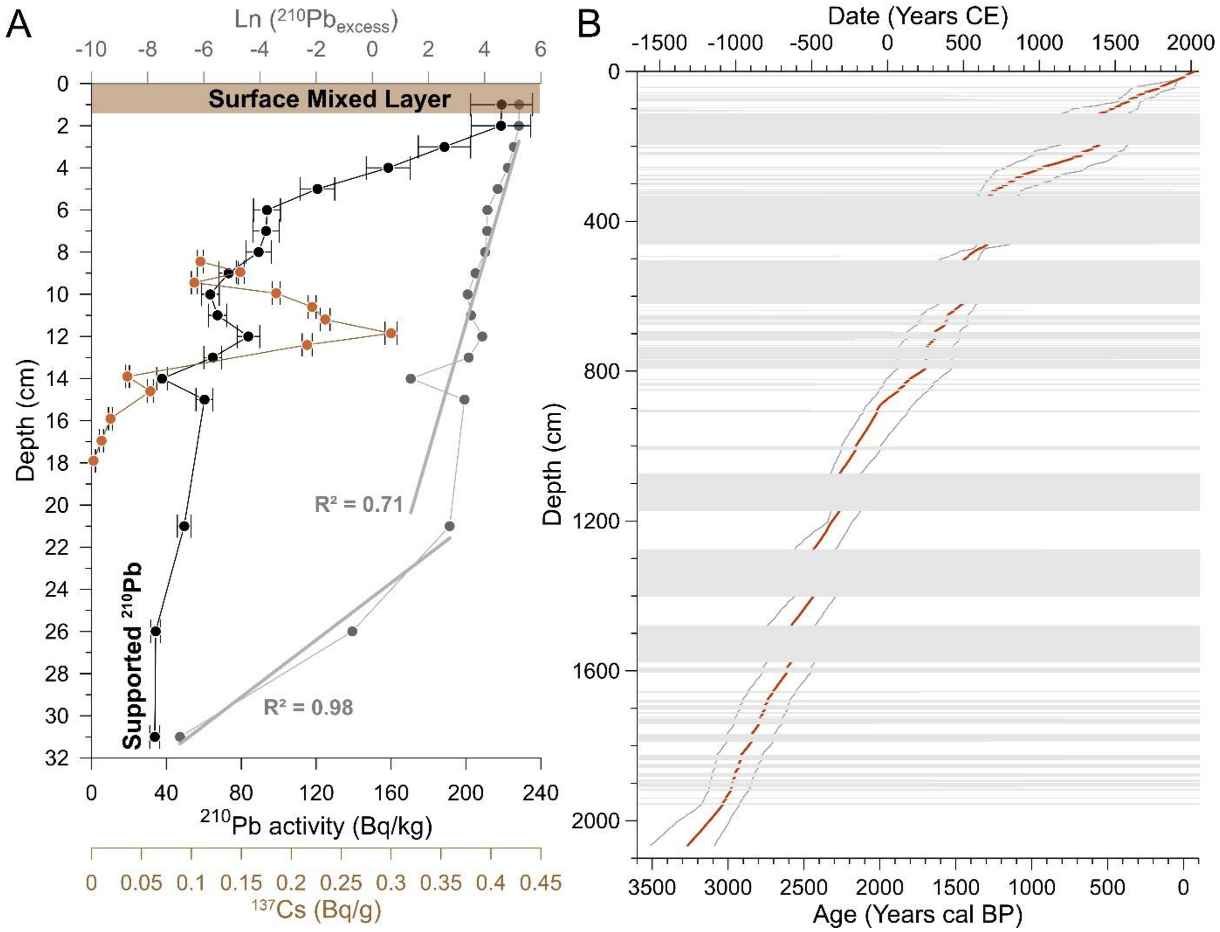

Figure 48. Age-depth model for GL23-20. A. ^{210}Pb activity profile (black curve), ^{210}Pb excess (grey curve), ^{137}Cs (brown curve). The brown bar represents the surface mixed layer. Linear fit curves for the ^{210}Pb excess profiles are used to infer sediment accumulation rates. B. Age depth model from R Tofu calculations: median age (red curve), minimum and maximum ages (grey curves), RDL (grey bars). X axis indicates ages in cal yr BP and date in yr CE.

3.6 RESULTS

3.6.1 Downcore physical, geochemical and magnetic properties

3.6.1.1 GL17-13 core

Sediment facies of the upper part of core GL17-13 are presented in Lapointe et al., (2025). At site GL13, varves are composed of 2 layers (Lapointe et al., 2025) including a basal layer of silty-clay sediment associated with settling of the distal plumes from the Naskaupi and Beaver rivers overflows and an upper clay cap rich in Fe associated with winter conditions when the lake is ice-covered. In Figure 49, we observe low variations in Ca/Fe profile. MDF_{NRM} varies around 35 mT, which is characteristic of low coercivity minerals such as magnetite. MDF_{ARM} is constant throughout the core, indicating that the concentration of magnetic particles activated by ARM is uniform within the entire core. At 262 cm, where Lapointe et al. (2025) identified a RDL, which is also visible in the high resolution image (Figure 49), we observe increased Ca/Fe value together with low k_{ARM} and small increase in MDF_{NRM}. On the zoomed profiles (Figure 49), we observe an abrupt increase followed by a gradual decrease upward in both Zr/Rb and Ca/Fe profiles. Zr/Rb being a well known grain size proxy (Croudace and Rothwell, 2015; Kylander et al., 2011), it could indicate the turbiditic nature of the RDL rather than hyperpycnite, for which we expect a gradual grain size increase, followed by a gradual grain size decrease (Mulder et al., 2003). However, grain size measurements or an observation in thin-section are required for further differentiation.

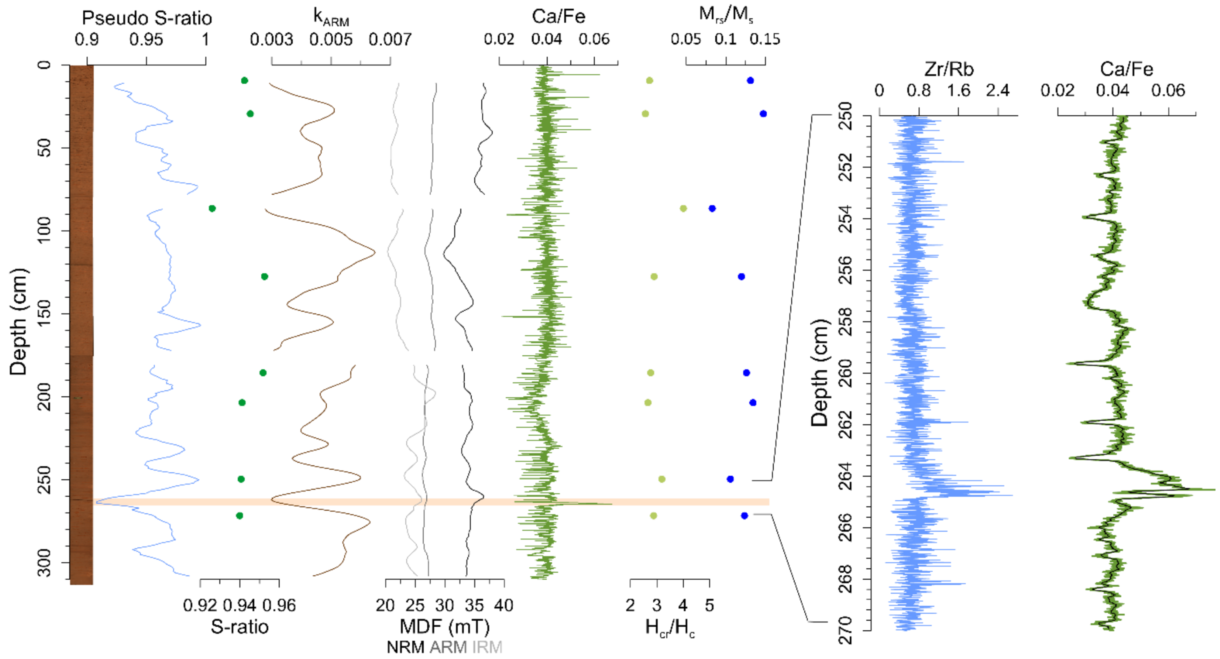

Figure 49. GL17-13 down core properties. High-resolution image, Pseudo S-ratio and S ratio, k_{ARM} (magnetic susceptibility of the ARM), MDF of the NRM, ARM and IRM, Ca/Fe from XRF analyses, Hcr/Hc and Mrs/Ms from hysteresis loop measurements. The thin yellow bar indicates the RDL. The zoom profiles on the right show Zr/Rb and Ca/Fe profiles for the RDL.

3.6.1.2 GL23-20 composite sequence

Sedimentary facies descriptions of core GL23-20 composite sequence presented in Kury et al. (2025), along with elemental composition and grain sizes, enabled to identify 75 RDL. At site GL-20, varves are composed of 2 to 3 layers including a thicker silty lower layer, topped with either a thinner greyish brown layer and a clayey silt cap or just a clayey silty cap (Kury et al., 2025). In Figure 50, k_{LF} values vary around 150 x 10^{-5} SI, with higher values up to 850 x 10^{-5} SI in RDL. a* values vary between 5 to 10, with lower values in RDL (down to 0), and some layers presenting values up to 40. L* varies inversely with a*, between 0-55. Pseudo S-ratio ($IRM_{0mT}/SIRM_{0mT}$) can be used as a proxy for magnetic mineralogy (Stoner and St-Onge, 2007). Values are close to 1 indicating globally low coercivity and ferrimagnetic mineralogy. Some RDL (112-197 cm, 736-793 cm, 1073-1173 cm, 1591-1604 cm) are characterized by lower values, around 0.8. Because the SIRM and IRM intensities measured by the magnetometer are so high, they are closer to the detection limit of the instrument, resulting in pseudo S-ratio being sometimes >1. For that reason, we use this ratio as a magnetic mineralogy indicator and combine it with discrete measurements such as the S-ratio, described below (4.2). k_{ARM}/k_{LF} ratio decreases in RDL, indicating coarser magnetic grain size in these layers. RDL identified in Kury et al. (2025) all present higher MDF variations, higher Ca/Fe and grain size values. D_{50} values vary around 2-7 µm and up to 400 µm in RDL, whereas D_{90} is comprised between 4 µm in normal sedimentation and 815 µm in RDL. k_{LF} values are decreasing towards the top, which is typical of normal grading in turbidites as seen previously in turbidites from the Saguenay Fjord (St-Onge et al., 2004) and Coronation Fjord (Rodríguez-Cuicas et al., 2023). Ca/Fe, D_{50} and D_{90} also depict a sharp increase at the base of the RDL and then a gradual decrease towards the top of the layer.

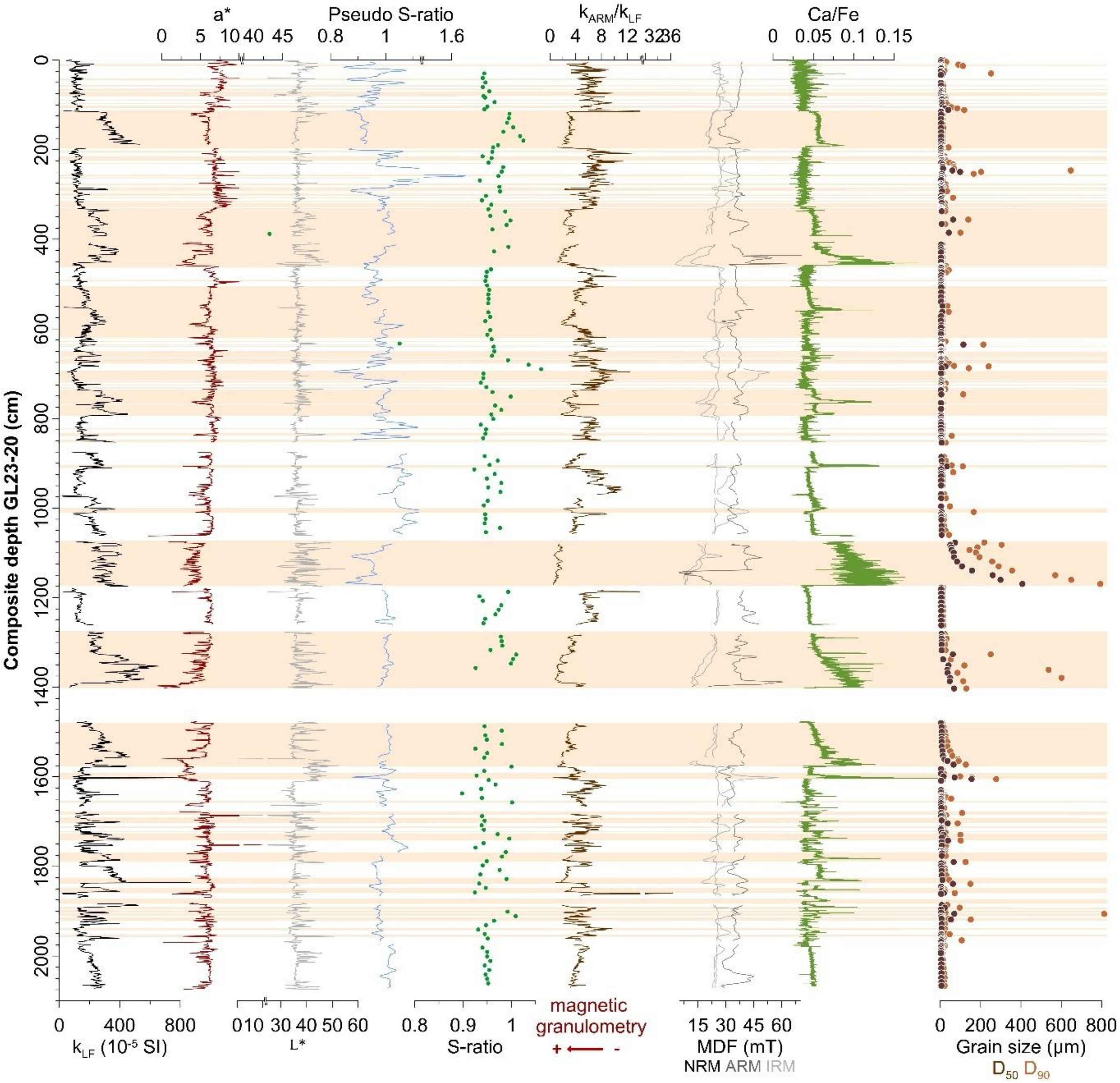

Figure 50. GL23-20 composite downcore properties. From left to right: magnetic susceptibility (k_{LF}), a*, L*, Pseudo S-ratio, S-ratio, k_{ARM}/k_{LF}, MDF (NRM, ARM and IRM), Ca/Fe and grain size data (D_{50} and D_{90}). Beige horizontal bars indicate RDL.

3.6.2 Rock magnetic results

3.6.2.1 GL17-13 core

Curves of magnetic susceptibility variations against temperature (Figure 51) all depict the Curie transition around 580°C characteristic of magnetite and most samples present a smaller magnetic susceptibility increase in their heating phase at 350°C. The non-reversible curves and the increase in magnetic susceptibility after cooling suggest the formation of strongly susceptible minerals. All samples present similar curves, attesting to the uniformity of the magnetic mineralogy in GL17-13 sediment core. Hysteresis loops (Figure 52) for all samples show comparable shape, reaching saturation >300 mT (around 500 mT), indicating the presence of higher coercivity minerals. IRM unmixing curves are similar, with the main coercivity between 55-60 mT, confirming the influence of higher coercivity minerals. The central ridge on the FORC diagram (Figure 52) characteristic of single domain particles, indicates micro coercivities between 0 and 50 mT. Spreading along the vertical axis suggests the presence of vortex state, (or pseudo single domain) particles (Roberts et al., 2017). The Day plot (Figure 55, Day et al., 1977) indicates that magnetic particles fall within the vortex state. Despite high coercivity minerals, magnetite seems to be one of the main components of the magnetic mineralogy of this core. Moreover, the mineralogy being stable throughout the core is an indication that this sediment meets the criteria to record reliable paleomagnetic variations.

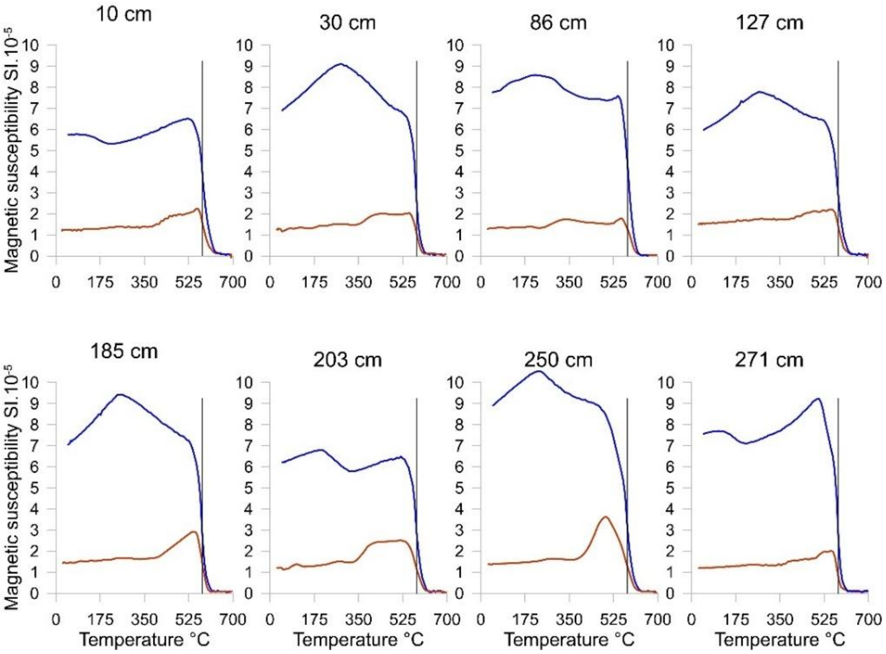

Figure 51. Magnetic susceptibility variations curves depending on the temperature. Heating curves in red, cooling curves in blue.

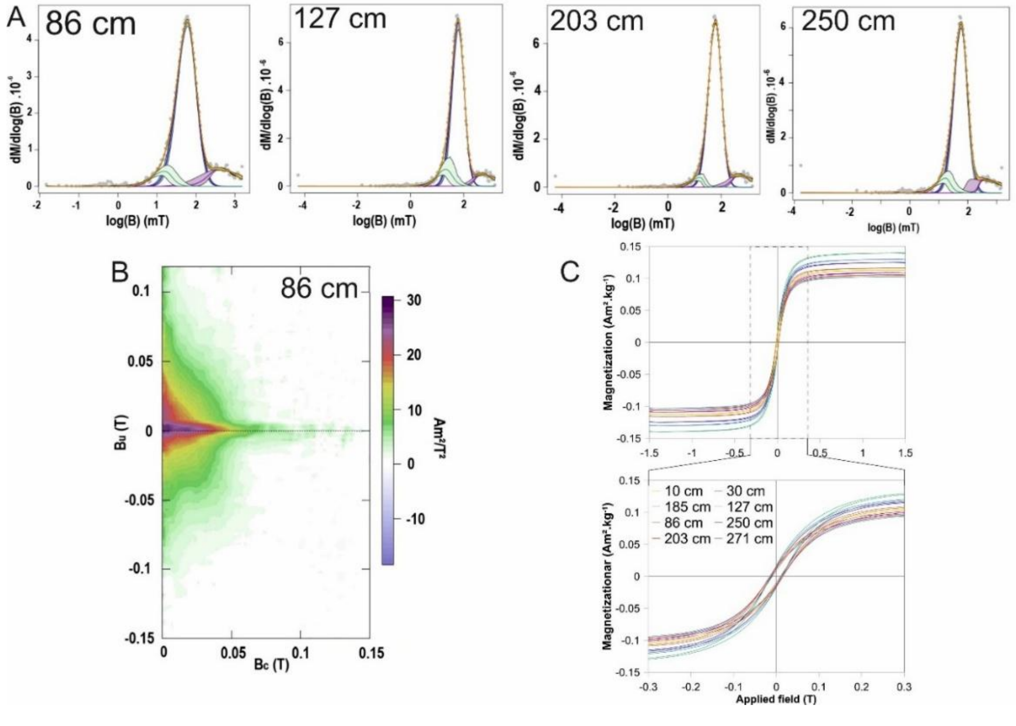

Figure 52. Rock magnetic results of core GL17-13 samples. **A**. IRM unmixed curves indicating the samples main coercivities. **B.** FORC diagram. **C.** Hysteresis loops**.**

3.6.2.2 GL23-20 composite sequence

Hysteresis loops of samples from GL23-20 composite sequence show diverse shapes, with different intensities of magnetization (Figure 53). Hysteresis loops for sediments at the top of the composite sequence (0-110 cm) indicates saturation at ~500 mT, similar to the sediment throughout the core, but with higher magnetization values (up to $8x10^{-7}$ Am²). Sediment at the bottom of the core presents much higher magnetization ($1.5x10^{-5}$ to $4x10^{-5}$ Am²), but similar saturation values. RDL hysteresis loops have more diverse shapes and magnetization values (from $1.7x10^{-7}$ to $1.7x10^{-6}$ Am²). RDL hysteresis loops were only measured at the top of the layers because of the coarser particles at the RDL base. King plot (Figure 54, King et al., 1983) illustrates that magnetic grain size for most samples which are not RDL sedimentation is <1 µm. Some samples show magnetic grain size between 1-5 µm. This is confirmed by the Day plot, where most samples show characteristic size of vortex state grains. RDL samples are more diverse in terms of magnetic particle size, up to 20 µm. MDF and ARM values look similar for the top of GL23-20 composite sequence and GL17-13. However, it is difficult to assess further similarities because some magnetic property analyses are not the same for the two cores (k_{LF} and VSM analyses).

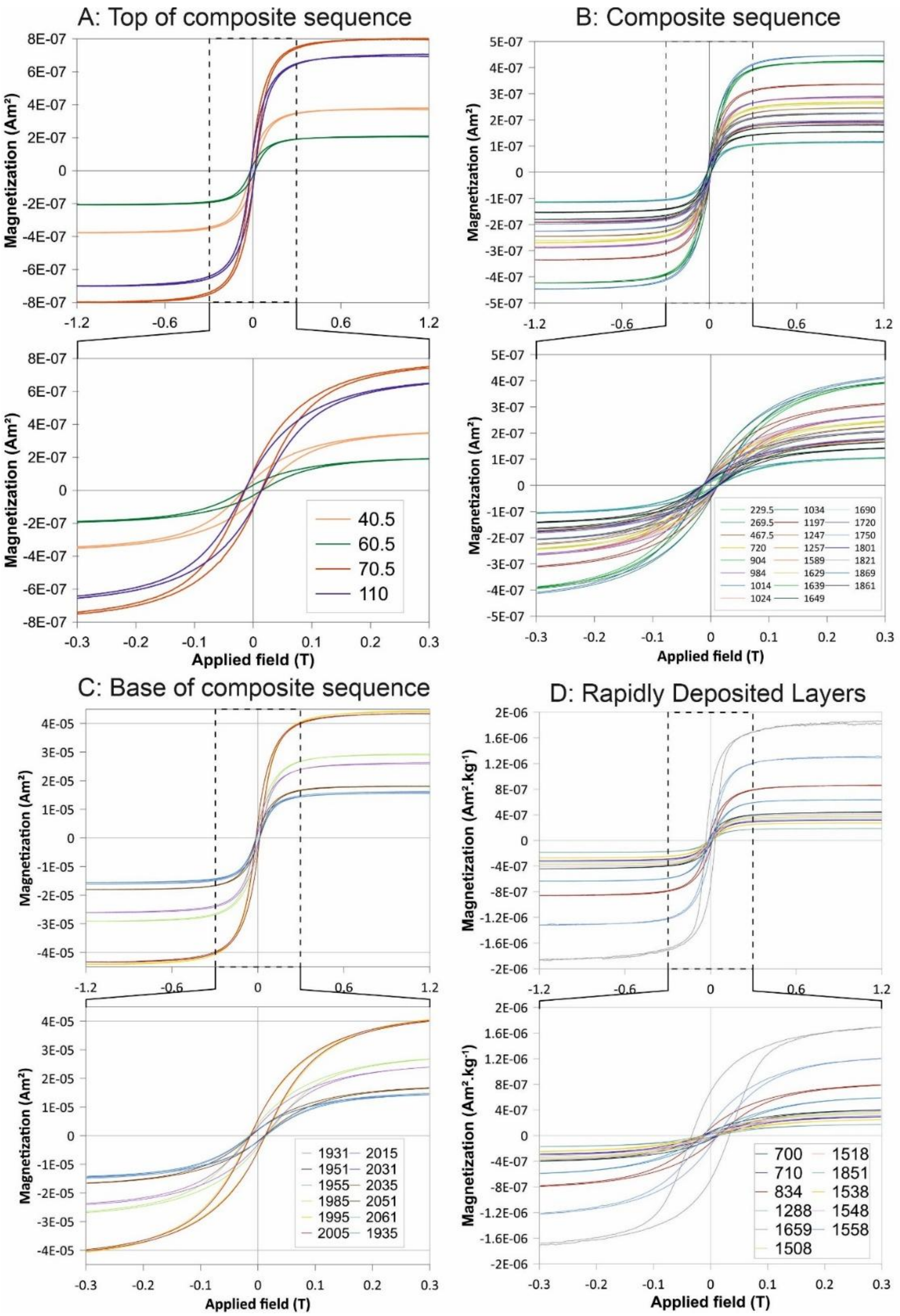

Figure 53. Hysteresis loops for GL23-20 composite core. **A.** Hysteresis loops for samples at the top of the composite sequence (0-200 cm). **B.** Hysteresis loops for samples in the composite sequence (200-1800 cm) **C.** Hysteresis loops for samples at the base of the composite sequence (1900-2050 cm) **D.** Hysteresis loops for RDL samples.

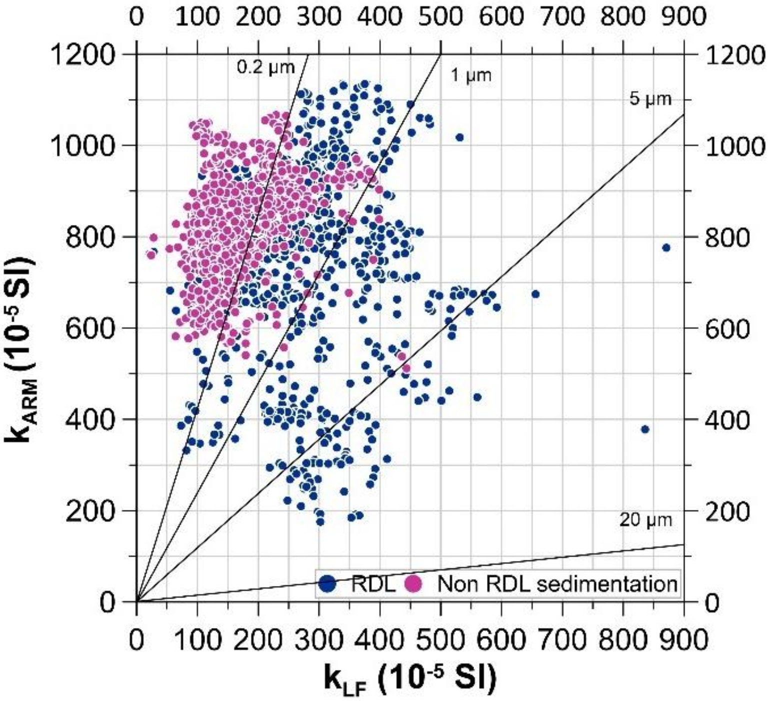

Figure 54. King plot (King et al., 1983). RDL samples are represented by blue dots, background sedimentation is represented by pink dots.

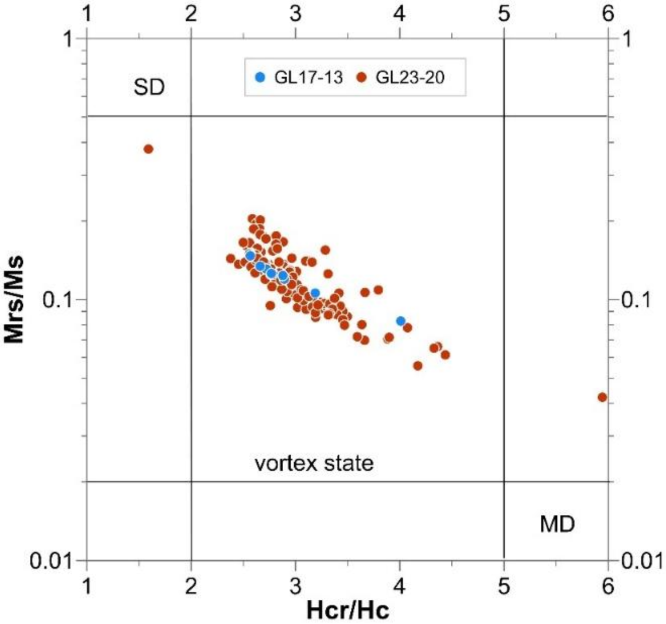

Figure 55. Day plot (Day et al., 1977). Blue dots are samples from core GL17-13. Red dots are samples from GL23-20 core.

3.6.3 Continuous paleomagnetic results

3.6.3.1 GL17-13 sediment core

GL17-13 core displays high NRM intensity (Figure 56), up to 0.3 A/m, with a small intensity decrease in the RDL layer (0.15 A/m). All laboratory induced magnetizations (ARM, IRM and SIRM) show no large changes in concentration, grain size or mineralogy of the magnetic particles within the core. Inclination values vary between 55° and 90°, around the GAD value (69.7°) and MAD values are <5°, except for the RDL which will be excluded from further reconstructions. Declination values show a large range of variations (360°).

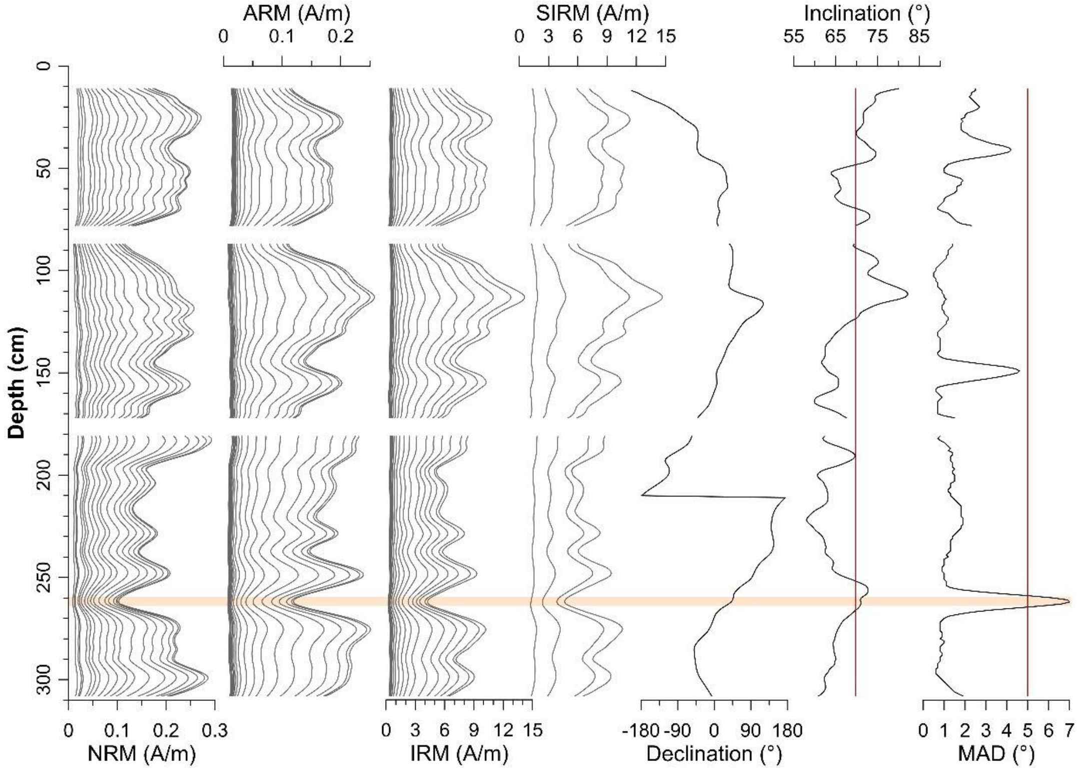

Figure 56. Continuous paleomagnetic analyses for GL23-20 composite sequence. From left to right: NRM, ARM, IRM and SIRM intensity for the different demagnetization steps mentioned in the methods, inclination and GAD values, declination values, MAD values. Beige horizontal bars indicate RDL.

Based on the above results, we argue that the magnetic record from core GL17-13 is suitable for paleodirections and paleointensity reconstitutions as it is composed of a strong, single component magnetization carried out predominantly by low coercivity minerals such as magnetite in the vortex state. We used both the slope (Tauxe et al., 1995; Valet and Meynadier, 1998) and the ratio methods (Channell et al., 2000; Stoner et al., 2000; Tauxe and Wu, 1990) to determine which normalizer is the more suitable between ARM and IRM (Figure 57). Both methods and both normalizers render similar normalized intensity profiles. The slope method displays correlation coefficients >0.97 for IRM and >0.98 for ARM. The determination coefficient R^2 (0.0057 for IRM and $4.5x10^{-5}$ for ARM) indicates that there is no correlation and resemblance between the normalizer and the normalized intensity. Figure 57f indicates changes in concentration of magnetic particles less than one order of magnitude, and very small changes in magnetic particle size throughout the core.

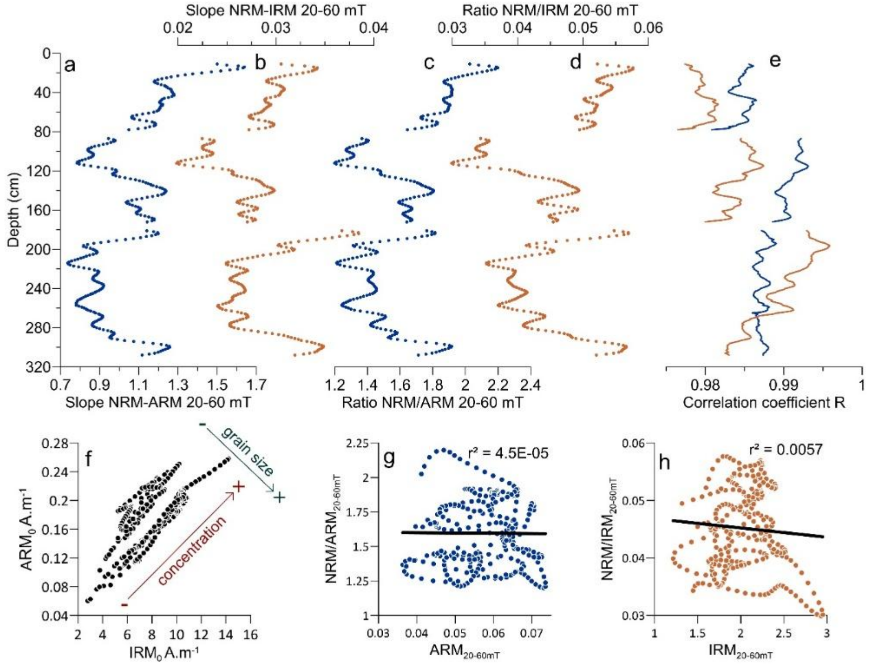

Figure 57. Relative paleointensity determination. **A.** Slope NRM-ARM 20-60 mT . **B.** Slope NRM-IRM 20-60 mT. **C.** Ratio NRM/ARM 20-60 mT. **D.** Ratio NRM/IRM 20-60 mT. **E.** Correlation coefficient (R) for ARM (blue curve) and IRM (brown curve) for the slope method. **F.** ARM against IRM values, indicator of magnetic grain-size and concentration variations. **G.** ARM determination coefficient r^2 for the ratio method. H. IRM determination coefficient r^2 for the ratio method.

3.6.3.2 GL23-20 composite sequence

Different NRM variations can be observed in the GL23-20 composite sequence (Figure 58). From the base of the sequence to ~1600 cm, we observe strongly variable NRM intensities between 0.1 A/m in RDL and 0.3 A/m in normal sedimentation. From 1600 to 850 cm, NRM intensities are more homogeneous between RDL and non RDL sedimentation, around 0.1 A/m with only two peaks at 0.3 A/m. From 850 cm to the surface, we notice again an alternance between strong NRM intensities, up to 0.6 A/m, and weaker intensities down to 0.1 A/m in RDL. ARM intensities are more uniform throughout the core, varying between 0.2-0.4 A/m, with lower intensities in RDL. In contrast, IRM shows highly variable variations, with very strong intensities in RDL, up to 25 A/m, and strong intensities in normal sedimentation layers, up to 10 A/m. SIRM depicts the same variations and similar intensities (up to 27 A/m) to IRM. It seems that magnetic particles in RDL are more activated by IRM or SIRM than ARM, indicating that they probably contain more high coercivity minerals, or higher grain size particles. Normal sedimentation still responds to IRM, indicating the presence of high coercivity minerals in these sediments as well. Inclination is highly variable, with some RDL presenting negative values. Values at the bottom of the sequence (1600-2060 cm) are less variable and closer to the GAD value. Declination values were rotated to a mean of 0, according to the GAD assumption, and depicts high variations, especially in RDL. For further PSV and RPI reconstructions, RDL were excluded and declination values were rotated again to a mean of 0 without the RDL values (Figure 58). Most RDL present MAD>5°, up to 32°. For the rest of the sediment, MAD<5° for most of the sequence, except some layers, which are not identified as RDL but still present MAD>5° (900-1050 cm, 1170-1275 cm, 2000-2060 cm).

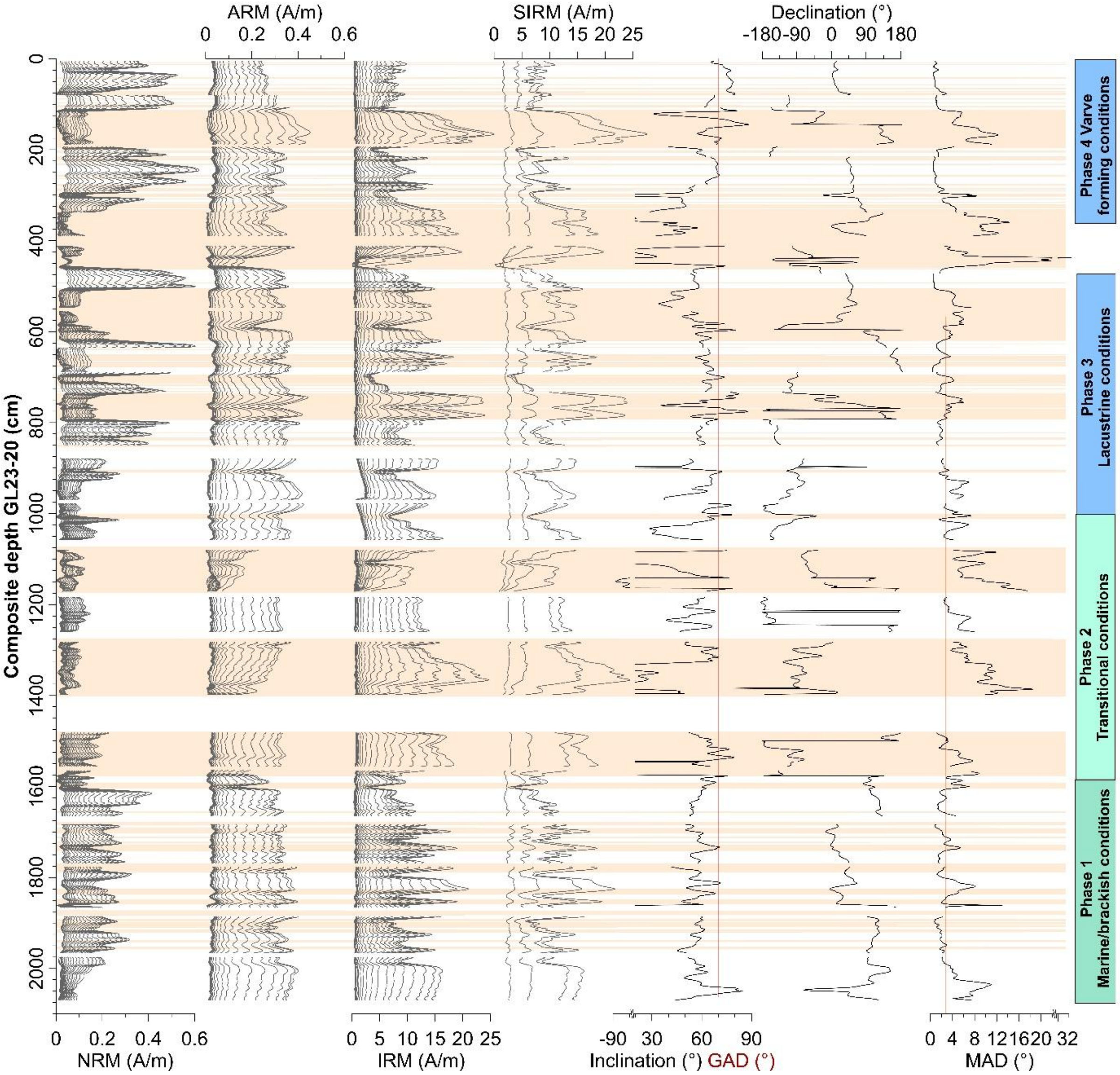

Figure 58. Continuous paleomagnetic analyses for GL23-20 composite sequence. From left to right: NRM, ARM, IRM and SIRM intensity, inclination and GAD values, declination values, MAD values. Beige horizontal bars indicate RDL. Blue and green rectangles indicate the changes in sedimentary environment indicated in Kury et al., (2025).

As just mentioned above, given the large intensity fluctuations of the different magnetization, and the several RDL interrupting the record, we do not think the entire composite sequence is suitable for paleomagnetic reconstructions Figure S16, S17, S18 in supporting information). Figure 59f indicates large changes in magnetic concentrations and grain sizes. The high determination coefficient r² (Figure 59h) indicates that IRM cannot be used as a normalizer for paleointensity and for that reason, we chose to use ARM, for core GL23-20-Up1 (Figure 59).

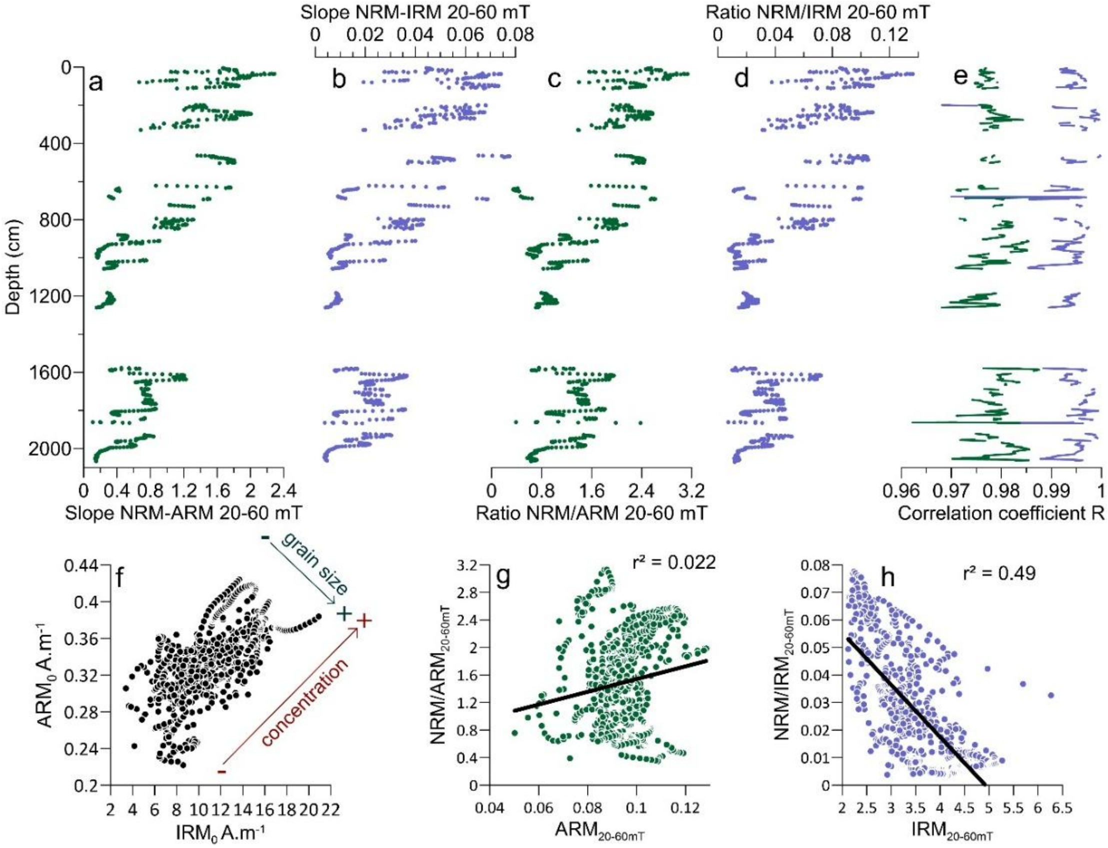

Figure 59. Relative paleointensity determination for GL23-20 composite sequence. **A.** Slope NRM-ARM 20-60 mT. **B.** Slope NRM-IRM 20-60 mT. **C.** Ratio NRM/ARM 20-60 mT. **D.** Ratio NRM/IRM 20-60 mT. **E.** Correlation coefficient (R) for ARM (green curve) and IRM (purple curve) for the slope method. **F.** ARM against IRM values, indicator of magnetic grain-size and concentration variations. **G.** ARM determination coefficient r² for the ratio method. **H.** IRM determination coefficient r² for the ratio method.

3.7 DISCUSSION

3.7.1 Identification and impact of the rapidly deposited layers on the detrital remanent magnetization

RDL are not reliable recorders of the geomagnetic field because they are instant deposits and often composed of coarse particles. Several studies (Bieber, 2022; Philippe et al., 2022; Rodríguez-Cuicas et al., 2023) investigate the impact of turbulence on the detrital remanence magnetization (DRM). GL23-20 composite core presents 75 RDL, 55 being <8 cm. U-channel measurements smooth the signal over 8 cm, thus we consider that the RDL signal is averaged with the normal sedimentation signal on RDL <8 cm. Among the 20 RDL >8 cm, eight are >20 cm (Figures 61 to 67, RDL 16, 33, 37, 49, 50, 56, 57 and 58). We studied several characteristics of the RDL including grain size parameters (D_{50} and D_{90}), elementary composition (Ca/Fe ratio), L*, a*, magnetic susceptibility parameters (k_{LF}, k_{ARM}/k_{LF}), MDF, inclination and MAD values. Ca/Fe ratio is generally used for turbidite/pelagic discrimination in marine environments, assessing textural character and sediment grading (Croudace and Rothwell, 2015; Rothwell et al., 2006). From what we observe here (Figures 50, 51 and 61 to 67), Ca/Fe peaks indicate the base of turbidites, even in a lacustrine environment. RDL 16, 33, 49, 50, 56, 57 and 58 were identified as type A in Kury et al., (2025), which refers to classic turbidites. RDL 37 was identified as type D, originating from slope failures (Kury et al., 2025).

Some RDL depict normal grading (RDL 16, 56, 58; Figures 61, 65, 67) in their D_{90} and Ca/Fe values. Other present peaks in other parts of the layer: for example, in RDL 37 (504-622 cm), D_{90} = 50 µm at 560 cm (Figure 62). RDL 33 present 2 peaks at 355 and 385 cm, with D_{90} = 140 µm and 95 µm respectively (Figure 62). The Ca/Fe is globally decreasing from the base of layers towards the top in all RDL except in RDL 37 where we observe a peak in the middle of the layer (Figure 62) and RDL 57 where we observe some peaks throughout the layer (Figure 65). L* and a* parameters do not depict any specific variations. Low field magnetic susceptibility k_{LF} decreases from the base towards the top of the layer in

RDL 16 (Figure 60) and especially 49 and 50 (Figure 63) and do not depict clear tendencies in RDL 33, 37, 56, 57 and 58 (Figures 62, 63, 65, 66, 67). It globally varies between 100 and 500 µm and up to 750 µm in RDL 57 (Figure 65). k_{LF}/k_{ARM} varies between 1 and 9 µm (RDL 33, 37, 49, 50, 57, 58) except for a peak at 28 µm in RDL 16 (Figure 60) and values between 0.5-2 µm in RDL 56 (Figure 64). MDF_{NRM} values vary between 10 and 50 mT with some higher values up to 60 mT (RDL 57) and 70 mT (RDL 33). MDF_{ARM} and MDF_{IRM} present stable variations. MDF_{NRM} presents higher values at the base of the layers in RDL 16, 33, 57, 58. We observe inclinations values between 30-90° in RDL 16, 37, 49 and 50, whereas RDL 33, 56, 57 and 58 present negative values, especially at the base of the layer, which is characteristic of turbidites (e.g. Philippe et al., 2022, 2023; Rodríguez-Cuicas et al., 2023; St-Onge et al., 2004; Tanty et al., 2016). Even though RDL 16 and 49 do not show negative inclination values at the base of the layer, they still present lower values. All layers present MAD values >5°, up to 20° or 30° for RDL 33 and 57. RDL presenting negative values of inclination, also show the highest MAD values, at the base of the layers too. We do not observe any particular common features between all RDL. Nonetheless, paleomagnetic parameters can be used to identify RDL: low inclination values, high MAD values, high k_{LF} at the base of the layer, with sharp contact underneath, decreasing towards the top.

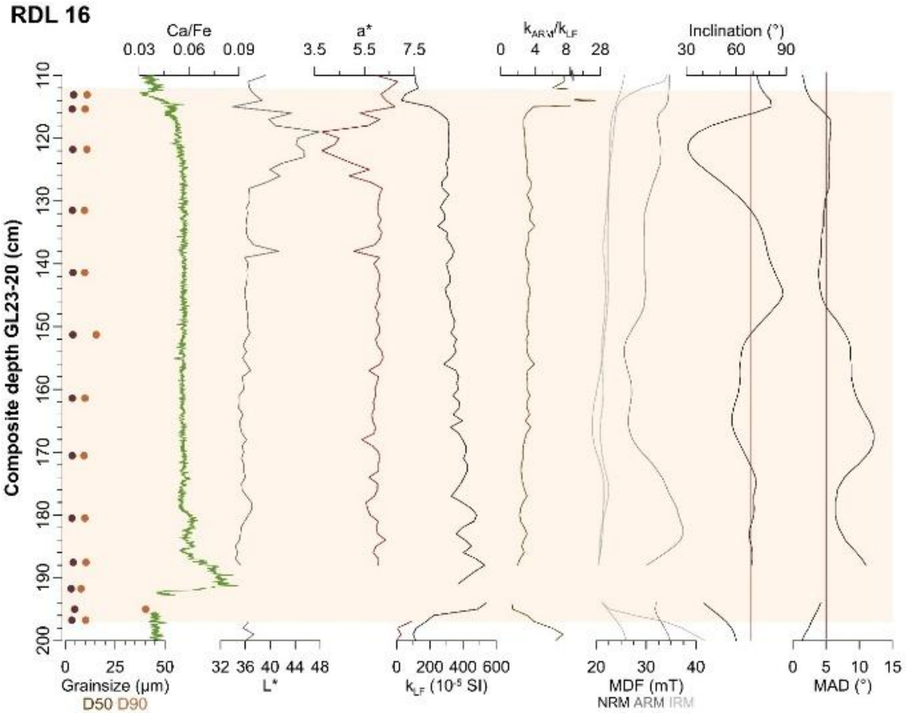

Figure 60. Physical, elemental and magnetic properties of RDL 16**.**

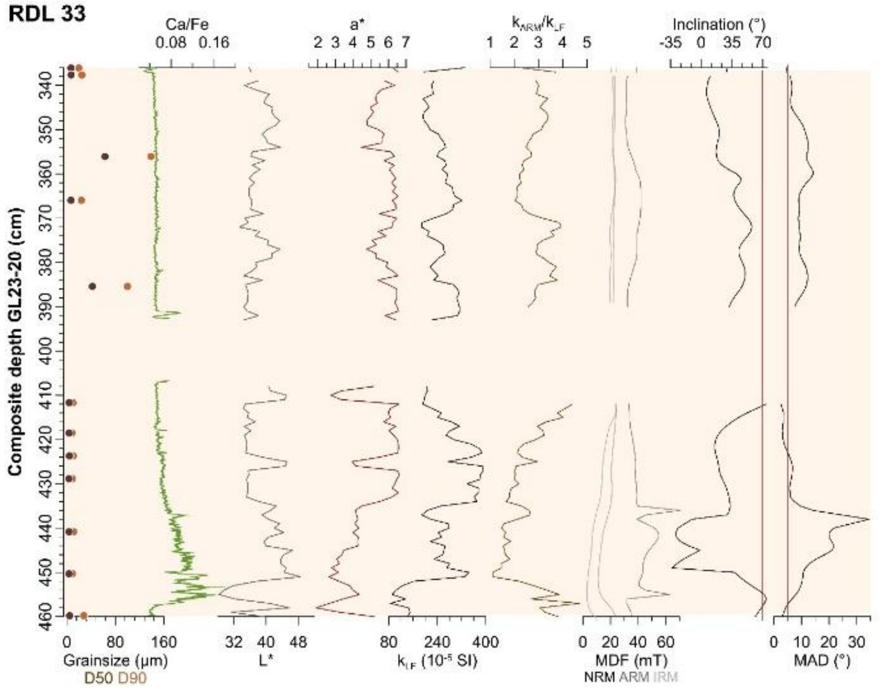

Figure 61. Physical, elemental and magnetic properties of RDL 33.

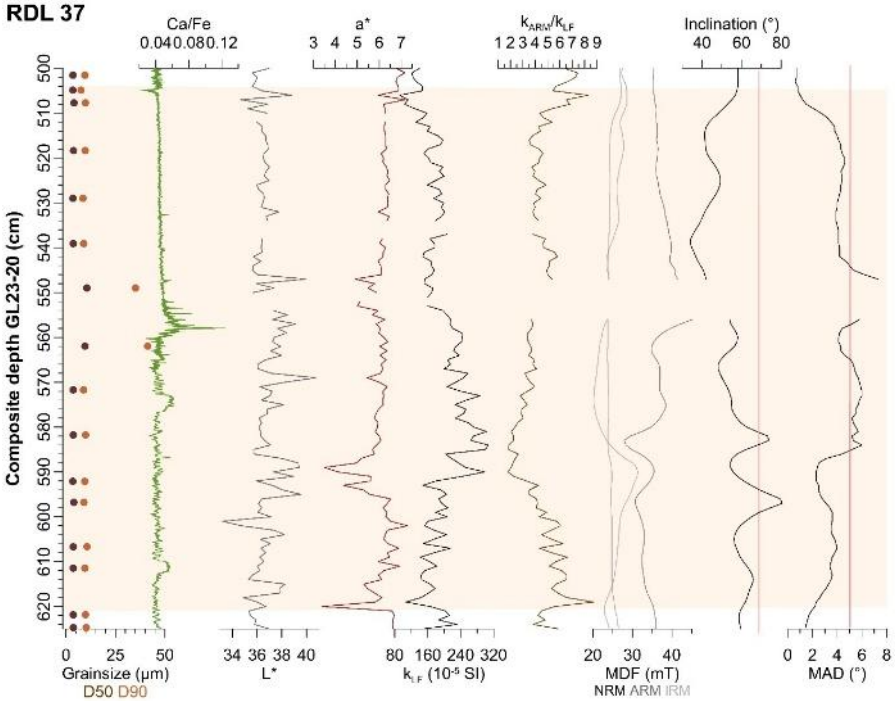

Figure 62. Physical, elemental and magnetic properties of RDL 37.

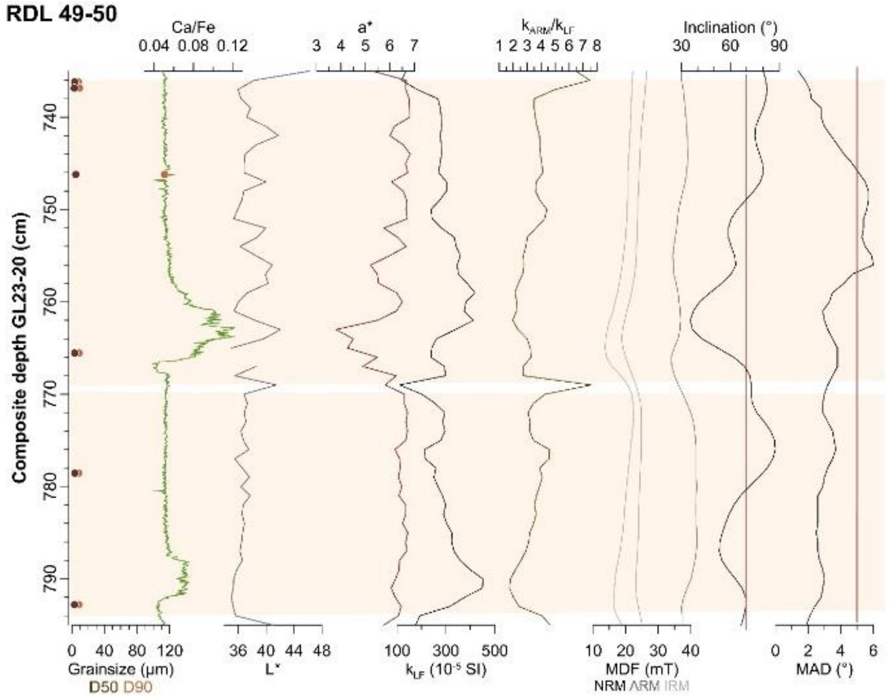

Figure 63. Physical, elemental and magnetic properties of RDL 49 and 50.

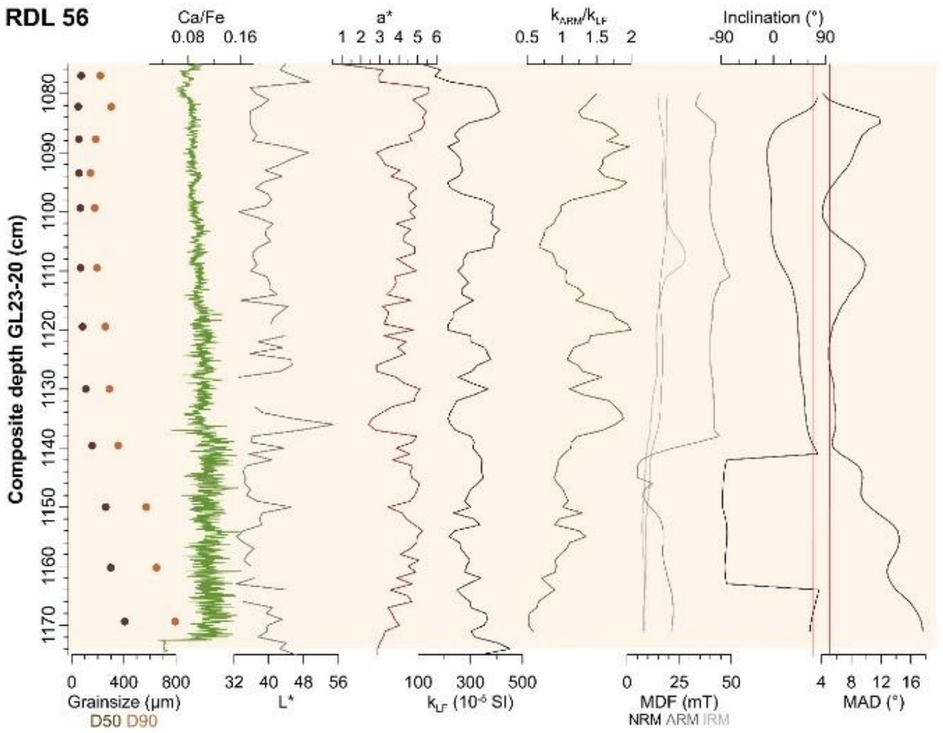

Figure 64. Physical, elemental and magnetic properties of RDL 56.

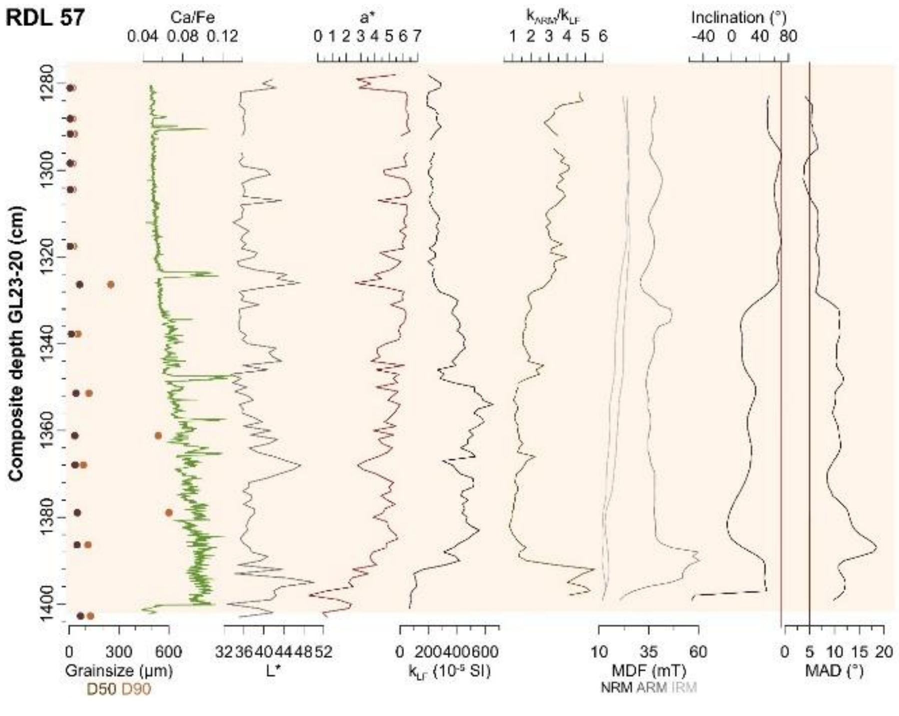

Figure 65. Physical, elemental and magnetic properties of RDL 57.

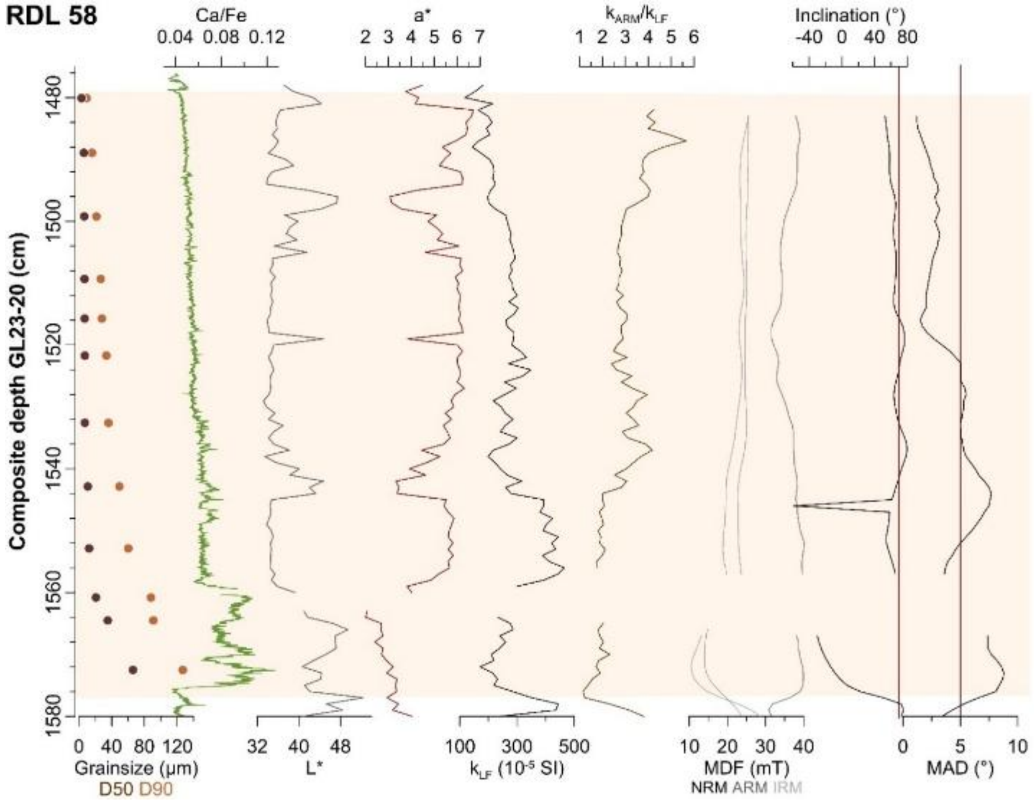

Figure 66. Physical, elemental and magnetic properties of RDL 58.

Philippe et al. (2022) observed a logarithmic dependance between the amplitude of inclination variation ($\Delta I = I_{max} - I_{min}$) and the RDL thickness, independently of the RDL nature (turbidite or hyperpycnite) and Tanty et al. (2016) observed a linear correlation between turbidite thickness and mean inclination anomaly. Our data (Figure 67) indicate similar results. The relation observed between RDL thickness and ΔI can be described both by a logarithmic function ($R^2=0.76$) and a linear function ($R^2=0.78$), probably because we observe two distinct groups of RDL thickness (<40 cm and >80 cm). We show only RDL thicker than 8 cm to avoid smoothed data due to the response function of the magnetometer.

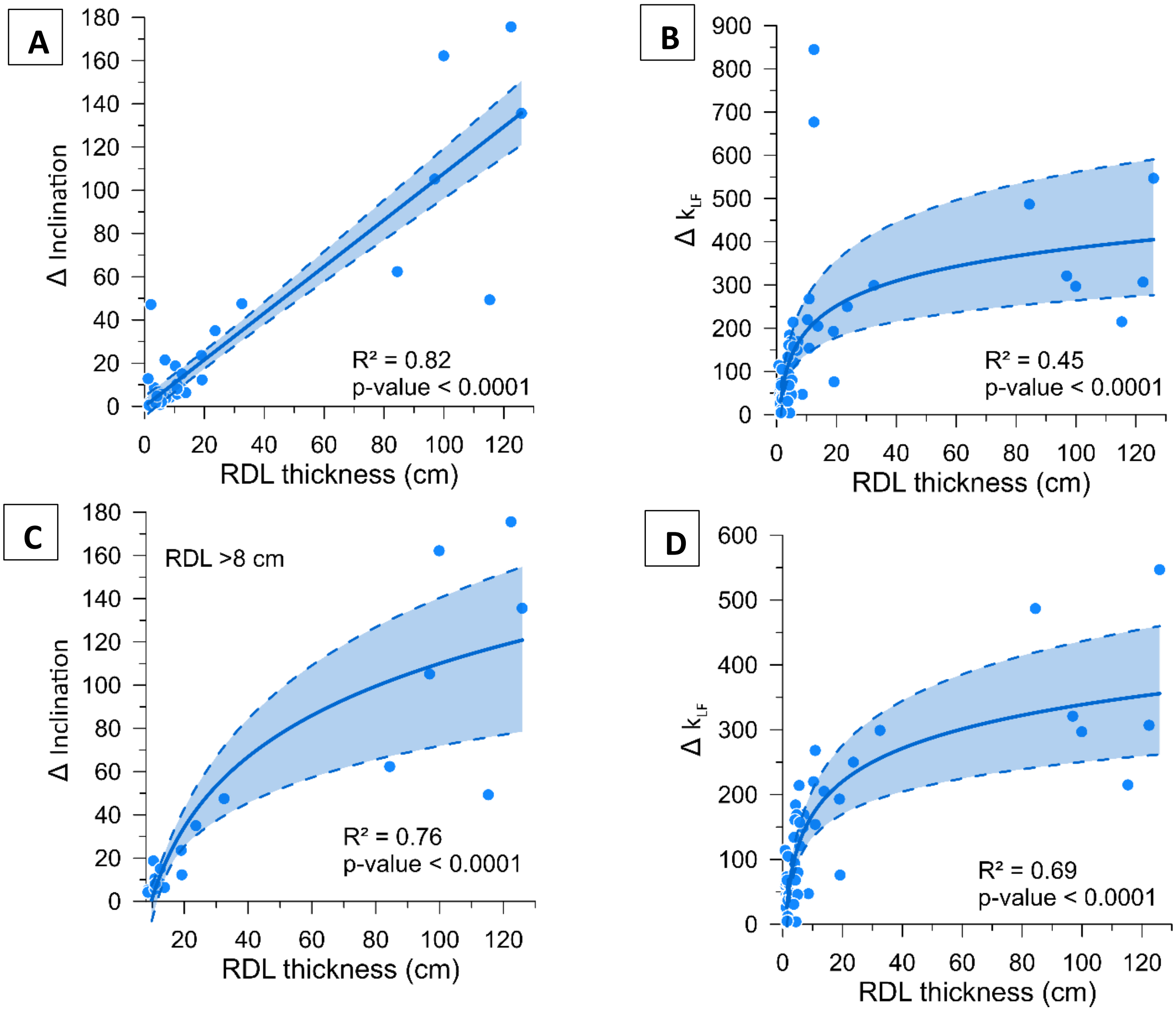

Figure 67. For all RDL, amplitude of inclination (**A**) and k_{LF} (**B**) changes as a function of RDL thickness. **C.** Amplitude of inclination changes for RDL>8cm thickness **D.** Amplitude of k_{LF} changes as a function of RDL thickness, excluding RDL 59 and 67, the two higher points in panel B. The blue line is the best fit logarithmic curve, dotted lines represent the confidence interval. Correlation coefficients and p-values are indicated on each graph.

A greater amplitude of magnetic susceptibility variation (Δk_{LF}) is observed in thicker RDL (Figure 68), described by a logarithmic function. Except for RDL 59 (1591.9-1604.4 cm) and RDL 67 (1825-18377.5 cm), which are thinner and present a high Δk_{LF}, there could be a correlation between the RDL thickness and Δk_{LF} (R^2=0.61), suggesting that thicker RDL reflects grading and higher turbulence.

On the other hand, we do not observe a specific correlation between ΔI and the RDL depth (Supporting information; Figure S20), which means that compaction does not induce inclination shallowing or deviation, as observed in previous studies (Philippe et al., 2022). Contrary to what is observed in Philippe et al., (2022), we do not observe a correlation between magnetic grain size changes ($\Delta k_{ARM}/k_{LF}$) and RDL thickness (Supporting information; Figure S20), nor between $\Delta k_{ARM}/k_{LF}$ and ΔI (Supporting information; Figure S20). Inclination shallowing does not seem to be influenced by sediment depth and compaction, but rather by the magnitude of the event and thus the turbulence within. Within major events (Figures 64, 66, 67), inclinations values are higher (closer to the GAD) at the top of the layer, corresponding to smaller grain size and probably quieter depositional environment, as seen in previous studies (Philippe et al., 2022). However, some RDL differs from that observation (Figures 61, 62).

3.7.2 Paleoenvironmental interpretations supported by paleomagnetic data

As previously described in Kury et al. (2025), the RDLs are mostly composed of turbidites or hyperpycnites. The paleomagnetic data support and illustrate the four phases of changes in sedimentary environment highlighted in Kury et al., (2025), as well as the processes for RDL deposition.

Phase 1 refers to marine/brackish conditions (2066-1580 cm, 3275-2590 cal yr BP), characterized by a decreasing marine influence, high energy depositional environment and possible tidal influence (Kury et al., 2025). Most RDL are thin, with ΔI<20°, low MAD and inclination deviation, consistently with smaller subaqueous flows and high lake levels leading to less frequent slope failures (Kury et al., 2025).

Phase 2 (1580-1000 cm, 2590-2155 cal yr BP) refers to transitional conditions. The water level decrease induced by late Holocene glacio-isostatic uplift leads to unconsolidated glaciogenic sediment exposure and to frequent slope failures inducing type A RDL or turbidites (Kury et al., 2025). Major RDL in phase 2 (Figures 65, 66, 67) all show highly negative inclination values and very large ΔI, attesting to the turbulence of the events originating from slope failures across the lake. NRM intensity is the lowest in phase 2, consistent with the turbulent conditions and large RDL, which leads to overall coarser grainsize.

Phase 3 (1000-470cm, 2155-1325 cal yr BP) refers to lacustrine conditions. In phase 3, RDL originate mostly from hyperpycnal flow probably originated from gullies or small rivers proximal to the coring site (Kury et al., 2025). Paleomagnetic data (Figures 63, 64) indicate less turbulent depositional environment, with inclination>30° and MAD <8°.

Phase 4 (360-0 cm, 1275 cal yr BP to present) refers specifically to varve-forming conditions in a stable environment with minimal post-deposition mixing and sediment inputs controlled by seasonal variations (Kury et al., 2025). In this interval, only one RDL is thicker than 8 cm (Figure 60). This RDL shows relatively high inclination values (>30°), but high ΔI (>60; Figure 67) indicating a turbulent environment. Kury et al. (2025) hypothesized that the RDL does originate from increased river discharge, but could rather be earthquake-triggered. RDL 16 (Figure 60) display characteristics of an homogenite-turbidite complex described in several environments and locations. The turbiditic base of the layer (197-180 cm) shows increased values of Ca/Fe, k_{LF} and grainsize (D_{90}). The upper part of the layer (180-112 cm) display lower values with minimum variations, characteristic of an "homogenite" resulting from a seiche effect (e.g. Bieber, 2022; Chapron et al., 1999; Siegenthaler, 2021). Above the homogenite, we observe the return to background sedimentation with lower k_{LF}, Ca/Fe values. Homogenite resulting from seiche effect usually originates from important events such as earthquake-triggered mass movement. The deep and narrow morphology of this part of the lake could have accentuated the seiche-like effect. These data supports the hypothesis from Kury et al., (2025) that this layer could be earthquake-triggered. However, we cannot link it with certainty to a known event. Earthquake-triggers layers were identified in the adjacent lake Melville associated to the

Kenamu fault and fracture (Syvitski et al., 2025) and dated at 1750±50 CE (200 cal yr BP) as well as in eastern Canada, corresponding to the well studied 1663 CE (290 cal yr BP) earthquake in the Saguenay Fjord and recorded in several locations of the St. Lawrence River (e.g. Mérindol et al., 2022; St-Onge et al., 2004). RDL 16 in this paper is dated at ~560 cal yr BP which is older than the two events mentioned above but with a rather large uncertainty (370-810 cal yr BP; Figure 48).

The overall oligotrophic (depleted in organic matter, OM) and suboxic to anoxic (poor in oxygen) conditions (Kury et al., 2025) probably prevented the alteration of magnetic minerals by oxidation or reduction processes, in addition to not diluting the magnetic signal by OM, which may explain the high NRM intensities (except for the RDL). Seasonal redox fluctuations in phase 4 observed in Kury et al., 2025 cannot be seen in the paleomagnetic data, as values are smoothed over 7-8 cm interval while XRF data have a much higher resolution (200 µm).

3.7.3 Paleomagnetic variations record over the last 3000 years

GL17-13 inclination variations were compared to GREENICE15k (Reilly et al., 2023), MD99-2220 record from the St. Lawrence Estuary (St-Onge et al., 2003) and to the standard mathematical description of the Earth's main magnetic field : International Geomagnetic Reference Field, 14th generation (Alken et al., 2021; Thébault et al., 2015) and GUFM1 model (Jackson et al., 2000) over the last 2500 years. The GREENICE15k record was projected to Grand Lake location via its VGP paths (Ólafsdóttir et al., 2019; Reilly et al., 2019) for comparison purposes. Similar variations can be observed, such as the inclination increase from 2500 to 2000 cal yr BP, the decrease between 2100 and 1800 cal yr BP, inclination low at 1500, inclination high just after 1000 cal yr BP, and the increase over the last 500 years (Figure 68). GL17-13 variations match the variations depicted by the International Geomagnetic Reference Field (IGRF) calculations.

The resolution of core GL17-13 is similar to GREENICE15k, which is one of the highest resolution paleomagnetic records in Northern North Atlantic for the Holocene. That resolution could even be increased by measuring the remanent magnetization with cubes rather than u-channels, to avoid the smoothing induced by the response function of the magnetometer sensors (Philippe et al., 2018).

Although the GL23-20 record is affected by disturbances, it shows a trend similar to that of the GL17-13 record, which supports its overall reliability. It also records overall lower inclination values than core GL17-13. The reliability of GL17-13 record is supported by the similarity with MD99-2220 record in Southeastern Canada between 300 and 1500 cal yr BP, when it shows the same trend as GL23-20 record. MD99-2220 record shows two inclination highs that are also described in GL17-13 record at 1000 cal yr BP and 300-500 cal yr BP.

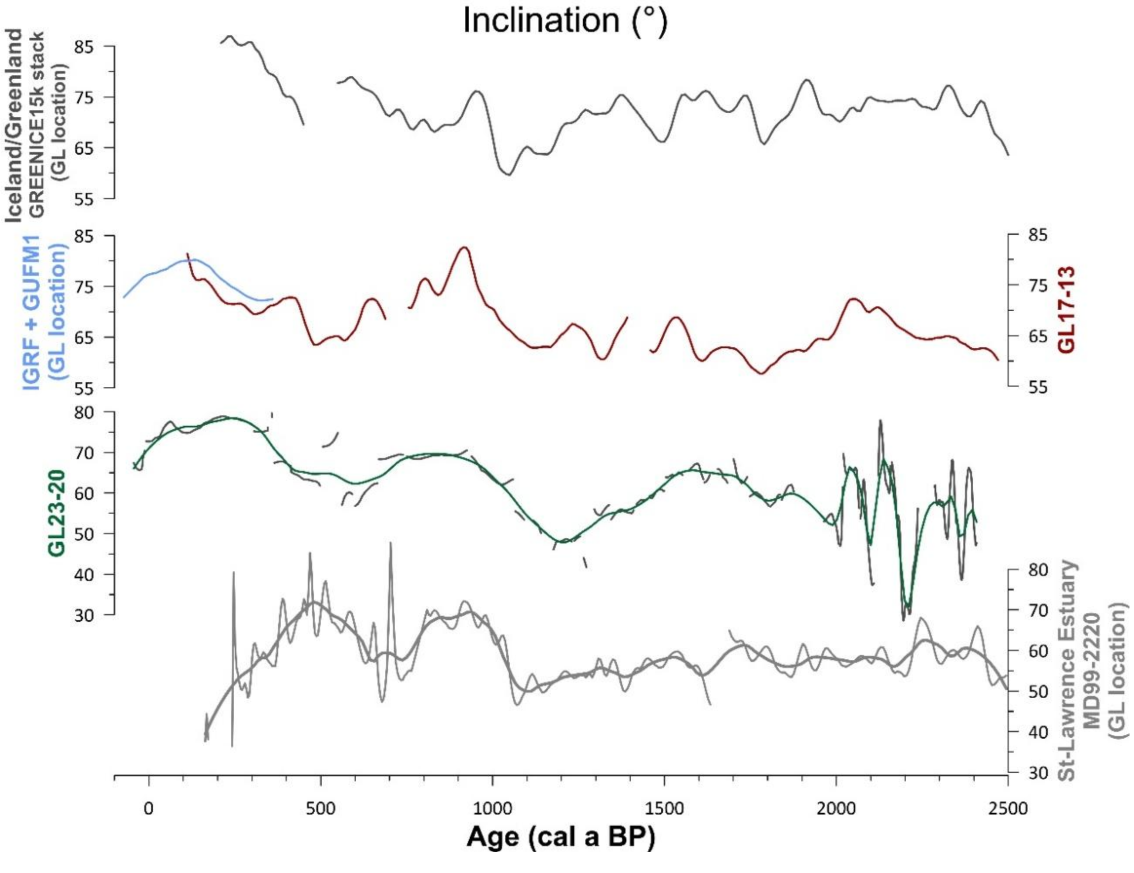

Figure 68. Inclination (°) comparison over the last 2500 years (cal yr BP) between GL17-13 record, GL23-20 record, GREENICE15k record, MD99-2220 record from the St. Lawrence Estuary and the IGRF and GUFM1 models. All records and models are projected to Grand Lake location via their VGP paths.

Grand Lake RPI record was then compared to the CALS3k.4 geomagnetic field model (Korte and Constable, 2011), Petermann RPI stack (Girard et al., 2024), U1305 RPI record (Stoner et al., 2013) and to MD99-2220 (St-Onge et al., 2003) (Figure 70). Common variations are observed with both Petermann stack and CALS3k.4 (Figure 70). Petermann and GL17-13 records show similarities between 2300-1600 years and since 900 cal yr BP, but show divergences between 2500-2300 and 1600-900 cal yr BP. The hypothesis for these differences could be that a regional geomagnetic feature had more influence over one of the two regions during these periods. GL17-13 being of higher resolution could also have recorded more fluctuations than the Petermann stack. The "westward drift" hypothesis was excluded, since Grand Lake and Petermann Fjord are located on the same longitude. In a previous study (Girard et al., 2024), a phase difference was identified between the Petermann RPI record and those from Europe/North Atlantic (including U1305). This discrepancy was attributed to east-west hemispherical field asymmetry, likely caused by the intensification of geomagnetic flux lobes. Given the geographic proximity of U1305 and Grand Lake records, it is reasonable to expect similar RPI variations in their records. Although the GL17-13 record exhibits greater fluctuations than U1305, both show comparable patterns between 2,500 and 1000 cal yr BP. However, more pronounced differences emerge over the last 1,000 years. In the most recent 500 years, the North American flux lobe has become more concentrated over the continent, as indicated by the CALS10k.2 geomagnetic field reconstruction (Constable et al., 2016). This increased concentration may explain the divergence between the U1305 and GL17-13 records, with U1305 being located further from the core influence of the flux lobe.

As previously stated, GL17-13 is particularly valuable as it captures recent geomagnetic variations, especially over the last 1000 years. Few records focus on the Late Holocene, largely because sediment cores are often disturbed at the top during coring operations or present low sedimentation rates, as seen in the GREENICE15k record. Moreover, the rather good similarity between GL17-13 and U1305 over the interval 1,700-2,500 cal yr BP and the overall similarity with MD99-2220 supports GL17-13 age model, despite the considerable uncertainty in that bottom part of the core.

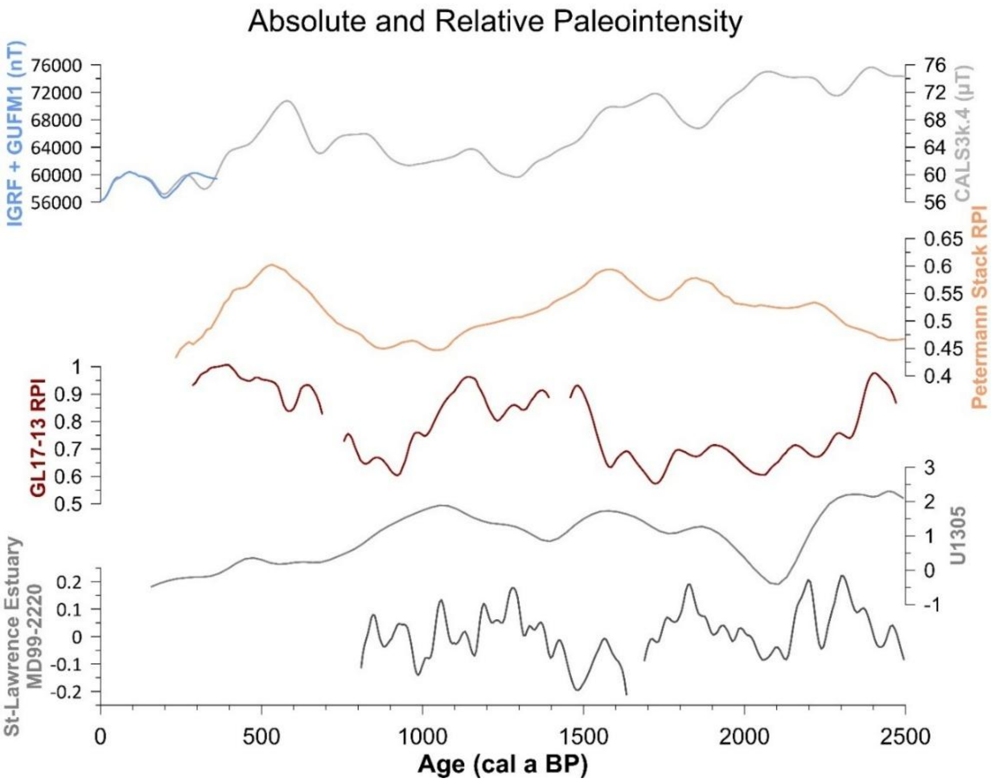

Figure 69. Absolute and relative paleointensity comparison over the last 2,500 years (cal yr BP) between IGRF and GUFM1 models, CALS3k.4 model, Petermann stack, GL17-13 record, U1305 record, and MD99-2220 record from the St-Lawrence estuary.

We compared the intensity variations displayed in Figure 70, with the CALS10k.2 geomagnetic field model at the Core-Mantle Boundary (Figure 71; Constable et al., 2016). GL17-13 record presents a high intensity peak 2,500 years ago, which could correspond to the high intensity in U1305 (2,300-2,500 cal yr BP) and to the two intensity peaks in MD99-2220 (2,200 and 2,300 cal yr BP). At that time period, three flux lobes (NW Canada, Western Europe/Northern North Atlantic and Siberia) of high intensity are described at the CMB by CALS10k.2, resulting in an extended zone of high intensity on the surface, including NW Canada, Europe and Siberia (Figure 71A). A low intensity around 2,000-2,100 cal yr BP is shown in GL17-13, U1305 and MD99-2220 records. CALS10k.2 describes a decreasing intensity, due to the separation of the flux lobes and their concentration on smaller zones, with lower intensities, which leads to U1305, MD99-2220 and GL17-13 locations to be away from the flux lobe influence (Figure 71B, C). During the interval 2,000-1,500 years, the North

American flux lobes moves toward Greenland and Northern North Atlantic, which could explain the difference between U1305 and Grand Lake at that time. A high intensity is observed in Grand Lake at 1,500-1,000 cal yr BP, as well as in U1305 and MD99-2220 records, even though less pronounced. From 1300 years ago, CALS10k.2 shows an elongation of the North American flux lobe in a larger zone, over Greenland, North Atlantic and North America (Figure 71D). It could result in the increasing intensity seen in the three records. At that time, Petermann Fjord is at the edge of the flux lobe, explaining the intensity decrease. From 1,000 to 800 cal yr BP, we observe a low intensity in Grand Lake and Petermann Fjord, and a diminution in U1305 record, which we cannot explain with the flux lobe dynamic, since it is still located over North America (Figure 71D). Lastly, we observe an increasing intensity in Grand Lake at 500-300 cal yr BP, an intensity decrease in Petermann Fjord, and a low intensity in U1305, which corresponds to the flux lobe separation and the North American flux lobe concentrated over North America (Figure 71E). Overall, the flux lobes dynamic, especially the North American flux lobe, at the CMB seems to explain paleointensity variations in Grand Lake.

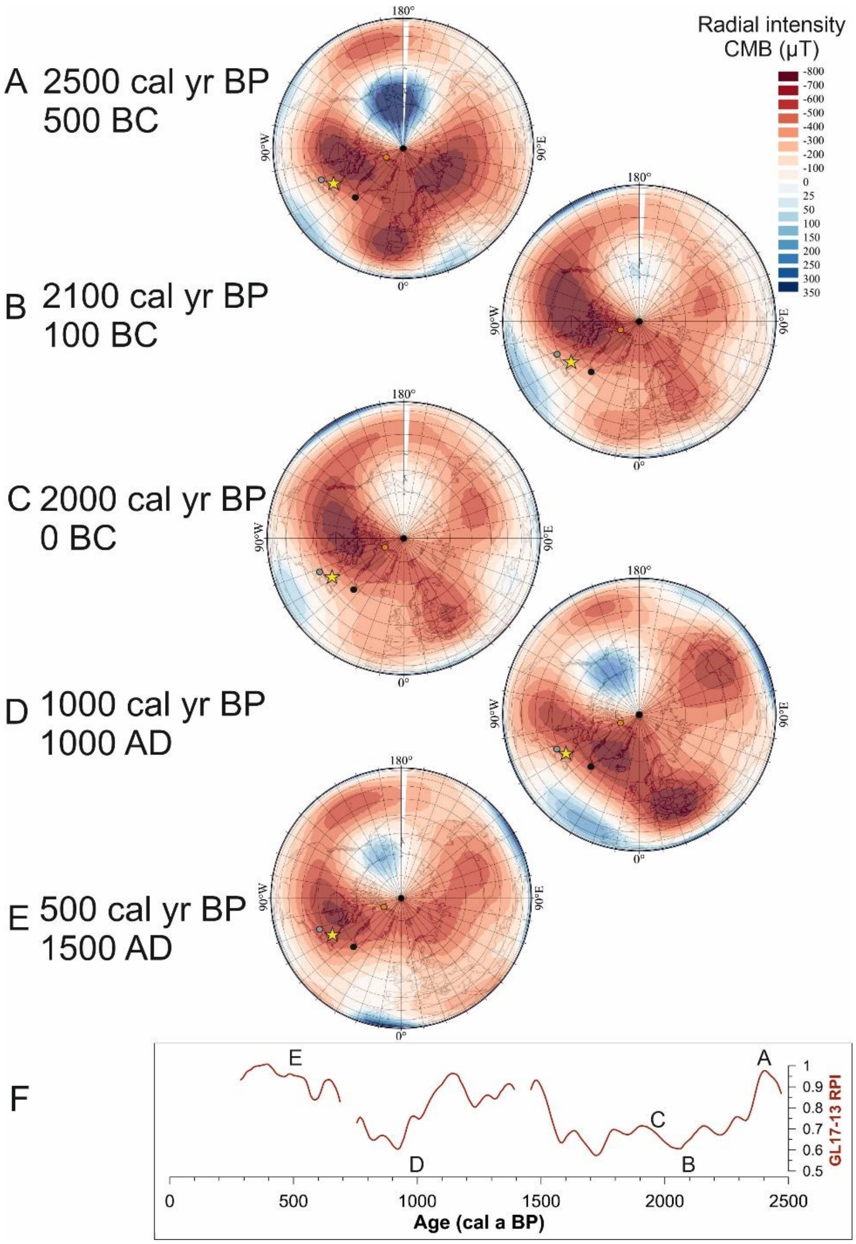

Figure 70. Projections of the geomagnetic field intensity at the core mantle boundary and the Earth surface from CALS10k.2 geomagnetic model (Constable et al., 2016, supporting information) at different time: 2500 cal yr BP (**A**), 2100 cal yr BP (**B**), 2010 cal yr BP (**C**), 1010 cal yr BP (**D**), and 500 cal yr BP (**E**). **F** represents GL17-13 RPI curve. The different time of CALS10k.2 projections are indicated with letters in the panel. Yellow stars indicate the location of Grand Lake; orange dot indicate the location of Petermann Fjord; grey dot indicate the location of MD99-2220; black dot indicate the location of U1305.

3.7.4 Focus on the last 350 years (-45 to 305 cal yr BP)

Although GL23-20 composite signal is highly interrupted by RDL, we were able to recover undisturbed and varved sediments in surface core GL23-20-Up1. This core has the advantage of presenting high-resolution variations and a robust annual chronology because of the presence of varves. As it captures the most recent sediment record, it enables us to link the recent paleomagnetic secular variations to the direct observations since the 19th century. We can therefore study the most recent paleomagnetic variations and compared them to the historical data derived from the IGRF total intensity (Figure 72) and GUFM1 model (Jackson et al., 2000) from 1645 to 2000 CE. Kury et al. (2025) identified 11 RDL in this core, all <1.5 cm depth, which led us to estimate that their impact on the paleomagnetic signal measured was negligible since the RDL represent only 16 % of the thickness of the core and they represent only one point of measure and values are smoothed over 7-8 cm (Philippe et al., 2018). GL23-20 RPI variations are comparable to IGRF and GUFM1 geomagnetic model intensities (Figure 72). From 1645 to 1840 CE, we observe the same variations, globally increasing intensity with a slight decrease around 1750 CE. After that, GL23-20 RPI shows an important decrease between 1840 and 1890 CE, while IGRF-GUFM intensities depict a slight decrease between 1840 and 1940 CE. Then, the GL23-20 RPI curve presents a high intensity at 1940 CE, while the other curve presents it around 1870 CE. The offset between the different curves since 1840 CE, could be attributed to a local field characteristic which could be responsible for GL23-20 RPI variations, while IGRF-GUFM is more global.

GL23-20 declination depicts the same trend as what is described by the model, except for a peak around 1900 CE. Likewise, the inclination records are similar since 1645 except for the last 50 years (2000-1950) where GL23-20 record depicts lower values. Although this represents a step forward in studying very recent variations in sediments, there are still some differences with the direct observations. It can be explained by the non-orientation of the core on the field that impacts the declination.

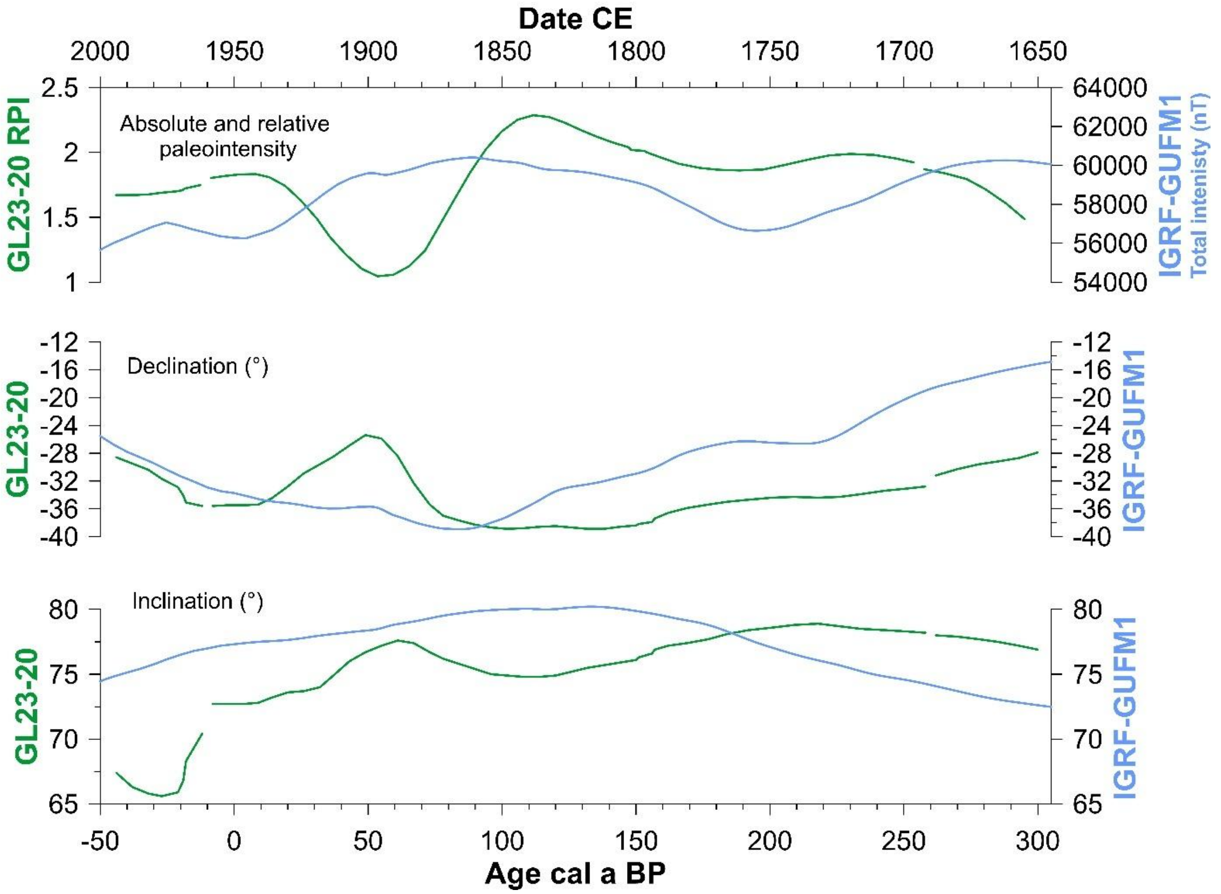

Figure 71. Intensity, declination and inclination comparisons between IGRF calculations and GUFM1 model (for Grand Lake location) and GL23-20 composite sequence (RPI calculated with the slope method).

3.8 SUMMARY AND PERSPECTIVES

This study highlights the potential of Grand Lake as a site for recording high-resolution paleomagnetic variations. Although some locations in the lake are disturbed by numerous RDL, the shallower GL17-13 core location, at the lake outlet, remains undisturbed and enables the high-resolution geomagnetic field variations recording of the last 2,500 years, depicting local variations, in addition to a more global signal. The resolution of core GL17-13 matches the well-resolved GREENICE15k record and the high-resolution MD99-2220 record from the St. Lawrence Estuary. Core GL17-13 captures the Late Holocene variations with a secular temporal resolution, and with the top of the GL23-20 composite sequence, links the recent direct observations of the last 400 years to the previous Holocene records from the Northern North Atlantic and Canadian Arctic. We also studied the magnetic properties (inclination, magnetic susceptibility, grain size) of RDL within GL23-20 composite sequence, and observed some similarities with previous studies. Inclination variations within the RDL seems influenced by the magnitude and turbulence of the event. At time of deposition, magnetic grain size tends to align with the flow direction, and turbulence leads to shallow or negative values at the bottom of the layers. Overall, the paleomagnetic data supports the paleoenvironmental interpretations from previous studies. For future work at Grand Lake, retrieving longer and declination-oriented cores in areas avoiding mass wasting events such as at the outlet of the lake, and increasing the resolution of the record by using cubes instead of u-channels, or by deconvoluting the signal should be considered.

3.8.1 Acknowledgments

We are grateful to the field campaign team: Quentin Beauvais, Bruno Cayouette, Arnaud De Coninck, Richard Niederreiter and Marie-Eugénie Jamba. We are grateful to our local guide Dave Blake. The field campaign was conducted on an Innu and Inuit-Metis land. We recognize and respect the rights of the Innu to conduct their own lives with a minimum of interference from outside interests. Juliette Girard received excellence scholarships from ISMER and the *Programme de Bourses d'Excellence pour les Étudiants Étrangers* of the *Fonds de Recherche du Québec - Nature et Technologies* (n°334533). This work was supported by NSERC Discovery and Northern Supplement grants (RGPIN-2014-05810 and RGPIN-2019-06593) awarded to Pierre Francus, Research Chair in Marine Geology, NSERC Discovery and Northern Supplement grants as well as Canada Foundation for Innovation funding awarded to Guillaume St-Onge and NSERC discovery grants awarded to Jean-Carlos Montero-Serrano.

3.9 REFERENCES

Alken, P., Thébault, E., Beggan, C.D., Amit, H., Aubert, J., Baerenzung, J., Bondar, T.N., Brown, W.J., Califf, S., Chambodut, A., Chulliat, A., Cox, G.A., Finlay, C.C., Fournier, A., Gillet, N., Grayver, A., Hammer, M.D., Holschneider, M., Huder, L., Hulot, G., Jager, T., Kloss, C., Korte, M., Kuang, W., Kuvshinov, A., Langlais, B., Léger, J.-M., Lesur, V., Livermore, P.W., Lowes, F.J., Macmillan, S., Magnes, W., Mandea, M., Marsal, S., Matzka, J., Metman, M.C., Minami, T., Morschhauser, A., Mound, J.E., Nair, M., Nakano, S., Olsen, N., Pavón-Carrasco, F.J., Petrov, V.G., Ropp, G., Rother, M., Sabaka, T.J., Sanchez, S., Saturnino, D., Schnepf, N.R., Shen, X., Stolle, C., Tangborn, A., Tøffner-Clausen, L., Toh, H., Torta, J.M., Varner, J., Vervelidou, F., Vigneron, P., Wardinski, I., Wicht, J., Woods, A., Yang, Y., Zeren, Z., Zhou, B., 2021. International Geomagnetic Reference Field: the thirteenth generation. Earth Planets Space 73, 49. https://doi.org/10.1186/s40623-020-01288-x

Banerjee, S.K., King, J., Marvin, J., 1981. A rapid method for magnetic granulometry with applications to environmental studies. Geophysical Research Letters 8, 333–336. https://doi.org/10.1029/GL008i004p00333

Bieber, A., 2022. Propriétés magnétiques et physiques de carottes sédimentaires prélevées le long du prisme d'accrétion des Petites Antilles : Risques naturels et influence de la lithologie sur le signal paléomagnétique. Université du Québec à Rimouski, Rimouski, QC, Canada.

Blaauw, M., Christen, J.A., 2011. Flexible paleoclimate age-depth models using an autoregressive gamma process. Bayesian Anal. 6. https://doi.org/10.1214/11-BA618

Bloemendal, J., Lamb, B., King, J., 1988. Paleoenvironmental implications of rock magnetic properties of late Quaternary sediment cores from the eastern Equatorial Atlantic. Paleoceanography 3, 61–87. https://doi.org/10.1029/PA003i001p00061

Blott, S.J., Pye, K., 2001. GRADISTAT: a grain size distribution and statistics package for the analysis of unconsolidated sediments. Earth Surf. Process. Landforms 26, 1237–1248. https://doi.org/10.1002/esp.261

Caricchi, C., Campuzano, S.A., Sagnotti, L., Macrì, P., Lucchi, R.G., 2022. Reconstruction of the Virtual Geomagnetic Pole (VGP) path at high latitude for the last 22 kyr: The role of radial field flux patches as VGP attractor. Earth and Planetary Science Letters 595, 117762. https://doi.org/10.1016/j.epsl.2022.117762

Channell, J.E.T., Stoner, J.S., Hodell, D.A., Charles, C.D., 2000. Geomagnetic paleointensity for the last 100 kyr from the sub-antarctic South Atlantic: a tool for inter-hemispheric correlation. Earth and Planetary Science Letters 175, 145–160. https://doi.org/10.1016/S0012-821X(99)00285-X

Chapron, E., Beck, C., Pourchet, M., Deconinck, J.-F., 1999. 1822 earthquake-triggered homogenite in Lake Le Bourget (NW Alps). Terra Nova 86–92. https://doi.org/10.1046/j.1365-3121.1999.00230.x

Constable, C., Korte, M., Panovska, S., 2016. Persistent high paleosecular variation activity in southern hemisphere for at least 10 000 years. Earth and Planetary Science Letters 453, 78–86. https://doi.org/10.1016/j.epsl.2016.08.015

Couette, P., Ghienne, J., Lajeunesse, P., Van Der Woerd, J., 2023. Climatic control on the retreat of the Laurentide Ice Sheet margin in easternmost Québec–Labrador (Canada) revealed by cosmogenic nuclide exposure dating. J Quaternary Science 38, 1044–1061. https://doi.org/10.1002/jqs.3525

Croudace, I.W., Rindby, A., Rothwell, R.G., 2006. ITRAX: description and evaluation of a new multi-function X-ray core scanner. SP 267, 51–63. https://doi.org/10.1144/GSL.SP.2006.267.01.04

Croudace, I.W., Rothwell, R.G. (Eds.), 2015. Micro-XRF Studies of Sediment Cores: Applications of a non-destructive tool for the environmental sciences, Developments in Paleoenvironmental Research. Springer Netherlands, Dordrecht. https://doi.org/10.1007/978-94-017-9849-5

Day, R., Fuller, M., Schmidt, V.A., 1977. Hysteresis properties of titanomagnetites: Grain-size and compositional dependence. Physics of the Earth and Planetary Interiors 13, 260–267. https://doi.org/10.1016/0031-9201(77)90108-X

Debret, M., Sebag, D., Desmet, M., Balsam, W., Copard, Y., Mourier, B., Susperrigui, A.-S., Arnaud, F., Bentaleb, I., Chapron, E., Lallier-Vergès, E., Winiarski, T., 2011. Spectrocolorimetric interpretation of sedimentary dynamics: The new "Q7/4 diagram." Earth-Science Reviews 109, 1–19. https://doi.org/10.1016/j.earscirev.2011.07.002

Dunlop, D.J., 2002. Theory and application of the Day plot (Mrs/Ms versus Hcr/Hc) 1. Theoretical curves and tests using titanomagnetite data. Journal of Geophysical Research: Solid Earth 107, EPM 4-1. https://doi.org/10.1029/2001JB000486

Dunlop, D.J., Ozdemir, O., 2007. Magnetization in rocks and minerals, in: Geomagnetism, Treatise on Geophysics. G. Scubert, Oxford, pp. 277–336.

Fitzhugh, W., 1973. Environmental Approaches to the Prehistory of the North. J. WASH. ACAD. SCI. 63.

Gagnon-Poiré, A., 2023. Reconstitution hydrologique millénaire dans la forêt boréale du Labrador à partir des sédiments varvés de Grand Lake (Ph.D.). Institut National de la Recherche Scientifique - Centre Eau Terre et Environnement.

Gagnon-Poiré, A., Brigode, P., Francus, P., Fortin, D., Lajeunesse, P., Dorion, H., Trottier, A.-P., 2021. Reconstructing past hydrology of eastern Canadian boreal catchments using clastic varved sediments and hydro-climatic modelling: 160 years of fluvial inflows. Clim. Past 17, 653–673. https://doi.org/10.5194/cp-17-653-2021

Gauss, C.F., 1833. Intensitas vis Magneticae Terrestris ad Mensuram Absolutam Revocata. Dieterich, Göttingen.

Girard, J., Reilly, B.T., St-Onge, G., Lagroix, F., Montero-Serrano, J., Stoner, J.S., Jennings, A.E., 2024. Paleomagnetic Secular Variations in North Greenland Around 81°N Over the Last 6,000 Years. Geochem Geophys Geosyst 25, e2024GC011620. https://doi.org/10.1029/2024GC011620

Gubbins, D., 2008. Geomagnetic reversals. Nature 452, 3.

Harrison, R.J., Feinberg, J.M., 2008. FORCinel: An improved algorithm for calculating first-order reversal curve distributions using locally weighted regression smoothing: FORCINEL ALGORITHM. Geochem. Geophys. Geosyst. 9. https://doi.org/10.1029/2008GC001987

Heaton, T.J., Bard, E., Bronk Ramsey, C., Butzin, M., Hatté, C., Hughen, K.A., Köhler, P., Reimer, P.J., 2023. A response to community questions on the Marine20 radiocarbon age calibration curve: marine reservoir ages and the calibration of 14C samples from the oceans. Radiocarbon 65, 247–273. https://doi.org/10.1017/RDC.2022.66

Heaton, T.J., Köhler, P., Butzin, M., Bard, E., Reimer, R.W., Austin, W.E.N., Bronk Ramsey, C., Grootes, P.M., Hughen, K.A., Kromer, B., Reimer, P.J., Adkins, J., Burke, A., Cook, M.S., Olsen, J., Skinner, L.C., 2020. Marine20—The Marine Radiocarbon Age Calibration Curve (0–55,000 cal BP). Radiocarbon 62, 779–820. https://doi.org/10.1017/RDC.2020.68

Jackson, A., Jonkers, A.R.T., Walker, M.R., 2000. Four centuries of geomagnetic secular variation from historical records. Philosophical Transactions of the Royal Society of London. Series A: Mathematical, Physical and Engineering Sciences 358, 957–990. https://doi.org/10.1098/rsta.2000.0569

Kamula, C.M., Kuzyk, Z.Z.A., Lobb, D.A., Macdonald, R.W., 2017. Sources and accumulation of sediment and particulate organic carbon in a subarctic fjard estuary:210 Pb,137 Cs, and δ13 C records from Lake Melville, Labrador. Can. J. Earth Sci. 54, 993–1006. https://doi.org/10.1139/cjes-2016-0167

King, J., Banerjee, S.K., Marvin, J., Özdemir, Ö., 1982. A comparison of different magnetic methods for determining the relative grain size of magnetite in natural materials: Some results from lake sediments. Earth and Planetary Science Letters 59, 404–419. https://doi.org/10.1016/0012-821X(82)90142-X

King, J.W., Banerjee, S.K., Marvin, J., 1983. A new rock-magnetic approach to selecting sediments for geomagnetic paleointensity studies: Application to paleointensity for the last 4000 years. Journal of Geophysical Research: Solid Earth 88, 5911–5921. https://doi.org/10.1029/JB088iB07p05911

Kirschvink, J.L., 1980. The least-squares line and plane and the analysis of palaeomagnetic data. Geophys J Int 62, 699–718. https://doi.org/10.1111/j.1365-246X.1980.tb02601.x

Korte, M., Constable, C., 2011. Improving geomagnetic field reconstructions for 0–3ka. Physics of the Earth and Planetary Interiors 188, 247–259. https://doi.org/10.1016/j.pepi.2011.06.017

Kury, Milena S, Francus, P., Chassiot, L., Antoniades, D., St-Onge, G., Girard, J., Lajeunesse, P., 2025. Untangling sedimentation processes in a deep fjord lake in Labrador: A high-resolution archive of past environment dynamics at Grand Lake. The Depositional Record 1–26. https://doi.org/10.1002/dep2.70020

Kury, Milena S., Francus, P., Chassiot, L., Dermot, A., St-Onge, G., Girard, J., Lajeunesse, P., 2025. Untangling sedimentation processes in a deep fjord-lake in Labrador: a high-resolution archiveof past environment dynamics at Grand Lake. The Depositional Record [in press].

Kylander, M.E., Ampel, L., Wohlfarth, B., Veres, D., 2011. High-resolution X-ray fluorescence core scanning analysis of Les Echets (France) sedimentary sequence: new insights from chemical proxies. Journal of Quaternary Science 26, 109–117.

Lapointe, F., Gagnon-Poiré, A., Francus, P., Lajeunesse, P., Gagnon, C., 2025. A new 1500-year-long varve thickness record from Labrador, Canada, uncovers significant insights into large-scale climate variability in the Atlantic. https://doi.org/10.5194/egusphere-2025-97

Livermore, P.W., Finlay, C.C., Bayliff, M., 2020. Recent north magnetic pole acceleration towards Siberia caused by flux lobe elongation. Nat. Geosci. 13, 387–391. https://doi.org/10.1038/s41561-020-0570-9

Löwemark, L., Bloemsma, M., Croudace, I., Daly, J.S., Edwards, R.J., Francus, P., Galloway, J.M., Gregory, B.R.B., Steven Huang, J.-J., Jones, A.F., Kylander, M., Löwemark, L., Luo, Y., Maclachlan, S., Ohlendorf, C., Patterson, R.T., Pearce, C., Profe, J., Reinhardt, E.G., Stranne, C., Tjallingii, R., Turner, J.N., 2019. Practical guidelines and recent advances in the Itrax XRF core-scanning procedure. Quaternary International 514, 16–29. https://doi.org/10.1016/j.quaint.2018.10.044

Maxbauer, D.P., Feinberg, J.M., Fox, D.L., 2016. MAX UnMix: A web application for unmixing magnetic coercivity distributions. Computers & Geosciences 95, 140–145. https://doi.org/10.1016/j.cageo.2016.07.009

Mazaud, A., 2005. User-friendly software for vector analysis of the magnetization of long sediment cores: software for vector analysis. Geochem. Geophys. Geosyst. 6. https://doi.org/10.1029/2005GC001036

Mérindol, M., St-Onge, G., Sultan, N., Lajeunesse, P., Garziglia, S., 2022. Earthquake-triggered submarine landslides in the St. Lawrence Estuary (Québec, Canada) during the last two millennia and the record of the major 1663 CE M ≥7 event. Quaternary Science Reviews 291, 107640. https://doi.org/10.1016/j.quascirev.2022.107640

Mulder, T., Syvitski, J.P.M., Migeon, S., Faugères, J.-C., Savoye, B., 2003. Marine hyperpycnal flows: initiation, behavior and related deposits. A review. Marine and Petroleum Geology 20, 861–882. https://doi.org/10.1016/j.marpetgeo.2003.01.003

National Centers for Environmental Information, 2023. State of the Geomagnetic Field 2023. https://doi.org/10.25923/CWW1-SC35

Nilsson, A., Muscheler, R., Snowball, I., 2011. Millennial scale cyclicity in the geodynamo inferred from a dipole tilt reconstruction. Earth and Planetary Science Letters 311, 299–305. https://doi.org/10.1016/j.epsl.2011.09.030

Ólafsdóttir, S., Reilly, B.T., Bakke, J., Stoner, J.S., Gjerde, M., Van Der Bilt, W.G.M., 2019. Holocene paleomagnetic secular variation (PSV) near 80° N, Northwest Spitsbergen, Svalbard: Implications for evaluating High Arctic sediment chronologies. Quaternary Science Reviews 210, 90–102. https://doi.org/10.1016/j.quascirev.2019.03.003

Philippe, É.G.H., St-Onge, G., Valet, J., Godbout, P., Egli, R., Francus, P., Roy, M., 2023. Influence of Seasonal Post-Depositional Processes on the Remanent Magnetization in Varved Sediments From Glacial Lake Ojibway (Canada). Geochem Geophys Geosyst 24, e2022GC010707. https://doi.org/10.1029/2022GC010707

Philippe, É.G.H., Valet, J., St-Onge, G., Thevarasan, A., 2018. Are Paleomagnetic Records From U-Channels Appropriate for Studies of Reversals and Excursions? Geochem. Geophys. Geosyst. 19, 4130–4142. https://doi.org/10.1029/2018GC007803

Philippe, É.G.H., Valet, J.-P., St-Onge, G., Egli, R., 2022. Impact of turbulence on magnetic alignment in sediments. Front. Earth Sci. 10, 1079229. https://doi.org/10.3389/feart.2022.1079229

Reilly, B.T., Stoner, J.S., Mix, A.C., Walczak, M.H., Jennings, A., Jakobsson, M., Dyke, L., Glueder, A., Nicholls, K., Hogan, K.A., Mayer, L.A., Hatfield, R.G., Albert, S., Marcott, S., Fallon, S., Cheseby, M., 2019. Holocene break-up and reestablishment of the Petermann Ice Tongue, Northwest Greenland. Quaternary Science Reviews 218, 322–342. https://doi.org/10.1016/j.quascirev.2019.06.023

Reilly, B.T., Stoner, J.S., Ólafsdóttir, S., Jennings, A., Hatfield, R., Kristjánsdóttir, G.B., Geirsdóttir, Á., 2023. The Amplitude and Timescales of 0–15 ka Paleomagnetic Secular Variation in the Northern North Atlantic. JGR Solid Earth 128, e2023JB026891. https://doi.org/10.1029/2023JB026891

Reimer, P.J., Austin, W.E.N., Bard, E., Bayliss, A., Blackwell, P.G., Bronk Ramsey, C., Butzin, M., Cheng, H., Edwards, R.L., Friedrich, M., Grootes, P.M., Guilderson, T.P., Hajdas, I., Heaton, T.J., Hogg, A.G., Hughen, K.A., Kromer, B., Manning, S.W., Muscheler, R., Palmer, J.G., Pearson, C., Van Der Plicht, J., Reimer, R.W., Richards, D.A., Scott, E.M., Southon, J.R., Turney, C.S.M., Wacker, L., Adolphi, F., Büntgen, U., Capano, M., Fahrni, S.M., Fogtmann-Schulz, A., Friedrich, R., Köhler, P., Kudsk, S., Miyake, F., Olsen, J., Reinig, F., Sakamoto, M., Sookdeo, A., Talamo, S., 2020. The IntCal20 Northern Hemisphere Radiocarbon Age Calibration Curve (0–55 cal kBP). Radiocarbon 62, 725–757. https://doi.org/10.1017/RDC.2020.41

Roberts, A.P., Almeida, T., Church, N.S., Harrison, R.J., Heslop, D., Li, Y., Li, J., Muxworthy, A.R., Williams, W., Zhao, X., 2017. Resolving the Origin of Pseudo-Single Domain Magnetic Behavior. Journal of Geophysical Research: Solid Earth 9534–9558. https://doi.org/10.1002/2017JB014860

Roberts, A.P., Heslop, D., Zhao, X., Oda, H., Egli, R., Harrison, R.J., Hu, P., Muxworthy, A.R., Sato, T., 2022. Unlocking information about fine magnetic particle assemblages from first-order reversal curve diagrams: Recent advances. Earth-Science Reviews 227, 103950. https://doi.org/10.1016/j.earscirev.2022.103950

Roberts, A.P., Hu, P., Harrison, R.J., Heslop, D., Muxworthy, A.R., Oda, H., Sato, T., Tauxe, L., Zhao, X., 2019. Domain State Diagnosis in Rock Magnetism: Evaluation of Potential Alternatives to the Day Diagram. J. Geophys. Res. Solid Earth 124, 5286–5314. https://doi.org/10.1029/2018JB017049

Rodríguez-Cuicas, M., Montero-Serrano, J., St-Onge, G., Normandeau, A., 2023. A 600-year marine record associated with the dynamics of the eastern Penny Ice Cap (Baffin Island, Nunavut, Canada). J Quaternary Science jqs.3531. https://doi.org/10.1002/jqs.3531

Ross, J.C., 1834. III. On the position of the North Magnetic Pole. The Royal Society 47–52. https://doi.org/10.1098/rstl.1834.0005

Rothwell, R.G., Hoogakker, B., Thomson, J., Croudace, I.W., Frenz, M., 2006. Turbidite emplacement on the southern Balearic Abyssal Plain (western Mediterranean Sea) during Marine Isotope Stages 1–3: an application of ITRAX XRF scanning of sediment cores to lithostratigraphic analysis. SP 267, 79–98. https://doi.org/10.1144/GSL.SP.2006.267.01.06

Siegenthaler, C., 2021. Seiches and the slide/seiche dynamics; subcritical and supercritical subaquous mass flows and their deposits. Examples from Swiss Lakes. Swiss J Geosci 114, 17. https://doi.org/10.1186/s00015-021-00394-6

Stoner, J.S., Channell, J.E.T., Hillaire-Marcel, C., Kissel, C., 2000. Geomagnetic paleointensity and environmental record from Labrador Sea core MD95-2024: global marine sediment and ice core chronostratigraphy for the last 110 kyr. Earth and Planetary Science Letters 183, 161–177. https://doi.org/10.1016/S0012-821X(00)00272-7

Stoner, J.S., Channell, J.E.T., Mazaud, A., Strano, S.E., Xuan, C., 2013. The influence of high-latitude flux lobes on the Holocene paleomagnetic record of IODP Site U1305 and the northern North Atlantic: Paleomagnetic Record of the N. Atlantic. Geochem. Geophys. Geosyst. 14, 4623–4646. https://doi.org/10.1002/ggge.20272

Stoner, J.S., St-Onge, G., 2007. Chapter Three Magnetic Stratigraphy in Paleoceanography: Reversals, Excursions, Paleointensity, and Secular Variation, in: Hillaire–Marcel, C., De Vernal, A. (Eds.), Developments in Marine Geology. Elsevier, pp. 99–138. https://doi.org/10.1016/S1572-5480(07)01008-1

St-Onge, G., Mulder, T., Francus, P., Long, B., 2007. Chapter Two Continuous Physical Properties of Cored Marine Sediments, in: Developments in Marine Geology. Elsevier, pp. 63–98. https://doi.org/10.1016/S1572-5480(07)01007-X

St-Onge, G., Mulder, T., Piper, D.J.W., Hillaire-Marcel, C., Stoner, J.S., 2004. Earthquake and flood-induced turbidites in the Saguenay Fjord (Québec): a Holocene paleoseismicity record. Quaternary Science Reviews 23, 283–294. https://doi.org/10.1016/j.quascirev.2003.03.001

St-Onge, G., Stoner, J.S., Hillaire-Marcel, C., 2003. Holocene paleomagnetic records from the St. Lawrence Estuary, eastern Canada: centennial- to millennial-scale geomagnetic modulation of cosmogenic isotopes. Earth and Planetary Science Letters 209, 113–130. https://doi.org/10.1016/S0012-821X(03)00079-7

Stuiver, M., Reimer, P.J., Reimer, R.W., 2018. CALIB 7.1 [WWW program] at http://calib.org. R Core Team: A Language and Environment for Statistical Computing, R Foundation for Statistical Computing.

Syvitski, J., Normandeau, A., Lajeunesse, P., 2025. Major Holocene glacio-isostatically-induced earthquakes triggered mass-transport deposits and seabed displacements in Lake Melville. Marine Geology 481, 107482. https://doi.org/10.1016/j.margeo.2025.107482

Tanty, C., Valet, J., Carlut, J., Bassinot, F., Zaragosi, S., 2016. Acquisition of detrital magnetization in four turbidites. Geochem Geophys Geosyst 17, 3207–3223. https://doi.org/10.1002/2016GC006378

Tauxe, L., Pick, T., Kok, Y.S., 1995. Relative paleointenisty in sediments: a pseudo-Thellier approach. Geophysical Research Letters 22, 2885–2888. https://doi.org/10.1029/95GL03166

Tauxe, L., Wu, G., 1990. Normalized remanence in sediments of the western equatorial Pacific: Relative paleointensity of the geomagnetic field? Journal of Geophysical Research: Solid Earth 95, 12337–12350. https://doi.org/10.1029/JB095iB08p12337

Thébault, E., Finlay, C.C., Beggan, C.D., Alken, P., Aubert, J., Barrois, O., Bertrand, F., Bondar, T., Boness, A., Brocco, L., Canet, E., Chambodut, A., Chulliat, A., Coïsson, P., Civet, F., Du, A., Fournier, A., Fratter, I., Gillet, N., Hamilton, B., Hamoudi, M., Hulot, G., Jager, T., Korte, M., Kuang, W., Lalanne, X., Langlais, B., Léger, J.-M., Lesur, V., Lowes, F.J., Macmillan, S., Mandea, M., Manoj, C., Maus, S., Olsen, N., Petrov, V., Ridley, V., Rother, M., Sabaka, T.J., Saturnino, D., Schachtschneider, R., Sirol, O., Tangborn, A., Thomson, A., Tøffner-Clausen, L., Vigneron, P., Wardinski, I., Zvereva, T., 2015. International Geomagnetic Reference Field: the 12th generation. Earth Planet Sp 67, 79. https://doi.org/10.1186/s40623-015-0228-9

Trottier, A., Lajeunesse, P., Gagnon-Poiré, A., Francus, P., 2020. Morphological signatures of deglaciation and postglacial sedimentary processes in a deep fjord-lake (Grand Lake, Labrador). Earth Surf. Process. Landforms 45, 928–947. https://doi.org/10.1002/esp.4786

Vaasma, T., 2008. Grain-size analysis of lacustrine sediments: a comparison of pre-treatment methods. Estonian J. Ecol. 57, 231. https://doi.org/10.3176/eco.2008.4.01

Valet, J.-P., Meynadier, L., 1998. A comparison of different techniques for relative paleointensity. Geophysical Research Letters 25, 89–92. https://doi.org/10.1029/97GL03489

Wardle, R.J., Paltanavage, A.H., Nolan, L.W., Leawood, T., 1997. Geological Map of Labrador. Geoscience Publications and Information Section.

Weeks, R., Laj, C., Endignoux, L., Fuller, M., Roberts, A., Manganne, R., Blanchard, E., Goree, W., 1993. Improvements in long-core measurement techniques: applications in palaeomagnetism and palaeoceanography. Geophysical Journal International 114, 651–662. https://doi.org/10.1111/j.1365-246X.1993.tb06994.x

Xuan, C., Channell, J.E.T., 2009. UPmag: MATLAB software for viewing and processing u channel or other pass-through paleomagnetic data. Geochemistry, Geophysics, Geosystems 10. https://doi.org/10.1029/2009GC002584

Zijderveld, J., 1967. AC demagnetisation of rocks: analysis of results. Methods in paleomagnetism.

Zolitschka, B., Francus, P., Ojala, A.E.K., Schimmelmann, A., 2015. Varves in lake sediments – a review. Quaternary Science Reviews 117, 1–41. https://doi.org/10.1016/j.quascirev.2015.03.019

3.10 SUPPORTING INFORMATION (FIGURES)

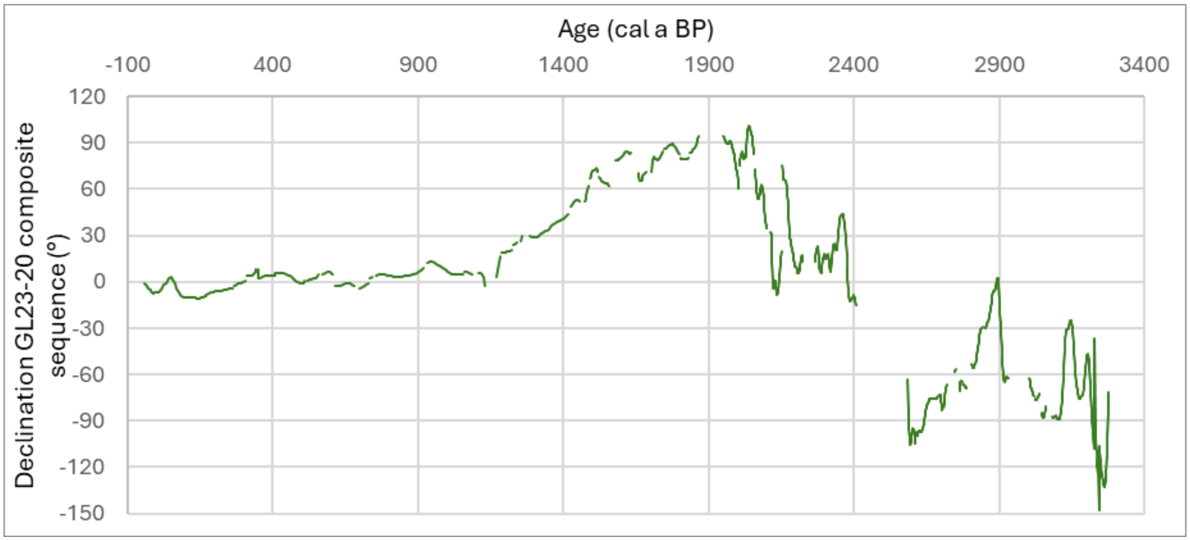

Figure S16. Declination record for GL23-20 composite sequence. Declination values were aligned between each section, excluding the RDL values and then rotated to a mean of zero, according to the GAD assumption.

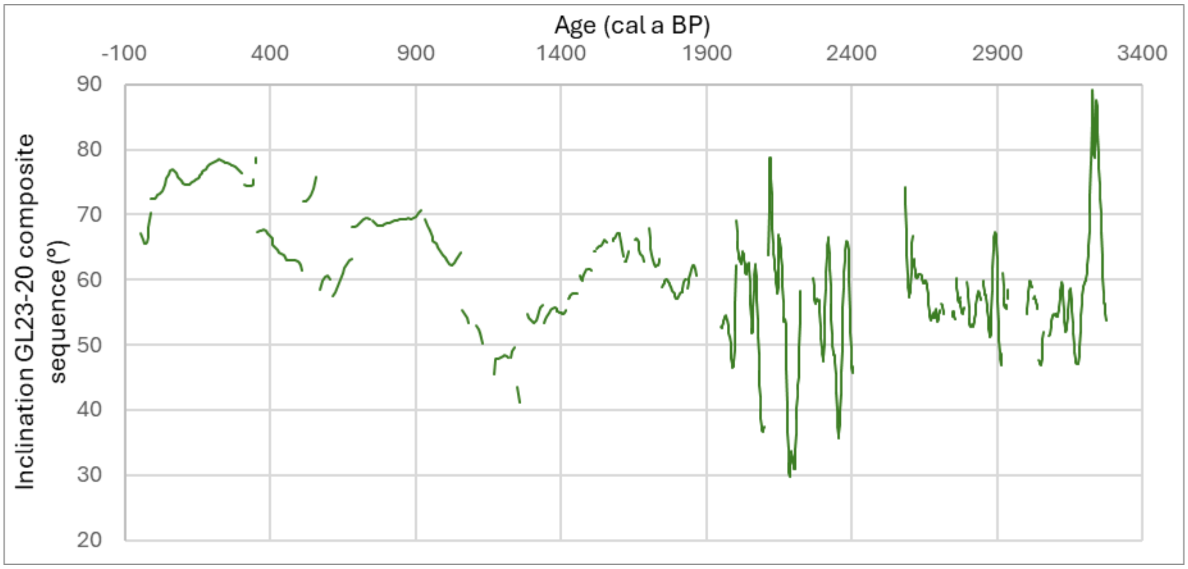

Figure S17. Inclination record for GL32-20 composite sequence.

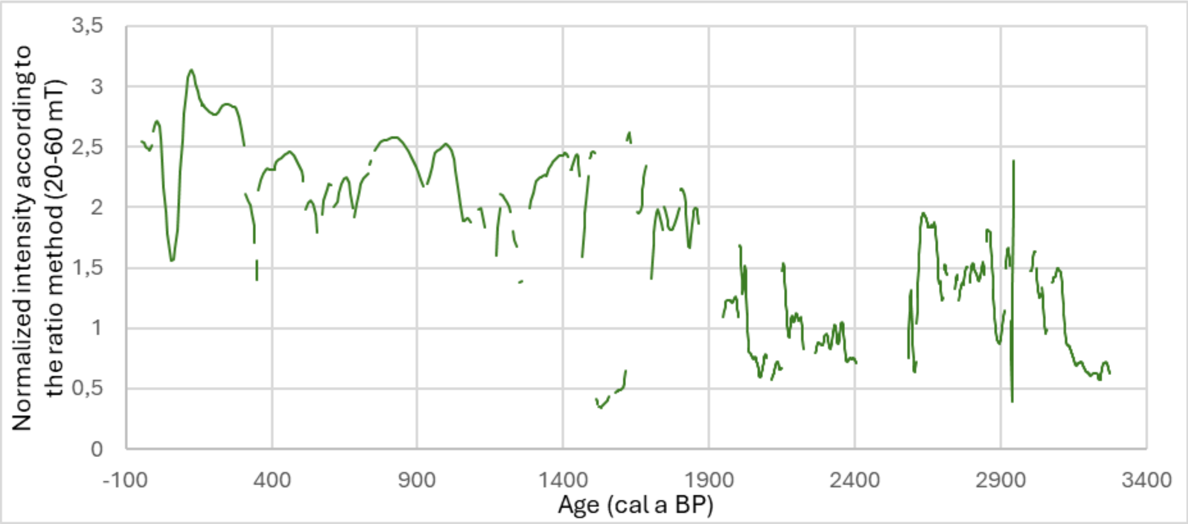

Figure S18. Normalized intensity for GL23-20 composite sequence, using the ratio method and the 20-60 mT demagnetization steps. The magnetization intensity is greatly affected by the numerous RDL and thus cannot be used as a RPI record for this study.

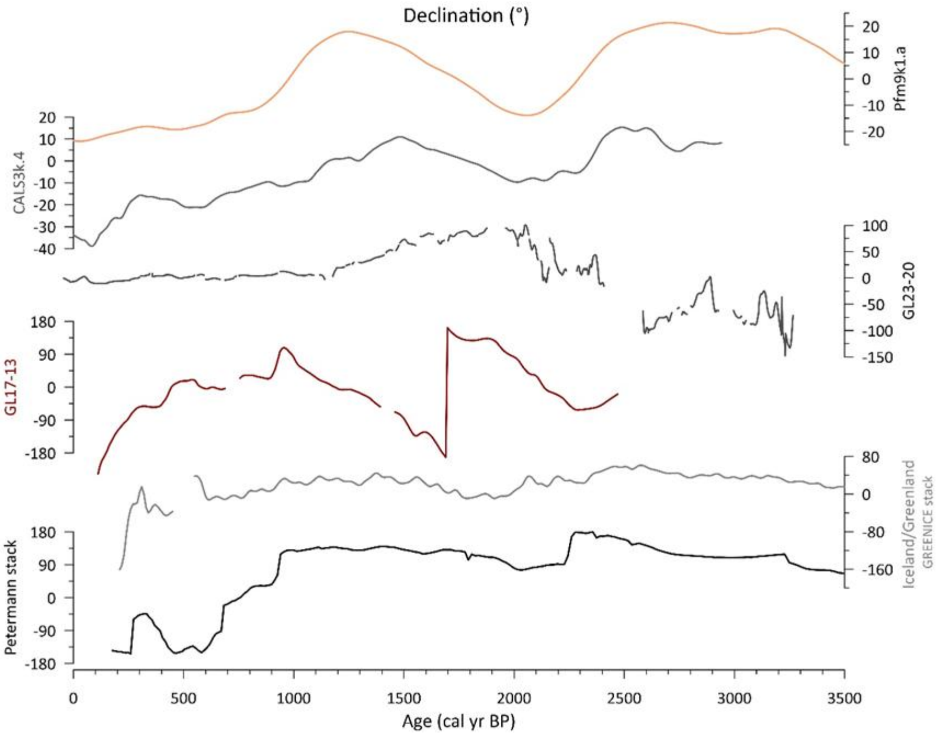

Figure S19. Comparison of several declination records and geomagnetic models: pfm9k.1 (Nilsson et al., 2011), CALS3k.4 (Korte and Constable, 2011), GL23-20 (this study), GL17-13 (this study), GREENICE15k (Reilly et al., 2023), Petermann stack (Girard et al., 2024).

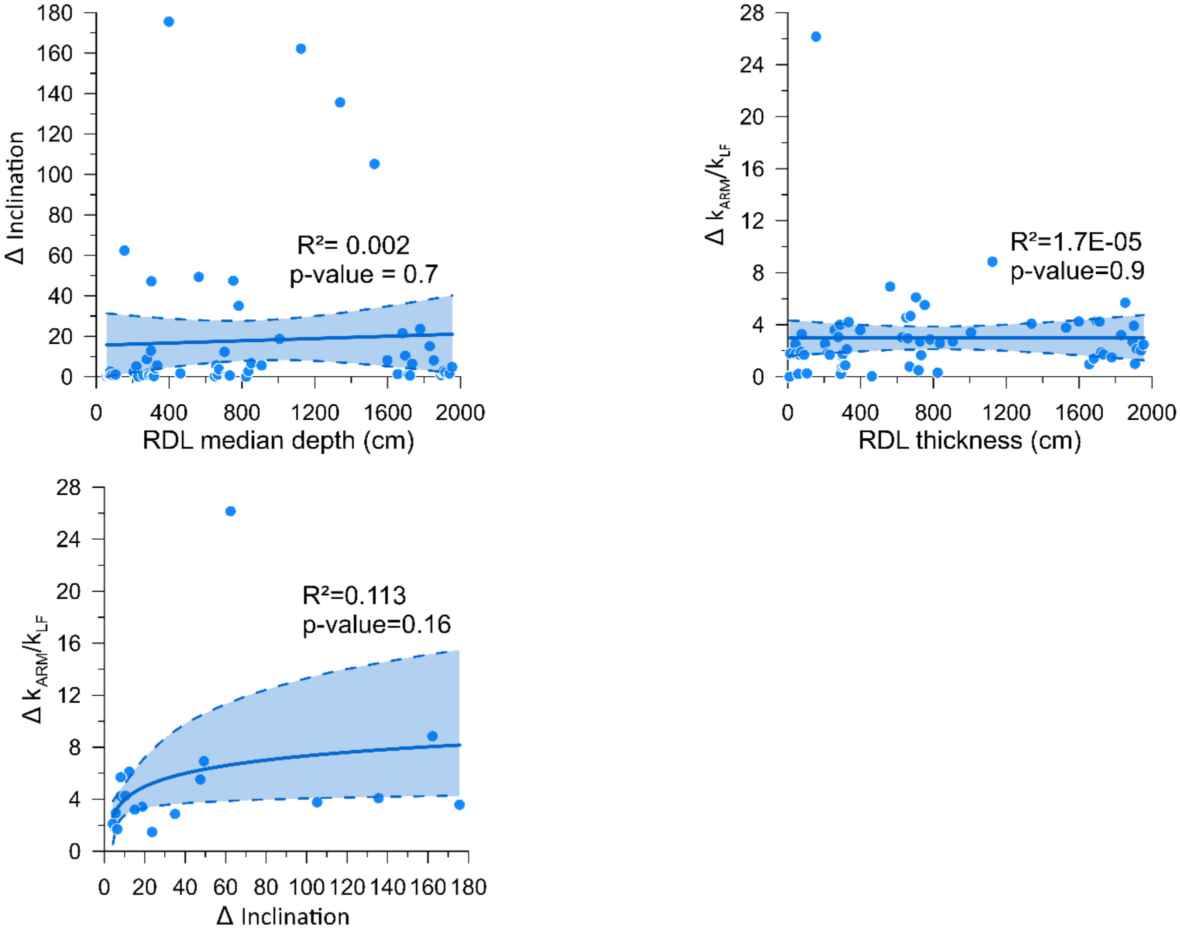

Figure S20. A. Amplitude of inclination changes as a function of RDL median depth, for RDL>8cm thickness. **B.** k_{ARM}/k_{LF} as a function of RDL thickness. **C.** Amplitude of k_{ARM}/k_{LF} changes as a function of the amplitude of inclination changes, for RDL with thickness > 8 cm. Blue lines indicate the best fit logarithmic curve, dotted lines indicate the confidence interval. Correlation coefficients and p-values are indicated for each graph.

CONCLUSION GENERALE

L’étude des séquences sédimentaires du fjord Petermann, de la marge nord-est du Groenland et de Grand Lake a permis de répondre à l’objectif principal, qui était de reconstituer les variations paléomagnétiques séculaires à millénaires (PSV) aux hautes et très hautes latitudes dans le but d’identifier de potentielles fluctuations rapides (migration du pôle géomagnétique virtuel), et de caractériser leur lien avec les différentes composantes du champ géomagnétique (lobes de flux géomagnétiques, cylindre tangentiel).

En particulier, les résultats des deux premiers chapitres ont permis de répondre au premier sous-objectif qui était de reconstituer les variations séculaires à millénaires du champ géomagnétique à très haute latitude (75-81°N) au cours de l’Holocène, tandis que le troisième chapitre a permis de répondre au deuxième sous-objectif, soit de reconstituer des variations multi-décennales à séculaires de l’Holocène supérieur, notamment en établissant un enregistrement précieux des variations du dernier millénaire. Combinés, les résultats de ces trois chapitres ont permis de répondre au troisième objectif, qui était de comparer les variations paléomagnétiques aux hautes et moyennes latitudes dans le but de déterminer les similarités et différences spatiales de variations géomagnétiques, notamment en lien avec les lobes de flux géomagnétiques.

Premier chapitre : variations paléomagnétiques à très hautes latitudes dans le fjord Petermann

Dans le premier chapitre, la compilation des données paléomagnétiques du fjord Petermann a permis d’actualiser le *stack* des variations d’inclinaison et de déclinaison produit par Reilly et al. (2019) et de produire un *stack* de paléointensité relative pour les derniers 6 000 ans. Ces données, comparées à d’autres enregistrements de la baie de Baffin, de la mer Tchouktches, de l’Atlantique Nord septentrional et du nord de l’Europe ont montré la reproductibilité des variations séculaires paléomagnétiques à travers l’Arctique au cours de l’Holocène. Notamment, les faibles valeurs d’inclinaison à environ 2,5 ka enregistrées dans le stack du fjord Petermann, sont visibles dans plusieurs enregistrements de l’Atlantique

Nord septentrional et de l’Arctique, ainsi que dans certains modèles géomagnétiques (pfm9k.2, Nilsson et al., 2022). Les variations de paléointensité relative (RPI) dans le fjord Petermann se révèlent asynchrones des variations de celles en Atlantique Nord et en Europe, tandis que le stack semble refléter les variations du moment dipolaire décrites par le modèle pfm9k.2. Les reconstitutions des trajectoires du pôle géomagnétique virtuel (VGP) ont montré des mouvements rapides entre l’est et ouest de l’hémisphère Nord, indiquant que la migration récente du pôle Nord magnétique n’est pas anormale à l’échelle de l’Holocène. Ces variations semblent liées aux variations d’intensité du champ géomagnétique et à la dynamique des lobes de flux géomagnétiques dans l’hémisphère Nord, ce qui vient corroborer les hypothèses de précédentes études. Le fjord Petermann s’est révélé un excellent site pour les reconstitutions paléomagnétiques, de par son taux d’accumulation de sédiments élevé, la présence de minéraux ferrimagnétiques de faible coercivité qui portent le signal magnétique, et la reproductibilité du signal paléomagnétique enregistré. Cette étude a montré que les enregistrements de PSV et de RPI dans l’Arctique peuvent être utilisés comme des points de contrôle pour la chronologie des sédiments en Arctique, où établir des modèles d’âge est parfois complexe à cause de plusieurs facteurs : peu de restes d’organismes carbonatés sont conservés du fait des eaux froides qui favorisent la dissolution du carbonate de calcium, la correction de l’âge réservoir notamment du fait de la présence de glace de mer.

Deuxième chapitre : influence de l’intensité des lobes de flux sur la migration du pôle géomagnétique virtuel

Dans le deuxième chapitre, trois carottes sédimentaires marines provenant du plateau continental du nord-est du Groenland et du Young Sound (Groenland), ont permis de reconstituer les PSV et RPI dans la région au cours de l’Holocène. Les trois enregistrements, caractérisés par une minéralogie ferrimagnétique de faible coercivité, montrent des variations similaires d’inclinaison, de déclinaison et RPI entre eux, démontrant la reproductibilité et la fiabilité du signal paléomagnétique. La comparaison avec d’autres enregistrements de référence met en évidence les similarités entre l’enregistrement de la carotte 073G, située sur la plateau continental nord-est du Groenland, et les enregistrements du nord de l’Europe et de l’Atlantique Nord septentrional, en particulier au cours des derniers 5 ka. Cela suggère que les PSV et la RPI du NE du Groenland et du nord de l’Europe à l’échelle millénaire pourraient avoir la même origine. De plus, la correspondance entre l’enregistrement de RPI de la carotte 073G et les taux de production des isotopes cosmogéniques confirme l’origine géomagnétique globale de ces variations et du signal de RPI, ainsi que la modulation géomagnétique du taux de production des isotopes à l’échelle millénaire selon, au moins sur les derniers 5 ka. La reconstitution des trajectoires du VGP, en lien avec les variations d’intensité globales du champ géomagnétique et plus précisément avec les lobes de flux, appuie les résultats du premier chapitre et d’autres études précédentes, suggérant que les lobes de flux géomagnétiques pourraient influencer la migration du VGP, en particulier lors des périodes de forte intensité. Enfin, cette thèse de doctorat montre également que le comportement du champ géomagnétique dans le Haut-Arctique (> 75°N) au cours des 5 derniers ka était similaire à celui de l'Atlantique Nord et de l'Europe. Les enregistrements de très hautes latitudes des deux premiers chapitres ont permis d’établir qu’il n’y a pas de lien évident des variations enregistrées en fonction de la localisation par rapport au cylindre tangentiel, contrairement à ce qui avait été supposé dans de précédentes études.

Troisième chapitre : variations paléomagnétiques récentes à très haute résolution et influence des processus sédimentaires sur l’acquisition de l’aimantation

Dans le troisième chapitre, des carottes sédimentaires lacustres en partie varvées ont été utilisées pour reconstituer les PSV et la RPI à très haute résolution à Grand Lake (Labrador, Canada) pour les derniers 2 500 ans. La carotte GL17-13, prélevée proche de l’exutoire du lac, à 75 m de profondeur, a permis de reconstituer les PSV et la RPI avec une résolution multi-décennale à séculaire, grâce au taux d’accumulation de sédiments élevé (>100 cm/ka). Une séquence sédimentaire de 20 m (GL23-20) a été prélevée lors d’une campagne de terrain suivante à 245 m de profondeur dans l’espoir d’obtenir une continuité de l’enregistrement pour le reste de l’Holocène. La séquence sédimentaire composite obtenue à partir des carottes s’est révélée contenir 75 couches déposées rapidement, interrompant le signal paléomagnétique, limitant ainsi son utilisation pour des reconstitutions paléomagnétiques. Bien que perturbée par ces nombreuses couches, la reconstitution du signal d'inclinaison vient supporter la tendance globale enregistrée dans la carotte GL17-13, indiquant ainsi la fiabilité de l'enregistrement des PSV dans les sédiments de Grand Lake pour les derniers 3000 ans. Les enregistrements d'inclinaison et de RPI de la carotte GL17-13 montrent des similarités avec des enregistrements de l'est du Canada (carotte MD99-2220, estuaire du St-Laurent, Québec, Canada), et du sud-est du Groenland (GREENICE15k, plateformes continentales du sud-est du Groenland et nord-ouest de l'Islande). Les variations récentes enregistrées dans la carotte de surface GL23-20-Up1, ainsi que l'enregistrement de 400 à 100 ans de la carotte GL17-13 permettent de faire le lien avec les variations récentes de la période historique décrites par le modèle GUFM et les calculs de IGRF. Pour résumer, dans ce chapitre, nous avons pu reconstituer un enregistrement précieux des derniers 1 000 ans, rarement conservé dans les études précédentes. La séquence sédimentaire GL23-20 nous a également permis d'aborder la question de l'impact des couches déposées rapidement sur l'enregistrement du signal paléomagnétique dans les sédiments. Ainsi, nous observons que l'amplitude de variation d'inclinaison au sein des événements est reliée à l'épaisseur de la couche et donc à l'importance de l'évènement et de la turbulence. De plus, les données paléomagnétiques viennent soutenir les hypothèses sur l'origine des événements déclencheurs de ces couches déposées rapidement, en particulier l'origine probablement sismique de la couche massive la plus récente

Asymétrie du champ géomagnétique et rôle des lobes de flux

Les données du premier chapitre ont mis en évidence une asynchronie des variations paléomagnétiques séculaires entre plusieurs sites. Tout d'abord, à partir des variations d'inclinaison, on observe que dans le fjord Petermann, la mer de Tchouktches et différents sites au sud du Groenland (U1305 et GREENICE15k), des variations similaires sont observées lorsque les enregistrements sont projetés à la localisation du fjord Petermann, tandis que les sites du nord de l'Europe n'enregistrent pas ces variations. Cette asymétrie est aussi mise en évidence par les variations de RPI, où on observe cette fois que les enregistrements de l'Atlantique Nord septentrional et de l'Europe sont différents et quasi asynchrones de l'enregistrement de Petermann, qui est lui très similaire aux projections d'intensité ainsi que du moment dipolaire du modèle géomagnétique pfm9k.2. Cependant, cette asymétrie ne semble pas constante au cours de l'Holocène. Ceci ne peut pas être démontré avec le stack Petermann qui ne couvre que les derniers 6 000 ans, mais plutôt avec les projections de certains enregistrements à la localisation du fjord. En effet, on observe des similarités à 9 ka entre les enregistrements du nord de l'Europe et les projections de GREENICE et du modèle pfm9k.2. L'asymétrie du champ mise en évidence dans le premier chapitre a également été observée dans le deuxième chapitre, où les enregistrements de la plateforme nord-est du Groenland présentent de très fortes similarités avec les enregistrements du nord de l'Europe.

La reconstitution des trajectoires du VGP à partir des enregistrements des deux premiers chapitres a permis d'observer un lien entre la localisation du VGP et position des lobes de flux géomagnétiques. Les lobes de flux pourraient ainsi jouer un rôle d'attracteur de VGP, particulièrement en période de forte intensité. Or, cette thèse met de l'avant l'hypothèse que la migration du VGP vers les basses latitudes en Europe soit liée à la forte intensité en Europe due à l'anomalie géomagnétique Levantine de l'âge de fer (*Levantine Iron Age Anomaly)* (Figure 73). Cette migration n'est cependant pas décrite par les enregistrements du chapitre 2, ce qui ne nous a pas permis de valider l'hypothèse du chapitre 1 (Figure 73). Un des freins à l'étude des VGP est notamment les valeurs de déclinaison qui, comme les carottes ne sont pas orientées selon le nord, sont relatives et moyennées à 0° selon l'hypothèse du dipôle axial géocentrique. Les précédents résultats soulignent l'importance de collecter des carottes orientées par rapport au nord magnétique afin de pallier ce problème, pour des travaux futurs. Établir des reconstitutions de trajectoires de VGP à partir de carottes orientées permettrait de valider l'hypothèse sur le rôle des composantes dipolaires fortes du champ géomagnétique dans la trajectoire de migration des VGP.

Variations paléomagnétiques dipolaires et non-dipolaires

Nos enregistrements ont permis de montrer que chacun des sites est influencé par des composantes non dipolaires du champ (*Levantine Iron Age Anomaly*, lobes de flux).

Cependant, la comparaison avec les taux de production d'isotopes cosmogéniques d'une part (chapitre 2), et les moments dipolaires globaux de modèles géomagnétiques d'autre part (chapitre 1), a souligné que les tendances globales des enregistrements de paléointensité relative répondent aux variations dipolaires du champ et représentent bien le champ géomagnétique global. Les enregistrements produits dans cette thèse décrivent des variations directionnelles (inclinaison, déclinaison, VGP) du champ magnétique terrestre de grande amplitude (9,5-7 ka puis 3,5-0 ka) en alternance avec des périodes de variations de plus faible ampleur (7-3,5 ka). Ces alternances d'amplitude de variations directionnelles sont soutenues par les enregistrements de paléointensité qui décrivent des variations importantes durant les derniers 3 ka, ainsi que par les modèles géomagnétiques (CALS10k.2, pfm9k.2) qui montrent une intensité plus faible pour la période (5-8 ka). De 9,8 à 8 ka, une tendance dipolaire est observée, bien qu'on se base ici sur l'enregistrement du nord-est du Groenland seulement. Le pic d'intensité décrit par les deux modèles à 9 ka est aussi observé dans l'enregistrement sédimentaire (Figure 73B, E). Pour la période suivante, l'intensité dipolaire est globalement plus faible de 8 à 6 ka, puis augmente de nouveau légèrement vers 6 ka. L'enregistrement de RPI du nord-est du Groenland suit cette tendance globale, avec des variations de plus faible amplitude. À partir des projections du modèle CALS10k.2 (Figure 73F, G, H ; chapitres 1 et 2), on observe des composantes dipolaires d'intensité moins importante que pour la période suivante. La tendance dipolaire globale au cours des derniers 3 ka est illustrée par la correspondance entre les variations de RPI de 073G avec les variations de ^{10}Be (R=-0,58) et ^{14}C (R=-0,7), ainsi que par les similarités globales entre l'enregistrement de Petermann et le modèle pfm9k.2 (Figure 73). Cependant, la forte contribution des éléments non-dipolaires observée sur les projections du modèle CALSk10.2 (Figure 73F, G, H) résulte en des différences de variations de RPI enregistrées à nos trois sites d'études (Tableau 11).

Tableau 11. Comparaison des enregistrements de RPI, de taux de production d'isotopes cosmogéniques et de moment dipolaire décrits par les modèles géomagnétiques à différents intervalles de temps des derniers 3 ka.

	RPI Petermann	RPI Grand Lake	RPI NE Groenland	Taux de production isotopes cosmogéniques	Moment dipolaire CALS10k.2	Moment dipolaire pfm9k.2
3 ka	Augmente	*N/A*	Creux, augmente	creux	Pic	Pic
2,5 ka	Faible	Forte	forte	Faible	Forte	Creux
2 ka	Forte, pic	Creux	Creux	Faible	Forte	Forte
1,5 ka	Forte	Forte	Faible	Faible	Très forte	Très forte
1 ka	Faible	Faible	Faible	Augmente	Diminue	Diminue

Les résultats et interprétations de ces trois chapitres apportent de nouvelles données importantes : de nouveaux enregistrements de bonne qualité et haute résolution de PSV pour les très hautes latitudes (chapitres 1 et 2), de nouveaux enregistrements de paléointensité relative à haute résolution et très hautes latitudes (chapitres 1, 2 et 3), un nouvel enregistrement des PSV et RPI pour les derniers 1 000 ans (chapitre 3), des reconstitutions des migrations du VGP au cours de l’Holocène (chapitres 1 et 2), tout en soulevant de nouvelles questions. Ces données viennent combler en partie le manque d’enregistrements à haute résolution des hautes latitudes, en particulier de RPI, qui manquent parfois dans les études paléomagnétiques.

Dans l’ensemble, cette thèse confirme que les variations spectaculaires récentes du champ géomagnétique ne sont pas anormales à l’échelle de l’Holocène. Des déplacements rapides du VGP sont décrits, coïncidant avec de fortes intensités des composantes dipolaires du champ, similaires aux variations actuelles où l’on observe une migration rapide du pôle nord magnétique à travers l’océan Arctique, en même temps que l’augmentation d’intensité du lobe de flux géomagnétique en Sibérie.

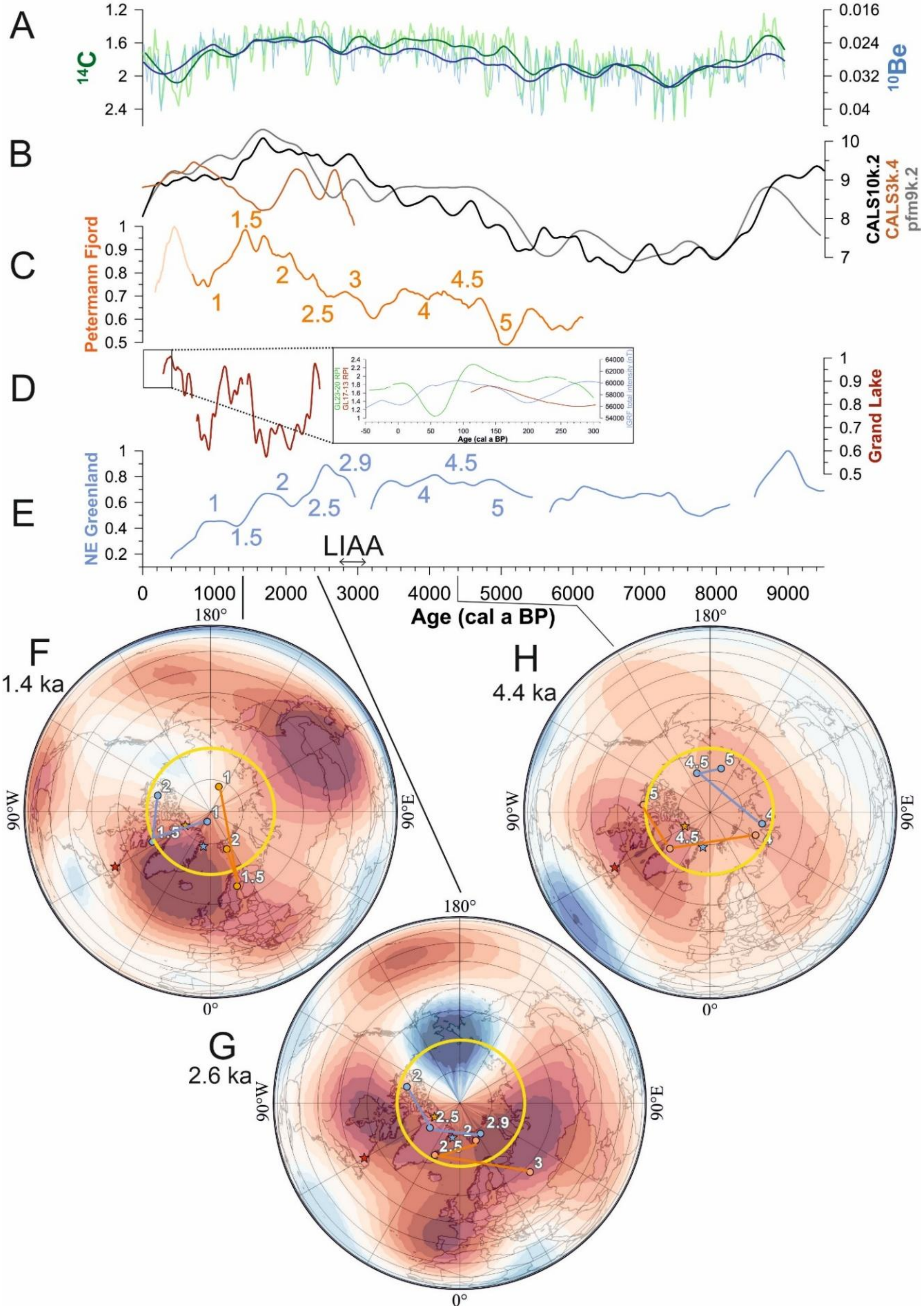
A
B
C
D
E
^{14}C
^{10}Be
1.2
1.6
2
2.4
0.016
0.024
0.032
0.04
CALS10k.2
CALS3k.4
pfm9k.2
10
9
8
7
Petermann Fjord
1
0.9
0.8
0.7
0.6
0.5
1.5
1
2
2.5
3
4
4.5
5
Grand Lake
GL23-20 RPI
GL17-13 RPI
IGRF total intensity (nT)
2.4
2.2
2
1.8
1.6
1.4
1.2
1
64000
62000
60000
58000
56000
54000
-50
0
50
100
150
200
250
300
Age (cal a BP)
NE Greenland
0.2
0.4
0.6
0.8
1
2.9
LIAA
0
1000
2000
3000
4000
5000
6000
7000
8000
9000
Age (cal a BP)
F
1.4 ka
G
2.6 ka
H
4.4 ka
180°
0°
90°W
90°E

Figure 72. Figure de synthèse. **A.** Taux de production moyennés des isotopes cosmogéniques ^{14}C (global) et ^{10}Be (hémisphère Nord). Les courbes plus foncées sont les courbes des tendances. **B.** Moments dipolaires globaux enregistrés par différents modèles géomagnétiques : CALS10k.2 (courbe noire) (Constable et al., 2016), pfm9k.2 (courbe grise) (Nilsson et al., 2022) et CALS3k.4 (courbe marron) (Korte and Constable, 2011). **C.** Petermann Fjord RPI stack (Girard et al., 2024). La partie claire de la courbe (0-700 ans) représente l'intervalle incertain décrit dans le chapitre 1. **D.** Enregistrement de paléointensité relative à Grand Lake (carotte GL17-13). L'encart agrandi contient les enregistrements de paléointensité relative établis à partir de la carotte GL17-13 (rouge), GL23-20 (vert) et l'intensité du champ (nT) (bleu) d'après les calculs d'IGRF et du modèle GUFM (Jackson et al., 2000) pour les derniers 400 ans. **E.** Enregistrement de paléointensité relative sur la marge Nord-Est du Groenland (carotte 073G). Les trois enregistrements de RPI ont chacun été normalisés à 1 afin de faciliter la comparaison. La flèche représente l'intervalle de temps où LIAA (Levantine Iron Age Anomaly) a été enregistré (Shaar et al., 2016, 2017). **F.** Projection de l'intensité globale du champ (moment dipolaire CALS10k.2 ; Constable et al., 2016) à 1,4 ka. **G.** Projection de l'intensité globale du champ (moment dipolaire CALS10k.2 ; Constable et al., 2016) à 2,6 ka. **H.** Projection de l'intensité globale du champ (moment dipolaire CALS10k.2 ; Constable et al., 2016) à 4,5 ka. Pour F, G, et H. Les étoiles représentent les sites d'études Grand Lake (rouge), Fjord de Petermann (orange) et la marge nord-est du Groenland (bleu). Les points représentent les reconstitutions du VGP à partir des enregistrements de Petermann (orange) et de 073G (bleu). Les cercles jaunes indiquent la position du cylindre tangentiel. La figure a été réalisée avec Grapher, CorelDraw et ArcGIS pour les cartes F, G, H, en utilisant un fond de carte provenant de la NOAA, Esri, USGS, contributeurs Open Street Map et de la communauté GIS. Les fichiers de traits de côte proviennent de GADM version 2.8 (*https://gadm.org*).

Perspectives

Une des perspectives majeures qui ressort de cette thèse de doctorat est d'approfondir la question de l'effet réservoir pour les datations au radiocarbone des échantillons marins (ΔR) qui a été abordée dans les trois chapitres, mais seulement en surface, à base d'hypothèses principalement. Pour les carottes 039G et 073G, cette question pourrait être abordée en utilisant une combinaison de plusieurs enregistrements avec des méthodes de datation différentes et indépendantes :

- l'enregistrement GREENICE, dont la chronologie est très bien contrainte par de forts taux d'accumulation de sédiments et une combinaison d'âges magnétique, radiocarbone et de téphrochronologie ;

- les enregistrements varvés et/ou lacustres, à taux d'accumulation de sédimentsélevés du nord de l'Europe ;

-et les enregistrements globaux des taux de production d'isotopes cosmogéniques qui sont directement reliés et corrélables aux variations d'intensité paléomagnétiques.

Un âge magnétique pourrait ainsi être établi à partir de ces différentes comparaisons et l'hypothèse de la potentielle dérive vers l'ouest pourrait être contrainte et probablement écartée comme vu précédemment dans les chapitres. Une identification plus précise de la minéralogie des carottes, combinée aux études précédentes d'assemblages de foraminifères qui ont permis d'identifier les masses d'eau en présence aux sites d'études au cours du temps, ainsi que l'ajout d'autres enregistrements dans la zone, comme dans le cadre de la thèse de doctorat de Mads Ramsgaard Stoltenberg (Université Aarhus, Danemark), pourrait aider à approfondir la question des variations du ΔR.

Dans le cadre du troisième chapitre, l'enregistrement lacustre varvé de Grand Lake pourrait cette fois servir de référence pour essayer de calculer les variations d'âge réservoir, avec la carotte MD99-2220 par exemple. Cela nécessiterait d'augmenter encore la résolution du signal paléomagnétique en sous-échantillonnant avec des cubes au lieu de u-channels, et ainsi éviter le lissage associé à la fonction de réponse du magnétomètre et/ou bien en déconvoluant le signal actuel. Récolter de nouvelles carottes plus longues, avec la plateforme UWITEC à l'exutoire du lac, permettrait d'étendre le signal au-delà des derniers 2 500 ans en évitant les nombreuses couches déposées rapidement. Des analyses de ^{10}Be sont en cours sur la carotte GL17-13 du chapitre 3 par François Lapointe de l'Université du Massachusetts, Amherst. Ces résultats pourront servir à préciser encore la chronologie de la carotte. En combinant ainsi des méthodes de datation différentes (paléomagnétisme, varves, ^{10}Be, ^{14}C), et du fait des forts taux de sédimentation à ce site, les incertitudes chronologiques seraient ainsi réduites. On obtiendrait alors un enregistrement des variations paléomagnétiques très bien contraintes chronologiquement, qui pourrait servir de référence dans les régions voisines, telles que pour la carotte MD99-2220 (St-Onge et al., 2003). De plus, il sera possible de caractériser plus précisément la modulation géomagnétique du taux de production des isotopes cosmogéniques. Globalement, le paléomagnétisme se révèle un outil de datation continue précieux aux hautes latitudes, en plus d’être une méthode non destructive.

La séquence composite GL23-20 à Grand Lake offre de nombreuses possibilités de caractériser les variations des paramètres magnétiques sédimentaires selon les conditions environnementales de dépôt des sédiments : nombreuses couches déposées rapidement de différentes natures (turbidites, hyperpycnites), résultant de différents évènements déclencheurs, transition progressive d’un milieu marin à un milieu lacustre. L’étude des couches déposées rapidement de la séquence sédimentaire GL23-20 pourra être approfondie, notamment en caractérisant les propriétés magnétiques évoquées dans le chapitre 3 (inclinaison, susceptibilité magnétique), selon le type de couche identifié et selon la phase d’environnement de dépôt (Kury et al., 2025), et ainsi déterminer plus précisément l’impact de la turbulence et des conditions de dépôt en général sur l’enregistrement de l’aimantation détritique rémanente.

Une autre perspective serait d’approfondir la question de l’asymétrie du champ, notamment est-ouest de hémisphère Nord, évoquée dans les deux premiers chapitres et la conclusion générale, ainsi que dans d’autres études (Nilsson et al., 2022 et les références incluses). En particulier, on observe une différence entre les enregistrements du Nord de l’Europe/NE du Groenland et du fjord Petermann, bien que les sites d’études des deux premiers chapitres soient éloignés de ~1000 km seulement. Quelle est donc la limite spatiale des variations enregistrées aux deux sites ? Où se situe le « point de bascule » entre l’influence du lobe de flux Nord-Américain et de la zone « Europe du Nord/NE du Groenland » ? Pour cela, un transect de carottes dans des localisations intermédiaires pourrait être utilisé pour reconstituer les enregistrements paléomagnétiques entre le fjord Petermann et le plateau du nord-est du Groenland (fjord Ryder par exemple), voire étendre plus loin, entre le plateau continental nord-est groenlandais et l’Europe du Nord (Svalbard, mers nordiques, par exemple), ou plus à l’ouest du fjord Petermann.

Mot de la fin

Le fjord Petermann, la plateforme continentale nord-est du Groenland, ainsi que Grand Lake se sont révélés être des sites d'études privilégiés pour reconstituer les variations séculaires directionnelles et de paléointensité relative au cours de l'Holocène, à très haute résolution (séculaires à multi-décennales). Dans l'ensemble, cette thèse a contribué à apporter des éléments de compréhension de la dynamique du champ magnétique terrestre aux hautes latitudes de l'hémisphère Nord, notamment sur les variations séculaires, les lobes de flux géomagnétiques, le pôle géomagnétique virtuel, ainsi que la modulation du taux de production des isotopes cosmogéniques. Ce travail soulève également des questions qui pourraient faire l'objet de nouveaux projets par la suite, notamment de mieux caractériser l'impact de l'environnement sédimentaire sur l'enregistrement (turbulence, aimantation rémanente détritique) et la reconstitution (incertitudes, profondeur de blocage de l'aimantation, établissement du ΔR) des variations paléomagnétiques.

RÉFÉRENCES BIBLIOGRAPHIQUES

Amerigian, C., 1974. Sea-floor dynamic processes as the possible cause of correlations between paleoclimatic and paleomagnetic indices in deep-sea sedimentary cores. Earth and Planetary Science Letters 21, 321–326. https://doi.org/10.1016/0012-821X(74)90168-X

Arndt, J.E., Jokat, W., Dorschel, B., 2017. The last glaciation and deglaciation of the Northeast Greenland continental shelf revealed by hydro-acoustic data. Quaternary Science Reviews 160, 45–56. https://doi.org/10.1016/j.quascirev.2017.01.018

Arndt, J.E., Jokat, W., Dorschel, B., Myklebust, R., Dowdeswell, J.A., Evans, J., 2015. A new bathymetry of the Northeast Greenland continental shelf: Constraints on glacial and other processes. Geochem Geophys Geosyst 16, 3733–3753. https://doi.org/10.1002/2015GC005931

Barletta, F., St-Onge, G., Channell, J.E.T., Rochon, A., 2010. Dating of Holocene western Canadian Arctic sediments by matching paleomagnetic secular variation to a geomagnetic field model. Quaternary Science Reviews 29, 2315–2324. https://doi.org/10.1016/j.quascirev.2010.05.035

Barletta, F., St-Onge, G., Channell, J.E.T., Rochon, A., Polyak, L., Darby, D., 2008. High-resolution paleomagnetic secular variation and relative paleointensity records from the western Canadian Arctic: implication for Holocene stratigraphy and geomagnetic field behaviour. Can. J. Earth Sci. 45, 1265–1281. https://doi.org/10.1139/E08-039

Bendtsen, J., Gustafsson, K.E., Rysggard, S., Vang, T., 2007. Physical conditions, dynamics and model simulations during the ice-free period of the Young Sound/Tyrolerfjord system. Meddr Grønland. Biosci 58, 46–59. https://doi.org/10.7146/mogbiosci.v58.142639

Bennike, O., Björck, S., 2002. Chronology of the last recession of the Greenland Ice Sheet. J Quaternary Science 17, 211–219. https://doi.org/10.1002/jqs.670

Bennike, O., Weidick, A., 2001. Late Quaternary history around Nioghalvfjerdsfjorden and Jøkelbugten, North-East Greenland. Boreas 30, 205–227.

Blott, S.J., Pye, K., 2001. GRADISTAT: a grain size distribution and statistics package for the analysis of unconsolidated sediments. Earth Surf. Process. Landforms 26, 1237–1248. https://doi.org/10.1002/esp.261

Bloxham, J., Gubbins, D., Jackson, A., 1989. Geomagnetic secular variation. Philosophical Transactions of the Royal Society of London. Series A: Mathematical, Physical and Engineering Sciences 329, 415–502.

Bloxham, J., Jackson, A., 1992. Time-dependent mapping of the magnetic field at the core-mantle boundary. Journal of Geophysical Research: Solid Earth 97, 19537–19563. https://doi.org/10.1029/92JB01591

Bonhommet, N., Babkine, J., 1967. Sur la presence d'aimentation inverse dans la Chaine des Puys. Comptes Rendus hebdomadaires des séances de l'Académie des sciences, B 264 92–94.

Bonhommet, N., Zahringer, J., 1969. Paleomagnetism and potassium–argon determinations of the Laschamp geomagnetic polarity event. Earth and Planetary Science Letters 6, 43–461969.

Brown, M.C., Donadini, F., Korte, M., Nilsson, A., Korhonen, K., Lodge, A., Lengyel, S.N., Constable, C.G., 2015. GEOMAGIA50.v3: 1. general structure and modifications to the archeological and volcanic database. Earth Planet Sp 67, 83. https://doi.org/10.1186/s40623-015-0232-0

Brunhes, B., 1906. Recherches sur la direction d'aimantation des roches volcaniques. J. Phys. Theor. Appl. 5, 705–724. https://doi.org/10.1051/jphystap:019060050070500

Buffett, B.A., 2000. Earth's Core and the Geodynamo. Science 288, 2007–2012. https://doi.org/10.1126/science.288.5473.2007

Bullard, E.C., 1949. The magnetic field within the earth. Proceedings of the Royal Society of London 433–453.

Campuzano, S.A., Gómez-Paccard, M., Pavón-Carrasco, F.J., Osete, M.L., 2019. Emergence and evolution of the South Atlantic Anomaly revealed by the new paleomagnetic reconstruction SHAWQ2k. Earth and Planetary Science Letters 512, 17–26. https://doi.org/10.1016/j.epsl.2019.01.050

Cande, S.C., Kent, D.V., 1992. A new geomagnetic polarity time scale for the Late Cretaceous and Cenozoic. Journal of Geophysical Research: Solid Earth 97, 13917–13951. https://doi.org/10.1029/92JB01202

Channell, J.E.T., Stoner, J.S., Hodell, D.A., Charles, C.D., 2000. Geomagnetic paleointensity for the last 100 kyr from the sub-antarctic South Atlantic: a tool for inter-hemispheric correlation. Earth and Planetary Science Letters 175, 145–160. https://doi.org/10.1016/S0012-821X(99)00285-X

Channell, J.E.T., Vigliotti, L., 2019. The Role of Geomagnetic Field Intensity in Late Quaternary Evolution of Humans and Large Mammals. Rev. Geophys. 57, 709–738. https://doi.org/10.1029/2018RG000629

Chave, A.D., Denham, C.R., 1979. Climatic changes, magnetic intensity variations and fluctuations of the eccentricity of the earth's orbit during the past 2,000,000 years and a mechanism which may be responsible for the relationship — A discussion. Earth and Planetary Science Letters 44, 150–152. https://doi.org/10.1016/0012-821X(79)90015-3

Constable, C., 1992. Link between geomagnetic reversal paths and secular variation of the field over the past 5 Myr. Nature 358, 230–233. https://doi.org/10.1038/358230a0

Constable, C., Korte, M., Panovska, S., 2016. Persistent high paleosecular variation activity in southern hemisphere for at least 10 000 years. Earth and Planetary Science Letters 453, 78–86. https://doi.org/10.1016/j.epsl.2016.08.015

Cooper, A., Turney, C.S.M., Palmer, J., Hogg, A., McGlone, M., Wilmshurst, J., Lorrey, A.M., Heaton, T.J., Russell, J.M., McCracken, K., Anet, J.G., Rozanov, E., Friedel, M., Suter, I., Peter, T., Muscheler, R., Adolphi, F., Dosseto, A., Faith, J.T., Fenwick, P., Fogwill, C.J., Hughen, K., Lipson, M., Liu, J., Nowaczyk, N., Rainsley, E., Bronk Ramsey, C., Sebastianelli, P., Souilmi, Y., Stevenson, J., Thomas, Z., Tobler, R., Zech, R., 2021. A global environmental crisis 42,000 years ago. Science 371, 811–818. https://doi.org/10.1126/science.abb8677

Couette, P., Ghienne, J., Lajeunesse, P., Van Der Woerd, J., 2023. Climatic control on the retreat of the Laurentide Ice Sheet margin in easternmost Québec–Labrador (Canada) revealed by cosmogenic nuclide exposure dating. J Quaternary Science 38, 1044–1061. https://doi.org/10.1002/jqs.3525

Creer, K.M., Irving, E., Runcorn, S.K., 1954. The direction of the Geomagnetic Field in Remote Epochs in Great Britain. Earth, Planets and Space 6, 163–168.

Dawes, P.R., Frisch, T., Garde, A.A., Iannelli, T.R., Ineson, J.R., Jensen, S.M., Pirajno, F., Sønderholm, M., Stemmerik, L., Stouge, S., Thomassen, B., Van Gool, J.A.M., 2000. Kane Basin 1999: mapping, stratigraphic studies and economic assessment of Precambrian and Lower Palaeozoic provinces in north-western Greenland. Geology of Greenland Survey Bulleztin 11–28.

deMenocal, P.B., Ruddiman, W.F., Kent, D.V., 1990. Depth of post-depositional remanence acquisition in deep-sea sediments: a case study of the Brunhes-Matuyama reversal and oxygen isotopic Stage 19.1. Earth and Planetary Science Letters 99, 1–13. https://doi.org/10.1016/0012-821X(90)90066-7

Dunai, T.J., Lifton, N.A., 2014. The Nuts and Bolts of Cosmogenic Nuclide Production. Elements 10, 347–350. https://doi.org/10.2113/gselements.10.5.347

Elsasser, W., Ney, E.P., Winckler, J.R., 1956. Cosmic-Ray Intensity and Geomagnetism. Nature 178, 1226–1227. https://doi.org/10.1038/1781226a0

Evans, J., Ó Cofaigh, C., Dowdeswell, J.A., Wadhams, P., 2009. Marine geophysical evidence for former expansion and flow of the Greenland Ice Sheet across the north-east Greenland continental shelf. J Quaternary Science 24, 279–293. https://doi.org/10.1002/jqs.1231

Falkner, K.K., Melling, H., Münchow, A.M., Box, J.E., Wohlleben, T., Johnson, H.L., Gudmandsen, P., Samelson, R., Copland, L., Steffen, K., Rignot, E., Higgins, A.K., 2011. Context for the Recent Massive Petermann Glacier Calving Event. EoS Transactions 92, 117–118. https://doi.org/10.1029/2011eo140001

Fitzhugh, W., 1973. Environmental Approaches to the Prehistory of the North. Journal of the Washington Academy if Sciences 63, 39–53.

Francus, P., Nobert, P., 2007. An integrated computer system to acquire, process, measure and store images of laminated sediments. Presented at the 4th International Limnogeology Congress, Barcelona.

Fulton, R., Ferguson, J., 1986. Surficial geology, Cartwright, Labrador, Newfoundland.

Funder, S., Kjeldsen, K.K., Kjær, K.H., Ó Cofaigh, C., 2011. The Greenland Ice Sheet During the Past 300,000 Years: A Review, in: Developments in Quaternary Sciences. Elsevier, pp. 699–713. https://doi.org/10.1016/B978-0-444-53447-7.00050-7

Gagnon-Poiré, A., 2023. Reconstitution hydrologique millénaire dans la forêt boréale du Labrador à partir des sédiments varvés de Grand Lake (Ph.D.). Institut National de la Recherche Scientifique - Centre Eau Terre et Environnement.

Gagnon-Poiré, A., Brigode, P., Francus, P., Fortin, D., Lajeunesse, P., Dorion, H., Trottier, A.-P., 2021. Reconstructing past hydrology of eastern Canadian boreal catchments using clastic varved sediments and hydro-climatic modelling: 160 years of fluvial inflows. Clim. Past 17, 653–673. https://doi.org/10.5194/cp-17-653-2021

Gauss, C.F., 1833. Intensitas vis Magneticae Terrestris ad Mensuram Absolutam Revocata. Dieterich, Göttingen.

Girard, J., Reilly, B.T., St-Onge, G., Lagroix, F., Montero-Serrano, J.-C., Stoner, J., Jennings, A.E., 2024. Paleomagnetic data (inclination, declination, relative paleointensity) in sediment core AMD1902-10GC from Petermann Fjord (Nares Strait, Northern Greenland). https://doi.pangaea.de/10.1594/PANGAEA.971852

Gillet, N., Jault, D., Finlay, C.C., Olsen, N., 2013. Stochastic modeling of the Earth's magnetic field: Inversion for covariances over the observatory era. Geochem Geophys Geosyst 14, 766–786. https://doi.org/10.1002/ggge.20041

Glatzmaiers, G., Roberts, P.H., 1995. A three-dimensional convective dynamo solution with rotating and finitely conducting inner core and mantle. PEPI 91, 63–75. https://doi.org/10.1016/0031-9201(95)03049-3

Glud, R.N., Rysgaard, S., Kühl, M., Hansen, J.W., 2007. The sea ice in Young Sound: Implications for carbon cycling. Meddr Grønland. Biosci 58, 62–85. https://doi.org/10.7146/mogbiosci.v58.142641

Gubbins, D., 2008. Geomagnetic reversals. Nature 452, 3.

Gubbins, D., 1999. The distinction between geomagnetic excursions and reversals. Geophys. J. Int. 137, F1–F4. https://doi.org/10.1046/j.1365-246x.1999.00810.x

Gubbins, D., Jones, A.L., Finlay, C.C., 2006. Fall in Earth's Magnetic Field is Erratic. Science 312, 900–902. https://doi.org/10.1126/science.1124855

Guyodo, Y., Channell, J.E.T., 2002. Effects of variable sedimentation rates and age errors on the resolution of sedimentary paleointensity records: variable sedimentation rates. Geochem.-Geophys.-Geosyst. 3, 1–18. https://doi.org/10.1029/2001GC000211

Hansen, K.E., Lorenzen, J., Davies, J., Wacker, L., Pearce, C., Seidenkrantz, M.-S., 2022. Deglacial to Mid Holocene environmental conditions on the northeastern Greenland shelf, western Fram Strait. Quaternary Science Reviews 293, 107704. https://doi.org/10.1016/j.quascirev.2022.107704

Hanslik, D., Jakobsson, M., Backman, J., Björck, S., Sellén, E., O'Regan, M., Fornaciari, E., Skog, G., 2010. Quaternary Arctic Ocean sea ice variations and radiocarbon reservoir age corrections. Quaternary Science Reviews 29, 3430–3441. https://doi.org/10.1016/j.quascirev.2010.06.011

Harland, W.B., Cox, A.V., Llewellyn, P.G., Pickton, C.A.G., Smith, A.G., Walters, R., 1983. A geologic Time Scale. Revue d'Ecologie.

Harrison, R.J., Feinberg, J.M., 2008. FORCinel: An improved algorithm for calculating first-order reversal curve distributions using locally weighted regression smoothing: FORCINEL ALGORITHM. Geochem. Geophys. Geosyst. 9. https://doi.org/10.1029/2008GC001987

Hartmann, G.A., Pacca, I.G., 2009. Time evolution of the South Atlantic Magnetic Anomaly. An. Acad. Bras. Ciênc. 81, 243–255. https://doi.org/10.1590/S0001-37652009000200010

Heaton, T.J., Bard, E., Bronk Ramsey, C., Butzin, M., Hatté, C., Hughen, K.A., Köhler, P., Reimer, P.J., 2023. A response to community questions on the Marine20 radiocarbon age calibration curve: marine reservoir ages and the calibration of 14C samples from the oceans. Radiocarbon 65, 247–273. https://doi.org/10.1017/RDC.2022.66

Heaton, T.J., Bard, E., Bronk Ramsey, C., Butzin, M., Köhler, P., Muscheler, R., Reimer, P.J., Wacker, L., 2021. Radiocarbon: A key tracer for studying Earth's dynamo, climate system, carbon cycle, and Sun. Science 374, eabd7096. https://doi.org/10.1126/science.abd7096

Heaton, T.J., Köhler, P., Butzin, M., Bard, E., Reimer, R.W., Austin, W.E.N., Bronk Ramsey, C., Grootes, P.M., Hughen, K.A., Kromer, B., Reimer, P.J., Adkins, J., Burke, A., Cook, M.S., Olsen, J., Skinner, L.C., 2020. Marine20—The Marine Radiocarbon Age Calibration Curve (0–55,000 cal BP). Radiocarbon 62, 779–820. https://doi.org/10.1017/RDC.2020.68

Helsley, C.E., Steiner, M.B., 1968. Evidence for long intervals of normal polarity during the cretaceous period. Earth and Planetary Science Letters 5, 325–332. https://doi.org/10.1016/S0012-821X(68)80060-3

Higgins, A.K., 2015. Descriptive text to the Geological map of Greenland, 1:500 000, Lambert Land, Sheet 9, Geological Survey of Denmark and Greenland map series. GEUS, Copenhagen.

Hoffman, K.A., 1992. Dipolar reversal states of the geomagnetic field and core-mantle dynamics. Nature 359.

Hoffman, K.A., Singer, B.S., 2008. Magnetic Source Separation in Earth's Outer Core. Science 321, 1800–1800. https://doi.org/10.1126/science.1159777

Hogan, K.A., Jakobsson, M., Mayer, L., Reilly, B.T., Jennings, A.E., Stoner, J.S., Nielsen, T., Andresen, K.J., Nørmark, E., Heirman, K.A., Kamla, E., Jerram, K., Stranne, C., Mix, A., 2020. Glacial sedimentation, fluxes and erosion rates associated with ice retreat in Petermann Fjord and Nares Strait, north-west Greenland. The Cryosphere 14, 261–286. https://doi.org/10.5194/tc-14-261-2020

Hospers, J., 1953. Reversals of the main geomagnetic field I, II. Proc. Kon. Nederl. Akad. Wetensch. B 56, 476–491.

Hughen, K.A., 2007. Chapter Five Radiocarbon Dating of Deep-Sea Sediments, in: Developments in Marine Geology. Elsevier, pp. 185–210. https://doi.org/10.1016/S1572-5480(07)01010-X

Hulot, G., Eymin, C., Langlais, B., Mandea, M., Olsen, N., 2002. Small-scale structure of the geodynamo inferred fromOersted and Mgasat satellite data. Nature 416, 620–623. https://doi.org/10.1038/416620a

Irving, E., Major, A., 1964. Post-Depositional Detrital Remanent Magnetization in a Synthetic Sediment. Sedimentology 3, 135–143.

Jackson, A., Jonkers, A.R.T., Walker, M.R., 2000. Four centuries of geomagnetic secular variation from historical records. Philosophical Transactions of the Royal Society of London. Series A: Mathematical, Physical and Engineering Sciences 358, 957–990. https://doi.org/10.1098/rsta.2000.0569

Jakobsson, M., Hogan, K.A., Mayer, L.A., Mix, A., Jennings, A., Stoner, J., Eriksson, B., Jerram, K., Mohammad, R., Pearce, C., Reilly, B., Stranne, C., 2018. The Holocene retreat dynamics and stability of Petermann Glacier in northwest Greenland. Nat Commun 9, 2104. https://doi.org/10.1038/s41467-018-04573-2

Jennings, A., Jenner, K., Normandeau, A., Roth, W., Andrews, J., Kelleher, R., Girard, J., Reilly, B., Campbell, C., Bennett, R., 2025. Retreat of the Boothia-Lancaster ice stream from its Last Glacial Maximum extent and its role in the origin of Baffin Bay Detrital Carbonate (BBDC) events 0, 1 and 2. Quaternary Science Reviews 358, 109353. https://doi.org/10.1016/j.quascirev.2025.109353

Jennings, A., Reilly, B., Andrews, J., Hogan, K., Walczak, M., Jakobsson, M., Stoner, J., Mix, A., Nicholls, K.W., O'Regan, M., Prins, M.A., Troelstra, S.R., 2022. Modern and early Holocene ice shelf sediment facies from Petermann Fjord and northern Nares Strait, northwest Greenland. Quaternary Science Reviews 283, 107460. https://doi.org/10.1016/j.quascirev.2022.107460

Johnson, H.L., Münchow, A., Falkner, K.K., Melling, H., 2011. Ocean circulation and properties in Petermann Fjord, Greenland. J. Geophys. Res. 116, C01003. https://doi.org/10.1029/2010JC006519

Jutterström, S., Anderson, L.G., 2005. The saturation of calcite and aragonite in the Arctic Ocean. Marine Chemistry 94, 101–110. https://doi.org/10.1016/j.marchem.2004.08.010

Kamula, C.M., Kuzyk, Z.Z.A., Lobb, D.A., Macdonald, R.W., 2017. Sources and accumulation of sediment and particulate organic carbon in a subarctic fjard estuary:210 Pb,137 Cs, and δ13 C records from Lake Melville, Labrador. Can. J. Earth Sci. 54, 993–1006. https://doi.org/10.1139/cjes-2016-0167

Kelleher, R., Jennings, A., Andrews, J., Brooks, N.K.S., Marchitto, T., Feng, S., Woelders, L., Normandeau, A., Jenner, K., Bennett, R., Brookins, S., 2022. Late glacial retreat of the Lancaster Sound Ice Stream and early Holocene onset of Arctic/Atlantic throughflow in the Arctic Island channels. Arctic, Antarctic, and Alpine Research 54, 395–427. https://doi.org/10.1080/15230430.2022.2110689

Kent, D.V., 1982. Apparent correlation of paleomagnetic intensity and climatic records in deep-sea sediments. Nature 538–539.

Kent, D.V., 1973. Post-depositional Remanent Magnetisation in Deep-sea Sediment. Nature 246, 32–34. https://doi.org/10.1038/246032a0

King, G.A., 1985. A Standard Method for Evaluating Radiocarbon Dates of Local Deglaciation: Application to the Deglaciation History of Southern Labrador and Adjacent Québec. gpq 39, 163–182. https://doi.org/10.7202/032600ar

Klassen, R.A., Thompson, F.J., 1993. Glacial history, drift composition, and mineral exploration, central Labrador.

Klenke, M., Schenke, H.W., 2002. A new bathymetric model for the central Fram Strait. Marine Geophysical Research 23, 367–378.

Korte, M., Constable, C., 2011. Improving geomagnetic field reconstructions for 0–3ka. Physics of the Earth and Planetary Interiors 188, 247–259. https://doi.org/10.1016/j.pepi.2011.06.017

Korte, M., Constable, C.G., 2005. Continuous geomagnetic field models for the past 7 millennia: 2. CALS7K: Geomagnetic field models. Geochem. Geophys. Geosyst. 6. https://doi.org/10.1029/2004GC000801

Kovaltsov, G.A., Mishev, A., Usoskin, I.G., 2012. A new model of cosmogenic production of radiocarbon 14C in the atmosphere. Earth and Planetary Science Letters 337–338, 114–120. https://doi.org/10.1016/j.epsl.2012.05.036

Kury, M.S., Francus, P., Chassiot, L., Antoniades, D., St-Onge, G., Girard, J., Lajeunesse, P., 2025. Untangling sedimentation processes in a deep fjord lake in Labrador: A high-resolution archive of past environment dynamics at Grand Lake. The Depositional Record 1–26. https://doi.org/10.1002/dep2.70020

Laj, C., Channell, J.E.T., 2007. Geomagnetic Excursions, in: Treatise on Geophysics. Elsevier, pp. 373–416.

Lal, D., Peters, B., 1967. Kosmische Strahlung IICosmic Rays II, in: Handbuch Der Physik/Encyclopedia of Physics. Springer Berlin, pp. 551–612.

Lapointe, F., Gagnon-Poiré, A., Francus, P., Lajeunesse, P., Gagnon, C., 2025. A new 1500-year-long varve thickness record from Labrador, Canada, uncovers significant insights into large-scale climate variability in the Atlantic. https://doi.org/10.5194/egusphere-2025-97

Larson, R.L., Pitman, W.C., 1972. World-Wide Correlation of Mesozoic Magnetic Anomalies, and its Implications. GSA Bulletin 83, 3645–3662. https://doi.org/10.1130/0016-7606(1972)83[3645:WCOMMA]2.0.CO;2

Laskar, J., Robutel, P., Joutel, F., Gastineau, M., Correia, A.C.M., Levrard, B., 2004. A long-term numerical solution for the insolation quantities of the Earth. A&A 428, 261–285. https://doi.org/10.1051/0004-6361:20041335

Lawrence, K.P., Tauxe, L., Staudigel, H., Constable, C.G., Koppers, A., McIntosh, W., Johnson, C.L., 2009. Paleomagnetic field properties at high southern latitude. Geochemistry, Geophysics, Geosystems 10. https://doi.org/10.1029/2008GC002072

Lecavalier, B.S., Fisher, D.A., Milne, G.A., Vinther, B.M., Tarasov, L., Huybrechts, P., Lacelle, D., Main, B., Zheng, J., Bourgeois, J., Dyke, A.S., 2017. High Arctic Holocene temperature record from the Agassiz ice cap and Greenland ice sheet evolution. Proc. Natl. Acad. Sci. U.S.A. 114, 5952–5957. https://doi.org/10.1073/pnas.1616287114

Lisé-Pronovost, A., St-Onge, G., Brachfeld, S., Barletta, F., Darby, D., 2009. Paleomagnetic constraints on the Holocene stratigraphy of the Arctic Alaskan margin. Global and Planetary Change 68, 85–99. https://doi.org/10.1016/j.gloplacha.2009.03.015

Liu, Q., Roberts, A.P., Rohling, E.J., Zhu, R., Sun, Y., 2008. Post-depositional remanent magnetization lock-in and the location of the Matuyama–Brunhes geomagnetic reversal boundary in marine and Chinese loess sequences. Earth and Planetary Science Letters 275, 102–110. https://doi.org/10.1016/j.epsl.2008.08.004

López-Quirós, A., Junna, T., Davies, J., Andresen, K.J., Nielsen, T., Haghipour, N., Wacker, L., Olsen Alstrup, A.K., Munk, O.L., Rasmussen, T.L., Pearce, C., Seidenkrantz, M.-S., 2024. Retreat patterns and dynamics of the former Norske Trough ice stream (NE Greenland): An integrated geomorphological and sedimentological approach. Quaternary Science Reviews 325, 108477. https://doi.org/10.1016/j.quascirev.2023.108477

Lowrie, W., Fichtner, A., 1997. Fundamental of Geophysics, First Edition. ed. Cambridge University Press, UK.

Lund, S., Keigwin, L., Darby, D., 2016. Character of Holocene paleomagnetic secular variation in the tangent cylinder: Evidence from the Chukchi Sea. Physics of the Earth and Planetary Interiors 256, 49–58. https://doi.org/10.1016/j.pepi.2016.03.005

Lund, S.P., Banerjee, S.K., 1985. Late quaternary paleomagnetic field secular variation from two Minnesota Lakes. Journal of Geophysical Research: Solid Earth 90, 803–825. https://doi.org/10.1029/JB090iB01p00803

Mackereth, 1971. On the variation in direction of the horizontal component of remanent magnetisation in lake sediments. Earth Planetary Science Letters 12, 332–338. https://doi.org/10.1016/0012-821X(71)90219-6

Marshall, M., Schlolaut, G., Nakagawa, T., Lamb, H., Brauer, A., Staff, R., Ramsey, C.B., Tarasov, P., Gotanda, K., Haraguchi, T., Yokoyama, Y., Yonenobu, H., Tada, R., 2012. A novel approach to varve counting using μXRF and X-radiography in combination with thin-section microscopy, applied to the Late Glacial chronology from Lake Suigetsu, Japan. Quaternary Geochronology 13, 70–80. https://doi.org/10.1016/j.quageo.2012.06.002

Masarik, J., Beer, J., 1999. Simulation of particle fluxes and cosmogenic nuclide production in the Earth's atmosphere. J. Geophys. Res. 104, 12099–12111. https://doi.org/10.1029/1998JD200091

Mazaud, A., 2005. User-friendly software for vector analysis of the magnetization of long sediment cores: software for vector analysis. Geochem. Geophys. Geosyst. 6. https://doi.org/10.1029/2005GC001036

Merrill, R.T., McFadden, P.L., 2003. The geomagnetic axial dipole field assumption. Physics of the Earth and Planetary Interiors 139, 171–185. https://doi.org/10.1016/j.pepi.2003.07.016

Merrill, R.T., McFadden, P.L., 1994. Geomagnetic field stability: Reversal events and excursions. Earth and Planetary Science Letters 121, 57–69. https://doi.org/10.1016/0012-821X(94)90031-0

Münchow, A., Padman, L., Fricker, H.A., 2014. Interannual changes of the floating ice shelf of Petermann Gletscher, North Greenland, from 2000 to 2012. J. Glaciol. 60, 489–499. https://doi.org/10.3189/2014jog13j135

Münchow, A., Padman, L., Washam, P., Nicholls, K., 2016. The Ice Shelf of Petermann Gletscher, North Greenland, and Its Connection to the Arctic and Atlantic Oceans. Oceanog. 29, 84–95. https://doi.org/10.5670/oceanog.2016.101

Nares, G., 1878. Results derived from the Arctic Expedition 1875-76.

National Centers for Environmental Information, 2023. State of the Geomagnetic Field 2023. https://doi.org/10.25923/CWW1-SC35

National Centers for Environmental Information, 2022. State of the Geomagnetic Field 2022. https://doi.org/10.25923/8R5D-FJ70

National Centers for Environmental Information, 2021. State of the Geomagnetic Field 2021. WMM Annual Report 13.

Nick, F.M., Vieli, A., Andersen, M.L., Joughin, I., Payne, A., Edwards, T.L., Pattyn, F., Van De Wal, R.S.W., 2013. Future sea-level rise from Greenland's main outlet glaciers in a warming climate. Nature 497, 235–238. https://doi.org/10.1038/nature12068

Nilsson, A., Holme, R., Korte, M., Suttie, N., Hill, M., 2014. Reconstructing Holocene geomagnetic field variation: new methods, models and implications. Geophysical Journal International 198, 229–248. https://doi.org/10.1093/gji/ggu120

Nilsson, A., Muscheler, R., Snowball, I., 2011. Millennial scale cyclicity in the geodynamo inferred from a dipole tilt reconstruction. Earth and Planetary Science Letters 311, 299–305. https://doi.org/10.1016/j.epsl.2011.09.030

Nilsson, A., Suttie, N., Stoner, J.S., Muscheler, R., 2022. Recurrent ancient geomagnetic field anomalies shed light on future evolution of the South Atlantic Anomaly. Proc. Natl. Acad. Sci. U.S.A. 119, e2200749119. https://doi.org/10.1073/pnas.2200749119

Occhietti, S., Parent, M., Lajeunesse, P., Robert, F., Govare, É., 2011. Late Pleistocene–Early Holocene Decay of the Laurentide Ice Sheet in Québec–Labrador, in: Developments in Quaternary Sciences. Elsevier, pp. 601–630. https://doi.org/10.1016/b978-0-444-53447-7.00047-7

Ogg, J.G., 2020. Geomagnetic Polarity Time Scale, in: Geologic Time Scale 2020. Elsevier, pp. 159–192. https://doi.org/10.1016/b978-0-12-824360-2.00005-x

Ólafsdóttir, S., Geirsdóttir, Á., Miller, G.H., Stoner, J.S., Channell, J.E.T., 2013. Synchronizing Holocene lacustrine and marine sediment records using paleomagnetic secular variation. Geology 41, 535–538. https://doi.org/10.1130/G33946.1

Ólafsdóttir, S., Reilly, B.T., Bakke, J., Stoner, J.S., Gjerde, M., Van Der Bilt, W.G.M., 2019. Holocene paleomagnetic secular variation (PSV) near 80° N, Northwest Spitsbergen, Svalbard: Implications for evaluating High Arctic sediment chronologies. Quaternary Science Reviews 210, 90–102. https://doi.org/10.1016/j.quascirev.2019.03.003

Olson, P., Aurnou, J., 1999. A polar vortex in the Earth's core. Nature 170–173.

Opdyke, N.D., 1972. Paleomagnetism of deep-sea cores. Reviews of Geophysics 10, 213–249. https://doi.org/doi:10.1029/RG010i001p00213

Opdyke, N.D., Channell, J.E.T., 1996. Magnetic Stratigraphy. San Diego: Academic press.

Pados-Dibattista, T., Pearce, C., Detlef, H., Bendtsen, J., Seidenkrantz, M.-S., 2022. Holocene palaeoceanography of the Northeast Greenland shelf. Clim. Past 18, 103–127. https://doi.org/10.5194/cp-18-103-2022

Pavón-Carrasco, F.J., De Santis, A., 2016. The South Atlantic Anomaly: The Key for a Possible Geomagnetic Reversal. Front. Earth Sci. 4. https://doi.org/10.3389/feart.2016.00040

Reilly, B.T., Stoner, J.S., Mix, A.C., Walczak, M.H., Jennings, A., Jakobsson, M., Dyke, L., Glueder, A., Nicholls, K., Hogan, K.A., Mayer, L.A., Hatfield, R.G., Albert, S., Marcott, S., Fallon, S., Cheseby, M., 2019. Holocene break-up and reestablishment of the Petermann Ice Tongue, Northwest Greenland. Quaternary Science Reviews 218, 322–342. https://doi.org/10.1016/j.quascirev.2019.06.023

Reilly, B.T., Stoner, J.S., Ólafsdóttir, S., Jennings, A., Hatfield, R., Kristjánsdóttir, G.B., Geirsdóttir, Á., 2023. The Amplitude and Timescales of 0–15 ka Paleomagnetic Secular Variation in the Northern North Atlantic. JGR Solid Earth 128, e2023JB026891. https://doi.org/10.1029/2023JB026891

Reimer, P.J., Austin, W.E.N., Bard, E., Bayliss, A., Blackwell, P.G., Bronk Ramsey, C., Butzin, M., Cheng, H., Edwards, R.L., Friedrich, M., Grootes, P.M., Guilderson, T.P., Hajdas, I., Heaton, T.J., Hogg, A.G., Hughen, K.A., Kromer, B., Manning, S.W., Muscheler, R., Palmer, J.G., Pearson, C., Van Der Plicht, J., Reimer, R.W., Richards, D.A., Scott, E.M., Southon, J.R., Turney, C.S.M., Wacker, L., Adolphi, F., Büntgen, U., Capano, M., Fahrni, S.M., Fogtmann-Schulz, A., Friedrich, R., Köhler, P., Kudsk, S., Miyake, F., Olsen, J., Reinig, F., Sakamoto, M., Sookdeo, A., Talamo, S., 2020. The IntCal20 Northern Hemisphere Radiocarbon Age Calibration Curve (0–55 cal kBP). Radiocarbon 62, 725–757. https://doi.org/10.1017/RDC.2020.41

Ribeiro, S., Sejr, M.K., Limoges, A., Heikkilä, M., Andersen, T.J., Tallberg, P., Weckström, K., Husum, K., Forwick, M., Dalsgaard, T., Massé, G., Seidenkrantz, M.-S., Rysgaard, S., 2017. Sea ice and primary production proxies in surface sediments from a High Arctic Greenland fjord: Spatial distribution and implications for palaeoenvironmental studies. Ambio 46, 106–118. https://doi.org/10.1007/s13280-016-0894-2

Rignot, E., Kanagaratnam, P., 2006. Changes in the Velocity Structure of the Greenland Ice Sheet. Science 311, 986–990. https://doi.org/10.1126/science.1121381

Rudels, B., Björk, G., Nilsson, J., Winsor, P., Lake, I., Nohr, C., 2005. The interaction between waters from the Arctic Ocean and the Nordic Seas north of Fram Strait and along the East Greenland Current: results from the Arctic Ocean-02 Oden expedition. Journal of Marine Systems 55, 1–30. https://doi.org/10.1016/j.jmarsys.2004.06.008

Rysgaard, S., Vang, T., Stjernholm, M., Rasmussen, B., Windelin, A., Kiilsholm, S., 2003. Physical Conditions, Carbon Transport, and Climate Change Impacts in a Northeast Greenland Fjord. Arctic, Antarctic, and Alpine Research 35, 301–312. https://doi.org/10.1657/1523-0430(2003)035[0301:pcctac]2.0.co;2

Sejr, M.K., Krause-Jensen, D., Rysgaard, S., Sørensen, L.L., Christensen, P.B., Glud, R.N., 2011. Air–sea flux of CO2 in arctic coastal waters influenced by glacial melt water and sea ice. Tellus B: Chemical and Physical Meteorology 63, 815. https://doi.org/10.1111/j.1600-0889.2011.00540.x

Shaar, R., Tauxe, L., Goguitchaichvili, A., Devidze, M., Licheli, V., 2017. Further evidence of the Levantine Iron Age geomagnetic anomaly from Georgian pottery. Geophys. Res. Lett. 44, 2229–2236. https://doi.org/10.1002/2016GL071494

Shaar, R., Tauxe, L., Ron, H., Ebert, Y., Zuckerman, S., Finkelstein, I., Agnon, A., 2016. Large geomagnetic field anomalies revealed in Bronze to Iron Age archeomagnetic data from Tel Megiddo and Tel Hazor, Israel. Earth and Planetary Science Letters 442, 173–185. https://doi.org/10.1016/j.epsl.2016.02.038

Simon, Q., Thouveny, N., Bourlès, D.L., Nuttin, L., Hillaire-Marcel, C., St-Onge, G., 2016. Authigenic 10Be/9Be ratios and 10Be-fluxes (230Thxs-normalized) in central Baffin Bay sediments during the last glacial cycle: Paleoenvironmental implications. Quaternary Science Reviews 140, 142–162. https://doi.org/10.1016/j.quascirev.2016.03.027

Singer, B.S., Jicha, B.R., Condon, D.J., Macho, A.S., Hoffman, K.A., Dierkhising, J., Brown, M.C., Feinberg, J.M., Kidane, T., 2014. Precise ages of the Réunion event and Huckleberry Ridge excursion: Episodic clustering of geomagnetic instabilities and the dynamics of flow within the outer core. Earth and Planetary Science Letters 405, 25–38. https://doi.org/10.1016/j.epsl.2014.08.011

Snowball, I., Muscheler, R., 2007. Palaeomagnetic intensity data: an Achilles heel of solar activity reconstructions. The Holocene 17, 851–859. https://doi.org/10.1177/0959683607080531

Stein, R., Nam, S.-I., Grobe, H., Hubberten, H., 1996. Late Quaternary glacial history and short-term ice-rafted debris fluctuations along the East Greenland continental margin. Geological Society, London, Special Publications 111, 135–151. https://doi.org/10.1144/GSL.SP.1996.111.01.09

Stoner, J.S., Channell, J.E.T., Hillaire-Marcel, C., 1995. Late Pleistocene relative geomagnetic paleointensity from the deep Labrador Sea: Regional and global correlations. Earth and Planetary Science Letters 134, 237–252. https://doi.org/10.1016/0012-821X(95)00134-X

Stoner, J.S., Channell, J.E.T., Hillaire-Marcel, C., Kissel, C., 2000. Geomagnetic paleointensity and environmental record from Labrador Sea core MD95-2024: global marine sediment and ice core chronostratigraphy for the last 110 kyr. Earth and Planetary Science Letters 183, 161–177. https://doi.org/10.1016/S0012-821X(00)00272-7

Stoner, J.S., Channell, J.E.T., Mazaud, A., Strano, S.E., Xuan, C., 2013. The influence of high-latitude flux lobes on the Holocene paleomagnetic record of IODP Site U1305 and the northern North Atlantic: Paleomagnetic Record of the N. Atlantic. Geochem. Geophys. Geosyst. 14, 4623–4646. https://doi.org/10.1002/ggge.20272

Stoner, J.S., Jennings, A., Kristjánsdóttir, G.B., Dunhill, G., Andrews, J.T., Hardardóttir, J., 2007. A paleomagnetic approach toward refining Holocene radiocarbon-based chronologies: Paleoceanographic records from the north Iceland (MD99-2269) and east Greenland (MD99-2322) margins: Holocene PSV and radiocarbon chronology. Paleoceanography 22, n/a-n/a. https://doi.org/10.1029/2006PA001285

Stoner, J.S., St-Onge, G., 2007. Chapter Three Magnetic Stratigraphy in Paleoceanography: Reversals, Excursions, Paleointensity, and Secular Variation, in: Developments in Marine Geology. Elsevier, pp. 99–138. https://doi.org/10.1016/S1572-5480(07)01008-1

St-Onge, G., Mulder, T., Francus, P., Long, B., 2007. Chapter Two Continuous Physical Properties of Cored Marine Sediments, in: Developments in Marine Geology. Elsevier, pp. 63–98. https://doi.org/10.1016/S1572-5480(07)01007-X

St-Onge, G., Stoner, J., 2011. Paleomagnetism Near the North Magnetic Pole: A Unique Vantage Point for Understanding the Dynamics of the Geomagnetic Field and Its Secular Variations. Oceanog. 24, 42–50. https://doi.org/10.5670/oceanog.2011.53

St-Onge, G., Stoner, J.S., Hillaire-Marcel, C., 2003. Holocene paleomagnetic records from the St. Lawrence Estuary, eastern Canada: centennial- to millennial-scale geomagnetic modulation of cosmogenic isotopes. Earth and Planetary Science Letters 209, 113–130. https://doi.org/10.1016/S0012-821X(03)00079-7

Suganuma, Y., Okuno, J., Heslop, D., Roberts, A.P., Yamazaki, T., Yokoyama, Y., 2011. Post-depositional remanent magnetization lock-in for marine sediments deduced from 10Be and paleomagnetic records through the Matuyama–Brunhes boundary. Earth and Planetary Science Letters 311, 39–52. https://doi.org/10.1016/j.epsl.2011.08.038

Suganuma, Y., Yokoyama, Y., Yamazaki, T., Kawamura, K., Horng, C.-S., Matsuzaki, H., 2010. 10Be evidence for delayed acquisition of remanent magnetization in marine sediments: Implication for a new age for the Matuyama–Brunhes boundary. Earth and Planetary Science Letters 296, 443–450. https://doi.org/10.1016/j.epsl.2010.05.031

Swarzenski, P.W., 2014. 210Pb Dating, in: Rink, W.J., Thompson, J. (Eds.), Encyclopedia of Scientific Dating Methods. Springer Netherlands, Dordrecht, pp. 1–11. https://doi.org/10.1007/978-94-007-6326-5_236-1

Syvitski, J.P.M., Lee, H.J., 1997. Postglacial sequence stratigraphy of Lake Melville, Labrador. Marine Geology 143, 55–79. https://doi.org/10.1016/s0025-3227(97)00090-x

Tarduno, J.A., Cottrell, R.D., Bono, R.K., Oda, H., Davis, W.J., Fayek, M., Erve, O.V. 'T, Nimmo, F., Huang, W., Thern, E.R., Fearn, S., Mitra, G., Smirnov, A.V., Blackman, E.G., 2020. Paleomagnetism indicates that primary magnetite in zircon records a strong Hadean geodynamo. Proc. Natl. Acad. Sci. U.S.A. 117, 2309–2318. https://doi.org/10.1073/pnas.1916553117

Tarduno, J.A., Cottrell, R.D., Watkeys, M.K., Hofmann, A., Doubrovine, P.V., Mamajek, E.E., Liu, D., Sibeck, D.G., Neukirch, L.P., Usui, Y., 2010. Geodynamo, Solar Wind, and Magnetopause 3.4 to 3.45 Billion Years Ago. Science 327, 1238–1240. https://doi.org/10.1126/science.1183445

Tauxe, L., 2010. Essentials of Paleomagnetism. University of Columbia Press.

Tauxe, L., 2006. Paleomagnetic principles and practice, Springer Science&Business Media. ed.

Tauxe, L., 1993. Sedimentary records of relative paleointensity of the geomagnetic field: Theory and practice. Reviews of Geophysics 31, 319–354. https://doi.org/10.1029/93RG01771

Tauxe, L., Pick, T., Kok, Y.S., 1995. Relative paleointenisty in sediments: a pseudo-Thellier approach. Geophysical Research Letters 22, 2885–2888. https://doi.org/10.1029/95GL03166

Tauxe, L., Wu, G., 1990. Normalized remanence in sediments of the western equatorial Pacific: Relative paleointensity of the geomagnetic field? Journal of Geophysical Research: Solid Earth 95, 12337–12350. https://doi.org/10.1029/JB095iB08p12337

Tauxe, L., Yamazaki, T., 2015. Paleointensities, University of California. ed. San Diego.

Tauxe, L., Yamazaki, T., 2007. Paleointensities, in: Scubert, G. (Ed.), Geomagnetism, Treatise on Geophysics. Oxford, pp. 509–564.

Terra-Nova, F., Amit, H., Hartmann, G.A., Trindade, R.I.F., Pinheiro, K.J., 2017. Relating the South Atlantic Anomaly and geomagnetic flux patches. Physics of the Earth and Planetary Interiors 266, 39–53. https://doi.org/10.1016/j.pepi.2017.03.002

Thellier, E., Thellier, O., 1959. Sur l'intensité du champ magnétique terrestre dans le passé historique et géologique. Ann. Geophys. 285–378.

Thompson, R., Oldfield, F., 1986. Environmental Magnetism, Springer Nature. ed. Allen & Uwin, London.

Tinto, K.J., Bell, R.E., Cochran, J.R., Münchow, A., 2015. Bathymetry in Petermann fjord from Operation IceBridge aerogravity. Earth and Planetary Science Letters 422, 58–66. https://doi.org/10.1016/j.epsl.2015.04.009

Trottier, A., Lajeunesse, P., Gagnon-Poiré, A., Francus, P., 2020. Morphological signatures of deglaciation and postglacial sedimentary processes in a deep fjord-lake (Grand Lake, Labrador). Earth Surf. Process. Landforms 45, 928–947. https://doi.org/10.1002/esp.4786

Usui, Y., Tarduno, J.A., Watkeys, M.K., Hofmann, A., Cottrell, R.D., 2009. Evidence for a 3.45-billion-year-old magnetic remanence: Hints of an ancient geodynamo from conglomerates of South Africa. Geochem Geophys Geosyst 10. https://doi.org/10.1029/2009GC002496

Valet, J.-P., Meynadier, L., 1998. A comparison of different techniques for relative paleointensity. Geophysical Research Letters 25, 89–92. https://doi.org/10.1029/97GL03489

Velle, J.H., Walczak, M.H., Reilly, B., St-Onge, G., Stoner, J.S., Fallon, S., Mix, A.C., Belanger, C., Forwick, M., 2021. High resolution inclination records from the Gulf of Alaska, IODP Expedition 341 Sites U1418 and U1419. Geophysical Journal International 229, 345–358. https://doi.org/10.1093/gji/ggab479

Verosub, K.L., 1977. Depositional and postdepositional processes in the magnetization of sediments. Reviews of Geophysics 15, 129–143. https://doi.org/10.1029/RG015i002p00129

Verosub, K.L., Banerjee, S.K., 1977. Geomagnetic excursions and their paleomagnetic record. Reviews of Geophysics 15, 145–155. https://doi.org/10.1029/RG015i002p00145

Verosub, K.L., Mehringer, J., Waterstraat, P., 1986. Holocene secular variation in western North Amercia: paleomagnetic record from Fish Lake, Harney County, Oregon. Journal of Physical Research: Solid Earth 91, 3609–3623. https://doi.org/10.1029/JB091iB03p03609

Vilks, G., Deonarine, B., Winters, G., 1987. Late quaternary marine geology of Lake Melville, Labrador.

Wardle, R.J., Paltanavage, A.H., Nolan, L.W., Leawood, T., 1997. Geological Map of Labrador. Geoscience Publications and Information Section.

Washam, P., Nicholls, K.W., Münchow, A., Padman, L., 2019. Summer surface melt thins Petermann Gletscher Ice Shelf by enhancing channelized basal melt. J. Glaciol. 65, 662–674. https://doi.org/10.1017/jog.2019.43

Weeks, R., Laj, C., Endignoux, L., Fuller, M., Roberts, A., Manganne, R., Blanchard, E., Goree, W., 1993. Improvements in long-core measurement techniques: applications in palaeomagnetism and palaeoceanography. Geophysical Journal International 114, 651–662. https://doi.org/10.1111/j.1365-246X.1993.tb06994.x

Winkelmann, D., Jokat, W., Jensen, L., Schenke, H.-W., 2010. Submarine end moraines on the continental shelf off NE Greenland – Implications for Lateglacial dynamics. Quaternary Science Reviews 29, 1069–1077. https://doi.org/10.1016/j.quascirev.2010.02.002

Xuan, C., Channell, J.E.T., 2009. UPmag: MATLAB software for viewing and processing u channel or other pass-through paleomagnetic data. Geochemistry, Geophysics, Geosystems 10. https://doi.org/10.1029/2009GC002584

Yoshimura, Y., 2022. The Cretaceous Normal Superchron: A Mini-Review of Its Discovery, Short Reversal Events, Paleointensity, Paleosecular Variations, Paleoenvironment, Volcanism, and Mechanism. Front. Earth Sci. 10, 834024. https://doi.org/10.3389/feart.2022.834024

Zwally, H.J., Giovinetto, M.B., Beckley, M.A., Saba, J.L., 2012. Antartic and Greenland Drainage Systems [WWW Document]. GSFC Cryospheric Sciences Laboratory. URL https://earth.gsfc.nasa.gov/cryo/data/polar-altimetry/antarctic-and-greenland-drainage-systems